On the viscoelasticity-induced particle migration in stirred vessels

Giovanni Meridiano

Department of Chemical Engineering
University College London

A thesis submitted for the degree of
Doctor of Philosophy from University College London

May 2023

I, Giovanni Meridiano confirm that the work presented in this thesis is my own. Where information has been derived from other sources, I confirm that this has been indicated in the thesis.

To the lily of the field and the bird of the air

Abstract

The objective of this thesis is the investigation of the behaviour of solid particles suspended in a viscoelastic liquid and subjected to mixing in a stirred vessel. In particular, the well-known phenomenon of viscoelasticity-induced particle migration, was observed for the first time in the flow field generated in stirred vessel. This thesis is divided in three parts.

First, we performed an experimental campaign aimed at the study of the mixing of a non-Newtonian liquid-solid suspension in a cylindrical vessel equipped with a dual-blade impeller. The experiments were performed with liquids with different rheological behaviours. Particle image velocimetry (PIV) was used to measure the velocity filed of the liquid while particle tracking velocimetry (PTV) was employed to measure velocity and concentration fields of the solids. We show that in the presence of viscoelasticity, the particles accumulate at the centre of the vortices created by the impeller.

We then focused on the viscoelasticity-induced migration in the flow field created by a Rushton turbine in an unbaffled vessel. We propose a scaling law for predicting the migration time as a function of the Weissenberg number (Wi). The experimental campaign shows that the particles migrate in the radial direction driven by the presence of gradients of shear-rate. Finally, the scaling law is validated against experimental data obtained at different Wi.

The third part, describes the development of CFD tool, based on the volume of fluid (VOF) framework, for the simulation of particles in viscoelastic fluids. The objectives were, (i) to use the VOF model to simulate a solid sphere in flow, and (ii) to simulate the rotational velocity of a sphere in a viscoelastic fluid. Although, the model was capable of simulating a solid sphere with good accuracy in the Newtonian case, the viscoelastic case failed to reproduce the results available in the literature

Impact statement

The significant level of sophistication of most formulated products and the everlasting need of achieving controlled and reproducible product quality, constitute a crucial challenge for the manufacturing of complex formulations. For some products, such as toothpaste, the ability of effectively including new functionalities and at the same time ensuring robustness of the manufacturing process has proven to be relevant for the overall health and well-being of consumers. One aspect of manufacturing that is central to this thesis is the mixing of solids in highly-viscous, complex fluids in mechanically agitated vessels. Regardless of the specific application, mixing is certainly one of the most important steps in many industrial processes. Its understanding can, and often does, leads to increased efficiency, reduced costs, and lower energy consumption, thereby benefiting both the producers and the consumers.

Among the various complex behaviours of solids in viscoelastic liquids, viscoelasticity-induced, cross-flow particle migration in stirred vessels emerged as a phenomenon of interest in this work. While the investigation of any novel or surprising experimental result is inherently of academic interest, the segregation of the solid phase caused by this phenomenon constitutes a clear hindrance to any mixing process. Additionally, a deep understanding of the causes of the migration phenomenon and their interaction with controllable process variables could lead to the exploitation of the migration as a separation device, which could prove useful in applications where conventional separation techniques fall short.

With the same objective in mind, the final part of this work explores the possibility of using a Volume of Fluid (VOF) computational approach as a tool for further investigation into viscoelasticity-induced particle migration. The relatively modest computational cost and easy implementation of this model, together with its wide availability in both commercial and open-source platforms, suggest that it could represent a useful tool for the simulation of multi-particle systems and large scale problems.

The key findings of this thesis provide insights into two crucial points. Firstly, solids in highly viscous, non-Newtonian fluids tend to segregate in specific areas of the flow, with the direction and velocity of the phenomenon being linked to the fluid dynamics of the flow and the rheological nature of the fluid. Secondly, the VOF method can be readily applied for the simulation of the dynamic of a single solid sphere in a viscoelastic fluid.

These novel findings hold great promise in developing new mixing and separation devices, as well as deepening our understanding of cross flow particle migration in complex, three-dimentional flows of non-Newtonian fluids.

Highlights

1. An experimental investigation was aimed to study the dynamics of solid particles in highly viscous, non-Newtonian fluids under agitation in a stirred vessel. The study utilized a toothpaste mixer design and demonstrated the effects of viscoelasticity-induced particle migration. The results showed that particles tend to accumulate in the core of the vortices formed in the flow domain and that the accumulation was caused by the viscoelasticity of the suspending liquid. The study contributes to the understanding of particle dynamics in non-Newtonian fluids and can be useful in industrial processes where such fluids are involved.

2. A second experimental campaign investigated the viscoelasticity-induced particle migration in a three-dimensional flow field generated by a Rushton turbine. The study aimed to validate a scaling law for predicting particle migration time as a function of the Weissenberg number and test the usefulness of simple heuristic arguments in capturing the phenomenon. The study used particle image velocimetry to reconstruct the three-dimensional velocity and deformation rate fields and particle tracking to measure the evolution of the particle distribution. The proposed scaling law was validated against experimental data obtained at different Weissenberg numbers, impeller diameters, and fluid compositions.

3. The VOF numerical method was utilized to simulate the rotational velocity of a solid sphere in a viscoelastic fluid at various Weissenberg numbers in a shear flow between parallel plates. The goal was to optimize simulation parameters for predicting the dynamics of solids in liquid and to investigate the impact of viscoelasticity on solid sphere rotation in simple shear flow. The study demonstrated successful outcomes in both aspects, highlighting the effectiveness of the VOF method for predicting rotational dynamics of solid particles in viscoelastic fluids under shear flow.

List of Publications and International Dissemination

This research led to the following publications in peer-reviewed academic journals:

- Weheliye, H. W., Meridiano, G., Mazzei, L., Angeli, P. Experimental investigation of the solid-liquid separation in a stirred tank owing to viscoelasticity. Physical Review Fluids., vol. 5, 2020.

- Migliozzi, S., G. Meridiano, Angeli, P., Mazzei, L P. Investigation of the swollen state of Carbopol molecules in non-aqueous solvents through rheological characterization. Soft Matter 16, 9799 – 9815, 2020.
- Meridiano, G., Weheliye, H. W., Mazzei, L., Angeli, P. Scaling law for the viscoelasticity-induced particle migration in stirred vessels. Journal of Non-Newtonian Fluid Mechanics, vol. 309, 2022.
- Meridiano, G., Mazzei, L., Angeli, P. Numerical investigation of the effect of viscoelasticity on the dynamics of a solid sphere in a shear flow using VOF. (in preparation)

Additionally, I was able to disseminate this work in the following international conferences:

- Meridiano, G., Weheliye, H. W., Mazzei, L., Angeli, P. Experimental and computational studies of the fluid dynamic behaviour of liquid-solid mixtures in agitated vessels, AIChE Meeting 2018, 28 October – 2 November 2018, Pittsburgh, USA.
- Meridiano G, Weheliye W, Mazzei L, Angeli P., Study of the mixing of solids in non-Newtonian media with PIV, 10th International Conference on Multiphase Flow (ICMF), May 19-24, 2019, Rio de Janeiro, Brazil.
- Meridiano, G., Weheliye, H. W., Mazzei, L., Angeli, P. Experimental investigation of the clustering of particles in non-Newtonian liquids in stirred vessels. Annual Meeting APS Division of Fluid Dynamics, 23 – 26 November 2019, Seattle, USA.

Table of Contents

List of Figures

List of Tables

List of Symbols and Abbreviations

Roman Symbols

$\langle C \rangle$	Average solids concentration
$\mathbf{A}$	Conformation tensor
$\mathbf{f}_b$	Body force per unit mass in the momentum conservation equation
$\mathbf{I}$	Identity matrix
$\boldsymbol{u}$	Velocity vector
$\boldsymbol{u}_r$	Compression velocity vector
a	Mobility factor in the Giesekus model
a_T	Temperature shift factor
c^*	Polymer characteristic overlapping concentration
d_t	Tracer diameter
De	Deborah number
e_i	unit vector in the direction i
G	Elastic modulus of the Hookean solid
G'	Storage modulus
G''	Loss modulus
Mw	Polymer molecular weight
N_1	First normal stress difference
N_2	Second normal stress difference
p	Thermodynamic pressure

S^* Shannon entropy

s_x Infinitesimal displacement along x

St Stokes number

T Temperature

T_0 Period of oscillation

t_C Droplet relaxation time according to Cox (1969)

t_r Droplet relaxation time according to Loewenberg and Hinch (1996)

v_g particle terminal velocity

Wi Weissenberg number

Greek Symbols

α Volume fraction

α Interfacial tension

$\mathbf{\nabla u}$ Velocity gradient tensor

$\boldsymbol{\sigma}$ Total fluid stress tensor

$\boldsymbol{\tau}$ Fluid stress tensor

$\boldsymbol{\Theta}$ Log-conformation tensor

δ loss tangent

$\dot{\gamma}_c$ Scale value of the shear rate

$\dot{\gamma}_{yx}$ yx component of the shear rate

$\dot{\gamma}^0_{yx}$ Shear amplitude of the sinusoidal oscillation

ε_{yx} Shear component of the deformation tensor

ε^0_{yx} Strain amplitude of the sinusoidal oscillation

η Newtonian viscosity

η' Dynamic viscosity

η'' Loss viscosity

$\eta(\dot{\gamma})$ Non-Newtonian viscosity

η_0 Zero-shear rate viscosity

η_k, λ_k Parameters for the kth mode of the generalised Maxwell model

η_p Polymer contribution to the viscosity

η_s Solvent contribution to the viscosity

κ Interface curvature

λ, λ_1 Fluid relaxation time

λ_2 Fluid retardation time

λ_Z Relaxation time according t Zimm's theory

$\dot{\gamma}$ Rate of deformation tensor

ν Kinematic viscosity

ω Angular frequency

ψ Phase angle between shear stress and shear rate in SAOS tests

Ψ_1 First normal stress coefficient

Ψ_2 Second normal stress coefficient

ρ fluid density

ρ_t Tracer density

τ_c Scale value of the stress

τ_p Polymer contribution to the stress tensor

τ_s Solvent contribution to the stress tensor

$\tau_{\dot{\gamma}}$ Time scale of variation of $\dot{\boldsymbol{\gamma}}$

τ_{yx} Shear component of the stress tensor

Superscripts

$\triangledown$ Upper convected time derivative

* Dimensionless quantity

Acronyms

CFD Computational Fluid Dynamic

CHT Circular Hough transform algorithm

CP Cone and plate

FFT Fast Fourier Transform

FV Finite Volume

LDA Laser Doppler Anemometry

LS Level-set method

PAA Polyacrylamide

PBT Pitched Blade Turbine

PBT Pitched blades turbine

PIV Particle Image Velocimetry

PMMA Poly(methyl methacrylate)

PP Parallel plate

PTV Particle Tracking Velocimetry

rpm Rotations per minutes

SAOS Small Amplitude Oscillatory Shear

SAOS Small amplitude oscillatory shear

VOF Volume Of Fluid

XG Xanthan gum

Chapter 1

Introduction

1.1 Scope of the research

The scope of this research is to investigate the phenomenon of viscoelasticity-induced particle migration in the complex, three-dimensional flow such as those observed in stirred tanks. The work was part of the wider aim to study the effect of complex rheological behaviours on the efficacy of conventional mixing systems, in the context of healthcare formulation manufacturing. The research is part of the EPSRC Future Formulations grant CORAL, a collaboration between the Departments of Chemical Engineering, Mechanical Engineering and Mathematics at UCL and is partly sponsored by the industrial partner GlaxoSmithKline.

1.2 Motivation

Complex formulations are a common feature of our daily lives, encompassing a wide range of items such as cosmetic and healthcare products, food, building materials, and inks. The composition of such materials usually includes multiple phases and active agents, which must be carefully balanced to achieve the desired functionality and texture of the final product. This level of sophistication, coupled with the need to ensure controlled and reproducible quality of the finished product, represents a significant challenge in manufacturing.

In certain sectors, such as oral health, the ability to efficiently incorporate novel product functionalities while maintaining a robust manufacturing process is not only important to manufacturers but also to the overall health and well-being of consumers (WHO, 2020). Toothpaste serves as a prime example, as it is a daily essential for millions of people worldwide, playing a fundamental role in maintaining good oral healthcare and preventing diseases. Typical toothpaste formulations comprise of a liquid phase (typically water), a dispersed phase as a rheology modifier, a solid phase with thickening and

abrasive properties, as well as active chemicals such as fluoride.

The manufacturing of toothpaste, like many other formulated products, involves a batch approach where raw materials are added sequentially in stirred vessels with complex geometries. However, these vessels are characterized by large volumes and complex flow fields, which can lead to dramatic concentration and temperature heterogeneity within the vessels for highly viscous, or complex fluids. This complexity makes it arduous to achieve precise control of the process conditions, and manufacturing protocols are often based on empirical experience rather than a clear scientific understanding of the system.

One specific challenge identified in this work is the segregation of the solid phase caused by the phenomenon of viscoelasticity-induced particle migration. The cross-streamlines, viscoelasticity-induced particle migration refers to the phenomenon where particles suspended in a viscoelastic fluid experience an unbalanced force that drives them in preferential directions. This effect is caused by the combined effect on a non-uniform flow field and the viscoelasticity of the suspending fluid. The migration of particles has important implications for various applications, including microfluidics, biotechnology, and material science (Yuan et al., 2018; Zhou and Papautsky, 2020). Most of the available literature of this phenomenon is limited to simple flow configurations (flow between parallel plates, channel or Couette flow, etc.). In these conditions, the relationship between the features of the underlying flow and the intensity of the viscoelastic forces causing the migration can be relatively easy to understand. The flow fields inside stirred vessels are not generally simple. They are almost always three-dimensional with regions of high shear, vortices, and eddies. We will show that in these conditions, the viscoelasticity of the fluid can induce particle migration, leading to the formation of clusters or aggregates, which can impact product quality and yield. At the same time, the complexity of the flow field prevents a straightforward analysis of the migration phenomenon and the consequent prediction of industrially relevant parameters like mixing efficiency or agglomeration time.

By gaining a better understanding of the underlying physics, it may be possible to develop new strategies for controlling (or maybe exploiting) particle migration, improving the efficiency and effectiveness of many industrial processes.

1.3 Research objectives

The proposed research aims at investigating the correlation between viscoelasticity-induced particle migration and the relevant rheological and flow dynamic quantities. Particular attention will be given to the analysis of the effects of the fluid relaxation time and the deformation rate generated by the rotation of the impellers, on the particle migration inside mixers. The goal is to develop a scaling law that can predict the characteristic migration time based on the relevant viscoelastic properties of the flow. To achieve this objective, advanced experimental techniques will be employed, including particle image velocime-

try (PIV) and particle-tracking velocimetry (PTV), to visualize the flow field and track the movement of the particles. The rheological properties of the fluid will be measured using a rotational rheometer, and the results will be used to validate the developed scaling law. The findings of this research will provide a deeper understanding of the complex interplay between viscoelasticity and particle migration in stirred vessels. The developed scaling law can be used to optimize the design and operation of industrial mixers for various applications, resulting in improved product quality and process efficiency.

A separate but at the same time relevant objective is to develop a Volume of Fluid (VOF) Computational Fluid Dynamics (CFD) approach for the simulation of the dynamic of solids suspended in a viscoelastic fluid. Although other approaches have been proven successful in simulating similar systems, a consensus on the best computational tools available for tackling such problems is still lacking. In this work, we will develop a VOF-based CFD approach that can simulate the dynamics of a single solid particle suspended in a viscoelastic fluid. Within this simulation framework, both the solid and the fluid phases will be treated as two fluids. The VOF method is a popular technique for simulating multiphase flows, which has been widely used in industry and academia due to its simplicity and accuracy. Our approach will be based on OpenFOAM, an open-source CFD code that has a large user community and is known for its robustness and flexibility. Most of the focus will be spent on the identification of the parameter space within which the assumed equivalence between a solid sphere and a highly viscous liquid is valid. The performance of this approach will be then evaluated by comparing its results with experimental data and other numerical methods available in the literature.

1.4 Thesis outline

This thesis is structured in six chapters. An introduction to the background and motivation for this work has been provided in this introductory chapter, together with the main objectives of the research. The literature review found in Chapter 2 aims to provide the fundamental theory necessary for the interpretation of the results presented in the following chapters. First, the concept of stirred vessels and their general working principle is introduced, together with a review on the state of the art on their use for the mixing of complex liquid-solid systems. Then, a general introduction on the rheology of complex fluids is presented with particular emphasis on their classification and characterization. This is followed by a more careful analysis on the mathematical description of viscoelastic fluids and an overview of the available constitutive equations and their range of application. The results are presented throughout Chapters 3 to 5. Given the variety of approaches used, each chapter contains a small introduction, its individual methodology, results and conclusions subsections.

Chapter 3 investigates the motion of solid particles dispersed in highly viscous poly-

mer suspensions agitated in a vessel by a dual paddles impeller. The impeller design was based on an existing mixing system for the manufacturing of toothpaste. First, the experimental methodology and findings are presented, demonstrating the accumulation of particles caused by the action of the viscoelasticity-induced particle migration. The study employs a refractive index matching method and a combination of particle image velocimetry and particle-tracking velocimetry techniques to measure the velocity fields of the solid and fluid phases simultaneously, along with the spatio-temporal distribution of the solids in the tank. The experimental data show that in a Newtonian ambient fluid, particles disperse uniformly in the plane of measurement, while in a strongly shear-thinning, viscoelastic ambient fluid, they tend to accumulate in the core of the vortices formed in the flow domain. The study also finds that the solids migrate to the core of the vortices when the ambient fluid is purely viscoelastic fluid.

In Chapter 4, the study is restricted to the purely viscoelastic case and a scaling law is proposed for predicting the characteristic particle migration time as a function of the viscoelasticity of the flow. The law is validated against experimental data obtained in a stirred vessel equipped with a Rushton turbine. The shape of the impeller was chosen as an intermediate level of complexity between the simple two-dimensional Poiseuille or Couette-flow usually encountered in the literature and the complex three-dimensional flows present in industral mixers. In particular, the three-dimensional flow field of a Rushton turbine could be easily studied in terms of its main directions of strain, which provided a better understanding of the migration dynamics and the underlying forces driving it. Particle image velocimetry is adopted to reconstruct the three-dimensional velocity and deformation rate fields generated by the rotation of the Rushton turbine in both Newtonian and viscoelastic fluids.

Chapter 5 focuses on the simulation of the rotation of a solid spherical particle in a shear flow between two parallel plates, using a multiphase VOF numerical scheme. The chapter begins with the mathematical description of the deformation of viscous droplet in simple shear flow and the presentation of the analytical solutions available in the literature. These equations allowed the prediction of the transient deformation of a viscous drop in simple shear flow as a function of the constitutive properties of the two phases. The VOF model is then used to derive the optimal values of the constitutive properties to assign to the dispersed phase. Finally, the model is used to derive the rotational velocity of a solid sphere suspended in a viscoelastic fluid in simple shear flow.

Finally, Chapter 6 summarises the final remarks of this research and gives recommendations for future research.

Chapter 2

Theoretical Background and Literature Review

The main purpose of this chapter is to summarise the relevant literature and present an overview of the theoretical background needed to interpret the results of this research. First, the state of the art on the use of stirred vessels for the mixing of liquid-solid suspensions is introduced. Then, generalities on the rheology of complex fluids and their mathematical modelling are presented, focusing on the most relevant material functions and constitutive equations used throughout the results chapters. This is followed by a description of some of the numerical algorithms available for the simulation of multiphase systems. Particular emphasis will be given to the volume of fluid (VOF) method and to its implementation in the open-source software OpenFoam.

2.1 Stirred vessels and laser based velocimetry

Mixing is an essential unit operation in the process industry playing a critical role in nearly 80% of the existing fields Atiemo-Obeng et al. (2004). Typical industrial mixing problems involve the blending of miscible liquids, the dispersing of gases in liquids, the creation of liquid-liquid emulsions and the suspension of solids in liquids. Solid-liquid mixing is one of the most important mixing processes as it plays a crucial role in many unit operations such as suspension polymerization, solid-catalyzed reactions, dispersion of solids, dissolution, leaching, crystallization and precipitation (Zlokarnik, 2001; Atiemo-Obeng et al., 2004).

Given the wide range of application, there is no single piece of equipment capable of performing efficiently in all possible conditions and engineers have developed several apparatuses with specific ranges of application (Nienow et al., 1997). Among these, stirred tanks are the most common piece of equipment used in industry to suspend solids in liquids, and are of particular interest for this research. The terms mixing tank, mechanically agitated tank and stirred tank are here used interchangeably.

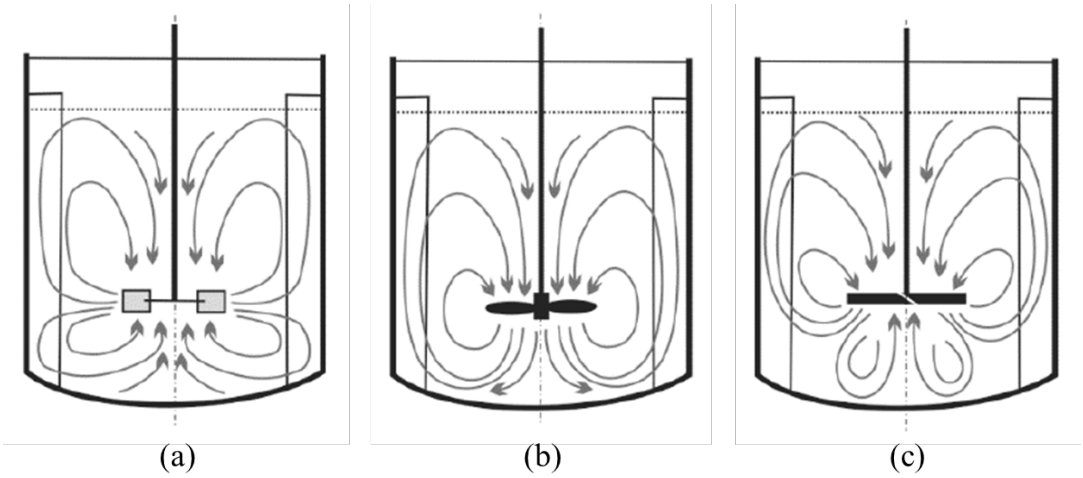

Figure 2.1: Circulation patterns in fully baffled tanks: (a) a double circulation loops with a radial impeller, (b) purely axial flow with a hydrofoil, and (c) angled discharge with a pitched-blade-turbine (PBT) pumping down (adapted from Jaszczur and Młynarczykowska (2020)).

Stirred tanks are usually constituted by a cylindrical vessel equipped with one or more mechanical stirrers. Although they are conceptually very simple, their design can be complex and is commonly based on experience. The geometric configuration of both impeller and tank, together with the fluid physical properties, in particular viscosity, dramatically affect the fluid dynamics of the system. Any rotating impeller in a mixing tank creates a characteristic, three-dimensional flow field constituted by a rotational flow (i.e. a flow in the angular direction), and additionally, a superimposed flow pattern that can be axial, radial or mixed (see. Fig. 2.1). The relative intensity of these two components depends on both the configuration of the system (i.e. position of the impeller, relative impeller to tank diameter, presence of baffles, etc.) and on the impeller shape. Examples of common shapes for industrial impellers are reported in Fig. 2.2. Exhaustive experimental work was conducted in the second half of the last century to characterise and study the flow fields generated by standard impeller designs (Metzner and Taylor, 1960; Nienow and Miles, 1978; Yianneskis et al., 1987; Kresta and Wood, 1993; Jaworski et al., 1996)

Many everyday items as well as many liquids of industrial interest are complex, or *non-Newtonian*, fluids. The exact definition of such class of fluids will be given in the following sections. For the moment, we will consider as non-Newtonian those fluids, suspensions, slurries or emulsions that produce a non-predictable (or "complex") response to the application of a stress. This complex response is often responsible for the poor mixing performances of typical impeller-tank configurations (Dickey, 2015).

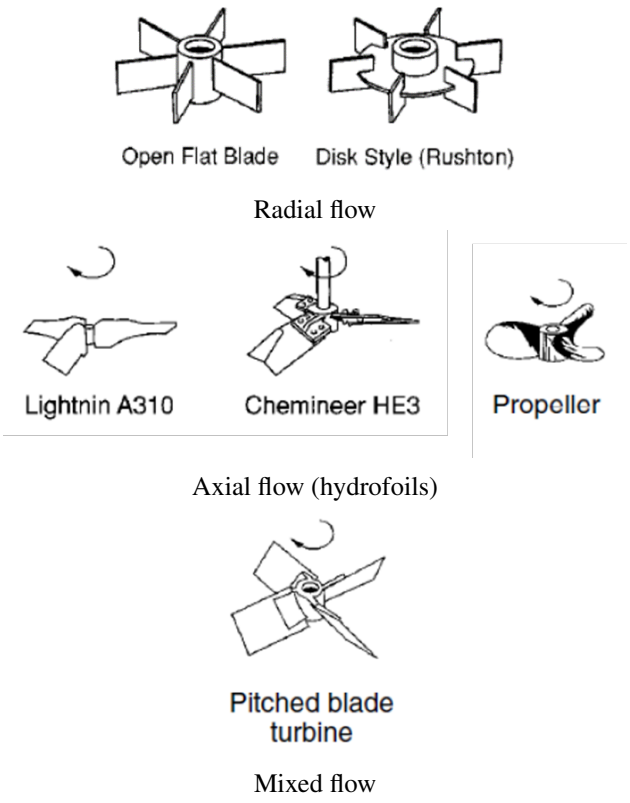

Figure 2.2: Common impeller designs (Atiemo-Obeng et al., 2004).

For example, non-Newtonian behaviour is usually accompanied by high viscosity (higher that 1 $Pa \cdot s$) at which point, the viscosity alone reduces the mixing efficiency by strongly reducing the circulation of fluid in the vessel (see Fig. 2.3a). Another more complex non-Newtonian behaviour includes the presence of a yield-stress (common in gel-like materials), that is, a minimum amount or force needs to be delivered to a fluid in order to initiate a flow. These fluids exhibit an initial high resistance to motion and/or

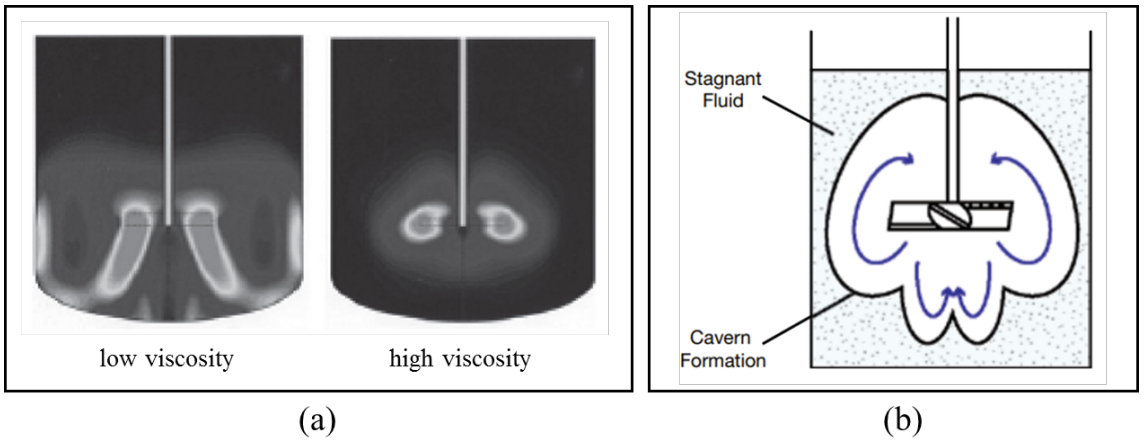

Figure 2.3: Examples of mixing issues: (a) Reduction of liquid circulation cause by high viscosity and, (b) formation of caverns around the impeller (adapted from Kresta et al. (2015) and Dickey (2015)).

the formation of caverns of moving fluid surrounded by an almost stagnant region (see Fig. 2.3b). The presence of an elastic response is also a typical feature of non-Newtonian fluids. Fluids of this kind can behave like dough or melts of polymeric materials and rotate together with the impeller in an almost solid-like fashion.

To prevent the aforementioned issues, specialized equipment, namely close-clearance impellers, are usually necessary for performing mixing in such conditions. These impellers are typically large in size, nearly the same size as the tank diameter, and provide gentle blending of liquids at low shear. The most common designs are the anchor and the helical ribbon impellers, shown in Fig. 2.4a and 2.4b. Another relevant example is found in the work of Cortada Garcia (2018), who described the mixing of non-Newtonian fluids in a dual coaxial impeller used for the manufacturing of oral healthcare products (Fig. 2.4c). This particular configuration was designed for the mixing of a highly viscous, non-Newtonian solution of glycerol, polyethylene glycol (PEG) and Carbopol with a solid phase.

(a) Anchor **(b)** Helical ribbon **(c)** Dual coaxial impellers

Figure 2.4: Examples of close-clearance impellers with , (a) Anchor impeller, (b) helical ribbon impeller and, (c) Dual impeller for toothpaste manufacturing constituted by one central, multi-paddles impeller and a secondary scraper (Cortada Garcia, 2018).

In stirred vessels, the degree of dispersion of the solid phase is generally classified into three levels: on-bottom motion, complete off-bottom suspension, and uniform suspension. These are illustrated in Fig. 2.5. Most of the studies on the mixing of solids-liquid systems in stirred vessels have focused on Newtonian fluids, usually operating in turbulent regime. Over the years, numerous solutions have been proposed for optimizing these systems. A detailed review of these solutions is beyond the scope of this article but can be found in the comprehensive works of Atiemo-Obeng et al. (2004) and Kresta et al. (2015).

The few studies on the laminar mixing of liquid-solid suspensions involved Newtonian fluids and aimed to evaluate how the configuration of the mixing device (e.g., shape and dimensions of impellers, presence of baffles, etc.), the properties of the phases and the operating conditions influence the system performance (Bertrand et al., 2018; Ibrahim and Nienow, 1999; Lassaigne et al., 2016; Li et al., 2011; Gong et al., 2018). For example,

Ibrahim and Nienow (1999) investigated the effect of the impeller shape on the value of the minimum impeller speed needed to suspend the solid phase (i.e., the "just-suspending speed," N_{js}) for a large range of Reynolds numbers, while Lassaigne et al. (2016) used a pitched blades turbine (PBT) to show that the N_{js} increases when the particle diameter, the solid volume fraction, or the liquid viscosity increase. Limited information is available on the solid-liquid mixing in viscoelastic fluids. To the author's knowledge, the few existing studies are limited to the critical impeller speed required for particle suspension and to the liquid phase mixing times (Kawase et al., 1997; Mollaabbasi and Mohebbi Najmabad, 2016).

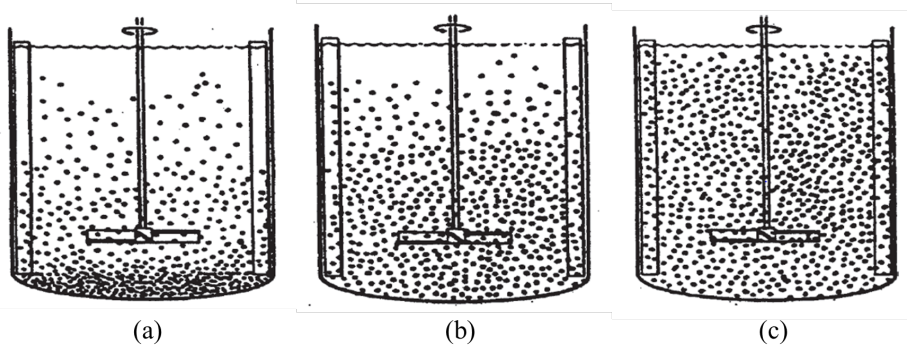

Figure 2.5: Degrees of suspension: (a) Partial suspension: some solids rest on the bottom of the tank for short periods; (b) Complete suspension: all solids are off the bottom of the vessel; (c) Uniform suspension: solids suspended uniformly throughout the vessel Atiemo-Obeng et al. (2004).

A phenomenon recently encountered when dealing with solid-liquid suspensions in stirred vessels is the spontaneous clustering of the solid phase. The involuntary accumulation of solids in separate regions of the flow represents a clear impairment to the mixing process and can affect negatively the quality of the products and/or the efficiency of the whole operation. The study by Wang et al. (2014) examined solid-liquid suspensions in Newtonian and non-Newtonian laminar flows, adopting a three-dimensional particle visualization method to expose the real-time trajectories of the particles. In their study, they showed that the particles clustered in the cores of the toroidal vortices created by the impeller rotation. In particular, the revolving blades of the impeller generated two coexisting, confined regions, above and below the blades, wherein the particles migrated. The migration was induced by inertial perturbations in the flow outside these regions, where, owing to the high shear rates present near the blades, the particle trajectories deviate from the path lines of the fluid, enabling the particles to cross the boundaries of these regions and settle into their cores.

In most of the studies reported above, the velocity fields were measured with laser-based techniques, such as particle image velocimetry (PIV) (Gabriele et al., 2011; Montante et al., 2012; Unadkat et al., 2009; Charalambidou et al., 2023; Samaras et al., 2020b,a) and Laser Doppler anemometry (LDA) (Guiraud et al., 1997; Micheletti and

Yianneskis, 2004; Virdung and Rasmuson, 2007a). When these techniques are applied to solid-liquid systems, especially dense ones, optical accessibility is a major limiting factor. Particles obstruct and scatter the laser light, which leads to results of poor quality. This is why the solid volume fraction in most of the studies mentioned above was limited to 1% (Guiraud et al., 1997; Montante et al., 2012; Unadkat et al., 2009). To overcome this problem, researchers have proposed to match the refractive index between the solids and the surrounding liquid (Gabriele et al., 2011; Micheletti and Yianneskis, 2004; Gong et al., 2018; Virdung and Rasmuson, 2007a; Li et al., 2018). The study by Gong et al. (2018) was the first to match the refractive indices of the solid and fluid phases in a laminar flow, and compared the mean fluid velocities obtained from experiments with those found numerically via CFD simulations.

As mentioned in Sec.1.2, accurately characterizing the velocity field inside a stirred vessel is crucial for understanding the effect of flow on solid particle migration. In this study, we will employ Particle Image Velocimetry (PIV) as the primary technique for this purpose.

2.1.1 Flow visualization in stirred vessels - PIV

The velocimetry technique based on particle images in its modern sense was introduced in the work of Adrian (1984). PIV is currently the state-of-the-art, optically based diagnostics tool for fluid dynamic. It involves injecting tracer particles into the fluid flow and illuminating them with a laser light sheet. A high speed camera and the laser are synchronised to take two consecutive snapshots of the flow. The velocity is then calculated from the displacement of the particles and the time difference between the two laser pulses. A schematic representation of all the steps involved in the PIV technique is reported in Fig. 2.6.

The selection of seeding particles is a crucial aspect of PIV systems. The main requirements are that the particles accurately follow the fluid flow without introducing any perturbations. This implies that, once the flow is initiated, the seeding particles rapidly relax to the local fluid velocity. This condition is achieved when the particle terminal velocity, denoted by v_g, is small relative to the fluid velocity and their Stokes number, denoted by St, is much less than 1. An exact definition of these terms will be give in Chapter 3. It is noted that St quantifies the particle response time to the fluid flow while v_g is the steady state velocity attained by a particle falling in a fluid under the action of gravity. Both these quantities depend on particle size, density and the fluid properties. Therefore, to ensure rapid relaxation of particles to the local fluid velocity, seeding particles with small diameters and a similar density to the fluid (ideally neutrally buoyant) are required.

The choice of particle material is dependent on the nature of the fluid being investi-

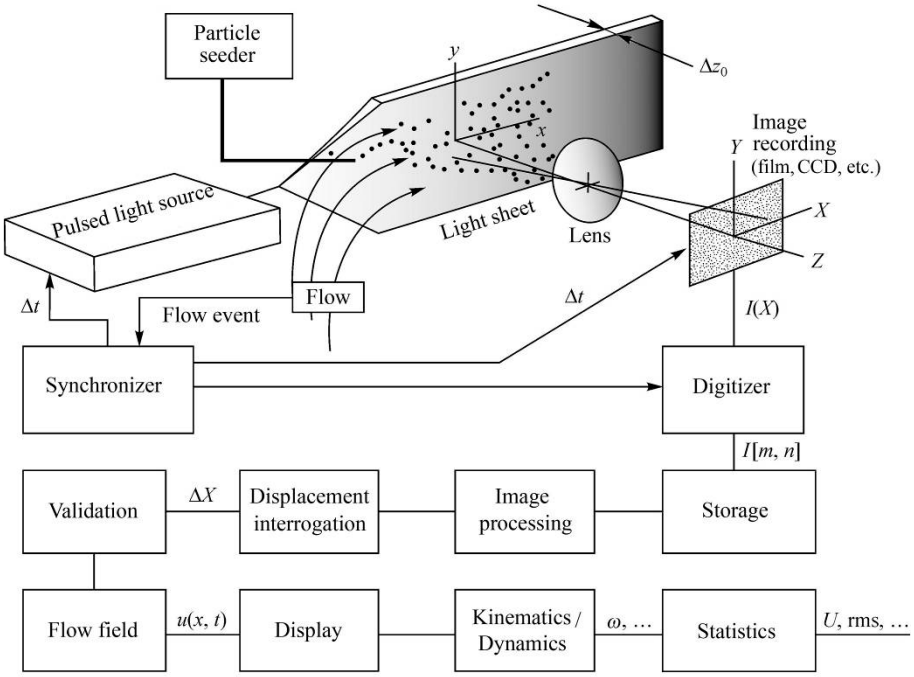

Figure 2.6: Schematic representation of the PIV method (Adrian, 1984).

gated. Typically, glass beads, polystyrene, polyethylene, aluminum flakes or oil droplets (for gas fluids) are used for macro PIV investigations, with a diameter range of 10 to 100 micrometers. Refractive index of the seeding particles should be different from that of the fluid being seeded to allow for scattering of the laser sheet by the particles towards the camera. In certain conditions, fluorescent particles may also be used.

PIV does not measure the velocities of each particle individually; instead, the local velocity of the fluid is obtained by tracking the displacement of an ensemble of particles within an interrogation window. An interrogation window (W) is a subset of the image, typically constitute by 16x16, 32x32, or 64x64 pixels, within which a certain number of seeding particles are located. When adequate hardware is used, the fluid can be completely masked so that the images show only the position of the particles that are emitting sufficiently intense light; in other words, those that are illuminated by the laser on the plane of interest. In these conditions, each interrogation window has a specific intensity distribution (I). The value of the average displacement for the interrogation window is then found by performing a cross-correlation analysis between the two images. The cross-correlation analysis involves calculating the correlation $C(\mathbf{s})$ between two images by shifting one image relative to the other and computing the correlation between the two images at each shift. The shift that produces the maximum correlation value corresponds to the displacement between the two images (Top of Fig. 2.7)

The mathematical expression of the cross-correlation function for an interrogation

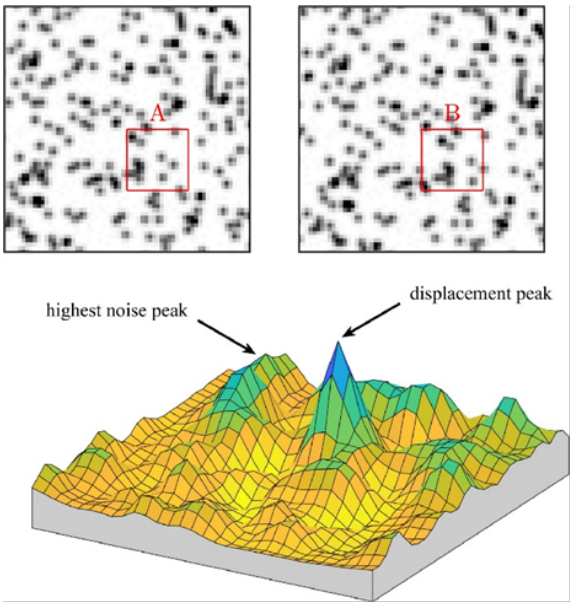

Figure 2.7: Top: Example of a section of a PIV image pair representing the particle image distribution at the time t_0 (left) and $t_0 + \Delta t$ (right). The interrogation windows A and B are highlighted by the red boxes. Bottom: The corresponding cross-correlation function features a distinct peak representing the particle image displacement (Scharnowski and Kähler, 2020).

window is:

$$C(\mathbf{s}) = \int_W I_1(\mathbf{x}) I_2(\mathbf{x}+\mathbf{s}) d\mathbf{x} \tag{2.1}$$

where I_1 and I_2 are the intensity distributions of the window on images 1 and 2 respectively, $\mathbf{x}$ is coordinates vector and $\mathbf{s}$ is the displacement or shift of the second image with respect to the first one. The representation of $C(\mathbf{X})$ in the $s_x - s_y$ plane is a series of peaks (Bottom of Fig. 2.7). The value of $\mathbf{s}$ corresponding to the largest peak is taken as the average displacement for that interrogation window.

It can be shown that the computation of Eq. 2.1 on an interrogation window with NxN points requires N^4 operations. This number of operations rapidly becomes very large (Bastiaans, 2000). In reality, the correlation between two images is evaluated by using Fourier's theory. This technique, sometimes referred to as phase-correlation, involves first calculating the Fast Fourier Transform (FFT) of each image and then compute the phase difference between the FFTs of the two images. Finally, the inverse FFT is used to obtain the displacement between the images in the spatial domain. The phase-correlation method, performed on the same NxN grid, requires $\mathcal{O}(N^2 \log_2 N)$ operations. A detailed derivation of this technique can be found in Bastiaans (2000).

2.2 Rheology and constitutive equations for viscoelastic fluids

In the previous sections, terms like ‘non-Newtonian’, ‘purely viscous shear-thinning fluids’, ‘viscoelastic fluids’ came up to indicate fluids with rheological behaviour that differs from simple Newtonian response. Despite this, a clear definition of these terms and of what can be classified as "non-Newtonian" property has not been given. Rheology is the branch of physics that aims at answering this question and more generally, studies the response of fluid materials to stress and deformation. Rheology is an extensive task, extremely useful to solve fluid dynamics problems involving complex fluids as well as to understand the microscopic structure of complex materials and formulations. Given the breadth of the subject, entire books have been devoted to the analysis of different aspects of the relationship between stress and deformation of different types fluid materials. The scope of this section is to introduce the concepts relevant to this research and the most important material functions used throughout the thesis to characterise the rheological behaviour of all the materials implemented.

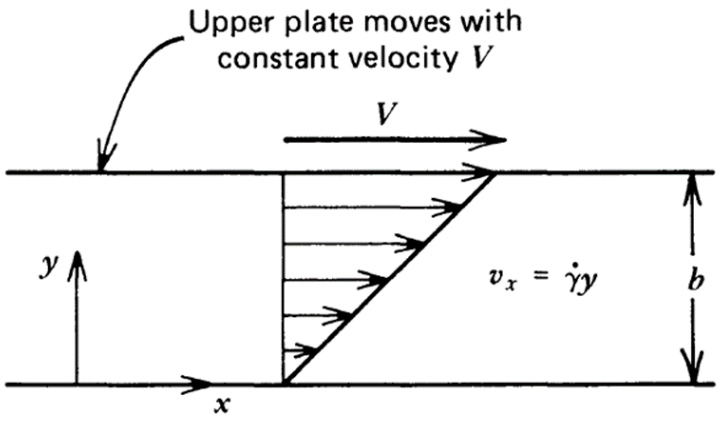

Figure 2.8: Unidirectional steady shear flow between parallel plates.

Fluids are classically classified according to their response, in terms of stress, to the action of an externally imposed deformation. The kind and intensity of this response depends on the characteristic of the imposed deformation as well as from the microstructure of the fluid. We can begin by defining one of the two standard kinds of flows, *shear* flow, that is often used to characterise the rheology of liquids. According to Bird et al. (1987a), a shear flow can be defined as the flow in which:

(i) It exists a one-parameter family of surfaces, the *shearing surfaces*, that move isometrically, that is, the relative distance between two points on a surface remains constant; and

(ii) the volume of every fluid element is constant.

An example of *homogeneous simple* shear flow is the one given by the following velocity field

$$u_x = \dot{\gamma}_{yx} y; \qquad u_y = 0; \qquad u_z = 0 \tag{2.2}$$

where $\dot{\gamma}_{yx}$ is the velocity gradient and the term homogeneous indicates that $\dot{\gamma}_{yx}$ is uniform throughout the flow. If additionally, $\dot{\gamma}_{yx}$ is independent of time, the flow is also said to be steady or *viscometric*[a]. The absolute value of $\dot{\gamma}_{yx}$ is called the *shear rate* $\dot{\gamma}$. A simple shear flow is easily generated between two parallel plates (Fig. 2.8) when on of the two plates moves along the x axis with constant velocity V. A fluid element within such a flow is subject to a deformation that can be expressed at every point as:

$$\varepsilon_{yx} = \frac{ds_x}{dy} \tag{2.3}$$

where ds_x is the differential distance covered by a fixed point in the infinitesimal time dt. ε_{yx} is called the *shear strain*, and represents the only non-zero component of the deformation tensor. In this context, the shear rate can also be expressed as:

$$\dot{\gamma} = \frac{d\varepsilon_{yx}}{dt} = \frac{du_x}{dy} \tag{2.4}$$

A constitutive equation, in the context of fluid rheology, is a mathematical expression that relates the *stress* (i.e. force per unit area) of a fluid element to the rate of deformation applied. The simplest form of constitutive equation is the "Newton's law of viscosity" which considers a linear relationship between these two quantities, where the proportionality constant is the Newtonian viscosity η. If one considers the case in Fig. 2.8, this relationship is:

$$\tau_{yx} = -\eta \frac{du_x}{dy} = -\eta \dot{\gamma} \tag{2.5}$$

Fluids obeying Eq. 2.5 are referred to as Newtonian fluids. The Newtonian viscosity is independent of the shear rate and is a characteristic property of the fluid and its temperature.

η is also an example of *material constant*, that is, a variable that can be used to characterise the rheological behaviour of a material. As it will be show, for non-Newtonian fluids, a variety of experiments can be performed in order to obtain different *material functions* that are dependent on shear-rate, frequency, time and so on. Throughout this work, the rheology of fluids was investigated only via shear rheology techniques. Accordingly, the subsequent sections focus on the description of the material functions that can be obtained in a viscometric shear flow and on the consequent classifications of non-

[a]For the sake of conciseness, a more rigorous definition of viscometric flow was not included, but interested readers can refer to Bird et al. (1987a, Chapter 3).

Newtonian fluids.

2.2.1 Material functions in shear flow

This section aims to introduce material functions in a simple shear flow, which are essential to understand the rheology of non-Newtonian fluids. However, before delving into the specifics of shear flow, it is necessary to generalize the definition of a Newtonian fluid and describe the stress tensor for both Newtonian and non-Newtonian materials in shear flow.

Newtonian Fluids

Newton's law in Eq. 2.5 can be extended to and arbitrary, three-dimensional, time dependent flow of an incompressible fluid as:

$$\boldsymbol{\sigma} = p\mathbf{I} + \boldsymbol{\tau} = p\mathbf{I} - \eta\dot{\gamma} \tag{2.6}$$

where $\boldsymbol{\sigma}$ is the *total* fluid stress tensor, p is the thermodynamic pressure (exerted by the fluid on the surrounding environment) and $\boldsymbol{\tau}$ is the deviatoric part of the total stress tensor, that is, the part associated with the motion of the fluid. For simplicity, we will refer to the symmetric tensor $\boldsymbol{\tau}$ simply as the fluid stress tensor. In Eq. 2.6, $\dot{\gamma} = (\boldsymbol{\nabla}\mathbf{u} + \boldsymbol{\nabla}\mathbf{u}^T)$ is the *rate of deformation tensor*.

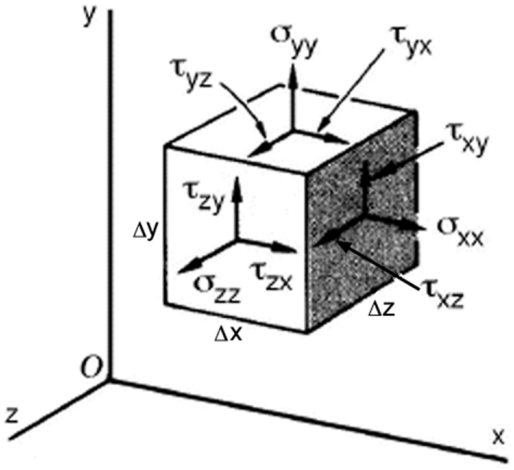

Figure 2.9: Stress tensor.

In the simple shear flow of Eq. 2.5, the rate of deformation tensor is:

$$\dot{\boldsymbol{\gamma}} = \boldsymbol{\nabla}\mathbf{u} + \boldsymbol{\nabla}\mathbf{u}^T = \begin{bmatrix} 0 & \frac{du_x}{dy} & 0 \\ \frac{du_x}{dy} & 0 & 0 \\ 0 & 0 & 0 \end{bmatrix} \tag{2.7}$$

and this leads to a total stress tensor of the form:

$$p\mathbf{I}-\eta\dot{\gamma}=\begin{bmatrix}p&0&0\\0&p&0\\0&0&p\end{bmatrix}+\begin{bmatrix}0&\tau_{yx}&0\\\tau_{yx}&0&0\\0&0&0\end{bmatrix}=\begin{bmatrix}p&0&0\\0&p&0\\0&0&p\end{bmatrix}-\eta\begin{bmatrix}0&\dot{\gamma}&0\\\dot{\gamma}&0&0\\0&0&0\end{bmatrix} \tag{2.8}$$

It follows that, for a Newtonian fluid in simple shear flow, the normal components of the stress tensor are identically zero ($\tau_{xx}=\tau_{yy}=\tau_{zz}=0$). At the same time, the symmetry of the stress tensor requires $\tau_{xy}=\tau_{yx}=-\eta\dot{\gamma}$.

Steady shear flow material functions

For a Newtonian fluid we know that in the simple shear flow between parallel plates, only the shear component of the stress τ_{yx} is non zero. However, for a general non-Newtonian fluid we have to assume that all six independent components of the stress are non zero. It is possible to prove however that for the flow of an incompressible, isotropic fluid, in the hypothesis that the stress depends only on the flow field, the stress tensor for the unidirectional, steady shear flow of Eq. 2.2 can be expressed as:

$$\boldsymbol{\sigma}=p\mathbf{I}+\boldsymbol{\tau}=\begin{bmatrix}p+\tau_{xx}&\tau_{yx}&0\\\tau_{yx}&p+\tau_{yy}&0\\0&0&p+\tau_{zz}\end{bmatrix} \tag{2.9}$$

where the presence of the diagonal components τ_{ii} indicates the possibility of the existance of normal stresses. From the experimental point of view, it is impossible to separate the pressure and the normal stress contribution from the measurement of normal forces acting on surfaces. This means that the only quantities of interest in simple shear flow are:

$$\begin{aligned}&\textit{Shear stress}: && \tau_{yx}\\&\textit{First normal stress difference}: && N_1=\tau_{xx}-\tau_{yy}\\&\textit{Second normal stress difference}: && N_2=\tau_{yy}-\tau_{zz}\end{aligned} \tag{2.10}$$

The hypothesis that the stress tensor depends only on the velocity field implicates that for a steady-state shear flow, the stresses thus defined are only function of the shear rate $\dot{\gamma}_{yx}$. To this end we can define the three material functions:

$$\tau_{yx}=-\eta(\dot{\gamma}_{yx})\dot{\gamma}_{yx} \tag{2.11}$$

$$\tau_{xx}-\tau_{yy}=N_1=-\Psi_1(\dot{\gamma}_{yx})\dot{\gamma}_{yx}^2 \tag{2.12}$$

$$\tau_{yy}-\tau_{zz}=N_2=-\Psi_2(\dot{\gamma}_{yx})\dot{\gamma}_{yx}^2 \tag{2.13}$$

where $\eta(\dot{\gamma}_{yx})$ is the non-Newtonian viscosity while $\Psi_1(\dot{\gamma}_{yx})$ and $\Psi_2(\dot{\gamma}_{yx})$ are respectively the first and second *normal stress coefficients*. The viscosity is the better understood and often most important property of non-Newtonian fluids. A more complete discussion of the dependence of the viscosity from the shear rate will be given later on but a typical behaviour is the one reported in Fig. 2.10. At low shear rates, the stress is proportional to the shear rate and the viscosity approaches a constant value η_0 named the *zero shear rate viscosity*. Increasing the rate of deformation, the viscosity of most non-Newtonian liquids decreases with the shear rate. In a $\log\eta$ versus $\log\dot{\gamma}$ graph, this manifests in the form of a linear region, or "power law" region, with negative slope.

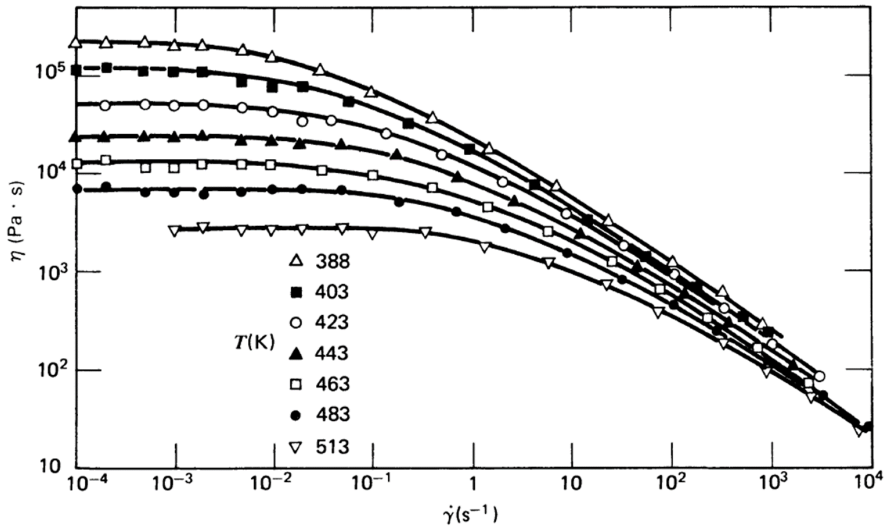

Figure 2.10: Non-Newtonian viscosity for a low-density polyethylene melt at different temperatures (Meissner, 1975).

An important property of the viscosity of most non-Newtonian fluids is that changing the temperature T does not change the functional dependence of $\eta(\dot{\gamma})$; it affects only the value of η_0 and the range of shear rates over which the viscosity transitions from a low-shear Newtonian region to a high-shear power law region. This property can be exploited to widen the range of shear rates accessible via a technique known as *time-temperature superposition* or *method of reduced variables*. Data obtained at different temperatures can be collapsed on a single master curve by plotting the reduced viscosity $\eta(T)\eta_0(T_0)/\eta_0(T)$ versus $a_T\dot{\gamma}$, where a_T is a shift factor. According to this method, the viscosity measured at T and $\dot{\gamma}$ is the same, after correcting for the effect of the temperature on η_0, to the viscosity measured at T_0 and shear rate $a_T\dot{\gamma}$.

The results of performing this procedure on experimental the data in Fig. 2.10 are reported in Fig. 2.11. Although the shift factor a_T is simply an empirical parameter that can be adjusted in order to collapse the curves of $\eta(\dot{\gamma})$, it is usually derived from the values of $\eta_0(T)$. For example the curve in Fig.2.11 was obtained with $a_T = \eta_0(T)/\eta_0(T_0)$. It is important to mention that the time-temperature superposition principle can be applied to

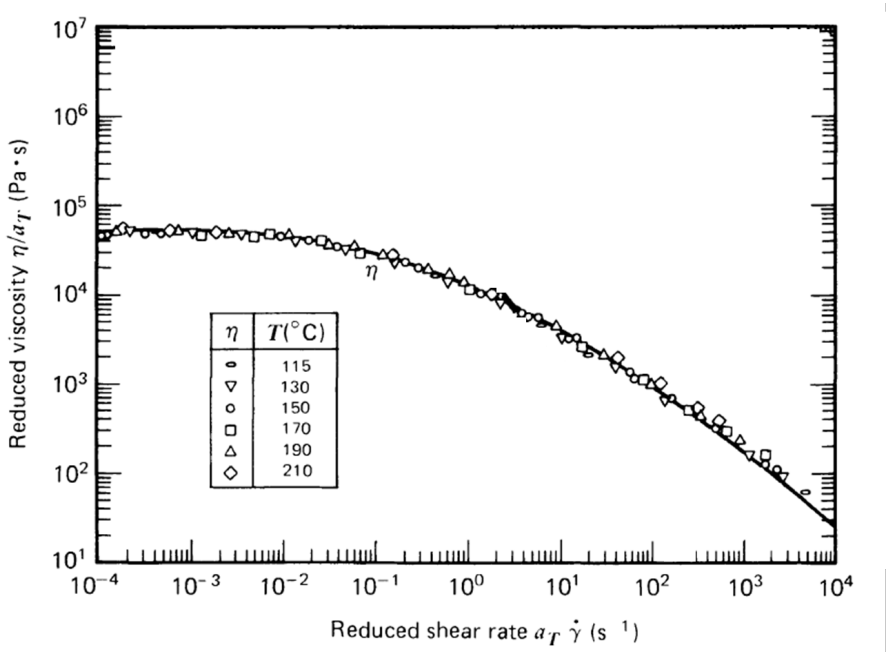

Figure 2.11: Master curve for Non-Newtonian viscosity for the same low-density polyethylene melt at of Fig. 2.10. The shift factor is $a_T = \eta_0(T)/\eta_0(T_0)$ and the reference temperature is $T_0 = 150\,^{\circ}\mathbf{C}$ (adapted from Laun (1978)).

all the other material functions obtainable in simple shear flow as will be used extensively throughout this thesis.

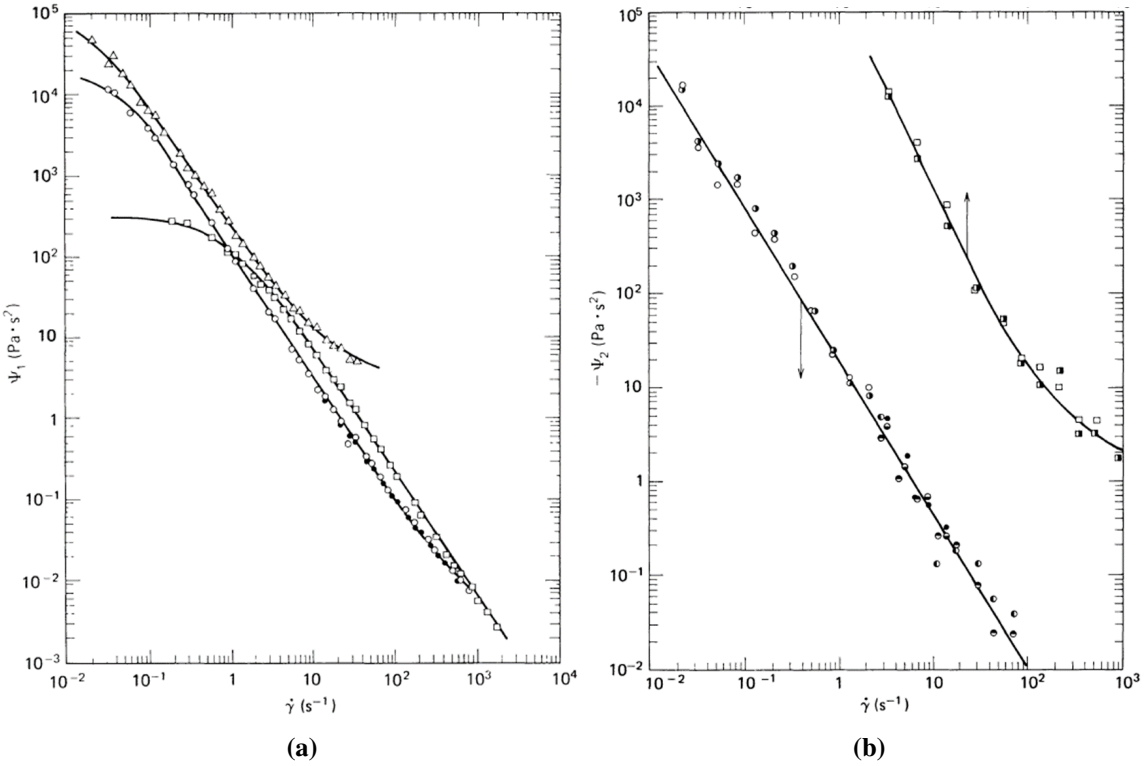

(a) **(b)**

Figure 2.12: Dependence of (a) the fist and (b) the second normal stress coefficients on the shear rate.

The trends of the first normal stress coefficients with shear rate are reported in Fig. 2.12a.

It can be seen that Ψ_1 has a large power law region in which it decreases with $\dot{\gamma}$, often by several orders of magnitude. At low rates, N_1 is proportional to $\dot{\gamma}^2$ so that Ψ_1 tends to a constant value $\Psi_{1,0}$. Finally, from Fig. 2.12b it is evident that the second normal stress coefficient is always negative for isotropic liquids and much smaller, usually 10%, of Ψ_1 (Maklad and Poole, 2021). Additionally, in the range of shear rates usually explorable with standard rheometers, Ψ_2 does not present either a high or low shear rate plateau.

Unsteady shear flow material functions

The only unsteady shear flow techniques used in this work is the *small-amplitude oscillatory shear* (SAOS) experiment. This techniques involves the measurement of the unsteady response of a fluid that is sheared between two parallel plates, with one of them oscillating in its own plane with angular frequency ω (we can imagine the situation in Fig. 2.8 where the upper plate oscillates with velocity $u_x(t) = V\cos\omega t$). It can be proven that the velocity across the gap can be considered linear in y as long as $\omega h^2/2\nu \ll 1$, where h is the height of the gap and ν is the kinematic viscosity of the fluid. In these situation, the shear strain and the shear rate can be written as:

$$\varepsilon_{yx}(0,t) = \varepsilon^0_{yx}\sin\omega t \tag{2.14}$$

$$\dot{\gamma}_{y,x}(t) = \dot{\gamma}^0_{yx}\cos\omega t \tag{2.15}$$

where ε^0_{yx} and $\dot{\gamma}^0_{yx} = \omega\varepsilon^0_{yx}$ are the amplitudes of the shear strain and shear rate oscillations. For non-Newtonian fluids, the shear stress of the fluid oscillates with the same frequency ω but is not in phase with either the strain or the shear. So that, in the limit of sufficiently small deformations, the stress is:

$$\tau_{yx}(t) = A(\omega)\varepsilon^0_{yx}\sin(\omega t + \delta) \tag{2.16}$$

$$\tau_{yx}(t) = B(\omega)\dot{\gamma}^0_{yx}\cos(\omega t - \psi) \tag{2.17}$$

where $\psi = \pi/2 - \delta$. If we separate the in-phase and out-of-phase parts of Eqs. 2.16 and 2.17 we can define two equivalent sets of material functions as:

$$\tau_{yx}(t) = -G'(\omega)\varepsilon^0_{yx}\sin\omega t - G''(\omega)\varepsilon^0_{yx}\cos\omega t \tag{2.18}$$

$$\tau_{yx}(t) = -\eta'(\omega)\dot{\gamma}^0_{yx}\cos\omega t - \eta''(\omega)\dot{\gamma}^0_{yx}\sin\omega t \tag{2.19}$$

where the amplitude and the phase angles in Eqs. 2.16 and 2.17 are releted to G' and G'' by:

$$A(\omega) = \sqrt{G'^2 + G''^2} \qquad \tan\delta = G''/G' \tag{2.20}$$

$$B(\omega) = \sqrt{\eta'^2 + \eta''^2} \qquad \tan\psi = \eta''/\eta' \tag{2.21}$$

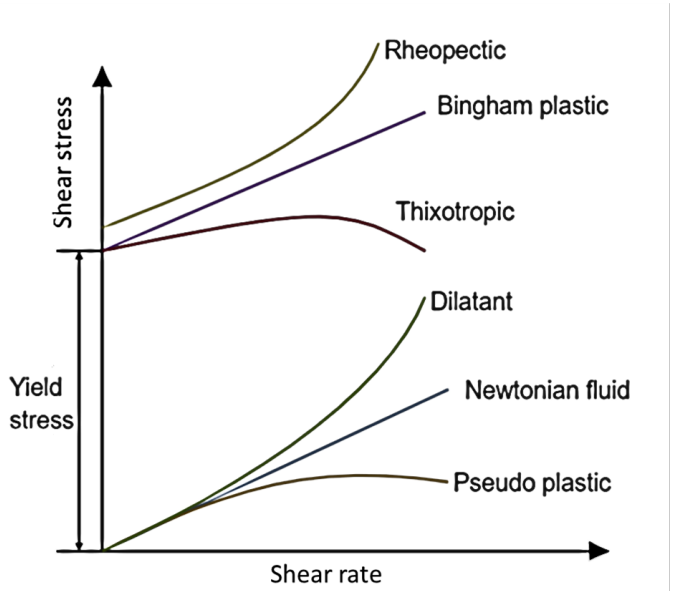

Figure 2.13: Example of generalised Newtonian fluid behaviour.

These material functions can be understood by considering that for a perfectly elastic solid the stress is always in phase with the applied deformation (i.e. $G'(\omega) = const$ and $G''(\omega) = 0$); while, for a Newtonian fluid, the stress is always in phase with the shear rate (i.e. $\eta'(\omega) = \eta$ and $\eta''(\omega) = 0$). For these reasons, G' $(= \eta''\omega)$ is called the *storage modulus* as it gives an estimation of the elastic energy stored in the material during the deformation. While G'' $(= \eta'\omega)$ is known as the *loss modulus* as it gives information about the viscous character of the fluid. Finally, η' is named the *dynamic viscosity* while the phase angle δ between stress and strain is given as *loss tangent* $\tan\delta$.

2.2.2 Generalised Newtonian fluids

In the previous sections, it was mentioned that the viscosity of many real fluids is not a constant value but it depends on the rate of deformation applied. Fig. 2.13 shows the qualitative behaviour of the shear stress as a function of the shear rate for different non-Newtonian fluids. The simplest way to describe this behaviour is by modifying the Newtonian constitutive equation and include a viscosity that depends of the rate of deformation. If a scalar value, the viscosity, has to depend on the tensor $\dot{\boldsymbol{\gamma}}$, it must depend only on those combination of components that are independent of the reference system, that is, the invariants of $\dot{\boldsymbol{\gamma}}$. As reported by Bird et al. (1987a, Chapter 4), the only invariant that is non-zero for an incompressible Newtonian fluid in shear flow is the second invariant $II = \frac{1}{2}(\dot{\boldsymbol{\gamma}} : \dot{\boldsymbol{\gamma}})$. The constitutive equation for a generalised Newtonian fluid is then:

$$\boldsymbol{\tau} = -\eta(\dot{\gamma})\dot{\boldsymbol{\gamma}} \tag{2.22}$$

$$\dot{\gamma} = \sqrt{II} = \sqrt{\frac{1}{2}\dot{\boldsymbol{\gamma}} : \dot{\boldsymbol{\gamma}}} \tag{2.23}$$

where Eq. 2.23 provides a definition of shear rate for a general three-dimensional flow. Although for some specific applications one can use measured data for $\eta(\dot{\gamma})$, it is often useful to introduce simple empirical models that are able to describe experimental value with sufficient accuracy. Over the years, many models were proposed and tested for different non-Newtonian fluids and some of them are reported in Table 2.1.

The most common type of time-independent non-Newtonian behaviour observed is pseudo-plasticity or shear-thinning. This behaviour is characterized by a viscosity that decreases with increasing shear rates. Both in the limit of very low and very high shear rates, most shear-thinning fluids exhibit Newtonian behaviour as shown schematically in Fig. 2.14. The limit values of the viscosity at very low and high shear rates are referred to as the zero shear viscosity, η_0 , and the infinite shear viscosity, η_∞, respectively. The region in which the viscosity decreases with $\dot{\gamma}$ is usually referred to as the "power-law region".

The behaviour just described can be captured by mathematical expressions for $\eta(\dot{\gamma})$ that decrease monotonically with the shear rate and present asymptotic values for both large and small values of $\dot{\gamma}$. Two commonly used models that exhibit these characteristics are the Cross and Carreau-Yasuda (C-Y) models, reported in Eqs. 2.25 and 2.26, respectively. The C-Y model is particularly versatile, as its five parameters provide sufficient flexibility to fit a wide variety of experimental $\eta(\dot{\gamma})$ curves. In addition to the two parameters that specify the Newtonian plateaus (η_0 and η_∞), the C-Y model includes three additional parameters: the Carreau characteristic time λ_c, which is typically associated with the inverse of the shear rate at which the shear-thinning behaviour begins; the flow index $0 < n < 1$, related to the steepness of the power-law region; and the index a, which is related to the smoothness of the shear-thinning transition.

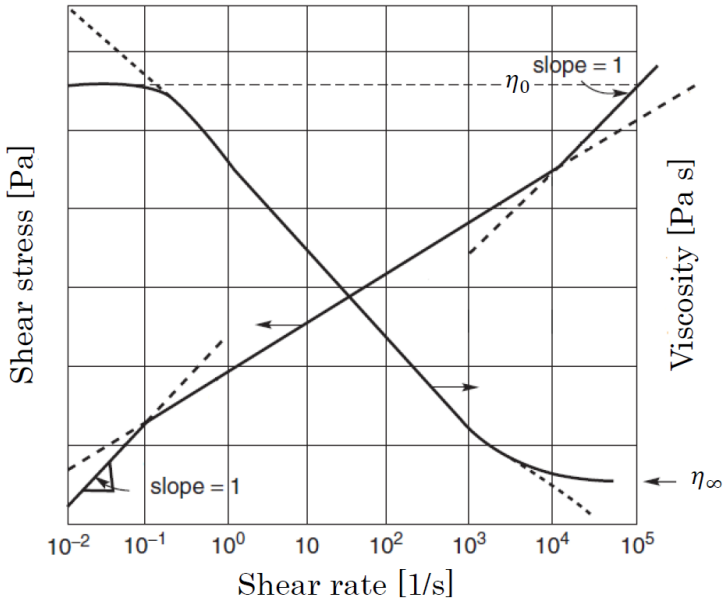

Figure 2.14: Shear-thinning behaviour (adapted from Chhabra and Richardson (2008).

Table 2.1: Different functional models for shear-thinning fluids

Model	$\eta(\dot{\gamma})$	
Power law	$\eta = K\dot{\gamma}^{n-1}$	(2.24)
Cross	$\frac{\eta-\eta_\infty}{\eta_0-\eta_\infty} = \frac{1}{1+K\dot{\gamma}^n}$	(2.25)
Carreau-Yasuda (C-Y)	$\frac{\eta-\eta_\infty}{\eta_0-\eta_\infty} = [1+(\lambda_c\dot{\gamma})wa^a]^{\frac{n-1}{a}}$	(2.26)
Ellis	$\eta = \frac{\eta_0}{1+\left(\frac{\tau}{\tau_{1/2}}\right)^{\alpha-1}}$	(2.27)

In some engineering applications, it is sufficient to capture the power-law region of the curve $\eta(\dot{\gamma})$. This region can be fitted by a simple *power law* model of the kind reported in Eq. 2.24. In Eq. 2.24, K and n represent two empirical fitting parameters, known as fluid consistency and flow index respectively. This model can be used for both shear-thinning and dilatant (shear-thickening) fluids, where in the former case n assumes values between 0 and 1 while in the latter $n > 1$.

It is worth noting that alternative approaches have been proposed to introduce simple expressions for a non-constant η in non-Newtonian fluids. For instance, instead of using the shear rate, other flow related invariants can be considered, such as the second invariant of the stress tensor, $II_\tau = \frac{1}{2}(\boldsymbol{\tau} : \boldsymbol{\tau})$. One such example is the Ellis model (Equation 2.27), where the viscosity is a function of the stress tensor magnitude $\tau = \sqrt{\frac{1}{2}\boldsymbol{\tau} : \boldsymbol{\tau}})$ while $\tau_{1/2}$ and α are two fitting parameters.

Although for most engineering applications, the generalised Newtonian fluid approach gives a good estimation of the flow rates and shearing forces in steady shear flow, it is however unable to explain the behaviour of most non-Newtonian fluids. One can notice for example that a time-dependent behaviour or the presence of normal stresses in shear flow cannot be predicted by a simple shear-dependent viscosity.

2.2.3 Viscoelastic fluids

Many materials of practical interest, such as polymeric liquids, suspensions, gels and pastes, are *viscoelastic*. A viscoelastic material is typically defined as a fluid that, when subjected to deformation, exhibits a stress response with both a viscous and an elastic component. The presence of an elastic response to a sudden deformation (or sudden cessation of a constant flow) can help to explain some of the peculiar behaviours exhibited by certain non-Newtonian fluids. For instance, if a polymer suspension is forced to flow in a straight tube by the application of a pressure gradient and the gradient is suddenly removed, the fluid will partially recede as shown in Fig. 2.15. In this example, some of

the energy provided to the fluid is stored as elastic energy by the stretching of the long polymer molecules. Once the forcing is removed, the molecules are allowed to recoil back to their original shape, causing the fluid to partially recede in the tube.

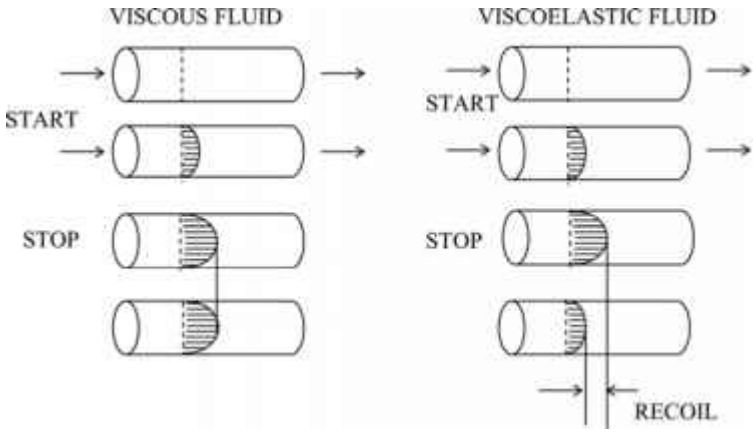

Figure 2.15: Elastic recoil (Steffe, 1996).

This section aims to provide a general introduction to the fluid viscoelasticity and its mathematical treatment. The most significant constitutive equations will be introduced and discussed, with particular emphasis on those used later on in this thesis. Additionally, some of the material functions used to estimate the parameters contained in said constitutive equations will be discussed.

Maxwell model

The first attempt to obtain a viscoelastic constitutive equation was made by Maxwell (1867). He proposed that a viscoelastic model could be obtained by the combination of Newton's law of viscosity and Hooke's law of elasticity. To better understand Maxwell's model, we need to introduce the concept of stress for a Hookean solid.

Consider the shearing deformation of a Hookean solid between parallel plates in Fig.2.16. At some time t_0, the solid is in an isotropic stress state with no additional external stress imposed. At time $t > t_0$, the upper plate is subject to an infinitesimal displacement $S(t_0,t)$ in the x direction. If the displacement in the material is a liner function of the distance, at any point we can write:

$$s_x(y,t_0,t) = \frac{S(t_0,t)}{B} y = \varepsilon_{yx}(t_0,t) y \tag{2.28}$$

where $\varepsilon_{yx}(t_0,t)$ is the yx component of the *infinitesimal strain tensor* $\boldsymbol{\varepsilon}$, which can be defined in terms of the *displacement gradient tensor* as $\boldsymbol{\varepsilon} = \nabla \mathbf{s} + \nabla \mathbf{s}^T$. Then, the shear

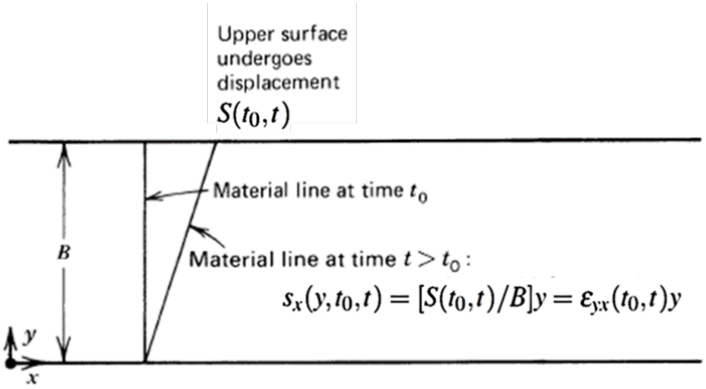

Figure 2.16: shear deformation between parallel plates (adapted from Bird et al. (1987a).

stress for a Hookean solid is:

$$\tau_{yx}(t) = -G\frac{\partial s_x}{\partial y} = -G\varepsilon_{yx}(t_0,t) \tag{2.29}$$

where G is the elastic modulus of the solid. Eq. 2.29 shows that the stress at time t is proportional to the strain at time t, referred to the isotropic stress state at time t_0. In other terms, the Hookean solid has a memory of its past stress state. As it will be seen, this concept of a memory can be extended to the Maxwell model. It is important to notice that the shear components of the rate of strain $\dot{\gamma}_{yx}$ and infinitesimal strain tensors are related by:

$$\varepsilon_{yx}(t_0,t) = \int_{t_0}^{t} \dot{\gamma}_{yx}(t')dt' \tag{2.30}$$

With reference to the simple shear flow in Fig. 2.8, the Maxwell model is:

$$\tau_{yx} + \frac{\eta_0}{G}\frac{\partial \tau_{yx}}{\partial t} = -\eta_0\dot{\gamma}_{yx} \tag{2.31}$$

where η_0 is the zero-shear rate viscosity. This equation can be generalised to an arbitrary, small displacement flow by employing the tensor form:

$$\boldsymbol{\tau} + \lambda\frac{\partial}{\partial t}\boldsymbol{\tau} = -\eta_0\dot{\boldsymbol{\gamma}} \tag{2.32}$$

where $\lambda = \eta_0/G$ is the fluid relaxation time. Eq. 2.32 is written in terms of material coordinates and therefore the time derivative is a material derivative. In a flow that is steady from a Lagrangian point of view (that is, from the point of view of an observer integral with the fluid element), Eq. 2.32 is a first order partial differential equation that can be integrated between t_0 and t yielding:

$$\boldsymbol{\tau}(t) + \eta_0\dot{\boldsymbol{\gamma}} = [\boldsymbol{\tau}(t_0) + \eta_0\dot{\boldsymbol{\gamma}}(t_0)]e^{-\frac{t}{\lambda}} \tag{2.33}$$

Hence, after a time of order λ, the stress relaxes to the value of a Newtonian fluid with

viscosity η_0. If on the other hand, $\dot{\boldsymbol{\gamma}}$ varied with a time scale $\tau_{\dot{\gamma}}$, the fluid behaviour can be understood introducing the following dimensionless variables:

$$\boldsymbol{\tau}^* \equiv \boldsymbol{\tau}/\tau_c; \qquad \dot{\boldsymbol{\gamma}}^* \equiv \dot{\boldsymbol{\gamma}}/\dot{\gamma}_c; \qquad t^* \equiv t/\tau_{\dot{\gamma}} \tag{2.34}$$

where the quantities with subscript c indicate a scale value for the corresponding variable. Thus, Eq. 2.32 can be written as:

$$\boldsymbol{\tau}^* + \frac{\lambda}{\tau_{\dot{\gamma}}}\frac{\partial}{\partial t}\boldsymbol{\tau}^* = -\frac{\eta_0\dot{\gamma}_c}{\tau_c}\dot{\boldsymbol{\gamma}}^* \tag{2.35}$$

The ratio $\lambda/\tau_{\dot{\gamma}}$ is defined as the *Deborah number De* and is the only important dimensionless number for the Maxwell fluid. if $De << 1$, the characteristic time of variation of the rate of deformation is large compared to the fluid relaxation time, so that a fluid element has sufficient time to relax before any substantial change in $\dot{\boldsymbol{\gamma}}$ has occurred. In this case, $\boldsymbol{\tau}^* \approx (\eta_0\dot{\gamma}_c/\tau_c)\dot{\boldsymbol{\gamma}}^*$ and the material behaves like a Newtonian fluid ($\boldsymbol{\tau}(t) = \eta_0\dot{\boldsymbol{\gamma}}(t)$). In the opposite case of $De >> 1$, the time derivative term dominates the left side of Eq. 2.35, hence, $(\lambda/\tau_{\dot{\gamma}})\frac{\partial}{\partial t}\boldsymbol{\tau}^* \approx -(\eta_0\dot{\gamma}_c/\tau_c)\dot{\boldsymbol{\gamma}}^*$. Integration with respect to time, taking into account the tensorial form of Eq. 2.30, returns $\boldsymbol{\tau}(t) \approx -(\eta_0/\lambda)\boldsymbol{\varepsilon}(t_0,t)$ which is the stress of a Hookean solid with modulus $G = \eta_0/\lambda$.

As will be shown later on, it is useful to express the Maxwell model in its integral form. To this end, Eq. 2.32 can be integrated with respect to time in the interval $t \in [-\infty \quad 0]$ with the requirement that $\dot{\gamma}(-\infty)$ is finite. The Maxwell constitutive equation can then be written as:

$$\boldsymbol{\tau}(t) = -\int_{-\infty}^{t}\left\{\frac{\eta_0}{\lambda}e^{-(t-t')/\lambda}\right\}\dot{\boldsymbol{\gamma}}(t')dt' \tag{2.36}$$

The quantity within brackets is the *relaxation modulus* of the Maxwell fluid. In this form, the Maxwell model states that the stress at time t depends of the values of the rate of strain at all past times $t' \leq t$, with a weighting factor that decays exponentially when moving backward in time. In other words, a Maxwell fluid has contains the notion of a fading memory of past strain states.

A simple two-parameters Maxwell model is often insufficient to describe the linear viscoelastic behaviour of certain materials. An attempt at generalising the Maxwell model can be made by introducing a linear dependence on the time derivative of $\dot{\boldsymbol{\gamma}}$ and obtain the constitutive equation:

$$\boldsymbol{\tau} + \lambda_1\frac{\partial}{\partial t}\boldsymbol{\tau} = -\eta_0\left(\dot{\boldsymbol{\gamma}} + \lambda_2\frac{\partial}{\partial t}\dot{\boldsymbol{\gamma}}\right) \tag{2.37}$$

which is known as the *Jeffrey model* and the constants λ_1 and λ_2 are the relaxation time and the *retardation time* respectively.

Another way to extend the applicability of the model is by building a superposition of

Maxwell models and obtain the constitutive equation of the *generalised Maxwell model*:

$$\boldsymbol{\tau}(t) = \sum_{k=1}^{n} \boldsymbol{\tau}_k(t); \qquad \boldsymbol{\tau}_k + \lambda_k \frac{\partial}{\partial t}\boldsymbol{\tau}_k = -\eta_k \dot{\boldsymbol{\gamma}} \tag{2.38}$$

where η_k and λ_k are the zero-shear viscosity and relaxation time of the kth mode and n is the total number of modes. Eq. 2.38 can be also integrated to obtain an expression similar to Eq. 2.36:

$$\boldsymbol{\tau}(t) = -\int_{-\infty}^{t} \left\{ \sum_{k=1}^{n} \frac{\eta_k}{\lambda_k} e^{-(t-t')/\lambda_k} \right\} \dot{\boldsymbol{\gamma}}(t')dt' \tag{2.39}$$

An estimation of the 2 parameters of the Maxwell model can be obtained from the linear viscoelastic material functions described in Sec.2.2.1. If we substitute Eq. 2.15 in Eq. 2.36, we derive the expressions for G' and G'' for a Maxwell fluid:

$$G'(\omega) = \frac{\eta_0 \lambda \omega^2}{1+\lambda^2\omega^2} \tag{2.40}$$

$$G''(\omega) = \frac{\eta_0 \omega}{1+\lambda^2\omega^2} \tag{2.41}$$

In an oscillatory shear flow, the characteristic time of variation of shear-rate depends on the oscillation frequency, $\tau_{\dot{\gamma}} \approx 1/\omega$. Hence, if both moduli are normalised by the elastic modulus $G_e = \eta_0/\lambda$, Eqs. 2.40 and 2.41 can be written as:

$$G'^{*}(\omega) = \frac{De^2}{1+De^2} \tag{2.42}$$

$$G''^{*}(\omega) = \frac{De}{1+De^2} \tag{2.43}$$

For $De \ll 1$, both moduli increase with De but at different rates, with $G'^{*} \approx De^2$ and $G''^{*} \approx De$. Whilst, for $De \gg 1$, $G'^{*} \approx 1$ and $G''^{*} \approx 1/De$, and the storage modulus reaches a constant value (i.e. Ge) and the loss modulus reduces to zero. The typical behaviour of a Maxwell fluid is depicted in Fig. 2.17. The transition from the viscous to the elastic regimes can be identified with the crossover of the two lines of G'^{*} and G''^{*}, in correspondence of $De = 1$. Notably, the inverse of the crossover frequency is equal to the fluid relaxation time.

Real fluids typically exhibit more complicated relaxation dynamics, which, in certain cases, can be accurately described using the generalized Maxwell model. The mathemat-

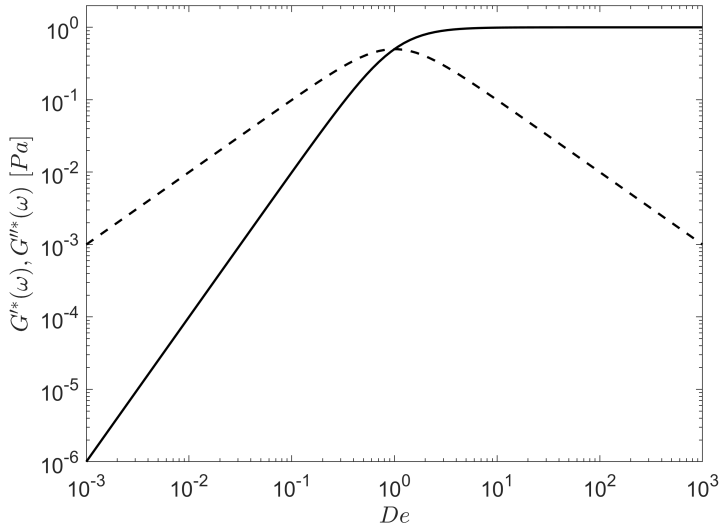

Figure 2.17: G' (solid lines) and G'' (dash lines) for a Maxwell fluid. The crossover point of G' and G'' correspond to the inverse of the fluid relaxation time. Hence, for $\omega \ll 1/\lambda$ the material behaves as a Newtonian liquid with $G' \propto \omega^2$ and $G'' \propto \omega$; for $\omega \gg 1/\lambda$ it behaves as an Hookean solid with $G' = \eta_0/\lambda^2$ and $G'' = 0$.

ical expressions of the two moduli for a generalised Maxwell fluid with n modes is:

$$G'(\omega) = \sum_{k=1}^{n} G'_k = \sum_{k=1}^{n} \frac{\eta_k \lambda_k \omega^2}{1+\lambda_k^2 \omega^2} \tag{2.44}$$

$$G''(\omega) = \sum_{k=1}^{n} G''_k = \sum_{k=1}^{n} \frac{\eta_k \omega}{1+\lambda_k^2 \omega^2} \tag{2.45}$$

An example of the use of an 8-modes generalised Maxwell model is reported in Fig. 2.18. On the same graphs are also reported the curves for each of the 8 single modes together with the corresponding relaxation times.

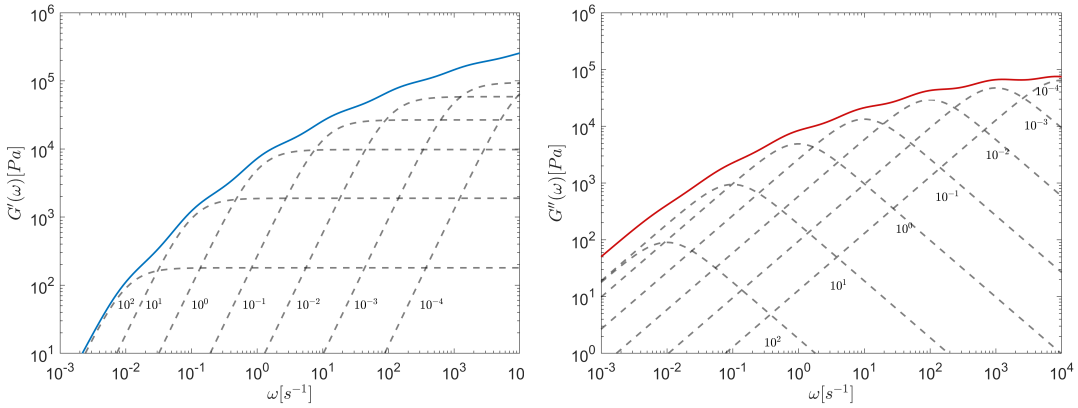

(a) **(b)**

Figure 2.18: (a) Storage modulus G' and (b) loss modulus G'' for a low-density polyethylene melt. Data fitted with an 8-modes generalised Maxwell model. Each single mode is reported with a dashed line together with the corresponding relaxation time (Data from Bird et al. (1987a)).

Despite their large use, linear constitutive equations like the Maxwell model present several limitations. For instance, they are unable to describe a shear-rate dependent viscosity or the presence of normal-stress phenomena as they are non-linear effects. As a result, more complex constitutive equations have been developed to overcome these limitations.

Non linear models

In this section a more general class of constitutive equation that can be used for arbitrary flow will be introduced. The general idea is to progressively include non linear terms (in either the stress or the strain rate) to linear constitutive equations. A first set of constitutive equations, known as *quasi-linear* models, can be obtained by reformulating the linear viscoelastic models reported in the previous section. A first example is the *upper convected Maxwell model* (UCM), where the material time derivative appearing in Eq. 2.32 has been replaced with the upper convected time derivative, $\overset{\triangledown}{\boldsymbol{\tau}} = \frac{D\boldsymbol{\tau}}{Dt} - [(\boldsymbol{\nabla}\mathbf{u})^{\intercal}\cdot\boldsymbol{\tau} + \boldsymbol{\tau}\cdot(\boldsymbol{\nabla}\mathbf{u})]$ where $\frac{D}{Dt}$ is the material time derivative:

$$\boldsymbol{\tau} + \lambda \overset{\triangledown}{\boldsymbol{\tau}} = -\eta_0 \dot{\boldsymbol{\gamma}} \tag{2.46}$$

By substituting the dimensionless quantities defined in Eq. 2.34 in Eq. 2.46, we obtain:

$$\boldsymbol{\tau}^* = \left(\frac{\lambda}{\tau_{\dot{\gamma}}}\right)\frac{D}{Dt}\boldsymbol{\tau}^* - (\lambda\dot{\gamma}_c)\left[(\boldsymbol{\nabla}\mathbf{u}^*)^{\intercal}\cdot\boldsymbol{\tau}^* + \boldsymbol{\tau}^*\cdot(\boldsymbol{\nabla}\mathbf{u}^*)\right] = -\left(\frac{\eta_0\dot{\gamma}_c}{\tau_c}\right)\dot{\boldsymbol{\gamma}}^* \tag{2.47}$$

In Eq. 2.47, two dimensionless numbers arise: the Deborah number, previously defined as the ratio of the relaxation time to the characteristic time scale of variation of the deformation rate tensor, and the *Weissenberg number*, which is defined as $Wi = \lambda\dot{\gamma}_c$. This dimensionless number is related to the non-linear part of the constitutive equation, which is responsible, as will be shown, for the appearance of normal stress phenomena.

The upper convected time derivative can also be substituted to the time derivatives of both the stress and strain rate tensors in Eq. 2.37. The result is the constitutive equation of the *convected Jeffreys model* or *Oldroyd-B fluid*:

$$\boldsymbol{\tau} + \lambda_1 \overset{\triangledown}{\boldsymbol{\tau}} = -\eta_0\left(\dot{\boldsymbol{\gamma}} + \lambda_2 \overset{\triangledown}{\dot{\boldsymbol{\gamma}}}\right) \tag{2.48}$$

Note that if $\lambda_2 = 0$, the Oldroy-B model reduces to the UCM model while for $\lambda_1 = \lambda_2$ it reduces to a Newtonian fluid with viscosity η_0.

Throughout the rest of the thesis, non-linear constitutive equation of the kind just introduced will be written in a form know as *split stress approach*. Accordingly, the stress

of viscoelastic fluid will be written as the sum of a solvent and polymer contributions,

$$\boldsymbol{\tau} = \boldsymbol{\tau}_s + \boldsymbol{\tau}_p \tag{2.49}$$

The solvent contribution is then modelled as a Newtonian fluid with viscosity η_s ($\boldsymbol{\tau}_s = \eta_s \dot{\boldsymbol{\gamma}}$) while the polymer contribution can be expressed with one of the non-linear models available. For instance, if $\boldsymbol{\tau}_p$ is expressed with the UCM of Eq. 2.46, the stress of the fluid in Eq. 2.49 becomes:

$$\boldsymbol{\tau} + \lambda \overset{\triangledown}{\boldsymbol{\tau}} = -(\eta_s + \eta_p) \left[\dot{\boldsymbol{\gamma}} + \frac{\lambda \eta_s}{\eta_s + \eta_p} \overset{\triangledown}{\dot{\boldsymbol{\gamma}}} \right] \tag{2.50}$$

which is identical to an Oldroyd-B model with $\eta_0 = \eta_s + \eta_p$, $\lambda_1 = \lambda$ and $\lambda_2 = \lambda \frac{\eta_s}{\eta_s + \eta_p}$. Some of the most common constitutive equations in the split stress tensor form are reported in Tab. 2.2.

Table 2.2: Common non-linear constitutive equations in the split stress tensor form.

Model	$\eta_s(\dot{\gamma})$	$\eta_p(\dot{\gamma})$	$\lambda(\dot{\gamma})$	Constitutive Equation	
Oldroyd-B	η_s	η_p	λ	$\boldsymbol{\tau}_p + \lambda \overset{\triangledown}{\boldsymbol{\tau}}_p = \eta_p(\nabla\mathbf{u} + \nabla\mathbf{u}^T)$	(2.51)
White-Metzner (C-Y)	η_s	$\eta_p[1 + (K\dot{\gamma})^a]^{\frac{n-1}{a}}$	$\lambda[1 + (L\dot{\gamma})^b]^{\frac{m-1}{b}}$	$\boldsymbol{\tau}_p + \lambda(\dot{\gamma}) \overset{\triangledown}{\boldsymbol{\tau}}_p = \eta_p(\dot{\gamma})(\nabla\mathbf{u} + \nabla\mathbf{u}^T)$	(2.52)
Giesekus	η_s	η_p	λ	$\boldsymbol{\tau}_p + \lambda \overset{\triangledown}{\boldsymbol{\tau}}_p + \alpha \frac{\lambda}{\eta_p}(\boldsymbol{\tau}_p \cdot \boldsymbol{\tau}_p) = \eta_p(\nabla\mathbf{u} + \nabla\mathbf{u}^T)$	(2.53)
*FENE-P	η_s	η_p	λ	$\boldsymbol{\tau}_p + \frac{\lambda}{f} \overset{\triangledown}{\boldsymbol{\tau}}_p = \frac{a\eta_p}{f}(\nabla\mathbf{u} + \nabla\mathbf{u}^T) - \frac{D}{Dt}\left(\frac{1}{f}\right)[\lambda\boldsymbol{\tau}_p + a\eta_p\mathbf{I}]$	(2.54)

* $f = \frac{L^2 + \frac{\lambda}{a\eta_p} tr(\boldsymbol{\tau}_p)}{L^2 - 3}$ and $a = \frac{L^2}{L^2 - 3}$

As already mentioned, the inclusion of non-linear terms in the constitutive equations allows the prediction of normal stresses in simple shear flow. With reference to the usual simple shear flow of Eq. 2.5, for an Oldroyd-B fluid the three components of the stress tensor are:

$$\begin{aligned} \tau_{yx} &= -\eta_0 \dot{\gamma}_{yx} \\ \tau_{xx} &= 2\eta_0(\lambda_1 - \lambda_2)\dot{\gamma}_{yx} \\ \tau_{yy} &= 0 \end{aligned} \tag{2.55}$$

This means that the Oldroyd-B model predicts a constant viscosity, a constant first normal stress coefficient $\Psi_1 = \Psi_{1,0} = 2\eta_0(\lambda_1 - \lambda_2)$ and a zero second normal stress coefficient.

Finally, it is also possible to include terms in the constitutive equation that are non-

linear in stress. An example is the *Giesekus model* expressed as:

$$\begin{aligned} \boldsymbol{\tau} &= \boldsymbol{\tau}_s + \boldsymbol{\tau}_p \\ \boldsymbol{\tau}_s &= \eta_s \dot{\boldsymbol{\gamma}} \\ \boldsymbol{\tau}_p + \lambda_1 \overset{\triangledown}{\boldsymbol{\tau}}_p - a\frac{\lambda_1}{\eta_p}\left\{\boldsymbol{\tau}_p \cdot \boldsymbol{\tau}_p\right\} &= -\eta_p \dot{\boldsymbol{\gamma}} \end{aligned} \tag{2.56}$$

where α is a dimensionless parameter named *mobility factor*. The inclusion of non-linear terms in the constitutive equations gives material function that are much more realistic. For instance, it is possible to obtain values of viscosity and first normal stress coefficients that rapidly decrease with shear rate. Additionally, the second normal stress coefficient is non-zero and can be adjusted relatively to the first normal stress coefficient as $\Psi_{1,0} = -(\alpha/2)\Psi_{2,0}$.

The constitutive laws reported in Table 2.2 can also be formulated in terms of the conformation tensor $\mathbf{A}(\mathbf{x},t)$, which can be considered as an approximate measure of the structural state of the fluid at the molecular level (Bird et al., 1987b). Although this approach originates from the elastic dumbbell models proposed in molecular theory, the formulation presented here is based on the macroscopic description proposed by Grmela and Carreau (1987) as reported by Fattal and Kupferman (2004). According to the authors, the polymeric stress tensor can be expresses in the form:

$$\boldsymbol{\tau}_p = \frac{g(\mathbf{A})}{Wi}(\mathbf{A} - \mathbf{I}) \tag{2.57}$$

where *We* is the already introduced Weissenberg number, and $g(\mathbf{A})$ is a scalar- valued function that only depends on the invariants of $\mathbf{A}$. Note that even though Eq. 2.57 is written using dimensionless variables, we kept the same notation for conciseness. The constitutive equation can then be written as an evolution equation for the conformation tensor:

$$\frac{\partial \mathbf{A}}{\partial t} + (\mathbf{u}\cdot\nabla)\mathbf{A} - (\nabla\mathbf{u})\mathbf{A} - \mathbf{A}(\nabla\mathbf{u})^{\mathsf{T}} = \frac{g(\mathbf{A})}{Wi}Q(\mathbf{A}) \tag{2.58}$$

where, the scalar function $g(\mathbf{A})$ and the polynomial $P(\mathbf{A})$ depend on the choice of constitutive model. The constitutive equations written in the conformation tensor form, are reported in Table 2.3. As it will be shown later, the log-conformation tensor approach, a variation of the conformation tensor approach, is the one used in the viscoelastic solvers `rheoInterFoam` for the numerical approximation of the polymer contribution to the stress tensor.

Table 2.3: Constitutive equations in the conformation and log-conformation tensor formulations

Model	conformation tensor	*log-conformation tensor
Oldroyd-B	$\boldsymbol{\tau}_p = \frac{\eta_p}{\lambda}(\mathbf{A}-\mathbf{I})$	$\boldsymbol{\Upsilon} = \frac{1}{\lambda}(e^{-\Theta}-\mathbf{I})$
White-Metzner (C-Y)	$\boldsymbol{\tau}_p = \frac{\eta_p}{\lambda(\dot{\gamma})}(\mathbf{A}-\mathbf{I})$	$\boldsymbol{\Upsilon} = \frac{1}{\lambda(\dot{\gamma})}(e^{-\Theta}-\mathbf{I})$
Giesekus	$\boldsymbol{\tau}_p = \frac{\eta_p}{\lambda}(\mathbf{A}-\mathbf{I})$	$\boldsymbol{\Upsilon} = \frac{1}{\lambda}[(e^{-\theta}-\mathbf{I}) - \alpha e^{\theta}(e^{-\Theta}-\mathbf{I})^2]$
**FENE-P	$\boldsymbol{\tau}_p = \frac{\eta_p}{\lambda}(f\mathbf{A}-a\mathbf{I})$	$\boldsymbol{\Upsilon} = \frac{f}{\lambda}(ae^{-\Theta}-f\mathbf{I})$

* For conciseness, the operator $\Upsilon = \frac{\partial\Theta}{\partial t} + \mathbf{u}\cdot\nabla\Theta - (\Omega\Theta - \Theta\Omega) - 2B$ was introduced

** $f = \frac{L^2 + \frac{\lambda}{a\eta_p} tr(\boldsymbol{\tau}_p)}{L^2-3}$ and $a = \frac{L^2}{L^2-3}$

2.3 Computational fluid dynamic for viscoelastic liquids and the volume of fluid method

In the following section, I will present a brief description of the numerical methods employed for the simulation of two-phase systems. The scope is to introduce all the relevant equations and parameters at play and facilitate the presentation of the results contained in Chapter 5. Particular emphasis will be posed on the *volume of fluid* (VOF) method with specific reference to its implementation in the open-source, finite-volumes solver OpenFoam. As it will be clarified later, both the multiphase Newtonian solver `interFoam` and the multiphase, viscoelastic solver `rheoInterFoam` will be used in this work. These solver employ the same form of the VOF method but differ in the mathematical description of the fluid stress tensor. In particular, the viscoelastic solver uses the split stress approach described in Sec.2.2.3, where the exact form of the polymer contribution to the stress tensor depends on the choice of constitutive equation. Accordingly, a brief description of the numerical implementation of viscoelastic constitutive equations will be presented.

2.3.1 The Volume of Fluid method

The simulation of fluid systems involving more than one phase is an old and rich field of study that has received constant attention from the scientific community. Within the modeling community, problems involving two fluid phases are referred to as two-phase flows. A classification of the most prominent classes of modelling approaches to two-phase flow is reported in Fig. 2.19.

A first distinction can be made based on the number of phases considered. In this context, two-fluid models employ two sets of equations (one for each phase) for the computation of the conservation of mass, momentum and energy while, as the word suggests, only one set of equations is required for one-fluid models. While two-fluid models are

found to be applicable for simple problems, they have proven to be unsuitable for realistic scenarios (Prosperetti and Tryggvason, 2009). When two-phase flows are simulated by solving a single set of equations for the whole flow field, it is necessary to locate the portions of the domain occupied by each phase. This is crucial in order to account for differences in the material properties of the different fluids and to add appropriate terms for interfacial phenomena, such as surface tension.

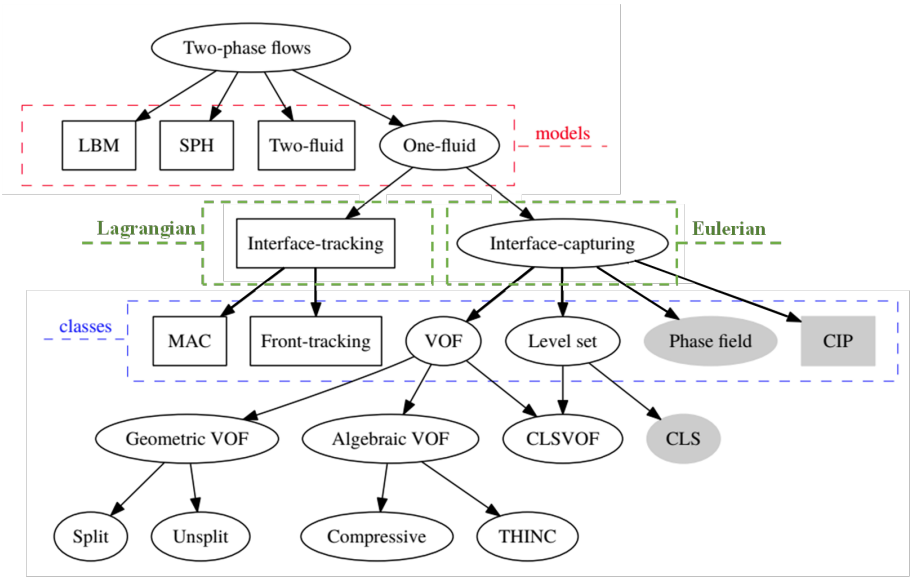

Figure 2.19: Classification of numerical methods for two-phase flows (adapted from Mirjalili et al. (2017)).

Broadly speaking, the one-fluid numerical models that have been proposed can be classified in two main categories, Lagrangian and Eulerian methods (Benson, 2002). Lagrangian methods employ specialized algorithms to track the position, as a function of time, of the interface (in the case of Front tracking) or of each phase (in the case of marker-and-cell (MAC)) from the beginning of the simulation. Although, Lagrangian formulations have proven to be highly reliable in certain conditions, they are also computationally demanding for problems involving rapidly evolving material boundaries, phase changes and large deformations or rotations of the interfaces.

On the other hand, in Eulerian formulations, the position of the interface is not explicitly tracked from the beginning of the computation. Instead, at the beginning of each time step, an indicator function is used to reconstruct (or "capture") the interface. At the end of the time step, when the flow field has been resolved, the indicator is transported with the fluid velocity. The choice of indicator or reconstruction algorithm allows the definition of different methods, usually referred to as *interface-capturing* methods. Among these methods, the Volume of Fluid (VOF), the Level-set (LS) and the Phase field methods are the most commonly employed numerical algorithms.

In the level set methods of Osher and Sethian (1988), a contouring function (the level-set function) is initialised on the entire domain as a signed distance from the interface

with a positive value in one phase and negative in the other (Fig. 2.20). The movement of the interface is captured by applying a transport equation to the contouring function. Since this transport equation does not represent a conservation law (because the level-set function is not a physical quantity), the LS method is not intrinsically mass conservative (Gibou et al., 2018).

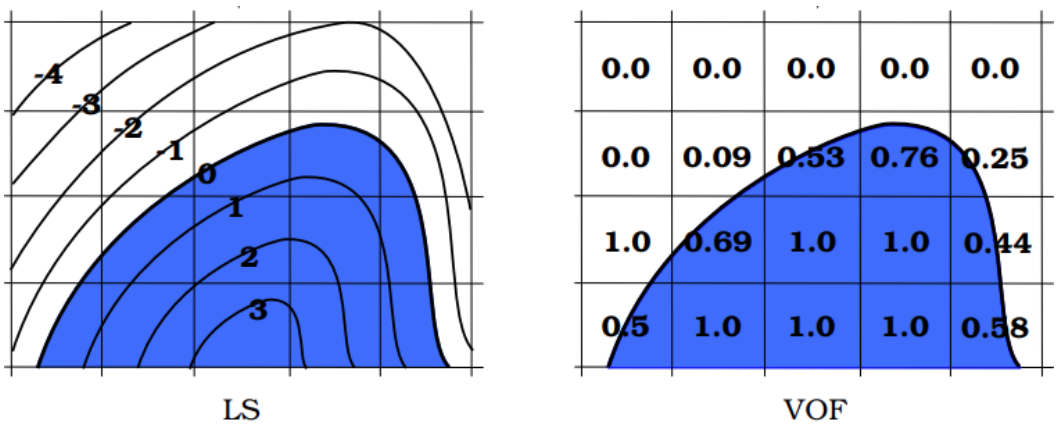

Figure 2.20: Schematic illustration of the LS and VOF methods

In the Phase fluid method, the transport equation governing the phase indicator function, which is similar to the one applied in the LS method, is modified by incorporating physical effects that govern thin interfaces. This approach offer some desirable properties that have attracted the interest of two-phase flow modelers in recent years (Anderson et al., 1998; Badalassi et al., 2003; Ding et al., 2007). Both the Level-set and Phase field methods have been widely investigated in the literature, and each method possesses its own set of advantages and disadvantages. A comprehensive examination of these methods can be found in Prosperetti and Tryggvason (2009) for the Level-set method and Mirjalili et al. (2017) for the Phase field method.

The most used interface-capturing method is indubitably the VOF method, firstly proposed by Hirt and Nichols (1981). In this class of finite volumes (FV) methods, a scalar indicator is used to track the volumes of the two fluids in each computational cell (Fig. 2.20). The physical volume fraction or phase fraction of one phase α is commonly used as the indicator function. Conventionally in the VOF method, the transport equation of the volume fraction, is solved along the continuity and conservation of momentum equations.

$$\frac{\partial \rho}{\partial t} + \nabla \cdot (\rho \mathbf{u}) = 0 \tag{2.59}$$

$$\frac{\partial (\rho \mathbf{u})}{\partial t} + \nabla \cdot (\rho \mathbf{u}\mathbf{u}) = -\nabla p + \nabla \cdot \boldsymbol{\tau} + \rho \mathbf{f}_b \tag{2.60}$$

$$\frac{\partial \alpha}{\partial t} + \nabla \cdot (\mathbf{u}\alpha) = 0 \tag{2.61}$$

where $\mathbf{u}$, p, and $\boldsymbol{\tau}$ are the velocity, pressure and stress tensor fields for a single fluid phase

with density ρ; while $\mathbf{f}_b$ represents the body forces per unit mass. In the VOF model, the latter term includes the gravitational and interfacial forces $\mathbf{f}_b = \mathbf{f}_g + \mathbf{f}_\gamma$. The volume fraction α varies in the interval $0 \leq \alpha \leq 1$, where the extremes of this interval identify areas of the flow where only one of the phases is present. Accordingly, gradients of α are only possible in correspondence of the interface. Throughout the computational domain, the two phases are considered as one effective fluid with properties calculated as weighted averages based on the distribution of the volume fraction.

$$\rho = \rho_1 \alpha + \rho_2 (1 - \alpha) \tag{2.62}$$

$$\eta = \eta_1 \alpha + \eta_2 (1 - \alpha) \tag{2.63}$$

where the subscripts 1 and 2 identify the two fluid phases.

VOF methods can be further divided in *geometric* and *algebraic* methods according to the numerical approach used to solve the phase fraction transport equation (Eq. 2.61). The geometric VOF method involve two main steps. Firstly, the interface is reconstructed in each computational cell utilizing the volume fraction field data. The interface is represented by a set of straight line segments (in 2D) or flat surfaces (in 3D). Various methods are available that differ in the precise way of calculating this line or surface from the volume fraction values. Two commonly used methods are the Simple Line Interface Calculation (SLIC) and Piecewise Linear Interface Calculation (PLIC). In SLIC, the interface is defined by a set of straight lines, each aligned with the mesh cell, while in PLIC, the interface is reconstructed as a set of linear segments perpendicular to the interface. Once the interface is reconstructed, in each cell the interface is advected by the underlying flow field. A comprehensive review of geometric interface-reconstruction methods is provided by Rider and Kothe (1998).

Finally, in algebraic VOF, the volume fluxes required to solve Eq. 2.61 can be formulated algebraically, without explicit interface reconstruction, by using the so-called High Resolution Differentiating Schemes (HRDS). This methods allows to avoid the computationally expensive explicit interface reconstruction at the cost of introducing the possibility of the loss of boundedness for α or the smearing of sharp interfaces. These risks are introduced by the choice of discretization scheme for the convective term in Eq. 2.61. Higher-order schemes are notoriously unbounded and result in a loss of total mass of fluid. On the other hand, first-order upwind (UW) schemes although bounded, introduce an unacceptable amount of numerical diffusion, while first-order downwind (DW) scheme produce enough negative numerical diffusion to artificially wrinkle the interface (Hirt and Nichols, 1981; Ubbink and Issa, 1999). Some authors proposed HRDS that are a combination of UW and DW schemes with the main objective of reducing the numerical diffusion of the interface. The most common are the e Compressive Interface Capturing Scheme for Arbitrary Meshes (CICSAM) of Ubbink and Issa (1999) and the

High Resolution Interface Capturing (HRIC) scheme by Muzaferija (1998).

VOF method in interFoam

The particular formulation used in this work is the algebraic VOF method implemented in the multiphase, transient solvers `interFoam` and `rheoInterFoam` available in OpenFoam v6 and in the utility rheoTool v4.0. As already mentioned, the resolution of the hyperbolic advection equation for the volume fraction (Eq. 2.61) is notoriously troublesome and can lead to serious numerical errors. Two critical issues in the simulation of free surface problems using VOF are the conservation of the phase fraction and the numerical diffusion of the interface. The problems are particularly evident in cases with high density or viscosity ratios, where even small errors in volume fraction can produce large errors in the calculation of the averaged physical properties. Additionally, errors in the evaluation of the interface curvature lead to the rise of an artificial flow at the interface known as spurious current (Scardovelli and Zaleski, 1999; Deshpande et al., 2012). To mitigate all the aforementioned problems, `interFoam` solves a different form of Eq. 2.61 that includes an artificial contribution to the convection of the phase fraction (Deshpande et al., 2012). If we consider a binary system where α is the volume fraction of phase 1, then $(1-\alpha)$ indicate the volume fraction of phase 2. We can write the two transport equations for each phase fraction as:

$$\frac{\partial \alpha}{\partial t} + \boldsymbol{\nabla}\cdot(\mathbf{u_1}\alpha) = 0; \tag{2.64}$$

$$\frac{\partial (1-\alpha)}{\partial t} + \boldsymbol{\nabla}\cdot[\mathbf{u_2}(1-\alpha)] = 0; \tag{2.65}$$

Assuming that the contributions of the velocities of each phase to the evolution of the free surface are proportional to the corresponding phase fraction, and defining the velocity of the effective fluid in a VOF model as a weighted average,

$$\mathbf{u} = \alpha\mathbf{u}_1 + (1-\alpha)\mathbf{u}_2 \tag{2.66}$$

we can rewrite Eq. 2.61 as:

$$\frac{\partial \alpha}{\partial t} + \boldsymbol{\nabla}\cdot(\mathbf{u}\alpha) + \boldsymbol{\nabla}[\mathbf{u}_r\alpha(1-\alpha)] = 0 \tag{2.67}$$

where $\mathbf{u}_r = \mathbf{u}_1 - \mathbf{u}_2$ is the relative velocity between the phases, designated as *compression velocity*. This artificial convection term assumes non-zero values only for $\alpha \neq 0,1$ and is therefore only active at the interface. The discretization of the compression term $\boldsymbol{\nabla}[\mathbf{u}_r\alpha(1-\alpha)]$ and the definition of the relative velocity $\mathbf{u}_r$ in Eq. 2.67 are used to control and minimise the diffusion of the interface without the need to use special schemes such as CICSAM. A detailed description of the derivation of $\mathbf{u}_r$ from the underlying flow

and volume fraction fields and the discretization of the compression term are reported by Deshpande et al. (2012).

An accurate calculation of the volume fraction field is necessary for the correct evaluation of the interface curvature that is required in the determination of the surface tension force term in Eq. 2.60. The interfacial force per unit volume f_γ is evaluated using the continuous surface force (CSF) model, valid for a constant surface tension (Brackbill et al., 1992).

$$\mathbf{f}_\gamma = \gamma\kappa\boldsymbol{\nabla}\alpha \tag{2.68}$$

where γ is the interfacial tension between the two fluids and κ represents the average curvature of the interface defined as,

$$\kappa = -\boldsymbol{\nabla}\cdot\left(\frac{\boldsymbol{\nabla}\alpha}{|\boldsymbol{\nabla}\alpha|}\right) \tag{2.69}$$

The treatment of the stress tensor appearing in Eq. 2.60 is different for the two solvers `interFoam` and `rheoInterFoam`. For the former, both phases are considered Newtonian fluids and the stress tensor is simply related to the rate of strain tensor $\boldsymbol{\tau} = \eta(\boldsymbol{\nabla}\mathbf{u} - \boldsymbol{\nabla}\mathbf{u}^\intercal)$, where the viscosity is calculated via Eq. 2.63. In `rheoInterFoam`, the stress tensor appearing in Eq. 2.60 is decomposed in its solvent and polymeric contributions as expressed in Eq. 2.49. The solvent contribution is modelled as a Newtonian stress with viscosity $\eta_s = \alpha\eta_{s,1} + (1-\alpha)\eta_{s,2}$, where $\eta_{s,i}$ is the solvent viscosity of the phase i. On the other hand, the polymeric stress is calculated as a weighted average based on the volume fraction of the phases (Davoodi et al., 2021):

$$\boldsymbol{\tau}_p = \alpha\boldsymbol{\tau}_{p,1} + (1-\alpha)\boldsymbol{\tau}_{p,2} \tag{2.70}$$

in cases where the ith phase is Newtonian, $\boldsymbol{\tau}_{p,i} = 0$.

The final form of the conservation of momentum equation implemented in the viscoelastic solver is:

$$\rho\left(\frac{\partial\mathbf{u}}{\partial t} + \mathbf{u}\cdot\boldsymbol{\nabla}\mathbf{u}\right) - \boldsymbol{\nabla}\cdot[(\eta_s+\eta_p)\boldsymbol{\nabla}\mathbf{u}] = -\boldsymbol{\nabla}p - \boldsymbol{\nabla}\cdot(\eta_p\boldsymbol{\nabla}\mathbf{u}) + \boldsymbol{\nabla}\cdot\boldsymbol{\tau}_p + \mathbf{f}_b \tag{2.71}$$

It features a stabilizing diffusive term ($\boldsymbol{\nabla}\cdot\eta_s\boldsymbol{\nabla}\mathbf{u}$) added to both sides of the expression (Pimenta and Alves, 2017). The use of the both-side-diffusion (BSD) technique increases the ellipticity of the momentum equation, which improves the solver stability especially for constitutive modesl that lack a solvent contribution to the stress tensor. Finally, the exact expression of $\boldsymbol{\tau}_{p,i}$ is of course dependent on the particular choice of constitutive equation for the viscoelastic fluid. The direct discretization of the polymeric stress in the integral form reported in Sec. 2.2.3 causes a loss of stability of the conventional Finite Volumes numerical methods. This issue, known as the "High Weissenberg Number Problem"

(HWNP), include large normal stresses near geometric singularities and worsening of the problem with grid refinement. This issue is resolved, in the context of `rheoInterFoam`, via the introduction of the Log-conformation approach

The Log-conformation approach

The numerical issues encountered in the simulation of flows with high values of Weissenberg numbers are well known in the literature. They are commonly explained by the loss of accuracy of the discretization methods in area of the flow experiencing an exponential growth of stresses (Fattal and Kupferman, 2004). Most of the solutions proposed in the literature involve a change of variables in the constitutive equation (Fattal and Kupferman, 2004; Afonso et al., 2012; Balci et al., 2011; Fattal and Kupferman, 2005). The solver `rheoInterFoam`, utilizes the log-conformation approach proposed by Fattal and Kupferman (2004, 2005). This method involves the reformulation of the constitutive equation in terms of the natural logarithm of the conformation tensor. This strategy naturally preserves the positive definiteness of the conformation tensor and linearizes the stress field in regions of exponential growth, leading to an improved stability of the solver. Here we report a brief presentation of the log-conformation approach but a detailed mathematical derivation can be found in the works of Fattal and Kupferman (2004, 2005). The relationship between the polymeric extra-stress tensor and the conformation tensor for different constitutive models is reported in Table 2.3.

The log-conformation formulation requires the definition of a new tensor $\boldsymbol{\Theta}$ as the natural logarithm of $\mathbf{A}$.

$$\boldsymbol{\Theta} = \ln(\mathbf{A}) = \mathbf{R}\ln(\boldsymbol{\Lambda})\mathbf{R}^{\mathsf{T}} \tag{2.72}$$

In Eq. 2.72, the positive definite conformation tensor $\mathbf{A}$ is diagonalized as $\mathbf{A} = \mathbf{R}\boldsymbol{\Lambda}\mathbf{R}^{\mathsf{T}}$, where $\mathbf{R}$ is a matrix whose columns are the eigenvectors of $\mathbf{A}$ and $\boldsymbol{\Lambda}$ is a diagonal matrix of the eigenvalues of $\mathbf{A}$. The constitutive equation for a generic viscoelastic liquid in the conformation tensor form (Eq. 2.58) can then be expressed in terms of $\boldsymbol{\Theta}$ as:

$$\frac{\partial \boldsymbol{\Theta}}{\partial t} + \mathbf{u}\cdot\boldsymbol{\nabla}\boldsymbol{\Theta} - (\boldsymbol{\Omega}\boldsymbol{\Theta} - \boldsymbol{\Theta}\boldsymbol{\Omega}) - 2\mathbf{B} = \frac{g\left(e^{\boldsymbol{\Theta}}\right)}{Wi}e^{-\boldsymbol{\Theta}}Q(e^{\boldsymbol{\Theta}}) \tag{2.73}$$

which represents the action of the deformation field on $\boldsymbol{\Theta}$ as a composition of a pure rotation $\boldsymbol{\Omega}$, and a symmetric volume-preserving deformation $\mathbf{B}$ aligned with the principal axes of $\boldsymbol{\Theta}$[b]. For the derivation of Eq. 2.73 and exact definitions of the tensors $\mathbf{B}$ and $\boldsymbol{\Omega}$, we refer to Fattal and Kupferman (2004) and Pimenta and Alves (2022). The expression of the right side of Eq. 2.73 depends on the choice of constitutive equation and some examples are reported in Table 2.3.

Each time step, Eq. 2.73 is solved along with the mass and momentum conservation

[b] Note that $\boldsymbol{\Omega}$ is in general different from the vorticity tensor

equations. Subsequently, $\boldsymbol{\Theta}$ is diagonalised as $\boldsymbol{\Theta} = \mathbf{R}\boldsymbol{\Lambda}^{\boldsymbol{\Theta}}\mathbf{R}^{\mathsf{T}}$ and the conformation tensor is recovered from the inverse of Eq. 2.72:

$$\mathbf{A} = \exp(\boldsymbol{\Theta}) = \mathbf{R}\exp(\boldsymbol{\Lambda})\mathbf{R}^{\mathsf{T}} \tag{2.74}$$

Finally, the polymeric stress tensor can be computed from Eq. 2.57 and used in the momentum equation.

Chapter 3

Experimental investigation of the solid-liquid separation in a stirred tank owing to viscoelasticity

This chapter reports on the experimental investigation of the dynamics of solid particles dispersed in highly viscous, non-Newtonian fluids under agitation in a stirred vessel. The choice of mixing system was based on an existing design for a toothpaste manufacturing mixer, which was previously studied by Cortada-Garcia et al. (2018). The objective of this study is to demonstrate the effects of viscoelasticity-induced particle migration in such systems.

Experimental data revealed that in a Newtonian ambient fluid, particles disperse uniformly in the plane of measurement, whereas in strongly shear-thinning viscoelastic ambient fluids, particles tended to accumulate in the core of the vortices formed in the flow domain. The migration of solids towards the vortex core was also observed in purely viscoelastic (Boger) fluids, and was found to be strictly linked to the viscoelastic nature of the fluid as determined by the evaluation of the characteristic migration time. Furthermore, the effect of viscoelasticity on the flow field was assessed, with particular attention given to the vortex sizes and circulation intensities.

Part of this chapter has been published in:
Weheliye, H. W., Meridiano G., Mazzei, L., Angeli, P. (2020). Experimental investigation of the solid-liquid separation in a stirred tank owing to viscoelasticity, Physical Review Fluids, 5, 063302.

3.1 Introduction

The use of mechanically agitated vessels, for the mixing and suspension of solids highly viscous non-Newtonian liquids, is an extremely common operation in many industries such as healthcare, formulation manufacturing, food, and energy. Despite this, most of the literature on mechanically agitated fluid-particle mixers is focused on the study of turbulent Newtonian flows.

Extensive literature exists in the field of solid-liquid stirred tanks, encompassing both experimental and computational approaches. Zwietering (1958) introduced the concept of the just-suspended speed (N_{js}), defined as the impeller speed at which no particles remain stationary on the tank bottom for more than 1-2 seconds, based on a significant amount of experimental observations. Since then, various researchers have measured N_{js} in diverse mixing configurations using different experimental techniques. For instance Electrical Resistance Tomography (ERT) has been used by a number of researchers to examine the impact of impeller type, impeller speed, impeller off-bottom clearance, and particle size on mixing efficiency (Hosseini et al., 2010; Carletti et al., 2014; Tahvildarian et al., 2011; Harrison et al., 2012). Additionally, Positron Emission Particle Tracking (PEPT) has been utilized as a non-intrusive Lagrangian flow visualization technique to obtain complete 3D velocity and concentration fields of both continuous and dispersed phases in opaque mixing equipment (Guida et al., 2009, 2010). A review focusing on different kinds of measurement techniques about particle concentrations in the solid-liquid stirred tanks has been reported by Tamburini et al. (2013). As for investigations about the flow field in stirred vessels, laser-based optical imaging techniques such as Laser Doppler Anemometry (LDA) (Guiraud et al., 1997; Micheletti and Yianneskis, 2004; Virdung and Rasmuson, 2007a) and Particle Image Velocimetry (PIV) (Virdung and Rasmuson, 2007b; Unadkat et al., 2009; Gabriele et al., 2011; Montante et al., 2012) are the most widely used. In applying these techniques to solid-liquid systems, a main limiting factor is the solids concentration which, in the studies referred to here, was less than 1% by volume. Measuring velocity in the presence of particles can be problematic due to the obstruction and scattering of laser light as the solids volume fraction increases. To address this issue, researchers have used Refractive Index Matching (RIM) methods. For example, Micheletti and Yianneskis (2004) employed a mixture of 1-methylnaphtalene, 1-chloronaphtalene, and tetraline as the continuous phase and poly(styrene-(1%)co-divinylbenzene) impurity-free monodisperse particles as the dispersed phase to study liquid velocity characteristics with solids volume fractions up to 2% using LDA. Virdung and Rasmuson (2007a) used a mixture of benzyl alcohol and ethanol with glass spheres as the continuous and dispersed phases, respectively, to investigate axial velocities and turbulence levels in a stirred tank with LDA, achieving a maximum solids volume fraction of 9%. In a following study, the same authors also utilized PIV with image analysis to separate particles and liquid in their

camera frames to measure velocities of both phases up to 1.5% solids by volume. Gabriele et al. (2011) used p-cymene and PMMA spheres as the continuous and dispersed phases, respectively, to investigate turbulence properties in a high throughput stirred vessel with PIV, achieving up to 5% (by volume) particles for both up-pumping and down-pumping configurations.

A phenomenon recently encountered when dealing with solid-liquid suspensions in stirred vessels is the spontaneous accumulation of the solid phase in specific areas of the flow, caused by a cross-flow migration (that is the movement of solids across the streamlines of the fluid phase). The involuntary accumulation of solids in separate regions of the flow represents a clear impairment to the mixing process and can affect negatively the quality of the products and/or the efficiency of the whole operation. The study by Wang et al. (2014) examined solid-liquid suspensions in Newtonian and non-Newtonian laminar flows, adopting a three-dimensional (3D) particle visualization method to expose the real-time trajectories of the particles. In their study, they showed that the particles accumulated in the cores of the toroidal vortices created by the impeller rotation. In particular, the revolving blades of the impeller generated two coexisting, confined regions, above and below the blades, wherein the particles migrated. The migration was induced by inertial perturbations in the flow outside these regions, where, owing to the high shear rates present near the blades, the particle trajectories deviate from the path lines of the fluid, enabling the particles to cross the boundaries of these regions and settle into their cores.

As will be shown, a similar phenomenon is observed in the absence of inertia when the suspending fluid is viscoelastic. The present study aims to investigate the motion of solid particles dispersed in highly viscous, viscoelastic fluids under agitation in a stirred vessel, with a particular focus on the accumulation phenomenon. This part of the research has two primary objectives: first, to show that the accumulation of the solid phase is exclusively caused by the viscoelasticity-induced cross-flow migration of the solid phase, and second, to relate the characteristic velocity of the migration to the intensity of the elastic character of the flow. To achieve these goals, a refractive index matching method was employed along with a combination of PIV and PTV techniques to simultaneously measure the velocity fields of the solid and fluid phases. A strongly shear-thinning viscoelastic fluid and two Boger fluids were employed in order to separate the effects of the elasticity from those of shear thinning. The tracking of the solid phase also allowed the estimation of the characteristic migration time, that is the time needed for the complete segregation of the solids. This time was measured at different values of the Weissenberg number, Wi, in order to estimate the effect of the viscoelasticity on the migration velocity.

3.2 Materials and methods

3.2.1 Rheological characterization

Table 3.1: Properties of the fluids and solid phases measured at 23°C.

Acronym	Glycerol [wt%]	$ZnCl_2$ [wt%]	H_2O [wt%]	Xanthan [ppm]	PAA [ppm]	ρ $[kg/m^3]$	η $[Pa \cdot s]$	r_n	Re
GZ_N	42	18	40	-	-	1630	0.25	1.487	65-100
GZ_{ST}	42	18	40	1300	-	1630	5.9-0.27	1.487	65-100
GW_N	98	-	2	-	-	1250	0.71	1.475	33-50
GW_{B1}	98	-	2	-	100	1250	≈0.8	1.475	33-50
GW_{B2}	98	-	2	-	200	1250	≈0.85	1.475	33-50

To investigate the effect of the rheological properties, five different fluids were used throughout the experimental campaign. Specifications about the compositions, density (ρ), viscosity (η) and refractive index (r_n) are provided in Table 3.1. Among these fluids, those labeled as *GZ* were composed of glycerol (42% by weight), water (18%), and zinc chloride (40%). The particular composition of *GZ* was chosen to ensure that the refractive indices of the fluid and solid phases were matched. As will be shown later, when the refractive indices of a fluid and its suspended solids match, it becomes possible to measure the velocity of both phases simultaneously. Two versions of *GZ* were prepared: a Newtonian fluid denoted as GZ_N, and a non-Newtonian, shear-thinning fluid denoted as GZ_{ST}. GZ_{ST} was obtained by the addition of 1300 ppm of Xanthan gum (XG, supplied by Sigma-Aldrich, UK), an organic bio-polymer that is well-known for inducing strong shear-thinning behaviour. The molecular weight of Xanthan Gum, not provided from the manufacturer, was obtained by Migliozzi et al. (2021) through gel permeation chromatography (GPC), yielding an average molecular weight of 1.76×10^6 g/mol. Similarly, the fluids labeled as *GW* were comprised of glycerol (98%) and water (2%). Three versions of *GW* were prepared: a Newtonian fluid denoted as GW_N, and two purely viscoelastic, or Boger, fluids denoted as GW_{B1} and GW_{B2}. These Boger fluids were obtained by respectively adding 100 and 200 ppm of polyacrylamide (PAA, supplied by Sigma-Aldrich, UK) having a molecular weight of $M_w = 5 - 6 \times 10^6$ g/mol, respectively.

Given the high viscosity of all the solvents, the polymer suspensions were prepared by initially creating stock solutions, which were subsequently diluted with the correct amount of solvent. Specifically, for fluid GZ_{ST}, a stock solution at 3250 ppm of XG in water was prepared by gently dispersing the 3.25g polymer powder in 1 kg of warm milli-Q water (DW, temperature kept at 40 °C). During this stage, the liquid was kept at a temperature of $40°C$ to reduce its viscosity and facilitate polymer dissolution. During the

dispersion step, it was important to keep a swirling flow in the container and gradually pour the powder in the centre of the vortex to avoid agglomeration. Similarly, for the two Boger fluids, the stock solutions were prepared by adding 5g of PAA to 1 Kg of warm milli-Q water (concentration of the stock solution was 5000 ppm). The stock solutions were then stirred gently with a magnetic stirrer for at least 24 hours to fully disperse the polymer powders.

An estimation of the expected rheological behaviour of polymer suspensions can be obtained through the evaluation of the polymer concentration regime. When the concentration of polymers is low, the suspension will typically exhibit a pure viscoelastic behaviour, whereas at high concentrations, it will become shear-thinning. The point at which the suspension transitions from dilute to semi-dilute is known as the characteristic overlapping concentration, or c^*. This concentration serves as a threshold for the dilute regime: concentrations below c^* are therefore considered dilute, and interactions between polymer molecules are assumed to be negligible. A standard criterion for the evaluation of c^* is to consider the reciprocal of the polymer intrinsic viscosity $[\eta]$ (Flory, 1953), i.e. $c^* = [\eta]^{-1}$. The intrinsic viscosity of a particular polymer is a function of the molecular weight of the polymer and on the solvent used. For a particular polymer suspension, $[\eta]$ can be estimated via the Mark-Houwink correlation once the molecular weight of the polymer Mw is known. The relation is typically given in the form:

$$[\eta] = K_M Mw^{a_M} \tag{3.1}$$

where K_M and a_M are the Mark-Houwink parameters that are only function of the solvent type and operating temperature. Estimations of the Mark-Houwink parameters for the two polymers of interest were obtained from the literature and are reported in Table. 3.2 (Madkour and Mark, 1999; Abed et al., 2016; Milas et al., 1985). Using these values, c^* was estimated to be approximately 710 ppm for PAA and 360 ppm XG. Therefore, the concentrations of PAA in the fluids GW_{B1} and GW_{B1} were low enough to remain in a dilute regime and expect that no shear-thinning effects should be observed, whilst the concentrations of XG in GZ_{ST} were well above c^* thus it should present a strong shear-thinning behaviour. Note that these values are only estimates and should not be intended as precise thresholds since the parameters in Table 3.2 were obtained by dissolving the polymers in water at 25°. Nonetheless, similarly to water, the solvents used in this study are considered to be "good solvents" for both XG and PAA Flory (1953). It is then reasonable to assume that the use of the parameters in Table 3.2 produce a good first order approximation of the intrinsic viscosity of the polymers.

In the following sections, it will become necessary to define the dimensionless Weissenber (Wi) number to quantify the elasticity of the flow. To this end, a characteristic relaxation time of the fluids involved, λ_Z, will be evaluated according to Zimm's theory

(Zimm, 1956; Abed et al., 2016; Del Giudice et al., 2017):

$$\lambda_z = \frac{F[\eta]Mw\eta_s}{RT} \tag{3.2}$$

where R is the ideal gas constant, T is the absolute temperature and η_s is the solvent viscosity. The factor F is given by:

$$F = \sum_{i=1}^{+\infty} \frac{1}{i^{3\mu}} \approx 0.53 \tag{3.3}$$

where μ is a parameter that depends on the quality of the solvent and is equal to 0.6 for soluble polymers suspended in a good solvent (Del Giudice et al., 2017). The value of the relaxation times calculated in this manner are also reported in Table 3.2. Note that the value of λ_z for XG is reported only for completeness given that Zimm's theory is strictly only applicable to dilute polymer suspensions.

Table 3.2: Mark-Houwink parameters used for the two polymers and corresponding intrinsic viscosities and Zimm's relaxation time.

	Mw [g/mol]	K_M [g/mL]	a_M [-]	$[\eta]$ [mL/g]	c^* [ppm]	λ_Z [s]
PAA	5×10^6	4.9×10^{-3}	0.8	1120.4	890	1.15
XG	1.76×10^6	1.7×10^{-4}	1.14	2246	450	0.22

All the experiments reported in the following sections were carried out in a temperature-controlled laboratory at 23°C. Hence, all the rheological measurements were conducted at the same temperature. The rheological properties of all the fluids were tested with an Anton Paar MCR302 stress-controlled rotational rheometer, equipped with a peltier plate to precisely control the operating temperature and a cone-plate measuring system (OD: 50 mm and truncation angle of 1°). For all measurement samples, the fluid menisci were covered with silicon oil (5 cSt) to seal the interface and avoid solvent evaporation. Steady-shear flow tests were performed to obtain flow curves of all the experimental fluids at 23°C. The tests were performed by ramping up the shear rate $\dot{\gamma}$ from 0.01 to 2000 s^{-1}. At each value of shear rates, both the torque and the normal force acting on the cone were measured. This allowed to measure the shear stress and the first normal stress difference simultaneously.

Viscosity values at different shear rates are presented in Fig. 3.1a for the three solutions displaying non-Newtonian behaviour. As it can be seen, GZ_{ST} shows a marked shear-thinning behaviour with a viscosity ranging between 5.9 and 0.27 $Pa \cdot s$. The viscosity curve for the shear-thinning fluid can be interpolated with the Carreau-Yasuda (C-Y) model:

$$\eta(\dot{\gamma}) = \eta_\infty + (\eta_0 - \eta_\infty)\left[1 + (\lambda_c \dot{\gamma})^a\right]^{\frac{n-1}{a}} \tag{3.4}$$

where η_∞ is the viscosity on the plateau where the shear rate is very high (in the limit to infinity), η_0 is the viscosity on the plateau where the shear rate is very small (in the limit to zero), λ_c is a time constant and n is the flow index. In the range of shear rates investigated, the viscosity drops by about one order of magnitude, with a shear index of 0.53 and a time constant of 12.3 s. As expected, the fluid GZ_{ST} also displays a measurable degree of elasticity. This can be observed in Fig. 3.1b in the form of an increasing first normal stress difference. Fig. 3.1a also reports the viscosity curves for the two Boger fluids GW_{B1} and GW_{B2}. Since the polymer concentration in these fluids is below the overlapping concentration, the viscosity remains almost constant throughout the entire measurement range. The two fluids also display a measurable normal force as shown by the curves of $N1(\dot{\gamma})$ in Fig. 3.1b. As expected, $N1$ increases with the shear rate and a larger concentration of PAA corresponds to larger values of $N1$. Noticeably, at values of $\dot{\gamma} \leq 100$, $N1 \propto \dot{\gamma}^2$ which is the expected behaviour of purely elastic fluids (James, 2009). This is also showed by the dashed straight line with slope 2 reported in Fig. 3.1b.

3.2.2 Experimental apparatus

Solid particles

To visualise the flow of the liquid phase in the presence of solids, we matched the refractive indices of the two phases. PMMA spherical particles of 1.5 mm diameter and refractive index r_n of 1.487 were employed as solid dispersed phase. The refractive indices of both GZ_N and GZ_{ST} fluids, measured with a Bellingham and Stanley Model 5 Abbe refractometer, were found to be equal to 1.487 ± 0.0005 (at 23 °C). The refractive indices were relatively insensitive to temperature (decreasing from 1.487 to 1.485 with a 5 °C temperature rise), so that no temperature correction was required. To avoid any overheating of the fluids, mainly caused by the rotating impeller, the experimental runs were kept short (below 30 minutes). The experiments were conducted at particle volumetric concentration ranging from 0 to 2%, within the dilute regime. At the values of N used, the particles were always sufficiently suspended and the air-liquid interface remained essentially flat. This allowed to avoid any image distortion resulting from the generation of a central vortex around the shaft of the impeller.

In the case of the GZ_N and GZ_{ST}, the matching of the refractive indices of the solid and liquid phases allowed the simultaneous measure of the fluid (via PIV) and the solids (via PTV) velocities. The velocity fields and the time evolution of the particle distribution fields for these fluids were measured at $N = 700$ and $N = 100$ rpm.

In contrast, the refractive indices of the two Boger fluids (with a $r_n = 1.475$ at 23 °C) differed significantly from those of the solids. Consequently, the velocity field of the liquid phase was determined via PIV in the absence of the solids. Subsequent experiments were conducted at the same impeller speed to measure the time evolution of the solids

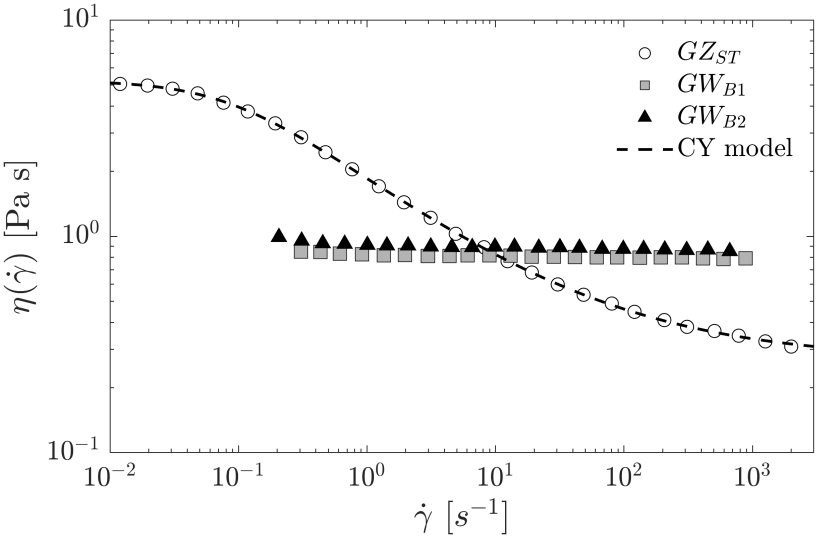

(a)

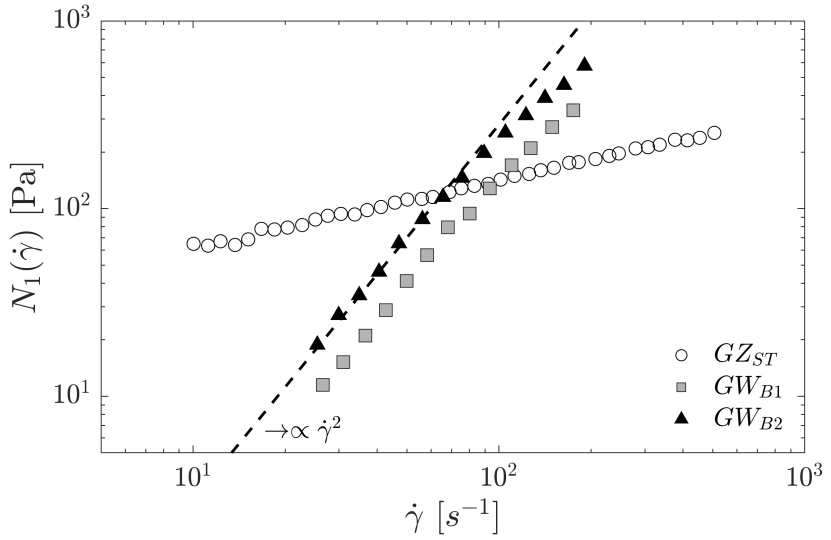

(b)

Figure 3.1: Material functions in simple shear flow of the three non-Newtonian fluids: (a) shear viscosity and (b) first normal stress difference.

distribution. The purely viscoelastic fluids were tested at impeller speeds $800 \leq N \leq 1500$ rpm.

Tank geometry

The experiments were carried out in a cylindrical flat-bottomed vessel of diameter $T = 50$ mm, as shown in the schematic diagram of Figs.3.2b and 3.2c. The liquid in the vessel was agitated by a stainless steel dual impeller with two flat blades (see Fig. 3.2b) of diameter $D = 37.5$ mm, blade height of $W = 6$ mm, impeller clearance from the bottom of the vessel of $C = 10$ mm, and a liquid height of $H = 60$ mm. The vessel was encased in a square trough, filled with the fluid mixture GZ_N in order to minimize the optical distortion resulting from the curvature of the cylindrical surface. Both the vessel and the trough were made of acrylic ($r_n = 1.495$) to match the refractive index of the working fluid and of the dispersed phase (PMMA). At the beginning of each run, the particles were placed at the top of the liquid in the vessel. To avoid air entrapment when the agitation started, a lid was placed on top of the liquid surface, so that the floating particles were entirely wetted (Fig. 3.2c). The Reynolds number, $Re \equiv \rho N D^2/\eta$, for the Newtonian ($GZ_N$ and GW) and Boger (GW_{B1} and GW_{B2}) mixtures was based on the impeller diameter D, impeller speed N, fluid density ρ , and constant viscosity η. For the shear-thinning fluid (GZ_{ST}), the Reynolds number was defined according to the procedure of Metzner and Otto (1957). First, an average shear rate $\langle\dot{\gamma}\rangle$ in the area surrounding the impeller is estimated as:

$$\langle\dot{\gamma}\rangle = k_s N \tag{3.5}$$

where the value of k_s depends exclusively on the impeller type and impeller-tank configuration. The impeller used in our work was similar to that adopted by Cortada-Garcia et al. (2018), for which $k_s = 15$. Although this number was not accurately measured for the specific system under examination, it is assumed that it provides a reasonable estimation of the order of magnitude of the shear rate around the impeller. With the value of $\langle\dot{\gamma}\rangle$ obtained from Eq. 3.5, the apparent viscosity of the shear-thinning fluid was calculated from Eq. 3.4. Thus, the Reynolds number for the GZ_{ST} fluid was given by:

$$Re = \frac{\rho N D^2}{\eta_\infty + (\eta_0 - \eta_\infty)\left[1 + (\lambda_c k_s N)^a\right]^{\frac{n-1}{a}}} \tag{3.6}$$

From the above, the average shear rates for the GZ_{ST} mixture at $N = 700$ rpm and 1000 rpm are 175 and 250 s^{-1}, respectively. This corresponds to $Re = 65$ and $Re = 100$. Notice that, both values of $\langle\dot{\gamma}\rangle$ lie within the shear-thinning regime of GZ_{ST}. Finally, the elastic character of the flow will be estimated via the definition of a Weissenberg number $Wi = \lambda_Z\langle\dot{\gamma}\rangle$ for the stirred vessel.

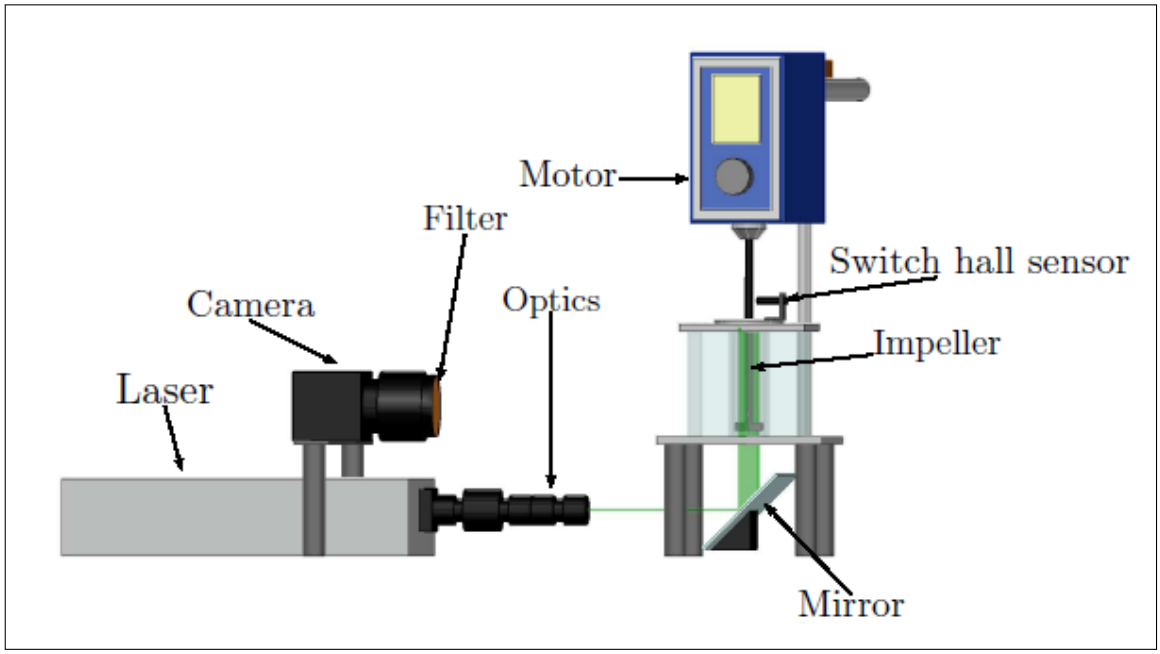

(a)

(b)

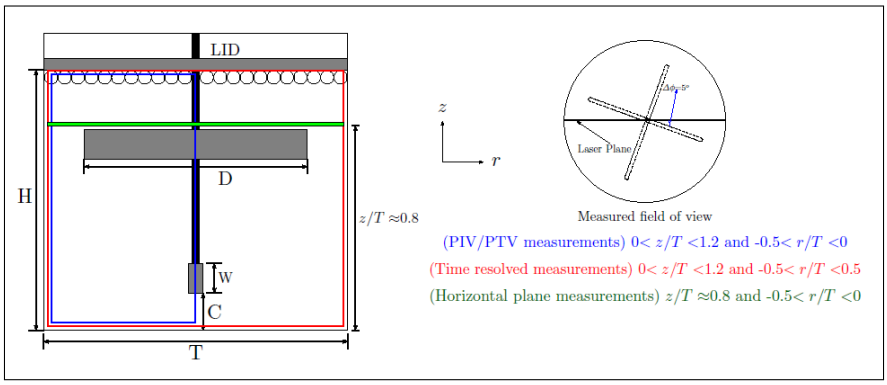

(c)

Figure 3.2: (a) Experimental setup for the PIV experiments, (b) 3D visualizations of the dual blade impeller and (c) schematic of the tank geometry showing visualization areas for both PIV/PTV and solid mixing configurations.

PIV measurements

The PIV setup included a dual cavity Nd:Yag green laser (532 nm) (Litron Laser, 14.5 Hz, 1200 mJ) and a straddling CCD camera with 2048 $\times$ 2048 pixels with a spatial resolution of 32 $\mu m/px$, equipped with a 105 mm Nikon lens. As tracers for the PIV measurements in the fluid phase, fluorescent polymer particles with 20 µm diameter made of melamine resin and coated with Rhodamine B were employed. For the experimental conditions investigated, the tracer relaxation time was negligible compared to the convection time $\left(St = \frac{\rho_t d_t^2 N}{18\eta} << 1\right)$, where ρ_t and d_t are the tracer density and diameter, respectively.

In the case of refractive index matching, the PMMA solids become invisible when fully submerged in the fluid. To overcome this, a small quantity of aqueous Rhodamine 6G dye was added to the suspending liquid to make the particles visible as black circles. The complete procedure for this is described in a later section. However, for experiments with the Boger fluids, where refractive indices were not matched, the PMMA particles were dyed with Rhodamine 6G. The dyeing process involved mixing the particles in an aqueous solution containing 0.1% weight of Rhodamine 6G for 24 hours. After that, the particles were strained and allowed to dry for an additional 24 hours, resulting in a thin layer of dye deposited on the spheres. Although this layer was not permanent and would leach into the fluid during the experiments, it was stable enough to carry out experiments lasting up to 60 minutes.

An orange filter with a cutoff wavelength at 570 nm was employed to ensure that only the light emitted from the tracers and the particles (maximum emission at 590 nm) was recorded by the camera. The laser and the camera were synchronized by means of a Laser Pulse Synchroniser (Model 610035 TSI) and they were controlled via the Insight 4G (TSI) software. The laser beam was guided through a collimator and two cylindrical lenses (25 mm and 15 mm) that transformed it into a narrow plane of 1 mm thickness. Measurements were obtained on both the vertical and horizontal planes. For the vertical plane measurements, the generated laser sheet was reflected on a 45° silver-coated mirror and entered the vessel from the bottom as shown in Fig. 3.2a. For the measurements on the horizontal plane, a horizontal laser sheet was generated just above the top impeller while the camera was positioned underneath the vessel (not shown in the figure). The images were captured using either phase-resolved or time-resolved measurements. For the former, the image capture was synchronized with the impeller blade position using a hall switch sensor. For each experiment, 100 image pairs were taken at the same phase angle (i.e., the angle between the upper blade of the impeller and the laser sheet) to produce 100 instantaneous velocity vector fields. The phase-resolved velocity field was then obtained by averaging the instantaneous vector fields.

Phase-resolved experiments were carried out for PIV/PTV measurements and the time between each laser pulse Δt varied depending on the speed of the impeller to ensure

that the tracers did not move out of the image plane during capture. To maximise the field of view in the vertical plane, the phase-resolved measurements were carried out on a plane at an angle of 5° to the top blade, as shown in the plane view on the right-hand side of Fig. 3.2c. Additionally, the measurement was limited to the left-hand side of the vessel (blue box in Fig. 3.2c). Vector fields on the horizontal plane were also obtained through phase-locked measurements on a single plane at $z/T = 0.8$. However, to calculate all the components of the shear rates, it was necessary to obtain PIV data on multiple horizontal and vertical planes. To this end, additional measurement were performed in the range $z/T = 0.78$ – 0.82, with intervals of $\Delta z/T = 0.02$, along with two vertical PIV measurements from $\phi = 5$ – $7°$ at an interval of $\Delta\phi = 2°$. For the same image magnification and spatial resolution, time-resolved measurements were carried out to investigate the time evolution of the distribution of the solids in the tank. In these tests, 1000 images ere captured with an image acquisition frame rates of 14.5 Hz, utilizing the whole field of view, as shown in Fig. 3.2c (red box).

Image analysis

Fig. 3.3a shows a typical raw image obtained from the PIV measurements in the GZ_{ST} mixture (1300 ppm xanthan gum) at $Re = 65$. In this image, the bright spots correspond to the tracers in the continuous phase, while the bright circles represent the suspended particles. The intensity values of the 8-bit images range from 0 (representing black) to 255 (representing white). To isolate the tracer particles and the edges of the solid spheres, the raw image in Fig.3.3a was binarised using an ad hoc threshold value determined from the intensity histogram. The resulting image is shown in Fig.3.3b. Subsequently, a median filter was applied to the binarized images to remove the tracer particles.

The edges of the particles were detected with the use of a circular Hough transform (CHT) algorithm (Atherton and Kerbyson, 1999). According to the algorithm, at each edge point of a single solid sphere it is possible to draw a series of circles with center in the edge point considered and a varying radius $r_{min} < r < r_{max}$. The definition of a range of radii is necessary as not all the solid spheres are expected to be located with their center laying exactly on the laser plane. Once every possible circle (employing every edge point and every value of the radius) has been drawn, the intersection point passed by the highest number of circles is selected as "real" center of the particle. Fig. 3.3c shows the result of the boundaries detection algorithm performed on the image in Fig. 3.3b.

The images shown in Fig. 3.3c displaying the positions of the particles, were then used in particle tracking velocimetry (PTV) and solids mixing analysis. The velocities of the particles was measured with the cross-correlation/relaxation (ICCRM) technique in the PTVlab toolbox by Brevis et al. (2011), which involves tracking the motion of individual particles between two successive camera frames. First, each particle is detected and localized on each camera frame; then, the two particle images in the two consecutive frames

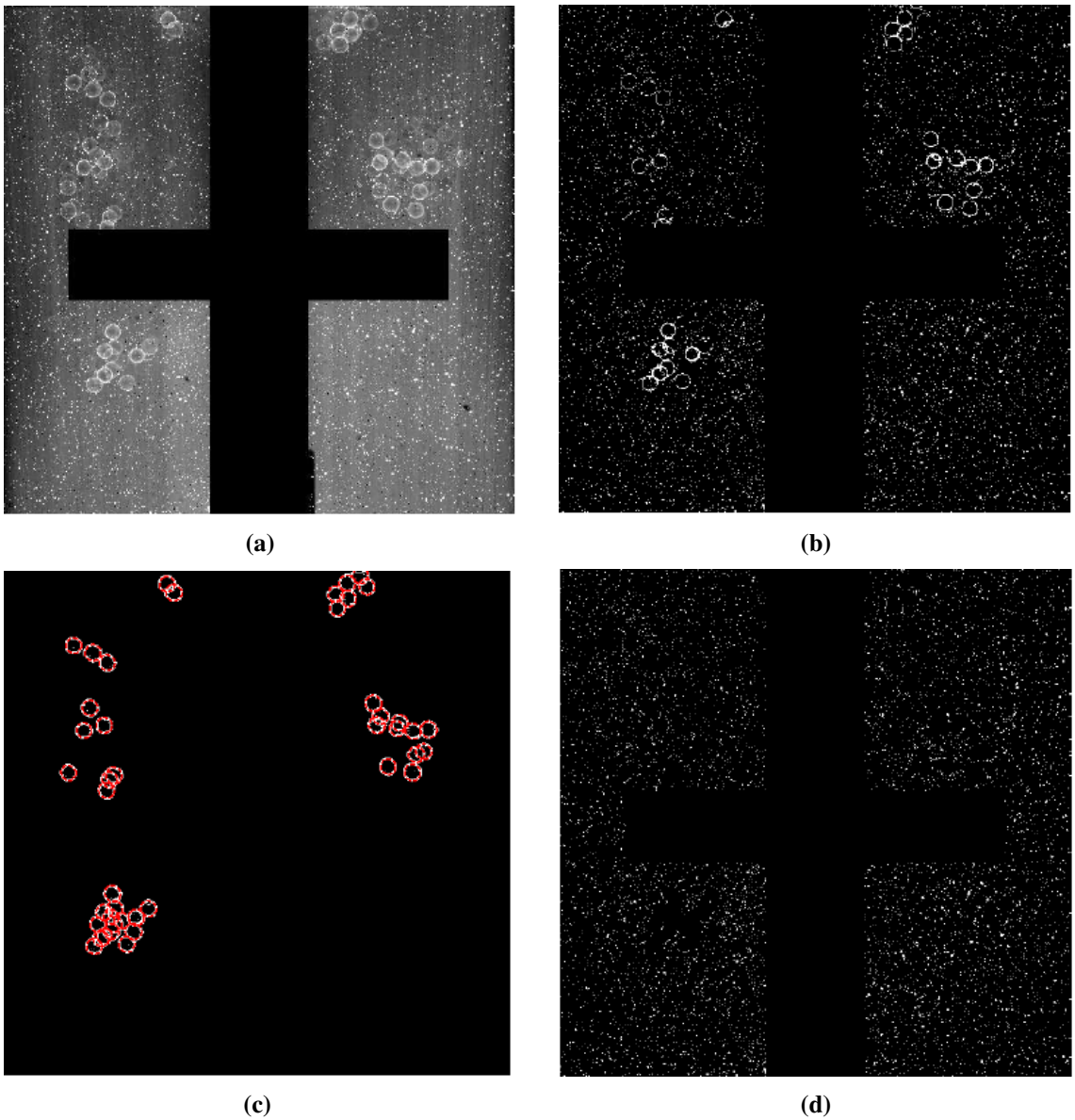

Figure 3.3: Image analysis during pretreatment stages, for $Re = 65$, GZ_{ST} mixture and particle volumetric concentration of 1%. (a) Raw PIV image, (b) binarized image without the dye, (c) image with the detected solids and (d) image with only the PIV tracer particles.

are "matched," i.e., identified as belonging to the same particle without ambiguity. This identification is performed via the two-step PTV algorithm, denoted ICCRM, that combines the well-known cross-correlation (CC) and relaxation method (RM). The difference between the positions of the two particle images gives the particle displacement between the two frames, while the time is given by the time difference between two consecutive images.

To quantify the degree of mixing of the particles in the tank over time, a similar method to that developed by Camesasca et al. (2006) was employed. According to their approach, the measurement plane was split in small sub-regions, denoted by the index i, and the Shannon entropy S_i was calculated in each one as follows:

$$S_i = -\sum_{j=1}^{2} p_j(i) \ln p_j(i) \tag{3.7}$$

where $p_1(i)$ is the ratio of the number of pixels filled by the solids over the total number of pixels in region i, while $p_2(i)$ is the ratio of the number of pixels filled by the fluid over the total number of pixels in sub-region i. The entropy for the whole field of view is then estimated as the average of the entropies of all the sub-regions:

$$S = \frac{1}{N_r} \sum_{i=1}^{N_R} S(i) \tag{3.8}$$

According to Brandani et al. (2013), the entropy S is a measure of the disorder present in a solid-liquid system. In a hypothetically perfectly mixed system, where particles are uniformly distributed throughout the field of view, the entropy value is $S = 1$. On the other hand, the initial state of a system, where all particles are situated at the top of the liquid prior to stirring, is characterized by a low value of entropy. By analyzing the time evolution of S, one can estimate the mixing state of the system over time.

Finally, by subtracting Fig. 3.3c from Fig. 3.3b, one can isolate the signal of the tracers, as shown in Fig. 3.3d. These images were then binarized to eliminate the effect of the dye. The velocity of the fluid was calculated from the tracer displacements between two consecutive images with the freeware package JPIV, using a 50% window overlap for a final interrogation window with resolution of 16×16 pixels. An amplitude filter was applied to each cross-correlation box to eliminate the vectors that substantially deviated from the median value (Westerweel and Scarano, 2005). Since the solid spheres were larger than an individual interrogation window, this caused a larger number of zero values in the liquid phase. These values were omitted when calculating the phase-average velocity fields.

In the experiments involving Boger fluids, where the refractive indices of both the fluids and particles were not matched, PIV measurements were carried out without the presence of solids. The time evolution of the solid dispersion was then obtained by per-

forming additional time-resolved tests after the addition of the dyed PMMA particles.

Steady-state flow

As it will become clear later, it was necessary to establish whether the fluid velocity field in the vessel could be considered fully developed before the particles were drawn in. To this end, the temporal evolution of the flow field was investigated for the case of the GZ_N fluid. The spatial mean fluid velocity magnitude $\left(\sqrt{u_r^2+u_z^2}\right)^*$ was calculated from the PIV measurements previously described, using the following equation:

$$\left(\sqrt{u_r^2+u_z^2}\right)^* = \frac{1}{A}\int_A \left(\sqrt{u_r^2+u_z^2}\right) dA \tag{3.9}$$

where u_r and u_z are the radial and axial fluid velocity components, respectively, on the plane of measurement and A denotes the area over which the integral is computed. In this case, A is the left-hand side of the vertical plane of measure (blue area in Fig. 3.2c). The mean velocity was estimated at several times. Each of these times referred to the same position of the impeller blades (phase angle $\phi = 5°$) but to a different number of revolutions from when the impeller was started. Hence, instead of reporting the mean velocity as a function of time, it is here reported as a function of the number of revolutions, N_s.

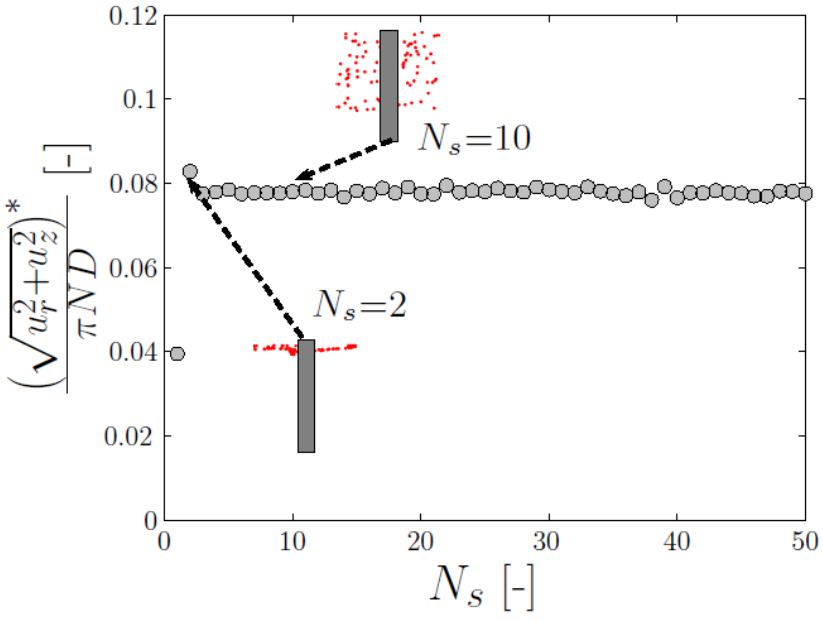

Figure 3.4: Variation of the dimensionless mean fluid velocity magnitude as a function of the number of revolutions N_s for the fluid mixture GZ_N and $Re = 65$.

Experimental results for GZ_N at $Re = 65$ are presented in Fig.3.4. The measurements were conducted in the presence of solids. The graph illustrates that initially, there is a sharp increase in the mean fluid velocity, which then stabilizes to a nearly constant value

after three revolutions ($N_s = 3$). The inset of Fig.3.4 shows that the solids are located at the free surface for $N_s = 2$, indicating that the solids are only drawn in when the flow has reached a steady state. By $N_s = 10$, the solids are uniformly distributed over the upper part of the vessel, as evident from the inset of Fig. 3.4.

3.3 Results

3.3.1 Shear-thinning fluid

We first examine the motion of the particles in the Newtonian mixture, GZ_N, at steady state. Fig. 3.5a shows the phase-averaged velocity fields of the fluid (left plot) and solid (right plot) phases at $Re = 65$. The phase-averaged velocity, $\langle u_i \rangle$, is given by:

$$\langle u_i \rangle = \frac{1}{N_\phi} \sum_{i=1}^{N_\phi} u_i \tag{3.10}$$

where u_i is the i-th component of the instantaneous velocity and N_ϕ corresponds to the number of measurements taken at a phase angle, $\phi = 5^\circ$. The velocity vectors have been normalized with the impeller tip speed. The flow field generated by the dual paddle impeller is similar to that reported in Cortada-Garcia et al. (2018), with the fluid ejected from the impeller radially towards the tank wall. The fluid then moves axially and curves towards the center line of the tank, where it is drawn towards the impeller. All the fluid appears to move and no stagnant zones can be identified.

Fig. 3.5a (right plot) seems to indicate that the solid spheres follow the fluid pathlines in their vortical motion with the velocity of each sphere being close to the local velocity of the fluid. This is expected as inertia effects are negligible. For this case, the density difference between the two phases is equal to 440 kgm^{-3} and the particle settling velocity due to gravity, U_t , is much less than the characteristic velocity of the fluid, πND ($U_t/\pi ND \approx 1 \times 10^{-3} << 1$). In addition, the particles Stokes number is less than unity ($St \approx 1 \times 10^{-3} << 1$), i.e., the particles relax quickly to the local fluid velocity. To confirm this, it was necessary to calculate the slip velocity between the two phases $u_s = |u_p - u_f|$ where u_p and u_f are the instantaneous particle and fluid velocities, respectively. To determine the slip velocity, a methodology similar to that proposed byFrédéric et al. (2003) and Derksen (2012) was employed. For every pair of images, each particle can be included in a correlation box sufficiently large to contain both the particle and the minimum amount of tracer necessary for the estimation of the fluid velocity. Employing the PTV and PIV algorithms, one can then measure both the velocities of the particle and that of the surrounding fluid. From this procedure, it was concluded that almost all the spheres have a ratio $|u_p - u_f|/|u_f| << 1$ at all times, with the maximum value of this ratio never exceeding 0.05.

Fig. 3.5b shows the contour plots of the averaged solid volume fraction, $\langle C \rangle$, and the tangential component of the vorticity, ω_θ, for the GZ_N mixture at $Re = 65$.

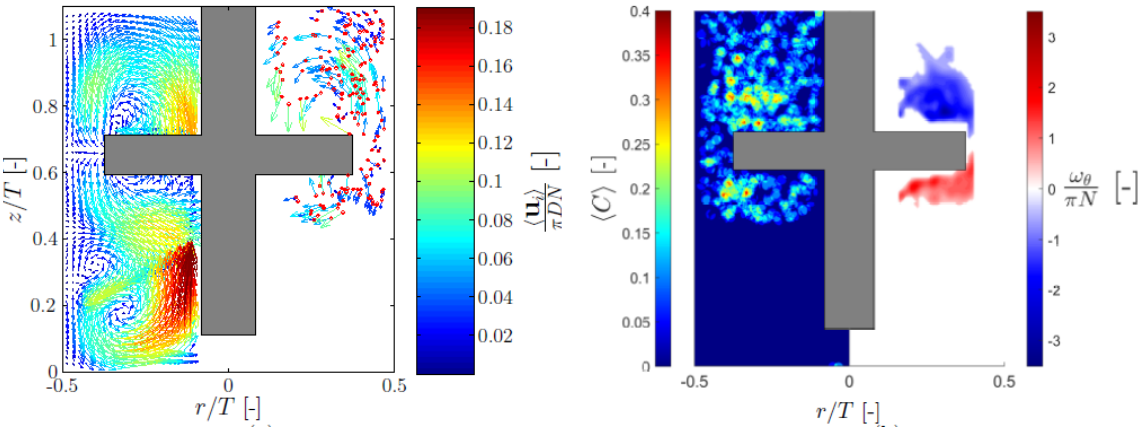

(a) **(b)**

Figure 3.5: (a) Fluid (left figure) and solid (right figure) phase-averaged velocity fields; (b) contour plots of the averaged solid volume fraction and dimensionless tangential component of the vorticity ω_θ in the upper part of the vessel. Both figure report the results for the fluid mixture GZ_N at $Re = 65$ and particle volumetric concentration of 1%.

The solid volume fraction distribution was determined by assigning a value "1" to pixels that fall inside a detected circle (see Fig. 3.3c) and "0" elsewhere. Averaging the pixel values over 50 images then provides an estimate for the time averaged local solids volume fraction field, $\langle C \rangle$, shown in the left image of Fig. 3.5b. As it can be seen, the solids are uniformly dispersed up to a minimum height of $z/T = 0.45$. The steady-state solids volume fraction field $\langle C \rangle$ in Fig. 3.5b is reached via two stages. Initially, solid particles were placed atop the denser, immobile liquid. The particles would only stay afloat if the cumulative effect of buoyancy and surface tension forces surpassed that of gravity. Upon initiation of impeller rotation and consequent fluid motion, additional fluid-particle interaction forces emerge, and in particular the drag force. In the first stage, this force overpowers the buoyancy and surface tension forces and drags the particles away from the surface and into the liquid bulk. In the second stage, the particles are dispersed in the tank by the flow field. In the case examined, the particles are drawn into the liquid bulk only at an impeller speed $N \geq 700$ rpm. At this speed, the flow reaches a steady state while the particles are still at the liquid surface (see Fig. 3.4). Upon entry into the flow domain, the solid particles rapidly relax to the local fluid velocities and subsequently travel along the fluid pathlines of the large vortical motions situated above the upper blade of the impeller. Although some particles were also observed to follow the pathlines of the vortex immediately beneath the upper blade, the particles never reach the bottom of the tank due to the segregation of the flow field produced by the dual blade impeller (Fig.3.5a, left plot).

Contrary to the observations made by Wang et al. (2014), who reported particle ac-

cumulation within the core of the vortices for a Newtonian ambient fluid and $St << 1$, we did not observe any accumulation of particles in the core of the vortices in this study. According to Wang et al. (2014), the solids take a considerable amount of time (up to 30 minutes) to accumulate, particularly for large particles ($d_p = 2.8$ mm). Nonetheless, even after 30 minutes, no indications of accumulation of the solid phase in the core of the vortices were observed in this study. Since the particles closely follow the fluid pathlines and no accumulation is observed in the vessel for the Newtonian ambient fluid, for the rest of the study it will be assumed that the role of inertia on the trajectory of the particles is negligible.

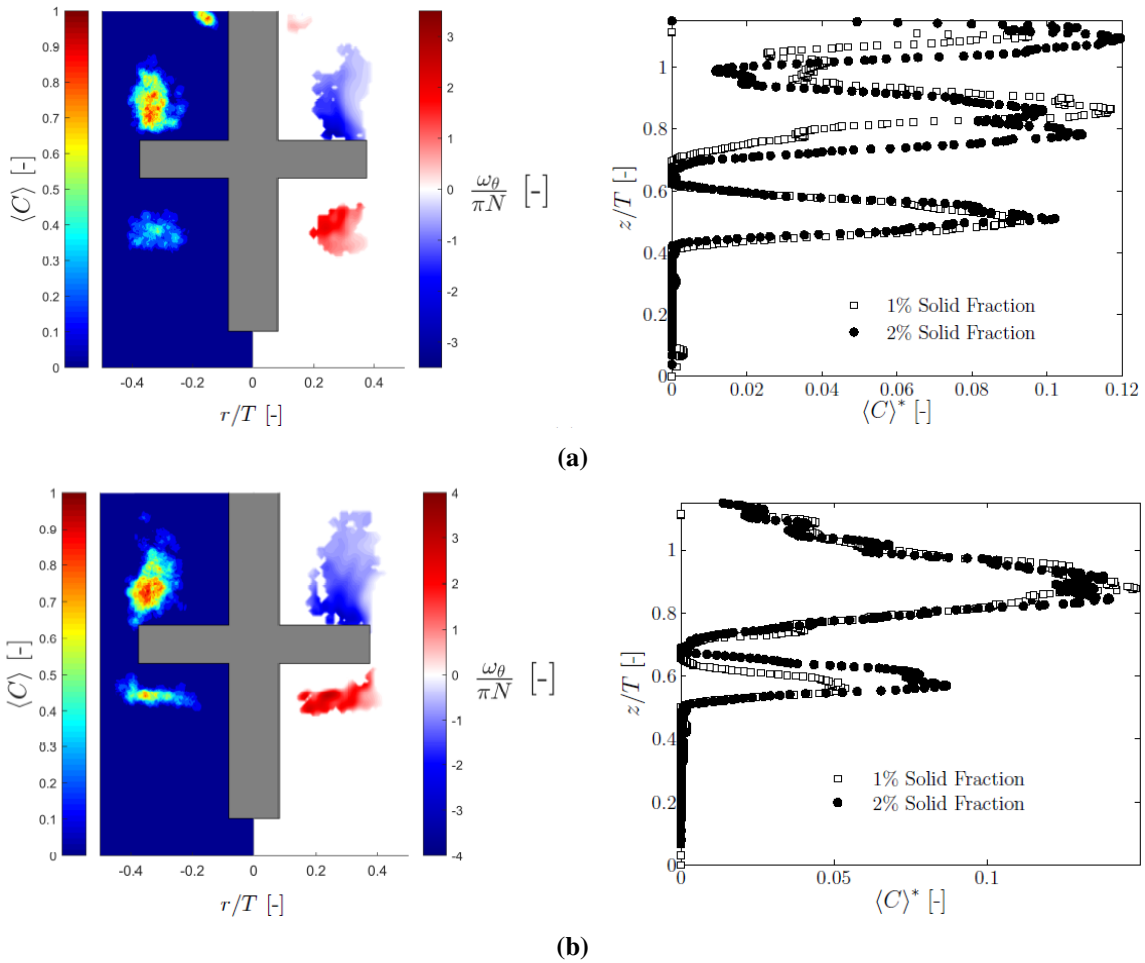

Figure 3.6: Contour plot of the averaged solid volume fraction and dimensionless tangential component of the vorticity ω_θ and radial concentration profile $\langle C \rangle^*$, for fluid mixture GZ_{ST} and particle volumetric concentrations of 1% and 2% at (a) $Re = 65$ and (b) $Re = 100$.

The effects of rheology of the suspending fluid on the distribution of solids in the vessel was first investigated via the use of the shear-thinning fluid GZ_{ST}. Fig. 3.6 presents the steady-state averaged solid volume fraction and tangential vorticity contour plots for two distinct values of Re, along with the corresponding averaged radial solid volume fraction profiles, denoted as $\langle C \rangle^*$. The quantity $\langle C \rangle^*$, defined as $\langle C(r) \rangle$, is computed over

a cross section of the vessel. As we can see from Fig. 3.6a, for $Re = 65$ the averaged solid volume fraction maps are substantially different from those observed for the Newtonian case. Now, solids accumulate in the three vortical regions of the flow, two immediately above the top impeller blade and one below it. The radial solid volume fraction profiles for two particle volumetric concentrations, 1% and 2%, are shown in the right image in Fig. 3.6a. For both, the main features of the profiles agree with the three accumulation areas identified in the left image in Fig. 3.6a.

When Re increases to 100, the two vortices in the top of the tank merge to form a larger one just above the top impeller blade, while the bottom vortex elongates along the radial direction and shifts closer to the top impeller blade (Fig. 3.6b). The changes in the flow field are reflected in the averaged solid volume fraction map. The particles now accumulate in the two large vortical regions above and below the top impeller blade. The axial solid volume fraction profile in the right image in Fig. 3.6b shows two main peaks for the two different particle volumetric concentrations investigated. The bottom peak is larger for the larger solid volume fraction. Moreover, for both particle concentrations, more solids are trapped in the top vortex. That is likely because, as the solids are drawn into the fluid, they first encounter the top vortex, so that most particles become entrapped there; only few particles manage to move further down in the vessel, ending up in the vortex below the top impeller. For $Re = 65$, the behaviour is similar, but less pronounced, and the averaged solid volume fractions are higher in the vortical structures above the impeller blade compared to those below.

The spatio-temporal distributions of the solids in the tank at the imaging plane for the GZ_N and GZ_{ST} fluids as well as the Shannon entropy S at $Re = 65$ are shown in Figs. 3.7a and 3.7b.

The supplementary videos reported by Weheliye et al. (2020) show how the solids distribute in the imaging plane over time for both fluids. For GZ_N (Fig 3.7a), the Shannon entropy follows a sigmoidal profile with the normalized time tN. The entropy is initially low, when all the particles are at the top of the liquid, as shown in diagram a above Fig. 3.7a. As tN increases, S increases monotonically because the flow draws the particles into the tank along the impeller shaft (diagram b in Fig. 3.7a). At $tN = 14.6$, where uniform solid mixing has been achieved in the vessel region above the bottom impeller, S plateaus at a value of 0.48. Similarly, in the non-Newtonian case (GZ_{ST}), the Shannon entropy starts from a low initial value, which rapidly increases with time up to a maximum value of around 0.42.

The observed maximum value of S for the GZ_{ST} mixture was found to be lower than that of the GZ_N mixture. This can be attributed to the fact that in the case of the GZ_{ST} mixture, particle accumulation occurs almost immediately after the solids are introduced into the vessel, prior to the complete dispersion. Consequently, the solids occupy a relatively smaller portion of the flow domain (as illustrated in diagram b above Fig. 3.7b), leading

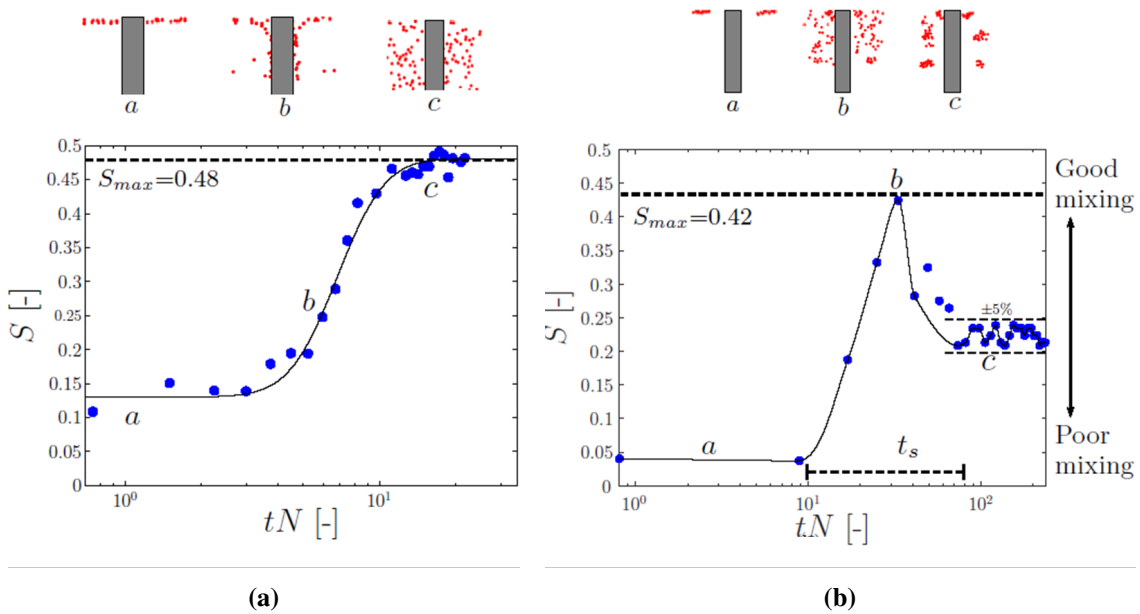

(a) **(b)**

Figure 3.7: Variation of the Shannon entropy S, with increasing tN at $Re = 65$ and particle volumetric concentration of 1% for (a) GZ_N; (b) GZ_{ST}.

to a lower S value. As tN increases, the Shannon entropy decreases, nearly plateauing at a value of 0.22 with a fluctuation of about $\pm$ 5%. The decrease of S reflects the reduction in the area of the image occupied by the particles, as shown in diagram c above Fig.3.7b.

3.3.2 Purely viscoelastic fluids

From the results presented, it was clear that the non-Newtonian nature of the suspending fluid was the cause of the accumulation of the solid phase. However, it was still unclear whether the particle migration seen in the Xanthan gum mixture was caused by the shear thinning of the viscosity or the elastic behaviour of the ambient fluid. For this reason, the experiments were repeated with the two purely viscoelastic fluids GW_{B1} and GW_{B2}. This allowed to effectively isolate the effects of elasticity from those of the shear-thinning viscosity. Furthermore, it should be noted that the density difference between the liquid and solid phases in these fluids is relatively small, with a value of approximately 60 kg/m^3. This is a representative value for various industrial processes involving the separation of solid particles from highly viscous liquids.

Fig. 3.8a shows the averaged solid volume fraction (left side) and tangential vorticity contour plots along with the corresponding velocity vector field (right side) in the plane of measurement, for the Newtonian GW mixture ($Wi = 0$) at $Re = 45$ and particle volumetric concentration of 1%. The contour plot of the averaged solid volume fraction shows that the solids are almost uniformly dispersed throughout the whole measurement plane. In contrast to the GZ_N case, the solid particles do reach the bottom of the vessel in this case.

This can be attributed to the lower density difference between the two phases, which is only 60 kg/m^3 for the *GW* mixture. This behaviour is in line with the findings of Takahashi and ichiro Sasaki (1999), who showed that the minimum height reached by the suspended phase is strongly dependent on the density difference between the phases.

When the PAA polymer is added (Fig. 3.8b) the averaged solid volume fraction map for the particles suspended in the GW_{B2} mixture at $Wi = 25$ is similar to that obtained for the suspension in the GZ_{ST} mixture (see Fig. 3.6). The solids have accumulated in each of the vortex cores of the flow. From the contour plot on right side of Fig. 3.8a, one can see that for the *GW* mixture, the vortices are formed around the upper and lower sides of the top blade. The intensity of the two vortices is comparable, although they are not symmetrically positioned with respect to the blade center line (i.e., with the upper vortex closer to it). At a phase angle of $\phi = 5°$, it is still possible to see the vortices generated by the bottom impeller at an angle of 95° from the bottom leading blade (after a quarter of impeller revolution). Their intensities are still significant and approximately equal to 93% of the upper blade vortices.

The intensity of the upper vortices in the GW_{B2} fluid at $Wi = 25$ shown in Fig. 3.8b (right side) is comparable to that for the *GW* case. However, the vortices at the bottom impeller have significantly dissipated after a quarter of a revolution, with intensity values decreased by about 36% and size shrunk by up to 40% compared to the Newtonian fluid.

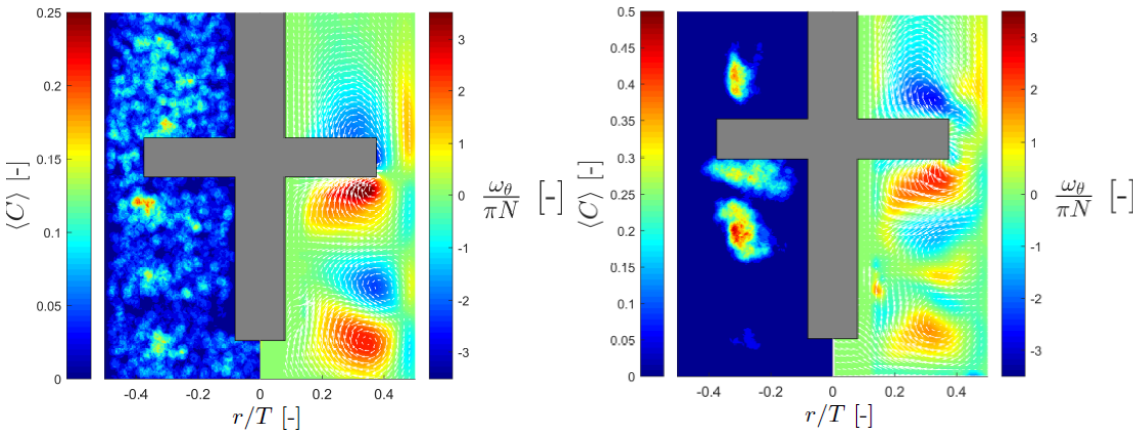

Figure 3.8: Averaged solid volume fraction (left side) and dimensionless tangential vorticity contour plots along with the dimensionless phase-averaged velocity field (right side) at $Re = 45$ and particle volumetric concentration of 1% for the fluids: (a) *GW* ($Wi = 0$) and (b) GW_{B2} ($Wi = 25$).

These features are summarized in Fig. 3.9, that shows the circulation intensity Γ^* for the different fluid mixtures at varying Reynolds number. Γ^* is calculated as follows:

$$\Gamma^* = \frac{1}{A_{\omega i}} \int_{A_{\omega i}} |\omega_\theta| dA_{\omega i} \tag{3.11}$$

where the integration is carried out over the area $A_{\omega i}$ where the dimensionless vorticity $\omega_\theta/\pi N$ is larger than 1. Fig.3.9a displays the areas $A_{\omega i}$ for the GW fluid, in the absence of particles at $Re = 45$. Figs.3.9b and 3.9c illustrate the variation of Γ^* for the GW, GW_{B1}, and GW_{B2} mixtures with respect to Re for the areas below the top ($A_{\omega 1}$) and the bottom ($A_{\omega 2}$) blades of the impeller, respectively. As Re increases, higher circulation intensity is observed in both regions.

In the absence of elastic stresses, the circulation intensity of the vortices located in areas $A_{\omega 1}$ and $A_{\omega 2}$ is similar for the GW mixture, at all values of Re. This can be seen by comparing the curves in Figures 3.9b and 3.9c. However, for the GW_{B1} and GW_{B2} mixtures, elastic stresses are present and increase with polymer concentration. This leads to a different behaviour of the upper and lower vortices. The vortices near the top blade are measured on a vertical plane at an angle of 5° behind the blade, and the circulation levels remain similar for all the fluids at all Re. On the other hand, the vortices generated by the bottom blade are measured at an angle of 95° (after 1/4 of a rotation) from the bottom leading blade. Here, the suppression of the circulation intensity caused by the elastic stresses on the vortices is evident as signaled by the curves in Fig. 3.9c. For example, at $Re \approx 50$ the circulation intensity of GW ($Wi = 0$) is almost 60% higher than that for GW_{B2} ($Wi = 28$). The suppression of the circulation intensity and the reduction of the vortex size in viscoelastic fluids have previously been reported in the literature and is attributed to the presence of the elastic stresses acting along the circular streamlines of the vortices (Palacios-Morales et al., 2015; Sousa et al., 2011).

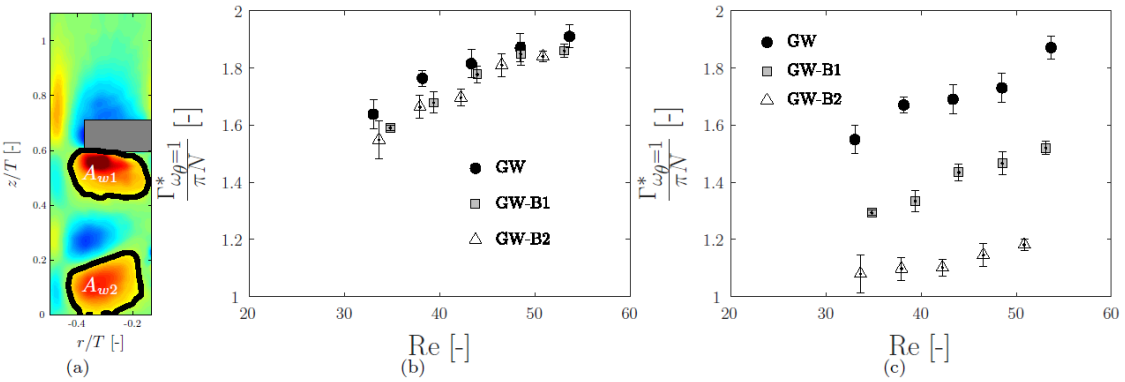

Figure 3.9: (a) Visualization of the area $A_{\omega i}$, over which the circulation Γ^* has been estimated (example for the fluid GW at $Re = 45$ and $Wi = 0$). Variation of the space-averaged dimensionless circulation intensity with increasing Re for (b) $A_{\omega 1}$ and (c) $A_{\omega 2}$.

These results suggest that the solid migration to the core of the vortices and the suppression of the vortices in the flow are caused by the viscoelasticity of the ambient fluid. As reported by D'Avino et al. (2017), cross-flow migration of solids has been observed for viscoelastic fluids in the absence of inertia in simple shear and pressure-driven flows

in channels with a constant cross section. For almost all the flows examined, the authors found that the solids migrated from regions of high to regions of low shear rate. In the case of a pipe flow, with the fluid flowing in the z direction, the radial migration arises from the combined action of the first normal stress difference N_1 and the shear rate gradients. For this simple shear flow, the first normal stress difference is given by $N_1 = \tau_{zz} - \tau_{rr} \propto \dot{\gamma}^2$. N_1 increases with the shear rate, and consequently the side of the particle facing the region of high shear rate is subject to a force larger than that acting on the side facing the region of low shear rate. The resultant force is responsible for the migration and is directed from regions of high (close to the pipe wall) to regions of low (close to the pipe center line) shear rates. Solid migration from high to low shear rate regions in viscoelastic fluids has also been reported in a concentric annulus configuration with a rotating inner cylinder (Karnis and Mason, 1966; Lormand and Phillips, 2004; D'Avino et al., 2012). In this flow geometry, the inner rotating cylinder produces a shear flow (in the $r-\theta$ plane) which stretches the polymer molecules around the cylinder in the azimuthal direction. This leads to a first normal stress difference that is larger close to the inner cylinder compared to the outer one. This generates an imbalance in the normal stresses around the particles, a condition that causes a cross-flow migration towards the outer wall, where the shear rate is low.

In the present study, the flow system resembles the concentric annulus flow described above, with the difference that the inner cylinder is equipped with impellers generating vortical flows above and below them. Therefore, to interpret the particle migration observed, measurements need to be taken in the horizontal plane (i.e., in the $r-\theta$ plane). Fig. 3.10a and 3.10b exhibit the averaged solid volume fraction and velocity vector fields for the mixtures GW and GW_{B2}, at $Re = 45$, for a particle volumetric concentration of 1% at $z/T = 0.8$. The flow fields for both mixtures are typical of rotating fluids with the maximum velocity magnitude located near the tip of the impeller and the minimum near the walls ($r/T = 0.5$) and near the edge of the shaft (i.e., $r/T = 0.05$). The volume fraction contour maps show a uniform distribution of the solids in the plane for GW, while for the GW_{B2} fluid the solids tend to localize in the region $r/T \approx 0.2\tilde{}0.38$.

To better understand the accumulation of the particles, the velocity components in the region where the migration occurs were analysed. The data in Fig. 3.11a show the radial (u_r), tangential (u_θ), and axial (u_z) velocity component profiles obtained for the mixture GW_{B2} at $\phi = 5^\circ$ and $z/T = 0.8$ above the upper blade of the impeller. For $Re = 45$ and $Wi = 25$, u_θ exhibits a parabolic-like profile with a maximum absolute value of 1 m/s at $r/T = 0.33$, which corresponds to the core of the vortex. The maximum absolute value of u_θ is an order of magnitude greater than the maximum absolute value of u_r and almost four times that of u_z. For the same fluid mixture a similar u_θ profile is obtained at $Re = 33$ and $Wi = 18$, where the maximum absolute value is 0.65 m/s and the slope of the profile is less steep than that obtained at $Re = 45$ and $Wi = 25$.

In order to identify areas of high shear, the components of the shear rate were com-

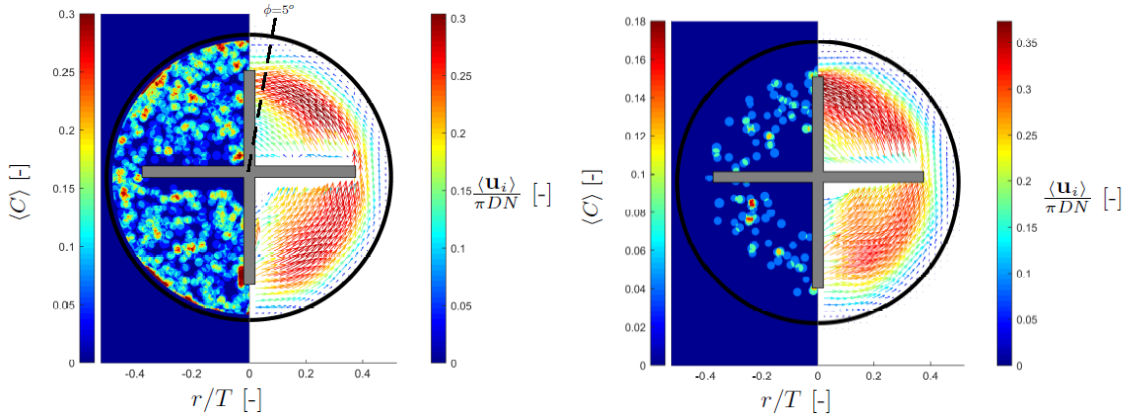

Figure 3.10: Horizontal plane measurements of the averaged solid volume fraction (left side) and dimensionless velocity field (right side) at $Re = 45$, $z/T = 0.8$ and particle volumetric concentration of 1% for the fluids: (a) GW at $Wi = 0$ and (b) GW_{B2} at $Wi = 25$.

puted from the velocity data. These rates have a direct impact on the direction and intensity of particle migration in the vessel. In Fig. 3.11b the components of the shear rate, $\dot{\gamma}_{\theta z}$, $\dot{\gamma}_{rz}$ and $\dot{\gamma}_{r\theta}$ are plotted against the radial coordinate for the same location $z/T = 0.8$. The three components are calculated as:

$$\dot{\gamma}_{\theta z} = \frac{\partial u_\theta}{\partial z} + \frac{1}{r}\frac{\partial u_z}{\partial \theta} \tag{3.12}$$

$$\dot{\gamma}_{rz} = \frac{\partial u_r}{\partial z} + \frac{\partial u_z}{\partial r} \tag{3.13}$$

$$\dot{\gamma}_{r\theta} = \frac{1}{r}\frac{\partial u_r}{\partial \theta} + r\frac{\partial}{\partial r}\left(\frac{u_\theta}{r}\right) \tag{3.14}$$

The $r-\theta$ component of the shear rate is an order of magnitude greater than the other two. The maximum absolute value of $\dot{\gamma}_{r\theta}$ occurs outside the vortex region, where $\dot{\gamma}_{r\theta}$ exhibits a nearly linear increase, while at the center of the vortex it reaches its minimum absolute value. This is in agreement with the literature on stirred tank reactors (Bouremel et al., 2009), where the rate of deformation is lowest at the core of the vortex and highest around the edges of the vortex. At $Re = 33$ and $Wi = 18$, a similar $\dot{\gamma}_{r\theta}$ profile is obtained, where the absolute values of $\dot{\gamma}_{r\theta}$ are smaller compared to those at $Re = 45$ and $Wi = 25$. We also compared the profiles of $\dot{\gamma}_{r\theta}$ obtained for the fluid mixtures GW ($Wi = 0$) and GW_{B2} ($Wi = 25$) at $Re = 45$ and $z/T = 0.8$, both shown in Fig. 3.11c. Both profiles show a similar trend where the shear rate has a minimum at the core of the vortex and the absolute value increases further away.

From previous considerations, we can deduce a dynamic of the accumulation phenomenon. In particular, it seems that the particles migrate radially to the core of the vortices under the combined action of the first normal stress difference $N1$ (i.e., the fluid elas-

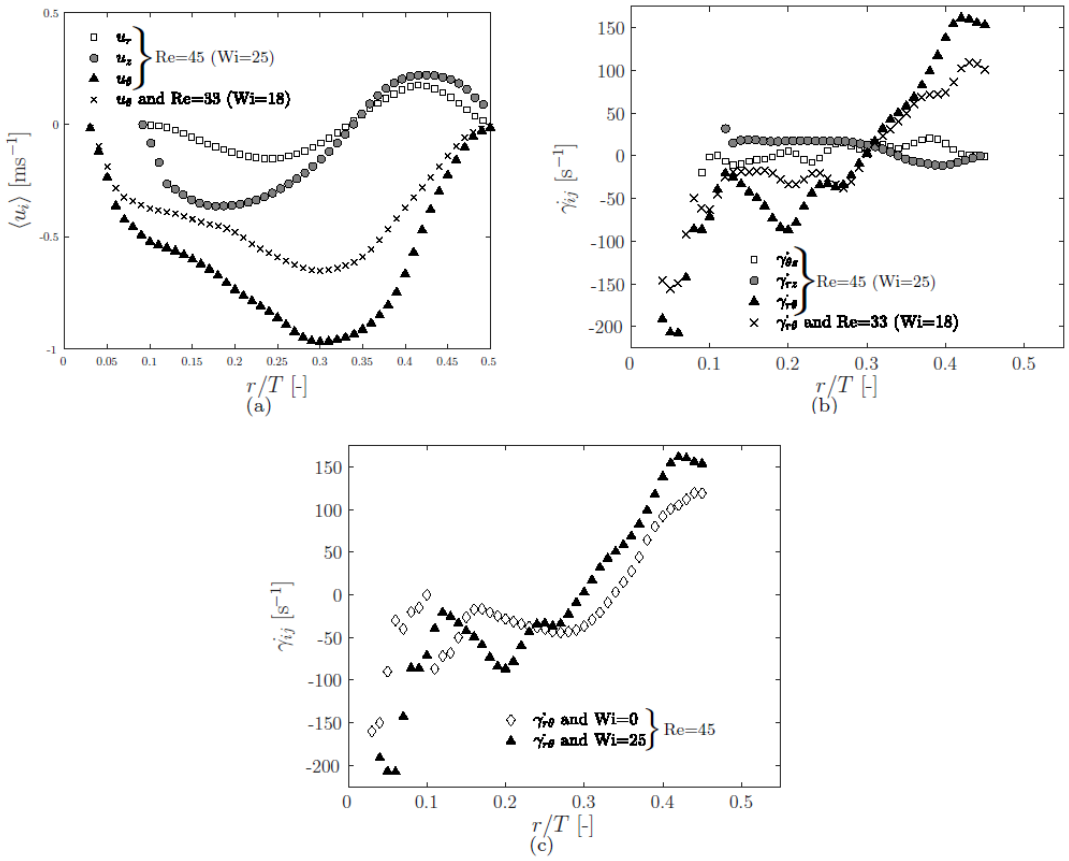

Figure 3.11: (a) Comparison of the radial profiles of the radial (u_r), tangential (u_θ), and axial (u_z) velocity profiles; (b) $\dot{\gamma}_{r\theta}$, $\dot{\gamma}_{\theta z}$ and $\dot{\gamma}_{rz}$ obtained from vertical and horizontal plane measurements for the fluid mixture GW_{B2} at $z/T = 0.8$. (c) Comparison of the $r-\theta$ component of the shear rate $\dot{\gamma}_{r\theta}$, for the fluid mixtures GW ($Wi = 0$) and GW_{B2} ($Wi = 25$) for $Re = 45$ at $z/T = 0.8$.

ticity) and the presence of gradients of shear rate in the horizontal plane (gradients in the component $\dot{\gamma}_{r\theta}$). The particle migration mechanism in the current system is summarized schematically in Fig. 3.12. As can be seen in Fig. 3.12a in a Newtonian ambient fluid, at different times, a single particle follows the same fluid pathline. This behaviour is expected, because the role of inertia on the trajectory of the particle is negligible. Fig. 3.12b shows that in a viscoelastic ambient fluid a single particle moves from one vortical pathline to another owing to the imbalance of radial forces acting on it. At the core of the vortex the shear rate has a minimum (see Fig. 3.11c) while further away the absolute value of the shear rate increases. Therefore, one side of the solid (in the radial direction), located far from the core of the vortex, faces a region of high shear rate while the other side faces a region of low shear rate. The imbalance of the shear rate causes a difference in the normal force (i.e., a force along in the r direction) across the particle which pushes it towards the center of the vortex. Once in the middle of the vortex the particle can only move in the tangential direction.

The impact of the viscoelasticity on the time required for complete accumulation of solids in the $r-z$ plane was also studied. Specifically, the dimensionless characteristic migration time t_sN was evaluated for mixtures GW_{B1} and GW_{B2} at different values of Wi. The migration time represents the duration from the first solid draw-down in the vessel to the complete accumulation of the solid phase. In practise, the value of t_sN was calculated as the time at which the Shannon entropy reaches 99% of its steady state value. The results are presented in Fig.3.13. For the dilute polymeric solutions considered here, the

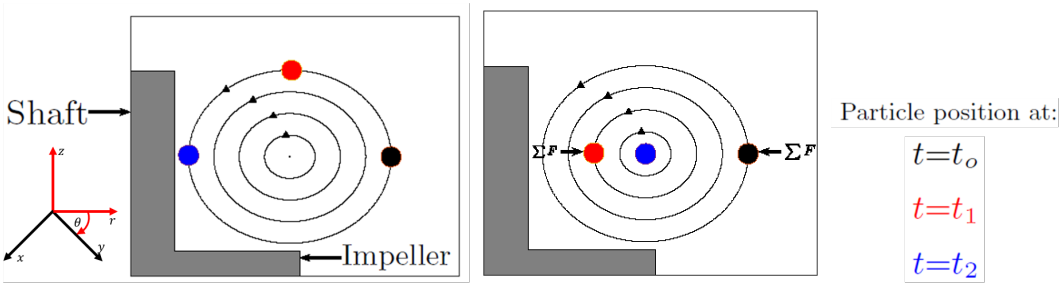

Figure 3.12: Schematic diagram of the vortex above the right top impeller and the dynamic of a single particle for (a) Newtonian and (b) purely viscoelastic ambient fluid. Particles located far from the center of the vortices experience a force that pushes always towards the center of the vortex. The force is directed radially and arises from the presence of gradients of $\dot{\gamma}_{r\theta}$.

elastic relaxation time λ is a constant and the Weissenberg number ($Wi = \lambda_z N$) is varied by increasing the impeller speed, N. As expected, the dimensionless migration time (t_sN) for both fluid mixtures decreased with increasing Wi, indicating faster solids migration in the vessel. Additionally, higher values of Wi were found to correspond to increased dominant shear rate ($\dot{\gamma}_{r\theta}$) as depicted in Fig.3.11c, leading to faster cross-flow migration due to the rise in $N1$.

It can also be seen that the dimensionless migration time t_sN for GW_{B1} is almost twice that for GW_{B2}, indicating that doubling the polymer concentration (which increases N_1), while keeping Wi constant, reduces t_sN by twofold. For similar Re, the solids migration times due to viscoelasticity shown in Fig. 3.13 are at least three orders of magnitude lower than those due to inertia measured by Wang et al. (2014). Finally, it is worth pointing out that the characteristic migration time reported here is not equivalent to the migration time reported in the literature by D'Avino et al. (2012) for a single particle, and therefore comparisons between the two times must be made with care.

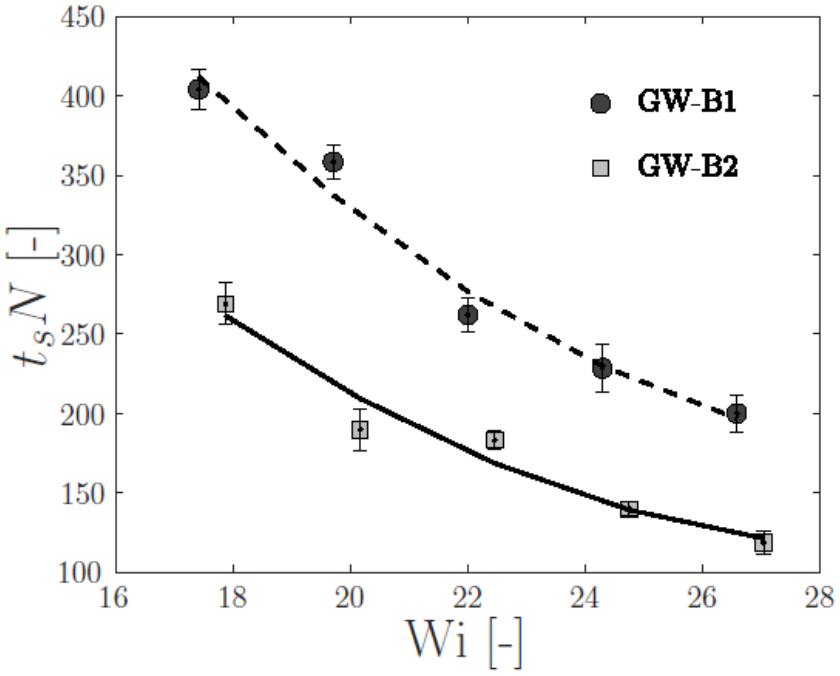

Figure 3.13: Variation of the dimensionless characteristic solids migration time, t_sN, with increasing Wi with a solid volume fraction of 1% for the fluids GW_B1 and GW_B2.

3.4 Conclusions

This chapter presents an experimental investigation on the viscoelasticity-induced migration of solid particles in a stirred vessel. Particle Image Velocimetry (PIV) and Particle Tracking Velocimetry (PTV) techniques were used to measure the velocity fields of the liquid and solid phases and the evolution of solid concentration in a tank equipped with a dual-blade impeller.

Results showed that in a Newtonian fluid, solid particles quickly relax to the local fluid velocity and disperse uniformly over time. However, in a non-Newtonian, shear-thinning fluid, an accumulation of solid particles at the core of the vortices was observed. To isolate the effect of fluid elasticity, the experiments were repeated with two purely viscoelastic (Boger) fluids. Results indicated that solid particles also accumulated at the core

of vortices in these fluids, with the accumulation time decreasing with increasing Weissenberg number (Wi) and polymer concentration. Additionally, vortex size and circulation intensity were found to decrease with increasing Wi. The observed particle migration phenomenon can be useful for separating solid particles from high-viscosity liquids, particularly when the densities of the particles and the ambient liquid are similar, making gravity settling ineffective. Furthermore, the migration time of solid particles induced by viscoelasticity was found to be at least three orders of magnitude lower than that observed for inertia-induced migration in previous studies.

Having encountered the viscoelasticity-induced migration in stirred vessel, the next chapter will be devoted to further understanding the nature of the phenomenon, the forces involved and their dependence on the fluid dynamics and rheological properties. While the experimental results reported here have established the correlation between viscoelasticity and migration, they did not provide reliable estimations of the migration time and/or velocity. This is because, in all the experiments, the migration has consistently been overlapped with the initial dispersion of the solids, making it impossible to obtain accurate measurements of the characteristic migration time. Furthermore, the estimation of fluid relaxation time via Zimm's theory did not take into account the degradation of polymers occurring in the vessel during prolonged stirring, leading to an overestimation of the relaxation time and subsequently of Wi. The upcoming chapter will address these challenges and offer a more nuanced understanding of the viscoelasticity-induced migration in stirred vessels.

Chapter 4

Scaling law for the viscoelasticity-induced particle migration in stirred vessels

Following the results reported in Chapter 3, we investigate the viscoelasticity-induced migration of solid particles immersed in the three-dimensional flow field created by the rotation of a Rushton turbine. At the same time, we propose a scaling law for predicting the characteristic particle migration time as a function of the Weissenberg number. Our choice of experimental setup and mixing system was aimed at building up the level of complexity from the simple, two-dimensional Poiseuille or Couette-flow usually encountered in the literature. In particular, we researched a three-dimensional flow field that could be easily studied in terms of its main directions of strain. The objective was to introduce a scaling law and to test the usefulness of simple heuristic arguments in capturing the viscoelastic-induced particle migration phenomenon even in these conditions.

Particle image velocimetry is adopted to reconstruct the three-dimensional velocity and deformation rate fields generated by the rotation of the Rushton turbine in both Newtonian and viscoelastic fluids; concurrently, particle tracking is used to measure the evolution of the particle distribution in the tank. The experimental campaign shows that the deformation rate field is essentially bi-dimensional and confined to the $r-\theta$ plane. Accordingly, the particles migrate only in the radial direction driven by the presence of gradients of shear rate on the $r-\theta$ plane. Finally, the scaling law is validated against experimental data obtained at different Weissenberg numbers, impeller diameters and fluid compositions. The results show good agreement between the scaling law and the experimental data.

Part of this chapter has been published in:
Meridiano G., Weheliye, H. W., Mazzei, L., Angeli, P. (2022). Scaling law for the viscoelasticity-induced particle migration in stirred vessels, Journal of Non-Newtonian

Fluid Mechanics, 309, 104918.

4.1 Introduction

The systematic study of the dynamics of particles in viscoelastic fluids started over half a century ago (Leal, 1979; Brunn, 1976b) with earlier works mainly reporting experimental observations, in simple flow cells, of complex behaviours, such as migration and accumulation of the particles. The experimental results were also qualitatively supported by theoretical predictions derived under the conditions of slow and slowly varying flows, and of small particle sizes (Leal, 1979; Brunn, 1976b; Ho and Leal, 1976; Brunn, 1976a). The development of more accurate experimental techniques, like particle velocimetry, allowed the detailed analysis of the dynamics of the particles in a wide range of flow conditions. Accurate simulations were also made feasible by the development of numerical algorithms capable of treating non-Newtonian fluids. As a result, several aspects of the particle motion in viscoelastic media have since been understood, especially for simple particle shapes, such as spheres. An accurate work reviewing a large part of the literature on this subject is that by D'Avino and Maffettone (2015). The main conclusion of the aforementioned studies is that migration is observed when there is an imbalance of viscoelastic normal stresses around the particles. This imbalance can be caused by the non-uniformity of the flow field in which the particles are immersed and/or by the particle-wall interactions. If present, the shear-thinning of the ambient fluid influences both the direction and velocity of the migration process. The effect of secondary flows has also been investigated, mainly by considering the migration of a sphere immersed in the pressure-driven channel flow of a viscoelastic fluid (Li et al., 2015; Villone et al., 2013). According to these studies, the secondary flow drastically changes the migration dynamics by affecting velocity, trajectory and equilibrium position of the particles.

In the previous chapter, a combination of particle image velocimetry (PIV) and particle tracking velocimetry (PTV) was used to investigate the different behaviours of solid particles stirred in Newtonian and viscoelastic ambient fluids. The solid phase consisted of monodisperse PMMA particles with a diameter of 1.5 mm, while the mixing system was an unbaffled cylindrical vessel stirred by a dual-blade paddle impeller. It was found that in a viscoelastic fluid the particles tended to accumulate at the centre of the vortices created by the impeller. The speed of this process was found to be related to the viscoelasticity of the flow; in particular, the dimensionless time scale of the migration process (equal to the time scale of the process multiplied by the impeller rotational speed) decreased exponentially with the Weissenberg number (equal to the relaxation time of the ambient fluid multiplied by the impeller rotational speed). Although those results constituted the first report on the viscoelasticity-induced particle migration in complex three-dimensional flows in stirred vessels, they only presented a qualitative relation be-

tween the migration speed and the viscoelasticity of the flow. The difficulty in obtaining accurate values for the migration time was the limiting factor for any quantitative analysis. This difficulty arose because the initial dispersion process of the particles in the ambient fluid overlapped with the beginning of the particle migration process.

In this chapter, we report on experiments that overcome this limitation and allow estimating the particle migration time accurately. Additionally, an heuristic argument similar to that of D'Avino and Maffettone (2015) is introduced to derive, via scaling, a novel expression for the particle migration velocity in stirred vessels. To verify the applicability of this expression, two sets of planar PIV measurements were employed to reconstruct the three-dimensional flow field created in an unbaffled cylindrical vessel by the rotation of a Rushton turbine, in both Newtonian and viscoelastic fluids. The Rushton turbine was chosen as a midpoint between the simple flows usually encountered in the literature for viscoelasticity-induced particle migration and the complex flow fields generated in industrial mixers. In particular, this turbine generates a well-characterized, three-dimensional flow field that can be easily studied in terms of its main directions of strain. To isolate the effect of normal stresses from other non-Newtonian properties (i.e. shear-thinning), the study is limited to viscoelastic fluids with constant viscosity (Boger fluids). The conditions of the migration tests were chosen to minimize the effect of both gravity and inertial forces on the particle dynamics.

The characteristic time of particle migration predicted by the scaling equation was compared with the experimental data obtained in a wide range of fluid elasticity, impeller diameter and impeller speed. The experimental particle migration velocity was accurately measured via particle tracking (PT) experiments that allowed the estimation of the degree of dispersion of the solid phase and its change in time.

4.2 Materials and methods

4.2.1 Experimental setup

The experiments were conducted in a flat-bottomed cylindrical vessel with a diameter $T = 50$ mm. The fluid was stirred with two different standard Rushton turbines with a diameter D of 17 and 35 mm. The impeller clearance from the bottom and the liquid height were 25 and 50 mm, respectively. To minimize the optical distortion arising from the curvature of the tank, we enclosed the vessel in a square trough filled with glycerol. The vessel, the trough and the 17 mm impeller were made of transparent acrylic material to maximize the volume of fluid accessible for measurements, while the 35 mm impeller was made of stainless steel. The solid phase consisted of acrylic spherical particles (density of 1.2 g cm^{-3}) with a diameter d_p of 500 μm coated in Rhodamine B (Cospheric). The difference between the refractive index of pure glycerol (1.475) and the acrylic (1.495)

was small enough to discount the effect of the light refraction on the images. Both the PIV and PT experiments were conducted using the same optical setup consisting of a continuous diode laser, a mirror and a high-speed camera. The light was generated using a Laserglow5 continuous laser (532 nm, 3000 mW) equipped with a spherical and a cylindrical lens mounted in series to create a 1 mm laser sheet. A Phantom high-speed camera was equipped with a 105 mm Nikon lens resulting in a spatial resolution of 50 $\mu m/px$. Finally, an orange filter was connected to the camera lens to eliminate any reflections of the laser light.

4.2.2 Rheology

Three ambient fluids were used. A Newtonian reference fluid (*GW*), made of a mixture of 96% glycerol and 4% water, and two dilute polymer solutions with nearly constant viscosity (Boger fluids). The polymer solutions were obtained by dissolving 100 ppm of polyacrylamide, PAA, ($M_w = 5 - 6 \times 10^6$ g/mol) in a mixture of glycerol, water and zinc chloride. Compositions and properties of the ambient fluids are reported in Table 4.1, while details about the preparation procedure can be found in chapter 3.

Table 4.1: Composition and physical properties of the ambient fluids measured at 23°C.

Acronym	Glycerol [wt%]	$ZnCl_2$ [wt%]	H_2O [wt%]	ρ $[kg/m^3]$	η_0 $[Pa \cdot s]$	η_p $[Pa \cdot s]$	λ $[ms]$
GW	96	-	4	1236	0.51	-	-
GW_{100}	98	-	2	1237	0.58	0.017	21
RI_{100}	16	45	39	1640	0.75	0.010	3.5

In Table 4.1, η_p and η_0 are the polymer contribution to the viscosity and the total viscosity of the mixture, while λ denotes the fluid relaxation time (see Chapter 2). To characterize the viscoelastic behaviour of the polymer solutions, two tests were conducted: small-amplitude oscillatory shear (SAOS) and steady-state simple shear tests. Both were conducted on an Anton Paar MCR302 rotational rheometer at a temperature ranging from 0 to 70°C for the shear tests and from 10 to 50°C for the SAOS tests. The larger temperature range required for the simple shear tests is motivated by the very small values of normal forces exhibited by the dilute polymer suspensions in the range of shear rate normally accessible by the rheometer (0.01–100 s^{-1}). All the data obtained at different temperatures were shifted to the reference temperature of 23°C through the method of reduced variables whose detail can be found in section 2.2.1. This technique enabled the extension of the interval of shear rates or angular frequencies accessible for the measurements. The rheometer was equipped with a 50 mm cone and plate (CP) for the steady-state simple shear tests and a 50 mm parallel plate (PP) measuring system for the SAOS tests.

The PP system allowed the use of the thermal expansion compensation function of the instrument, which automatically adjusts the gap between the plates when the temperature is changed. This function allowed conducting the sequence of shear tests at different temperature on a single fluid sample. The non-uniformity of the shear-rate profile inside the gap of the PP system required the use of the Rabinowitsch-Mooney correction, which was automatically performed by the software of the rheometer.

Polymer solutions are susceptible to mechanical degradation when subject to intense shear for a prolonged time. The degradation is caused by the breaking of the long molecular chains of the suspended polymer and results in a drastic change of the rheological properties of the fluid (Mackenzie and Jemmett, 1971). To estimate the magnitude of this degradation, each fluid was subjected to intense stirring at 1500 rpm for 1.5 hours into our mixing system, while the rheological properties were measured at regular intervals of 30 min. To estimate the relaxation times, the experimental data were fitted with the multimode Giesekus constitutive equation, with a number of modes n between 1 and 3. In particular, the stress of the fluid, $\boldsymbol{\tau}$, is defined as:

$$\boldsymbol{\tau} = \boldsymbol{\tau}_s + \sum_{k=1}^{n} \boldsymbol{\tau}_{p,k} \tag{4.1}$$

$$\boldsymbol{\tau}_{p,k} + \lambda_k \overset{\triangledown}{\boldsymbol{\tau}}_{p,k} + \alpha_k \frac{\lambda_k}{\eta_{p,k}} (\boldsymbol{\tau}_{p,k} \cdot \boldsymbol{\tau}_{p,k}) = \eta_{p,k} \dot{\boldsymbol{\gamma}} \tag{4.2}$$

where the subscript k indicates the parameters of the $k-th$ mode of the constitutive equation. For brevity, the exact expressions of the material functions $G'(\omega)$, $G''(\omega)$ and $\Psi_1(\dot{\gamma})$ for the Giesekus model are not reported here but can be found in Bird et al. (1987a, ch. 7, p. 368). The multimode Giesekus model was preferred to the more common multimode Maxwell model because it was able to successfully predict both the linear viscoelastic properties obtained by the SAOS tests and the non-linear shear-thinning of the first normal stress coefficient obtained in the steady-state simple shear tests.

The results of both the SAOS and the simple shear experiments for the two viscoelastic fluids are reported in Fig. 4.1. A high degree of polymer degradation can be detected after 30 min of stirring. This is clearly shown by the sizable reduction in storage modulus for both GW_{100} (Fig.4.1a) and RI_{100} (Fig.4.1b). The overlapping between the curves obtained after 30 min and 1.5 hours indicates that most of the mechanical breaking of the polymer chains happens in the first half hour of stirring. After this time, no further degradation is evident. It is interesting to notice that the value of the loss modulus does not change considerably due to the polymer degradation; this is because the impact of the polymer degradation on the value of the total viscosity of the solution is relatively small. A corresponding reduction of the first normal stress coefficient can also be observed for both fluids (Fig.4.1c) and 4.1d). In a similar way, it appears that most of the reduction of the normal force is observed after 30 min of stirring although some degradation is still

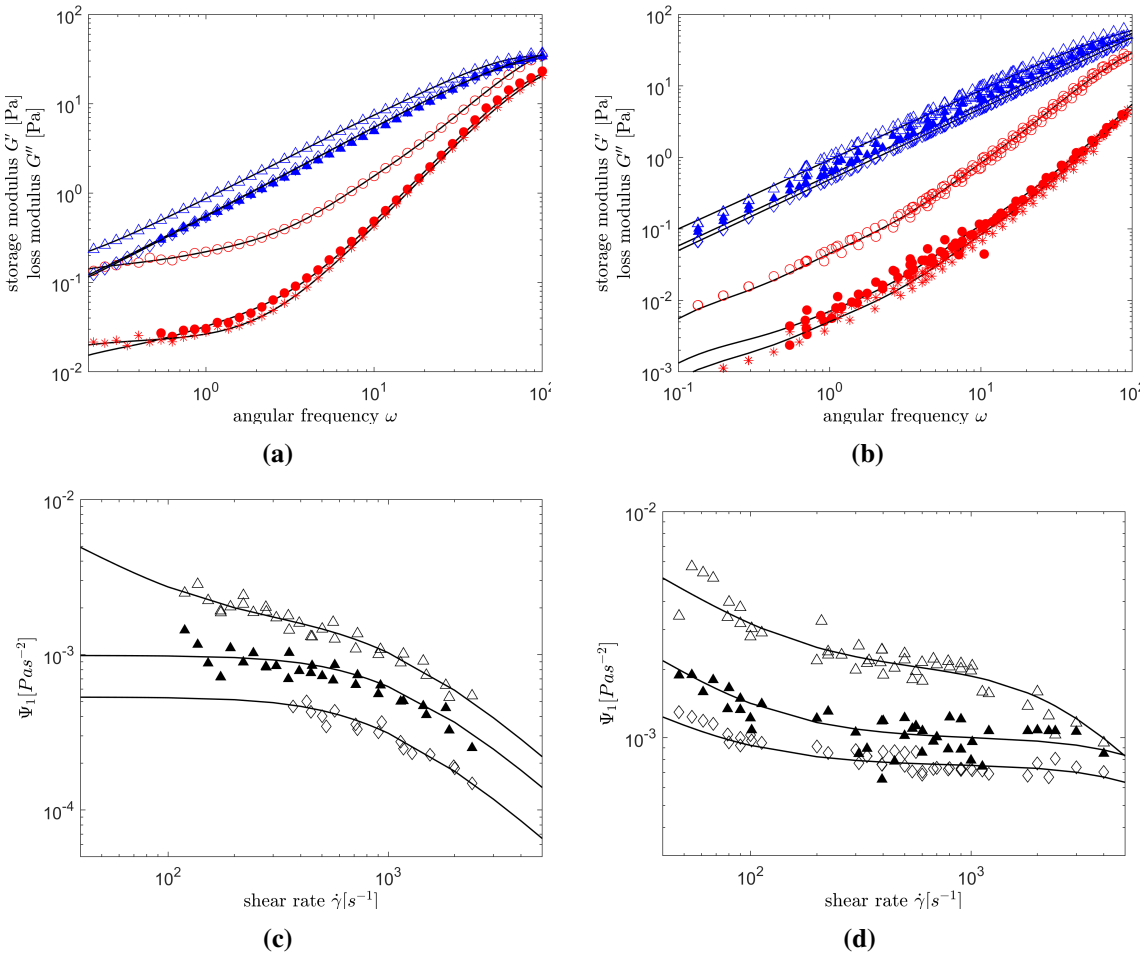

Figure 4.1: SAOS experimental data and model fitting at three different stirring times for (a) GW_{100} and (b) RI_{100}: (△) G'' at 0 min; (▲) G'' at 30 min; (◇) G'' at 90 min; (○) G' at 0 min; (●) G' at 30 min; (✳) G' at 90 min. Simple shear experimental data and model fitting at three different stirring times for (c) GW_{100} and (d) RI_{100}: (△) Ψ_1 at 0 min; (▲) Ψ_1 at 30 min; (◇) Ψ_1 at 90 min.

observed after 90 min. Finally, the close fit between the data predicted by the model and the experimental results proves that the polymer solution can be successfully modelled with the Giesekus constitutive equation.

As we will show in section 4.3.2, the migration of the solid phase can last up to 40 minutes. Considering the previous results, we conclude that the polymer degradation and the relative change of the fluid relaxation time would seriously hinder the estimation of the Weissenberg number (Wi) of the flow. To account for this phenomenon, prior to any migration test, the polymer solution was loaded in the mixing system and stirred for 90 min at 1500 rpm. At the end of this phase, the breaking of the polymer chains was assumed to be complete. Finally, all the rheological properties considered depend strongly on the fluid temperature. To assess the extent of the temperature change induced by the mechanical stirring, the temperature of the fluid was measured at the beginning and at the end of each test. For all the conditions considered, the temperature difference was found to be below 2 °C. The final values of the viscosity and relaxation time were then

considered constant throughout the experiments.

4.2.3 Particle image velocimetry

The reconstruction of the 3D velocity field was carried out for the Newtonian reference fluid and the GW_{100} viscoelastic fluid. It was assumed that the effect of the fluid viscoelasticity on the fluid dynamics inside the tank only depends on the polymer concentration via the value of Wi and is not affected by the composition of the Newtonian solvent in which the polymer is dissolved. In other words, when stirring either GW_{100} or RI_{100} at a specific value of Wi, the resulting flow fields are considered hydrodynamically equivalent. However, it should be noted that these two fluids have different densities and relaxation times, so equivalent Wi values do not necessarily imply equivalent Re. In the context of this section, the equivalence of the two systems refers to the fact that the influence of viscoelasticity on the flow field, such as changes in vortex shape/intensity or shifts in local extrema of velocity, is solely dependent on Wi.For this reason, the fluid RI_{100} was not subjected to the PIV tests.

The two mixtures were stirred with the 35 mm Rushton turbine at two impeller speeds, $N = 333$ and 666 rpm; this corresponds to $Wi = 1.15$ and 2.3 for the fluid GW_{100} at 333 and 666 rpm, respectively. 20 µm fluorescent polymeric particles were employed as tracers for the PIV measurements. The tracer particles were made of melamine resin and coated with Rhodamine B, which at room temperature has a high fluorescent intensity. For the experimental conditions investigated, the tracer relaxation time was negligible compared to the convection time ($St \equiv \frac{\rho_t d_t^2 N}{18\eta_0} << 1$, where ρ_t and d_t are the tracer density and diameter, respectively). Concurrently, the terminal velocity and the slip velocity resulting from inertial effects are several orders of magnitude smaller that the fluid velocity, guaranteeing that the tracer rapidly relaxes to the local value of the fluid velocity.

Schematic diagrams of the PIV setups for the horizontal and vertical plane measurements are provided in Fig. 4.2a and 4.2b, respectively. In the remainder of the paper, a cylindrical coordinate system (r, θ, and z) with origin in the center of the base of the vessel will be used. To reconstruct the velocity field, two sets of 2D PIV tests were conducted in the horizontal and vertical directions. Several works in the literature report on the flow field produced by a Rushton turbine in conditions similar to those investigated in this work (Mavros et al., 1998; Liné et al., 2013; Rice et al., 2006; Yoon et al., 2005; Hill et al., 2000). Some of these works use stereo-PIV to measure the entire 3D velocity field in the vessel. Although this technique has been extensively validated, in the present work it was found that the use of 2D PIV measurements ensured a higher spatial resolution for the measured vector field.

The horizontal PIV measurements were carried out at intervals of $\Delta z/T = 0.02$ in the height interval $z/T = 0 - 0.48$ (see Fig. 4.3a). At the beginning of each test, the

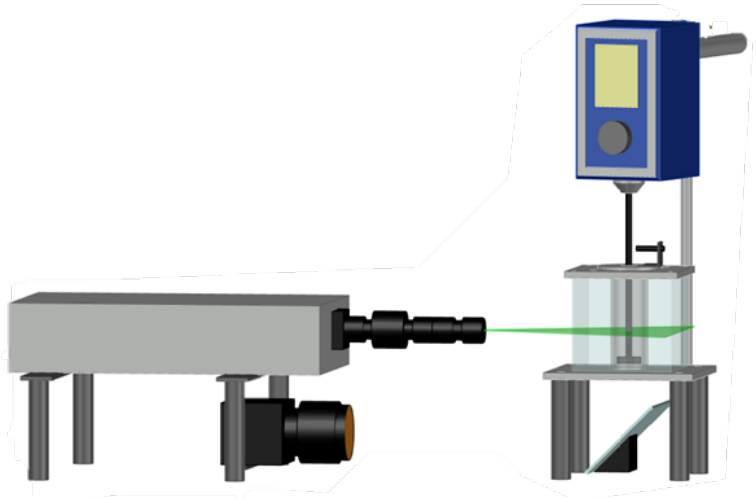

(a)

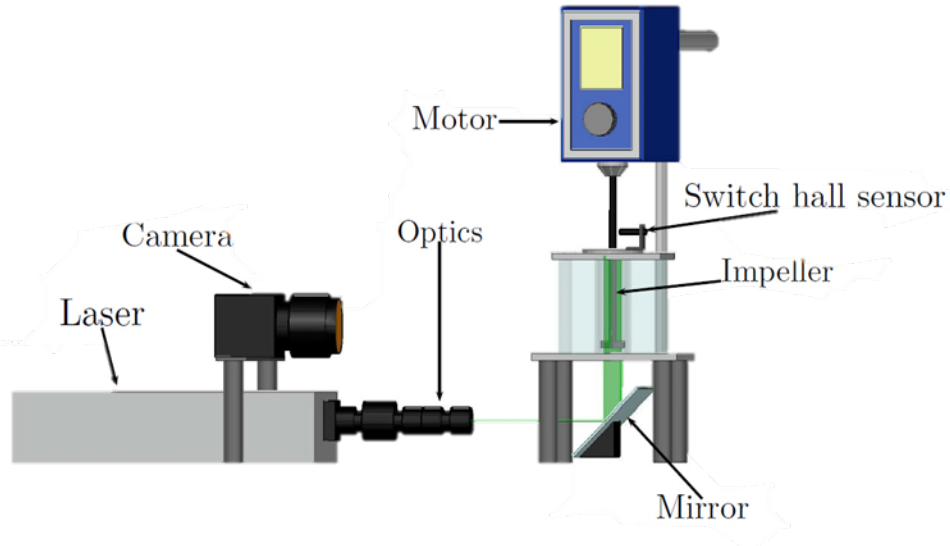

(b)

Figure 4.2: PIV setups for the horizontal measurements (a) and vertical measurements (b).

position of the laser plane was adjusted at the desired z level. The image capture was then synchronized with the impeller position using a hall switch sensor. This allowed capturing images at a fixed impeller phase angle θ (i.e. the azimuthal angle or rotation of the impeller around the vertical axis z) equal to 0°. A total of 100 images pairs (corresponding to 100 impeller rotations) were captured for each horizontal plane; on each plane, the velocity field was then obtained by averaging the 100 instantaneous vector fields. The vertical velocity field was obtained through time-resolved measurements. In this case, the laser plane was kept in the same vertical position throughout the tests (see Fig. 4.3b) and the image acquisition was not synchronized with the impeller phase angle. Starting from an angle $\theta = 0$, a total of 3000 images were captured with an acquisition rate f of 1000 Hz and 2000 Hz for $N = 333$ rpm and 666 rpm, respectively. This allowed obtaining images with a resolution $\Delta\theta = \frac{N}{60}\frac{360}{f} = 2^\circ$. The displacement of the tracer between the images

at θ_i and θ_{i+1}, with $i = 1,\ldots,90$ was used to calculate the velocity field at the angle $\frac{\theta_i+\theta_{i+1}}{2}$. For each phase angle, a total of 33 velocity fields were obtained and subsequently averaged. The independence of the PIV results from the sample size is shown in Fig. A.1 in Appendix B.

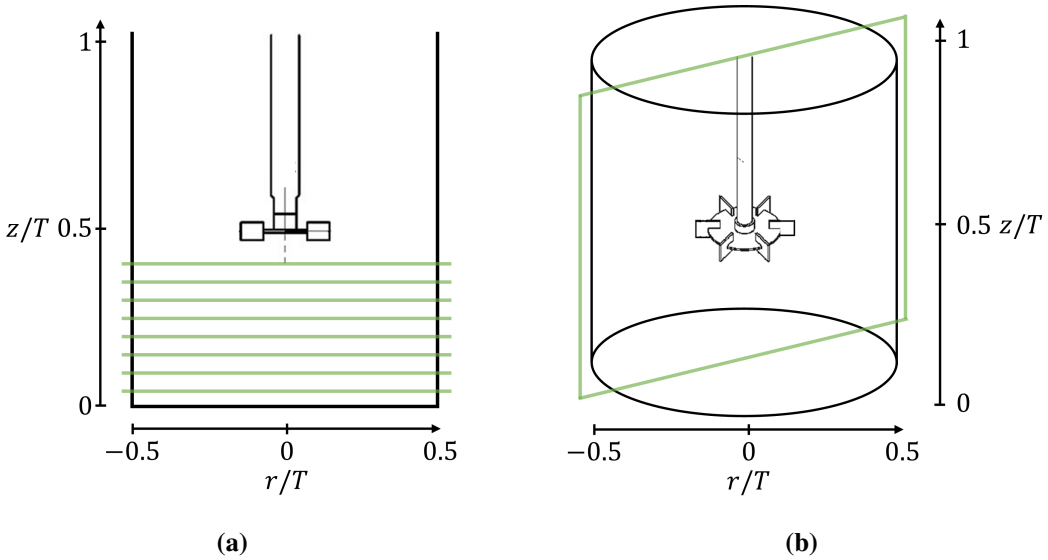

Figure 4.3: Schematic representation of the locations of horizontal measurements (a) and vertical measurements (b).

Each velocity field was calculated from the tracer displacements between two consecutive images with the freeware package JPIV, using a 50% window overlap for a final interrogation window with resolution of 16×16 pixels. An amplitude filter was applied to each cross-correlation box to eliminate the vectors that substantially deviated from the median value. Note that both the u_r and u_z components of the fluid velocity along the θ direction were directly available from the vertical measures, while the horizontal tests provided u_r and u_θ along the z direction. In order to obtain the full 3D velocity field in the stirred tank, we first azimuthally stacked the vertical measurements. Subsequently, the horizontal measurements were stacked along the z direction. The exact placement of the horizontal velocity vectors was decided by comparing the values of the u_r components obtained from both the horizontal and the vertical measurements.

4.2.4 Particle tracking

The particle tracking experiments were performed with the optical system in the configuration shown in Fig. 4.2b. The objective of these tests was to determine the particle migration time as a function of the Weissenberg number defined as the product of the fluid relaxation time and the characteristic scale value of the shear rate ($Wi \equiv \lambda\dot{\gamma}_c$). The scale value of the shear rate was chosen as the average shear rate in the fluid surrounding

the impeller. This value was calculated according to Metzner and Otto (1957) as follows:

$$\dot{\gamma}_c = k_s N \tag{4.3}$$

where k_s is the Metzner and Otto constant that mainly depends on the shape of the impeller. Although Eq. 4.3 was originally derived for inelastic shear-thinning fluids, Seyssiecq et al. (2003) derived the values of k_s for a Rushton turbine for a wide array of viscoelastic fluids. Their work reports a value of k_s ranging from 9 to 12. In this work the intention is to capture the order of magnitude of the migration velocity, hence it was assumed a value of $k_s = 10$. Finally, the migration time is defined as the time at which no significant change in the distribution of the particles can be detected. Experiments were conducted with both the 17 mm and the 35 mm turbines at a rotation speed N ranging from 200 to 1200 rpm for both the Newtonian and the two viscoelastic fluids. This resulted in Wi values between 0.05 and 2 and $Re \equiv \frac{\rho N D^2}{\eta_0}$ values between 5 and 15. At the beginning of each test, 1.5 g of acrylic spheres (equivalent to a volume fraction of 1%) were placed on the liquid surface. The system was then stirred at 2000 rpm for 5 min until a homogeneous particle distribution was achieved. At this point, the impeller speed was adjusted to the desired value and the recording was started.

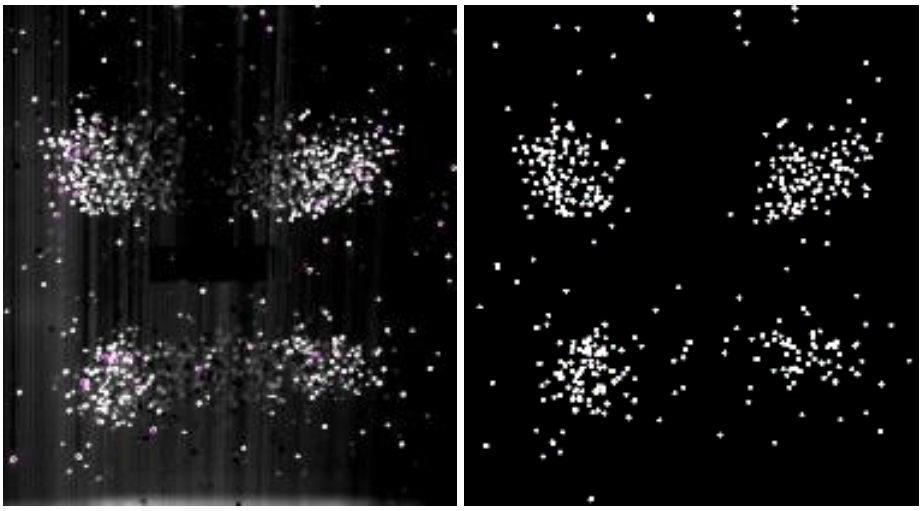

(a) **(b)**

Figure 4.4: (a) raw PT image; (b) image with the detected solids for RI_{100} at $Wi = 1.33$.

The PT tests were performed with the impeller phase angle locked at 0°. The images were acquired with a frequency of 0.6 Hz for a time ranging from 15 min to 2 hours depending on the impeller velocity and the migration speed. Fig. 4.4a shows a typical raw image obtained from a PT experiment for the fluid RI_{100} at $Wi = 1.33$. The bright circles correspond to the suspended solid particles. Based on the intensity histogram of the raw image, we used a threshold value to binarise the images and isolate the solid spheres. To detect the edges of the solid particles, a circular Hough transform algorithm

(CHT) was employed. The CTH algorithm provided the position and the diameter of all the solid particles crossing the 1 mm laser plane. In order to account only for the particles that fully cross the laser plane, all the spheres with a diameter lower that 0.5 mm were discarded. The image shown in Fig. 4.4b, clearly displaying the position of the particles, was then used for the analysis of the migration phenomenon. The degree of dispersion of the solid phase was estimated through the use of the Shannon entropy function (S):

$$S = \sum_{i=1}^{M} \sum_{j=1}^{2} p_j(i) \ln p_j(i) \tag{4.4}$$

where M is the number of sub-regions in which the image is divided, and $p_j(i)$ is the ratio between the number of pixels occupied by the $j-th$ phase and the total number of pixels in the $i-th$ sub-region. A more detailed description of this function and its calculation are reported in Chapter 3.

4.2.5 Strain rate tensor

The scaling law that we will propose in Section 4.3.3 is derived for a spherical particle immersed in a bi-dimensional, rotating shear flow. However, usually the flow field created by a rotating turbine is complex and three-dimensional. In order to assess the extent to which the flow field created by a Rushton turbine can be conceptually reduced to a bidimensional rotating shear flow on the $r-\theta$ plane, the rate of strain (or deformation) tensor field was analysed. The velocity gradient ($\nabla \mathbf{u}$) can be decomposed into a symmetric part $\dot{\boldsymbol{\gamma}}$, called strain rate tensor, and an antisymmetric part $\boldsymbol{\Omega}$, referred to as rotation rate tensor. The physical components of the strain and rotation rate tensors with respect to a cylindrical coordinate system are reported in the following equations:

$$\dot{\boldsymbol{\gamma}} = \begin{bmatrix} \frac{\partial u_r}{\partial r} & \frac{1}{2}\left[r\frac{\partial}{\partial r}\left(\frac{u_\theta}{r}\right) + \frac{1}{r}\frac{\partial u_r}{\partial \theta}\right] & \frac{1}{2}\left[\frac{\partial u_r}{\partial z} + \frac{\partial u_z}{\partial r}\right] \\ \frac{1}{2}\left[r\frac{\partial}{\partial r}\left(\frac{u_\theta}{r}\right) + \frac{1}{r}\frac{\partial u_r}{\partial \theta}\right] & \frac{1}{r}\frac{\partial u_\theta}{\partial \theta} + \frac{u_r}{r} & \frac{1}{2}\left[\frac{1}{r}\frac{\partial u_z}{\partial \theta} + \frac{\partial u_\theta}{\partial z}\right] \\ \frac{1}{2}\left[\frac{\partial u_r}{\partial z} + \frac{\partial u_z}{\partial r}\right] & \frac{1}{2}\left[\frac{1}{r}\frac{\partial u_z}{\partial \theta} + \frac{\partial u_\theta}{\partial z}\right] & \frac{\partial u_z}{\partial z} \end{bmatrix} \tag{4.5}$$

$$\boldsymbol{\Omega} = \frac{1}{2}\begin{bmatrix} 0 & \omega_z & -\omega_\theta \\ -\omega_z & 0 & \omega_r \\ \omega_\theta & -\omega_r & 0 \end{bmatrix} \tag{4.6}$$

where the vorticity ω is defined as:

$$\omega = \left(\frac{1}{r}\frac{\partial u_z}{\partial \theta} - \frac{\partial u_\theta}{\partial z}\right) e_r + \left(\frac{\partial u_r}{\partial z} - \frac{\partial u_z}{\partial r}\right) e_\theta + \left(\frac{1}{r}\frac{\partial}{\partial r}(r u_\theta) - \frac{1}{r}\frac{\partial u_r}{\partial \theta}\right) e_z \tag{4.7}$$

where e_r, e_θ and e_z are (mutually normal) unit vectors in the r, θ and z directions, respectively. Following the approach proposed by Bouremel et al. (2009), the principal

components of the strain rate tensor (Eq. 4.8) were calculate in order to analyse the strain dynamics in different regions of the vessel.

$$\nabla \boldsymbol{u} = \begin{bmatrix} S_{11}^* & 0 & 0 \\ 0 & S_{22}^* & 0 \\ 0 & 0 & S_{33}^* \end{bmatrix} + \frac{1}{2} \begin{bmatrix} 0 & \omega_3^* & -\omega_2^* \\ -\omega_3^* & 0 & \omega_1^* \\ \omega_2^* & -\omega_1^* & 0 \end{bmatrix} \tag{4.8}$$

with S_{11}^*, S_{22}^* and S_{33}^* the eigenvalues of $\dot{\boldsymbol{\gamma}}$ and ω_1^*, ω_2^* and ω_3^* the components of the vorticity vector along the local principal axes of the strain rate tensor. The local principal axes are defined by the eigenvectors associated with the eigenvalues S_{11}^*, S_{22}^* and S_{33}^*. The change of vector basis allows identifying the local velocity of deformation in the directions of the principal axes (i.e. velocities of stretching or compression). In particular, if $S_{ii}^* > 0$ (no summation over the index i is implied) the fluid element is stretched in the i direction, whereas if $S_{ii}^* < 0$, it is compressed. The values of the three components of the strain rate tensor can also be used to assess the intensity of the deformation in the three principal directions relative to each other. In particular, if one of the three components is small compared to the other two, the deformation field can be essentially regarded as bi-dimensional.

4.3 Results

4.3.1 Velocity field and flow structure

An overview of the three components of the velocity field for the fluid GW_{100} at $Re = 4.3$ and $Wi = 0.44$ is reported in Fig. 4.5. All the velocities are normalised with the impeller tip speed πDN. The fluid is stirred with the 37 mm Rushton turbine. The 37 mm impeller was made of stainless steel; therefore, only the lower part of the tank was accessible to measurements. To provide sufficient information about the flow field, we divided both plots in six sectors, each reporting the component of the velocity over an angle of 60° for six axial positions z/T (i.e. 0.39, 0.41, 0.43, 0.44, 0.46 and 0.48) with the axial coordinate decreasing counter-clockwise and impeller rotating in the clockwise direction. The overall flow can be described as the superposition of a rotational flow around the z axis and of a rotational flow in the $r-z$ plane. In this plane, the fluid moves in the positive r direction with the maximum radial velocity in correspondence of the edge of the palettes of the impeller. The fluid then slows down as it approaches the walls of the vessel. On reaching the wall, the radial component of the fluid velocity rapidly reduces to zero, while the axial component increases. The stream then divides into two equal parts directed above and below the axial position of the impeller and circulates back returning to the impeller region. Unsurprisingly, the value of the angular component of the velocity is an order of magnitude larger than the other two; hence, the dominating motion is represented

by the rotation around the z axis. It is known that unbaffled stirred tanks usually present a central vortex at the liquid-air interface. Given the small value of the Reynolds number, at all the conditions examined the central vortex remains small and confined to a small area around the shaft of the stirrer.

As it will be shown in Section 4.3.2, the migration of the particles is caused by the presence of an elastic force acting in the radial direction. The intensity of this force is not uniform along the z axis and it reaches its maximum value in the vicinity of the impeller. This means that the secondary flow described above contributes to the dynamics of the migration insofar as it continuously circulates the solids in the $r-z$ plane and leads the particles to move on helicoidal pathlines around the z axis.

Fig. 4.6a and 4.6b show the contour plot of the normalised angular component of the vorticity for both the Newtonian fluid and the viscoelastic fluid GW_{100} at $Re = 4.3$ and $Wi = 0$ and 0.44, respectively. From Fig. 4.6a it can be seen that in the Newtonian case the rotation of the turbine creates the characteristic toroidal vortex flow-structure, with the maximum value of the angular vorticity located at the tip of the impeller and at $z/T = 0.48$ and $r/T = 0.35$. The vorticity then decreases when moving further away from the impeller both in the radial and in the axial directions. Note that the vortex created by the turbine affects the volume of fluid from $r/T = 0.2$ to $r/T = 0.40$ and only gradually decreases in intensity when moving further away along the z direction. As Fig. 4.6b shows, the viscoelasticity of the fluid substantially changes the shape of the vortical structures. In particular, the toroidal vortex present in the Newtonian case loses its continuity and breaks into smaller trailing vortices that depart from the tip of the turbine. The intensity of the vorticity is also reduced, the maximum value of the normalized angular component reducing from 2.2 for the Newtonian case to 1.6 for the viscoelastic case. It can also be observed that the centre of the vortex shifts in both the radial and axial directions and is now located at $z/T = 0.44$ and $r/T = 0.3$. The difference between the two flow fields can be clearly observed in Fig. 4.6c and 4.6d, where the three-dimensional structure of the vortex is shown by plotting iso-vorticity surfaces at $\omega_\theta/\pi N = 1.5$.

The contour plots of the principal components of the strain rate tensor S^*_{11}, S^*_{22} and S^*_{33}, for the fluid GW_{100} at $Wi = 0.44$ are shown in Fig. 4.7a - 4.7c for six values of z/T. The strain rate S^*_{11} is positive over the entire plane of measure, while S^*_{22} is everywhere negative. This indicates that the fluid is always stretched along the principal direction associated with S^*_{11} and compressed along the direction associated with S^*_{22}. On the other hand, S^*_{33} changes sign from positive to negative, indicating the presence of both areas of stretching and compression. The strain rates S^*_{11} and S^*_{22} are always dominant, as their dimensionless absolute values reach a peak of 1.5, while for S^*_{33} it is $-0.4 < S^*_{33}/\pi N < 0.4$. All three strain rates assume local absolute maxima close to the impeller blades for every z/T considered. Although not reported in Fig. 4.7, it is important to notice that the eigenvectors associated to S^*_{11} and S^*_{22} are everywhere parallel to the $r-\theta$ plane and

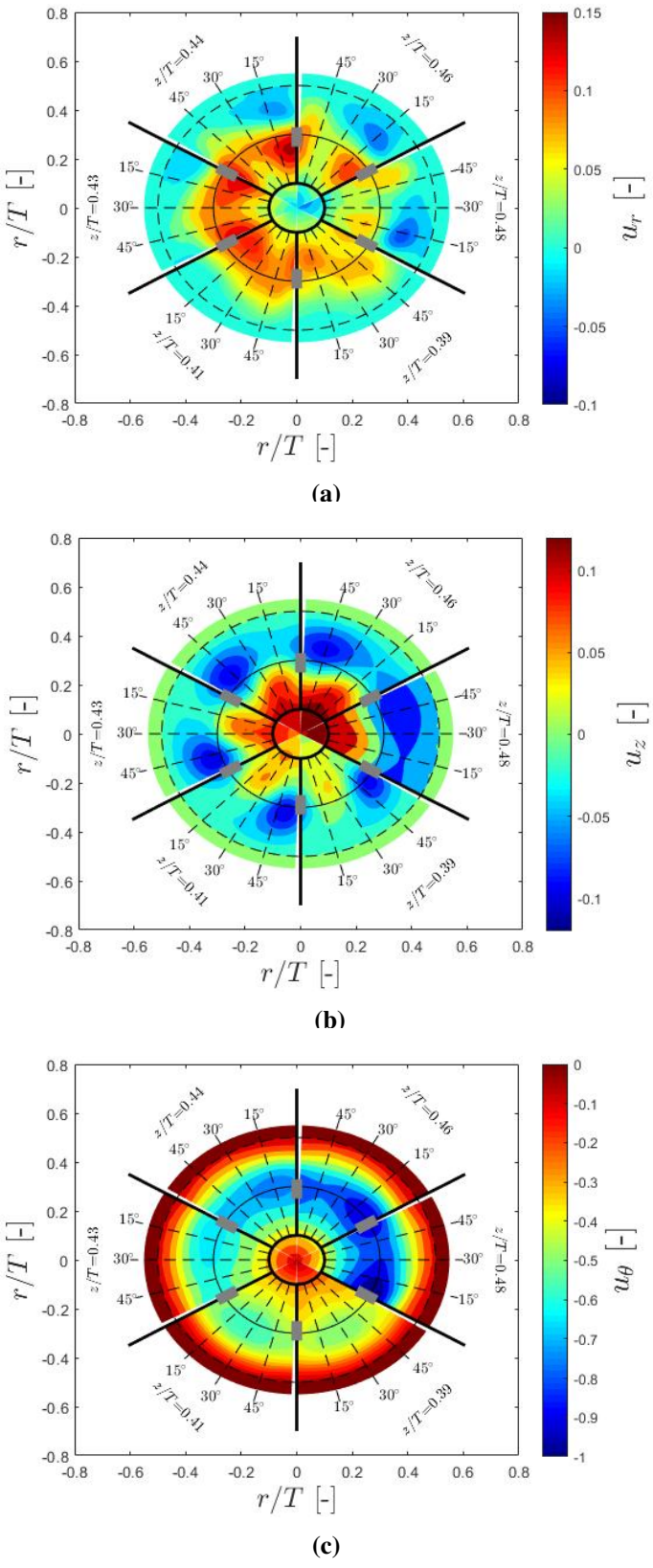

Figure 4.5: Dimensionless radial (a), axial (b) and angular (c) components of the velocity field for the fluid GW_{100} at $Re = 4.3$ and $Wi = 0.44$.

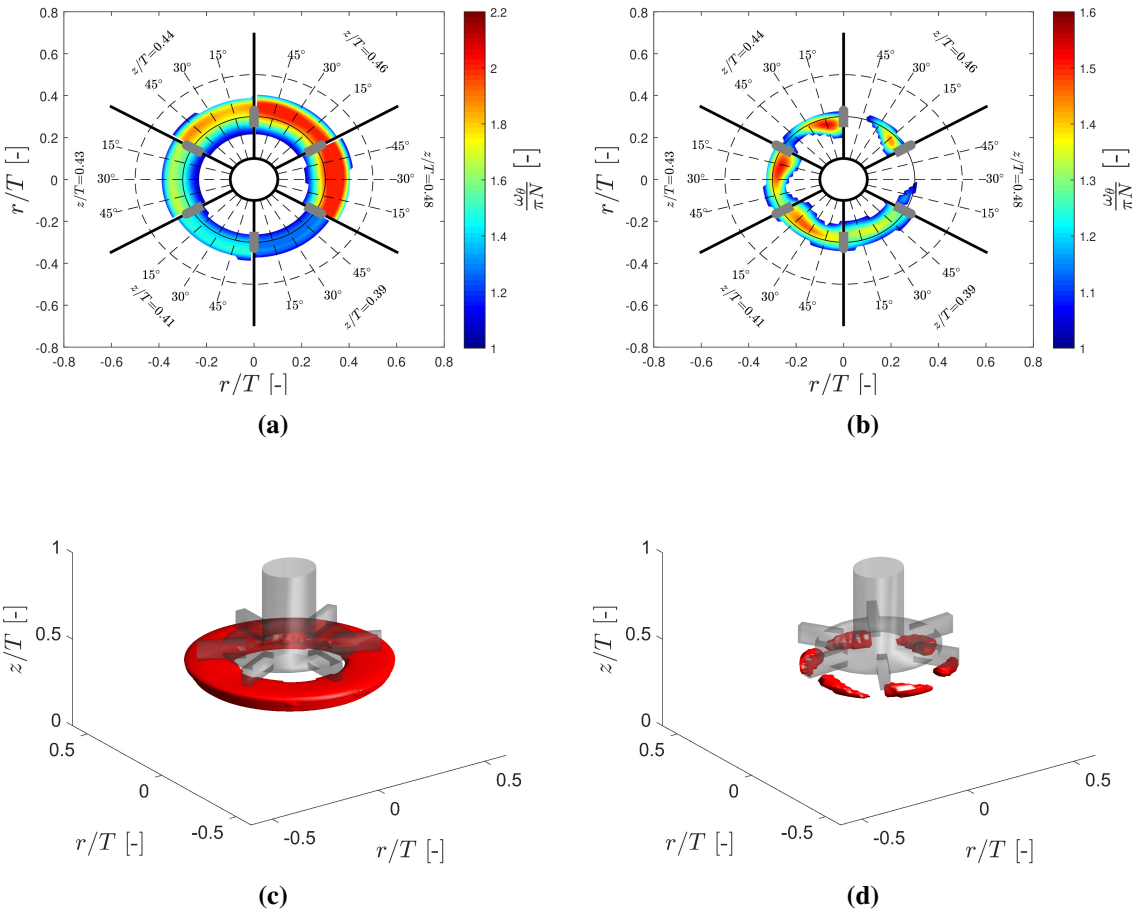

Figure 4.6: Vorticity plot and vortex structure for *GW* (a) and (c) and GW_{100} (b) and (d) at $Re = 4.3$ and $Wi = 0.44$. In both cases, the impeller rotates in the clockwise direction.

orthogonal to each other, while the one associated with S^*_{33} is everywhere parallel to the z direction. Apart from a small area around the tip of the impeller blades, the strain rate S^*_{33} is everywhere close to zero. This indicates that the local deformation of the flow is essentially bi-dimensional and controlled by two strain rates of stretch and compression mutually orthogonal to each other and parallel to the $r-\theta$ plane.

As reported by D'Avino and Maffettone (2015), one of the necessary conditions for viscoelastic particle migration is the presence of shear rate gradients. In the nearly bi-dimensional rotating shear flow described so far, the only relevant component of the rate-of-strain tensor is that associated with the coordinates r and θ. Fig. 4.7d reports the normalised, absolute value of this component. It is possible to observe that for every value of z/T, the absolute value of $\dot{\gamma}_{r\theta}$ shows a non-monotonic behaviour when moving in the positive r direction, with the presence of two areas of maximum and minimum shear. For example, at $z/T = 0.48$, $\dot{\gamma}_{r\theta}$ initially decreases from the value of 1 at $r/T = 0$ to the value of 0 at $r/T = 0.3$, it then increases until reaching its maximum value of 1.5 at $r/T = 0.41$, and then sharply decreases until reaching a value of 0 next to the wall.

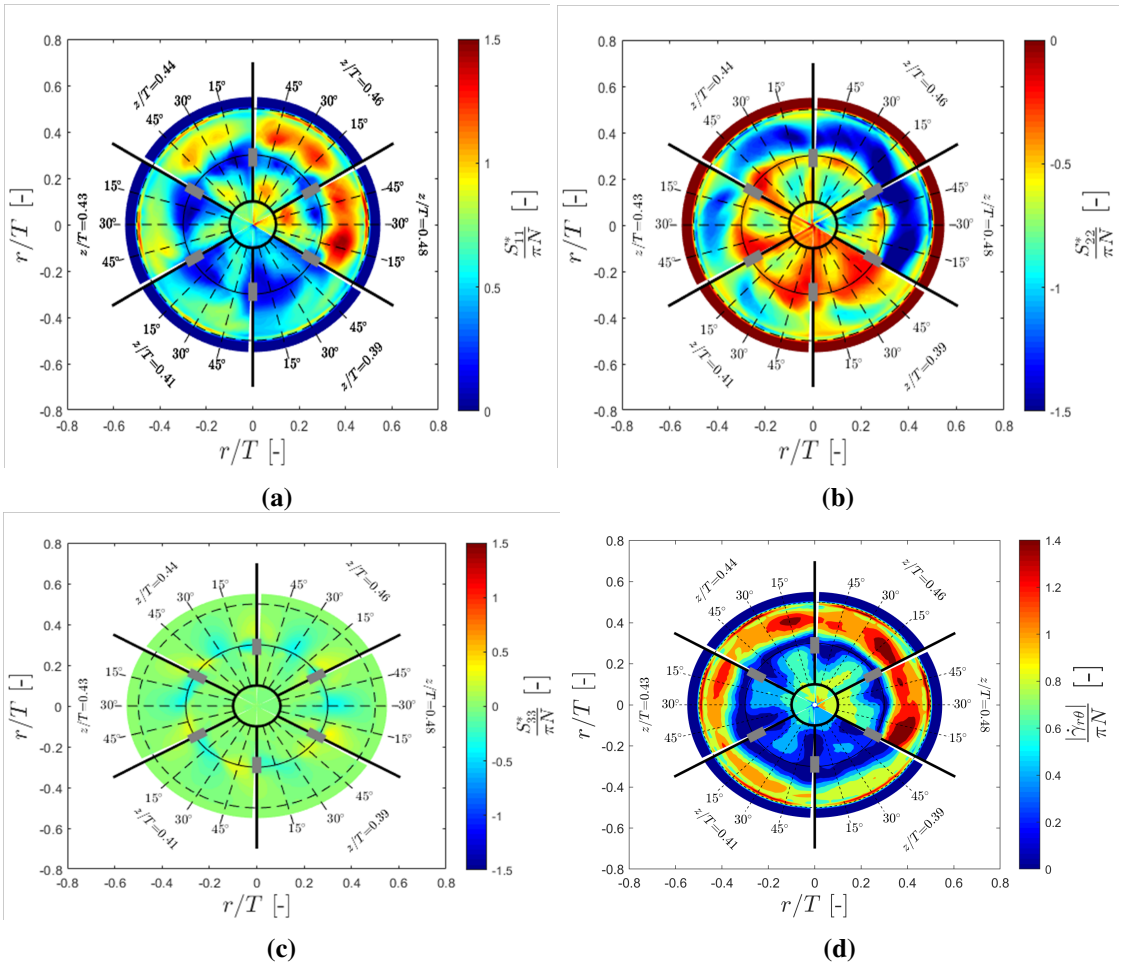

Figure 4.7: Normalised principal strains (a,b,c) and absolute value of the $r-\theta$ component of the strain rate tensor (d) for GW_{100} at $Re = 4.3$ and $Wi = 0.44$. The impeller rotates in the clockwise direction.

Moving along the axial direction, the maximum absolute value of $\dot{\gamma}_{r\theta}$ decreases from 1.5 at $z/T = 0.48$ to 1 at $z/T = 0.39$. In addition, the radial position of the maximum of $\dot{\gamma}_{r\theta}$ moves to increasing value of r/T while the size of the area of low shear rates widens. The variation of $\dot{\gamma}_{r\theta}$ is responsible for the migration of the particles in the $r-\theta$ plane toward lower absolute values of shear rates.

4.3.2 Migration experiments

A second set of experiments was carried out to track the distribution of the solid particles in the tank and its evolution in time. At the beginning of each test, the solid particles were placed on top of the liquid surface. The liquid was then stirred at an impeller speed of 2000 rpm for 5 min. After 3 min of stirring at 2000 rpm, the particles were uniformly dispersed throughout the flow. If stirring continues, the Newtonian and viscoelastic systems show two radically different behaviours.

Fig. 4.8a compares the average solid volume fraction ($\langle C \rangle$) and the normalised angu-

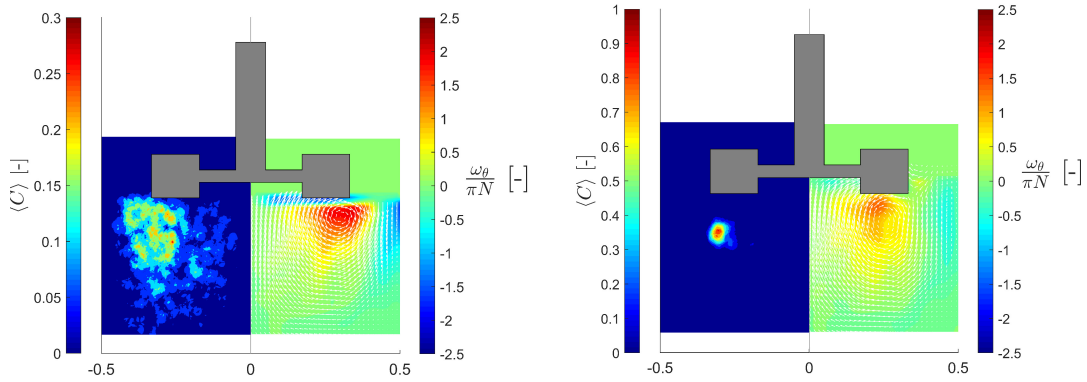

(a) **(b)**

Figure 4.8: Vorticity contour plot and particles concentration for *GW* (a) and RI_{100} (b) at $Re = 10$ and $Wi = 0$ and 0.35, respectively.

lar vorticity contour plots, after 90 min of stirring, for the fluids *GW* and RI_{100} at $Re = 10$ and $Wi = 0$ and 0.35, respectively. For the Newtonian case, no significant change in the particle distribution is observed. The solids remain uniformly distributed up to 90 min after the stirring is initiated. For the viscoelastic case, on the other hand, Fig. 4.8b shows an accumulation of the solid phase at the centre of the vortex created by the rotation of the impeller. The migration velocity was estimated by calculating the degree of disorder of the liquid-solid system represented by the Shannon entropy index (S^*). Fig. 4.9a and 4.9b show the evolution of the Shannon entropy with time for the Newtonian fluid, *GW*, and for the viscoelastic fluid, RI_{100}, at $Re = 10$ and $Wi = 0$ and 0.35, respectively. In these graphs, the time $t = 0$ corresponds to the moment at which the impeller rotational velocity is reduced from 2000 rpm to the desired final value. At the conditions of the experiments, the particles Stokes number $\left(St \equiv \frac{\rho_s d_p^2}{18\eta_0} N\right)$ was much less than unity; thus, the velocities of the particles relax rapidly to their dynamic equilibrium values. If the particles have the same density as the ambient fluid (which is the case for the fluids *GW* and GW_{100}), this equilibrium value is equal to the local velocity of the fluid. Although the density of the fluid RI_{100} is higher than the density of the solids, both the terminal velocity of the spheres $\left(v_t = \frac{g d_p(\rho_s - \rho_f)}{18\eta_0}\right)$ and the slip velocity induced by inertia are still negligible compared to the fluid velocity $\left(\frac{v_t}{\pi N} \approx 10^{-5}$ while $\frac{u_i}{\pi N} \approx 10^{-3}\right)$. We can then assume that in both fluids (*GW* and RI_{100}) the particles rapidly relax to the local equilibrium and that when this happens, the effect of gravity and inertia are negligible. At this stage, the particles are uniformly dispersed into the flow and no migration is evident. To facilitate the comparison, the value of S^* was normalised by dividing it by the maximum value reached during the mixing. In both cases, S^* assumes its maximum value at the beginning of the experiment. For the Newtonian case, there is no appreciable change of S^* throughout the duration of the test (that is, the particles are uniformly dispersed in the liquid and remain that way);

S^*/S_{max} remains almost constant at a value of 1 with fluctuation of $\pm$ 3%. Contrarily, the Shannon entropy for the viscoelastic fluid reduces sharply from the initial value of 1 at $t = 0$ to the value of 0.54 at $t = 30$ min. This decrease reflects the reduction of the region of the tank occupied by the particles and can be used to estimate the time required for the particle cross-streamline migration. In particular, the final migration time is taken to be the time at which the Shannon entropy reaches 99% of its final value.

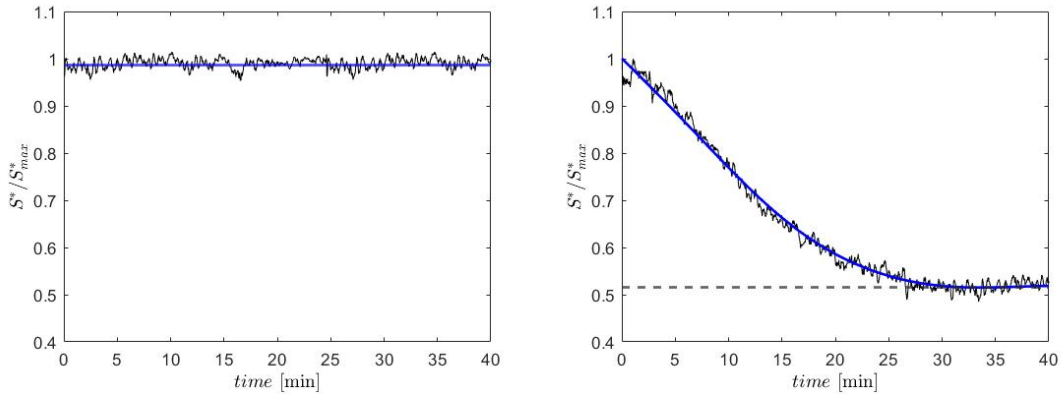

Figure 4.9: Normalised Shannon entropy for *GW* (a) and RI_{100} (b) at $Re = 10$ and $Wi = 0$ and 0.35, respectively.

4.3.3 Scaling law for viscoelasticity-induced particle migration

Here, we propose a simple heuristic argument to understand the nature of particle migration in stirred vessels and identify the parameters that influence this phenomenon. Consider a nonuniform two-dimensional shear flow, for example that created in the gap between two concentric cylinders (Taylor-Couette flow), where the inner cylinder rotates with an angular velocity Ω while the outer cylinder is stationary.

Consider a sphere of radius a and density ρ_s moving in the streamwise (θ) direction at the same velocity as the fluid (Fig. 4.10a). We can assume that the particle is neutrally buoyant, so that its density is the same as the fluid density (ρ_f). In the absence of forces acting on the sphere in the direction normal to the flow (r direction), the particle would simply move along with the fluid in a circular trajectory concentric with the two cylinders. Experimental evidence (Ho and Leal, 1976; Karnis and Mason, 1966; D'Avino et al., 2012) shows that if the suspending fluid is viscoelastic, the particle moves towards the decreasing shear rate direction, i.e. towards the outer cylinder. The migration is caused by an imbalance of the viscoelastic normal force acting across the particle. To derive an expression for the migration velocity v_m, we first write a balance of forces on the particle. Divide the sphere in half using an imaginary cutting plane normal to the velocity gradient direction. Each hemisphere is subject to a radial force arising from the fluid elasticity.

The magnitude of this force depends on the average shear rate acting on each hemisphere. For the first hemisphere:

$$F(r) \sim a^2 \tau_{rr}(r) \tag{4.9}$$

where τ_{rr} is the *rr*-component of stress tensor of the fluid. For the second hemisphere, we write:

$$F(r+a) \sim a^2 \tau_{rr}(r+a) \sim a^2[\tau_{rr}(r) + aD_r\tau_{rr}(r)] \sim F(r) + a^3(\tau_{rr,c}/r_c) \tag{4.10}$$

Here, $\tau_{rr,c}$ is the scale of τ_{rr} and r_c is the characteristic length along which the shear-rate (and thus τ_{rr}) changes significantly. It is assumed that $a/r_c << 1$. Then, the total force acting on the particle is:

$$F_E \sim \varepsilon a^2 \tau_{rr,c} \tag{4.11}$$

with $\varepsilon \equiv a/r_c$. This force causes the particle to accelerate in the *r*-direction and is balanced by the fluid drag force. Assuming that the Stokes law is valid, we can write:

$$F_D \sim \eta_0 a u_c \tag{4.12}$$

where F_D is the drag force, η_0 the fluid viscosity and u_c the velocity scale in the radial direction. At equilibrium, the value of u_c can be obtained by equating Eq. 4.12 and Eq. 4.11; this yields:

$$u_c \sim \frac{a\varepsilon\tau_{rr,c}}{\eta_0} \tag{4.13}$$

All the relations above are expressed in terms of the normal stress scale. This makes sense, insofar as the normal stress is the cause of particle migration. However, it might be useful to eliminate $\tau_{rr,c}$, relating it to the shear rate scale and the fluid viscoelastic properties. If we write the fluid stress tensor as a superposition of solvent and polymer contributions ($\boldsymbol{\tau} = \boldsymbol{\tau}_s + \boldsymbol{\tau}_p$), which is the form usually adopted for polymer solutions (Bird et al., 1987a; Macosko, 1994), it can be proven that in a bidimensional Taylor-Couette flow the *rr*-component of the stress arises only if $\boldsymbol{\tau}_p \neq 0$ with its exact expression depending on the constitutive model chosen (Bird et al., 1987a). In general, we can write:

$$\tau_{rr,c} \sim \eta_p \lambda \dot{\gamma}_c^2 \tag{4.14}$$

where η_p is the polymer contribution to the viscosity of the solution, $\eta_0 = \eta_s + \eta_p$, λ is the relaxation time, and $\dot{\gamma}_c$ is the scale of the shear rate. Eq. 4.14 implies a constant value of the first normal stress coefficient. As shown in Fig. 4.1c and 4.1d, the liquids used in this study exhibit a shear-thinning of the first normal stress coefficient at high shear rates. Despite this fact, Eq. 4.14 can still be used in the region of Wi numbers where the first normal stress coefficient remains constant; i.e. $Wi < 5$ for RI_{100} and $Wi < 7$ for GW_{100}.

Substituting Eq. 4.14 in Eq. 4.13, we obtain:

$$u_c \sim \frac{\eta_p}{\eta_0} a\lambda\varepsilon\dot{\gamma}_c^2 \tag{4.15}$$

Finally, we can rearrange Eq. 4.15 to derive a direct expression for the dimensionless characteristic migration time $t_c \equiv \frac{r_c}{u_c}\dot{\gamma}_c$:

$$t_c \sim \frac{\eta_0}{\eta_p}\frac{1}{\varepsilon^2 Wi} \tag{4.16}$$

The scaling law described so far has been derived in the hypothesis of a sphere immersed

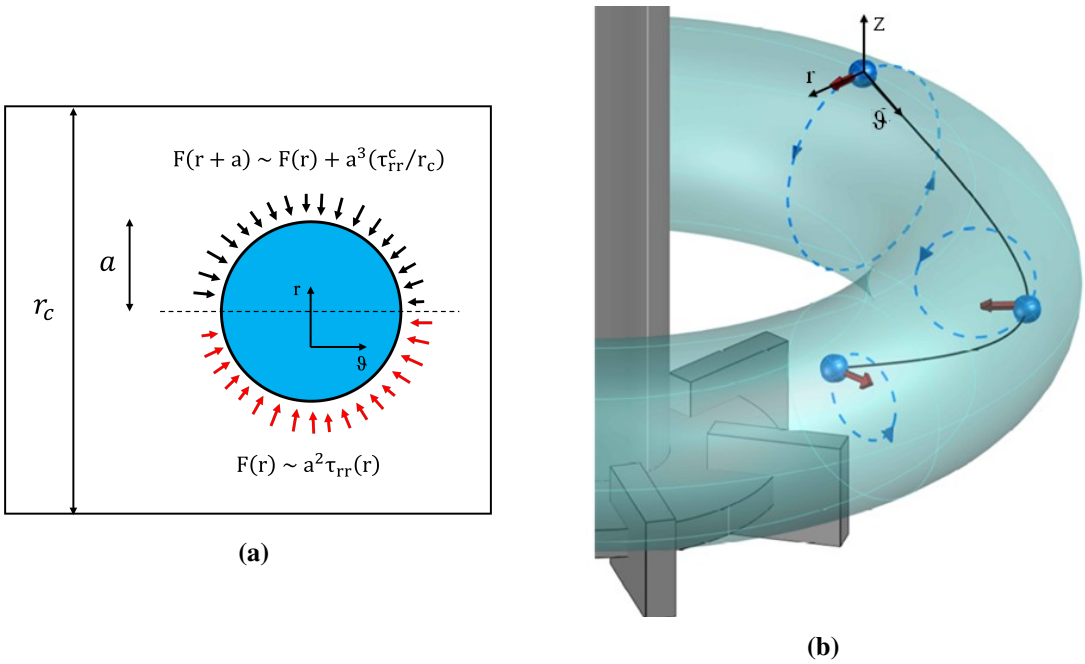

Figure 4.10: (a) Schematic of the elastic force acting on the sphere, and (b) particle path line in the stirred vessel.

in a viscoelastic fluid subject to a nonuniform, two-dimensional rotating shear flow (like the one present in a Taylor-Couette apparatus). In the previous section, it was shown that the three-dimensional flow created by a Rushton turbine, in an unbaffled vessel, in laminar regime can be visualised as the superposition of a main rotational flow around the z axis and a secondary rotational flow in the $r-z$ plane. It was also shown that the rate of deformation in the z direction is negligible in comparison to the planar deformation rates in the $r-\theta$ plane. This means that, at least with regard to the rate-of-strain tensor, the flow field can essentially be considered bi-dimensional. Furthermore, the variation of $\dot{\gamma}_{r\theta}$ along the radial direction (Fig. 4.7d) indicated that in the $r-\theta$ plane, the rotating flow is nonuniform.

Fig. 4.10b shows a schematic representation of the trajectory of the spheres. Following the movement of the liquid, the spheres rotate around both the z axis and in the $r-z$ plane.

During their motion, they are subjected to the elastic force arising from the presence of gradients of shear rate in the $r-\theta$ plane. These gradients are always oriented along r and directed toward decreasing absolute values of the shear rate. The result is that the spheres move along a spiral pathline ending at the centre of the toroidal vortex created by the impeller. To apply Eq. 4.16 to the stirred vessel, we need to assign a value to all the characteristic quantities involved. The characteristic shear rate $\dot{\gamma}_C$ was chosen as the average shear rate defined in Eq. 4.3 with value of $ks = 10$, while the characteristic length scale of the flow was assumed equal to the impeller diameter D. The migration

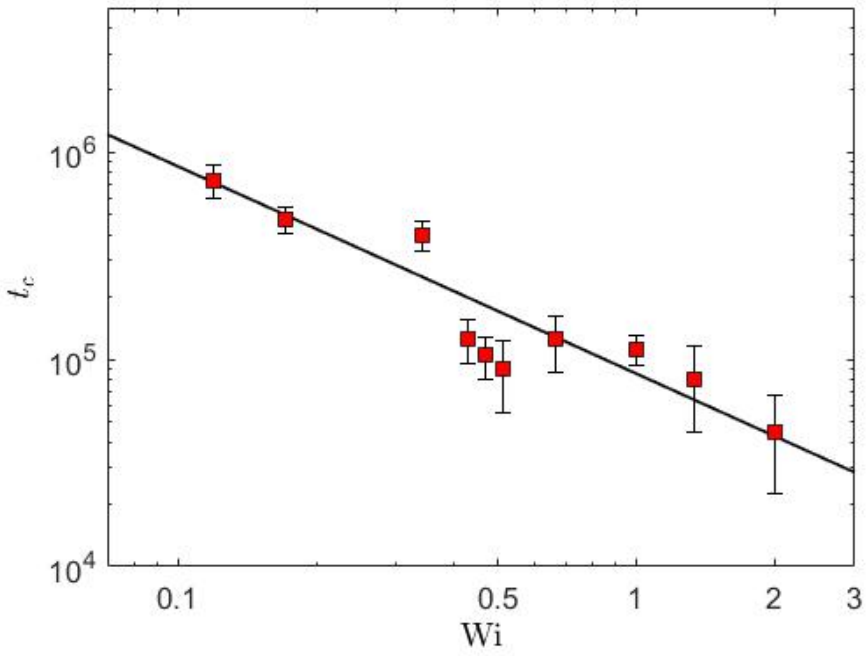

Figure 4.11: Dimensionless characteristic migration time as function of the Wi number. Experimental data (red squares) and model prediction.

time predicted by the heuristic scaling was validated against the data obtained from the migration experiments. The results are shown in Fig. 4.11 in terms of dimensionless characteristic migration time as a function of the Wi number. In agreement with the scaling law, the experimental data show an inverse dependence between t_c and Wi as highlighted by the plotted line $t_c = k/Wi$. Here, the constant k is used as a simple fitting parameter as the scaling law proposed is only expected to capture the order of magnitude of the time scale of the migration. However, it is interesting to notice that the value of k in Fig. 4.11 is found equal to 8.55×10^4, very close to the value of $\frac{\eta_p}{\eta_0}\frac{1}{\varepsilon^2}$ that, in the conditions examined, is equal to 8.89×10^4 and 3.67×10^4 for RI_{100} and GW_{100}, respectively.

4.4 Conclusions

In this chapter, a heuristic argument capable of predicting the characteristic migration time of solid particles suspended in a viscoelastic medium in a stirred vessel has been introduced. Planar PIV was used to reconstruct the three dimensional velocity profile produced by a Rushton turbine in an unbaffled vessel and to assess the effect of the fluid elasticity on the flow field. The reconstruction of the flow field was also used to assess the applicability of the scaling law to the flow in exam. It was found that the velocity field could be reduced to a nonuniform rotating shear flow around the z axis. Particle tracking experiments were also conducted in order to estimate the degree of dispersion of the solid phase and its evolution in time. In accordance with the literature, the experimental data confirmed that in a viscoelastic fluid the solid particles migrate across the streamlines and accumulate in areas of low shear rate. The characteristic velocity of this migration was estimated by calculating the degree of dispersion of the solid phase, through the Shannon entropy index, as a function of time. The experimental data were then used to validate the proposed scaling law. The scaling law was tested against data obtained with different viscoelastic fluids, impeller speeds and impeller diameters. The good agreement between the experimental data and the proposed equation confirms the validity of the scaling argument.

The results reported in this work show that solid particles immersed in the flow field produced by a Rushton turbine segregate in particular areas of the flow under the effect of the viscoelasticity-induced cross-flow migration. At first glance, this behaviour seems to be an obstacle to the mixing process for which stirred vessels are usually employed. On the other hand, the same phenomenon could be used for the continuous separation of solids from solid-liquid suspensions in those circumstances when settlers and filters prove to be inconvenient. This is especially for the separation of neutrally (or nearly neutrally) buoyant solids immersed in viscous, non-Newtonian fluids (Fig. A.1).

Chapter 5

Numerical investigation of the effect of viscoelasticity on the dynamics of a solid sphere in a shear flow using VOF

In this chapter, I report on the ability of the VOF method to predict the effect of viscoelasticity on the rotational velocity of a solid spherical particle immersed in the shear flow between two parallel plates. The objectives are (i) to describe the use of a VOF numerical scheme for the simulation of the motion of a solid body in flow, and (ii) to use the same model in order to derive the rotational velocity of a solid sphere in a viscoelastic fluid at different values of the Weissenberg number (Wi). To this end, initial simulations with a Newtonian fluid were performed in order to test the numerical approach and optimize the parameters of the simulation. Particular emphasis was given to the estimation of the optimal constitutive properties assigned to the solid phase. The same case was also used to perform a grid independence study. Subsequently, simulations for the viscoelastic case were performed at different values of the Weissenberg number. The non-Newtonian phase was modelled with the Oldroyd-B constitutive equation and the results were compared with those available in the literature.

5.1 Introduction

As reported in Chapter 2, the problem of the rotation of a solid sphere in a viscoelastic fluid subject to shear flow is a fundamental fluid-dynamic problem that has been studied extensively (D'Avino and Maffettone, 2015). The problem under exam is the rotation of a single, neutrally buoyant, non-Brownian, inertialess spherical particle in an unbounded liquid subject to shear flow. This problem, for the case of a Newtonian fluid, was first addressed by Einstein (Einstein, 1905, 1911), who reported that the particle rotates at a rate ω that depends on the applied shear rate $\dot{\gamma}$ and is given by:

$$\omega = \frac{\dot{\gamma}}{2} \tag{5.1}$$

This result is obtained by solving the mass and linear momentum balance equations, in the limit of creeping flow, for a free spherical particle immersed in an unbounded simple shear flow (Leal, 2007). This theoretical prediction has been confirmed by several experimental observations where the rotational velocity was either measured directly (Trevelyan and Mason, 1951; Snijkers et al., 2009) or derived from inferred quantities such as suspension viscosity and streamlines (Vand, 1948; Cox et al., 1968).

Early experimental observations of the rotation rate in non-Newtonian fluids were limited to small *De* (Bartram et al., 1975; Gauthier et al., 1971a,b). In these conditions of slow flow, the elastic forces are weak enough that the rotation rate was found to be identical to the Newtonian case. The recovery of the Newtonian behaviour at vanishing *De* was also predicted by the analytical solutions proposed by Brunn (1976b), and confirmed by more recent works (Greco et al., 2005, 2007; Koch and Subramanian, 2006). The rotation rate at non-vanishing *De* was also investigated experimentally for a wide array of particle shapes and suspending liquids (Astruc et al., 2003; Snijkers et al., 2009). Although the data are scattered, all the experiments confirm that the viscoelasticity of the suspending fluid causes a decrease of the rotation rate of the sphere with respect to the Newtonian case.

The net decrease of the rotation rate has also been observed through direct numerical simulations (DNS) by a number of authors. Hwang et al. (2004) performed 2D numerical simulations of a single particle suspended in an Oldroyd-B fluid in a sliding bi-periodic domain. The authors reported smaller values of the rotation rate with increasing *De*. The same results were confirmed by 3D numerical simulations for different constitutive equations (D'Avino et al., 2008; Ji et al., 2011). The effect of different rheological behaviours was highlighted by the implementation of both purely viscous models (Newtonian and shear-thinning) and viscoelastic models. Purely viscous models did not produce any change in the rotation velocity with respect to the Newtonian case. Conversely, simulations performed with constitutive equations accounting for the fluid elasticity showed

a reduction of the rotational velocity as a function of De. In unconfined and dilute systems, the slowing effect was not influenced by the shear-thinning of the fluid viscosity and by the presence of a second normal stress difference. These results agree with recent analytical solutions proposed by Housiadas and Tanner (Housiadas and Tanner, 2011a,b). Additionally, transient results show a correlation between the time evolution of the rotation rate and the first normal stress difference N_1, suggesting the importance of this material function on the slowing effect.

All the aforementioned results were obtained using different multiphase DNS frameworks, often implemented using in-house software. Although these models greatly extended our understanding of the effect of the fluid rheology on the particle dynamics, they are complex, application-specific and usually limited to the study of single particle systems. Additionally, these models cannot be easily implemented in commercially available solvers, limiting their applicability to the simulation of simple lab scale problems. In recent years, the development of reliable numerical schemes for the computation of viscoelastic constitutive equations has led to the wide availability of commercial and open-source solvers for single and multiphase systems. Despite this fact, a benchmark tool for the direct simulation of viscoelastic liquid-solid systems is still lacking. With this in mind, in the next section I explore the possibility of using a volume of fluid (VOF) model for the simulation of the dynamics of a solid sphere suspended in a viscoelastic fluid. This approach is not completely new as Ström et al. (2011) used a similar approach for the handling of solid particles in rarefied gases. The relatively modest computational cost and easy implementation of the VOF model, together with its wide availability in both commercial and open-source platforms, suggest that it could represent a useful tool for the simulation of multi-particle systems and large scale problems.

5.2 Modeling a solid sphere as a fluid droplet - Newtonian simulations

As mentioned in Chapter 1, in a two-phase system the VOF model describes each phase as a different fluid with distinct physical properties. To make a fluid droplet correctly mimic the behaviour of a solid sphere, two criteria need to be met: (i) the droplet must maintain a spherical shape throughout the entirety of the simulation; (ii) the reduction of momentum transfer from the suspending fluid to the droplet must be negligible; this implies a negligible internal circulation in the fluid droplet. Ström et al. (2011) suggest that a measure of the conformance to the second criterion can be obtained by the analysis of the ratio of the drag force on a fluid particle to that on a solid sphere in Stokes flow:

$$\frac{F_{Stokes,fluid}}{F_{Stokes,solid}} = \frac{6\pi\eta a\frac{3\beta+2}{3\beta+3}U}{6\pi\eta aU} = \frac{3\beta+2}{3\beta+3} \tag{5.2}$$

where β is the viscosity ratio between the fluid making up the particle and the fluid flowing around it, a is the radius of the particle and U is the fluid velocity far away from the particle. If one assumes that the drag is the only mechanism responsible for the transfer of momentum between the phases, then Eq. 5.2 is an expression of the reduction of momentum transfer due to the representation of the solid phase as a fluid. To meet the requirement (ii) (the reduction of momentum transfer from the suspending fluid to the droplet must be negligible), we must ensure that the ratio in Eq. 5.2 is close to one (that is, $\beta \to \infty$), because that would indicate a complete equivalence between the fluid and solid drag forces. To meet the requirement (i) (the droplet must maintain a spherical shape throughout the entirety of the simulation), we have to study the effect of the viscosity ratio, of the surface tension and of the flow conditions on the dynamic deformation of a fluid droplet. To this end, we will now briefly introduce the mathematical description of the problem as it is traditionally presented in the literature.

5.2.1 Drop deformation in simple shear flow

When a neutrally-buoyant, inertialess, spherical drop of viscosity η_1, embedded in a second immiscible liquid of viscosity η_2, is subjected to a shear flow, the stresses of the external fluid on the drop surface cause the drop to translate, rotate and deform. In the limit of slow flow (that is, Stokes or creeping flow), for Newtonian fluids the dynamical equation is linear, and so the flow can be studied by exploiting the superposition technique. A purely shearing flow can be split in three component flows: a uniform flow (associated with the value of the undisturbed velocity field of the ambient fluid at the center of the particle), a rigidly rotating flow (associated with the anti-symmetric part of the velocity gradient of the purely shearing flow), and a purely straining flow (associated with the symmetric part of the velocity gradient of the purely shearing flow). The first flow makes the particle translate, the second induces rigid rotations only, while the third induces pure deformations only. Since the translation and rigid rotation do not deform the particle, to study the particle deformation, one can consider only the purely straining flow. The linearity of the Stokes equation ensures that the same result are valid in a purely shearing flow. This approach was employed by Taylor (1934) to estimate the deformation of a viscous droplet suspended in a second liquid subject to pure straining flow. The droplet deformation can be quantified using the deformation parameter D initially proposed by Taylor (1934). For small deformations, at steady state the droplet assumes an ellipsoidal shape and D can be defined in terms of the major, L, and minor, B, axes of the ellipsoid (see Fig. 5.1):

$$D = \frac{L-B}{L+B} \tag{5.3}$$

This small deformation will only cause a small change in the stress distribution in both fluids. Therefore, at the interface, we can write:

$$\sigma_t^1 - \sigma_t^2 = 0 \tag{5.4}$$

$$\sigma_n^1 - \sigma_n^2 = -2\gamma\mathscr{H} \tag{5.5}$$

Eq. 5.4 and 5.5 represent the continuity of tangential stress and the balance of normal forces at the interface. Accordingly, σ^i is the stress exerted by phase i at the interface, while the indices n and t indicate the components of stress force vector $n \cdot \sigma^i$ in the directions normal and tangential to the interface. These components are defined as $\sigma_n^i = \boldsymbol{n} \cdot \sigma^i \cdot \boldsymbol{n}$ and $\sigma_t^i = \boldsymbol{n} \cdot \sigma^i \cdot \boldsymbol{t}$, where $\boldsymbol{n}$ is the normal unit vector to the interface, pointing into phase 2, and $\boldsymbol{t}$ is the tangential unit vector. Finally, $\mathscr{H}$ is the local mean curvature of the interface that can be expressed as:

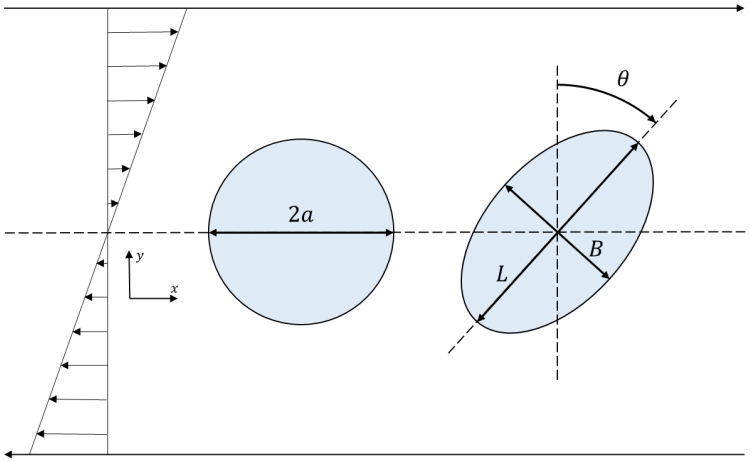

Figure 5.1: Representation of the initial and deformed states of a sheared droplet.

$$\mathscr{H} = -\frac{1}{2}\partial_s \cdot \boldsymbol{n} \tag{5.6}$$

where ∂_s denotes the surface gradient operator. The sign of $\mathscr{H}$ depends on the direction of the unit vector $\boldsymbol{n}$. In general, $\mathscr{H} < 0$ when $\boldsymbol{n}$ points away from the local center of curvature. Therefore, for example, for a spherical droplet of radius a, $\boldsymbol{n}$ is the unit vector normal to the droplet and pointing into the suspending liquid (i.e., away from the center of curvature), the mean curvature is negative and equal to $-(1/a)$. An equivalent expression for the mean curvature is:

$$\mathscr{H} = \frac{1}{2}\left(\frac{1}{R_1} + \frac{1}{R_2}\right) \tag{5.7}$$

where $1/R_1$ and $1/R_2$ are the principal curvatures at the point in question. Considering the definition of the stress tensor ($\sigma = p\boldsymbol{I} + \tau$), we can use Eq. 5.7 to express Eq. 5.5 as

follows:

$$\boldsymbol{n}\cdot(\tau^1-\tau^2)\cdot\boldsymbol{n}+(p^1-p^2)=-\gamma(R_1^{-1}+R_2^{-1}) \tag{5.8}$$

A similar equation is reported by Taylor (1934) for a nearly spherical droplet in a pure straining flow:

$$\tau^1_{rr}-\tau^2_{rr}=-\gamma(R_1^{-1}+R_2^{-1})+constant \tag{5.9}$$

where τ^i_{rr} is the rr component of the viscous stress tensor of the fluid, expressed in a spherical coordinate system $(r-\theta)$ with origin at the center of the droplet[a]. Taylor also reports an analytical expression for $\tau^1_{rr}-\tau^2_{rr}$ for the slow flow around a nearly spherical droplet:

$$\tau^2_{rr}-\tau^1_{rr}=\eta_2\dot{\gamma}\frac{19\eta_1+16\eta_2}{\eta_1+\eta_2}\left(\frac{x^2-y^2}{a^2}\right) \tag{5.10}$$

where x and y are the coordinates of a Cartesian coordinate systems with origin at the center of the droplet. Eq. 5.10 together with Eq. 5.9 can be used to calculate the final shape of the nearly spherical drop that satisfies the balance of normal forces. In terms of D, the results can be expressed as:

$$D=Ca\frac{19\beta+16}{16(\beta+1)} \tag{5.11}$$

where $Ca=a\eta_2\dot{\gamma}/\sigma_{12}$ is the capillary number, σ_{12} is the interfacial tension between the two phases and $\dot{\gamma}$ the shear rate in the suspending fluid. Eqs. 5.10 is only valid for small deformations and is obtained by assuming that the contribution to the normal stress due to viscous forces is small compared with that due to surface tension. This means that Eq. 5.11 is valid only for $Ca\ll 1$. In a similar way, Taylor also obtained the asymptotic value for D in the case of a highly viscous droplet ($\beta\gg 1$), obtained neglecting the effect of the surface tension.

$$D=\frac{5}{4\beta} \tag{5.12}$$

Eq. 5.11, valid in the limit $Ca\ll 1$, indicates that the effects of the interfacial tension and of the fluid viscosity on the final deformation of the droplet are almost completely expressed through Ca as the ratio $\frac{19\beta+16}{16(\beta+1)}\approx 1$. We also notice the additional result that, in the limit of large β, the steady-state deformation is independent of Ca and inversely proportional to the viscosity ratio. This suggests that a large value of β is a condition sufficient to ensure the sphericity of the fluid droplet at steady state.

The transient response to start up of the flow was described theoretically by Cox (1969) and Rallison (1980) in terms of the temporal evolution of the deformation parameter D and the angle θ (i.e. the orientation angle formed between the major axis of the drop and the direction perpendicular to the flow (Fig. 5.1)). The solution was obtained

[a]Note that for small deformation, at every point of the droplet interface $\boldsymbol{n}\cdot\tau^i\cdot\boldsymbol{n}=\tau^i_{rr}$

via a perturbation expansion around small values of the deformation, without any explicit restriction on Ca or β other than those which are implied by the assumption that the deformation remains small. The response depends on both β and Ca and can be illustrated by the following equations:

$$D(t) = D_0 \left[1 - 2e^{-\frac{20\dot{\gamma}t}{19Ca\beta}} \cos(\dot{\gamma}t) + e^{-\frac{40\dot{\gamma}t}{19Ca\beta}} \right]^{\frac{1}{2}} \tag{5.13}$$

$$\theta(t) = \frac{\pi}{4} - \frac{1}{2} \arctan \left(\frac{19\beta \left[e^{-\frac{20\dot{\gamma}t}{19Ca\beta}} \cos\dot{\gamma}t - 1 \right] + \frac{20}{Ca} e^{-\frac{20\dot{\gamma}t}{19Ca\beta}} \sin\dot{\gamma}t}{-\frac{20}{Ca} \left[e^{-\frac{20\dot{\gamma}t}{19Ca\beta}} \cos\dot{\gamma}t - 1 \right] + 19\beta e^{-\frac{20\dot{\gamma}t}{19Ca\beta}} \sin\dot{\gamma}t} \right) \tag{5.14}$$

where D_0 is the steady state deformation given by:

$$D_0 = \frac{5(19\beta + 16)}{4(1+\beta)\sqrt{(19\beta)^2 + (20/Ca)^2}} \tag{5.15}$$

The steady state value of the angle θ can be obtained from Eq. 5.14 by letting $t \to +\infty$.

$$\theta_0 = \frac{\pi}{4} + \frac{1}{2} \arctan \left(\frac{19}{20} \beta Ca \right) \tag{5.16}$$

Since the deformation parameter D (and D_0) is taken to be positive, it can be shown that the values of the angle θ must be such that (Cox, 1969):

$$\pi/4 \leq \theta \leq 3\pi/4 \tag{5.17}$$

$$\pi/4 \leq \theta_0 \leq \pi/2 \tag{5.18}$$

The value of the deformation given by Eq. 5.15 is seen to be small either when β is large, or when Ca is small, or when both β is large and Ca is small. To substantiate this claim, Table 5.1 reports the expressions for the steady-state deformation and orientation angle in the limits of large β and small Ca. It can be observed that all expressions in the table predict a vanishingly small droplet deformation. Additionally, the steady state deformation of the droplet, given by Eq. 5.15, yields the same results as obtained by Taylor (1934) in two cases.

1. Firstly, when the capillary number $Ca \ll 1/\beta$ or $Ca \ll 1$, whichever is more restrictive, the distortion is opposed by the action of the surface tension and Eq. 5.15 and 5.16 reduce to:

$$D_0 = Ca \frac{19\beta + 16}{16(\beta + 1)} \tag{5.19}$$ and $$\theta_0 = \frac{\pi}{4} \tag{5.20}$$

where Eq. 5.19 is equivalent to the expression reported by Taylor (1934) (Eq. 5.11).

In this scenario, there are three possibilities. If $\beta \gg 1$, then the condition $Ca \ll 1/\beta$ is more restrictive than $Ca \ll 1$, and simply requiring $Ca \ll 1$ is not sufficient to obtain the same result as Eq. 5.19. If $\beta \approx 1$, then the conditions $Ca \ll 1/\beta$ and $Ca \ll 1$ are equivalent. This scenario is the one referred to in the works of Torza et al. (1972) and Rallison (1984). Finally, if $\beta \ll 1$, then the condition $Ca \ll 1$ is more restrictive than $Ca \ll 1/\beta$.

2. Secondly, when the internal viscosity of the droplet is high ($\beta \gg 1$) and $Ca \gg 1/\beta$, or alternatively when $Ca \ll 1$ and $\beta \gg 1/Ca$, the droplet shape is maintained through rotation, as explained in Rallison (1984), and the steady deformation is:

$$D_0 = \frac{5}{4\beta} \qquad (5.21) \qquad \text{and} \qquad \theta_0 = \frac{\pi}{2} \qquad (5.22)$$

where Eq. 5.21 is equivalent to the second expression reported by Taylor (1934) (Eq. 5.12).

Table 5.1: Expressions of the steady state deformation (D_0) obtained from Eq. 5.15, for the four combinations of β and Ca that result in small deformations.

	$\boldsymbol{Ca >> 1/\beta}$	$\boldsymbol{Ca << 1/\beta}$
$\boldsymbol{\beta >> 1}$	$D_0 = \frac{5}{4\beta}; \quad \theta_0 = \frac{\pi}{2}$	$D_0 = Ca\frac{19\beta+16}{16(\beta+1)}; \quad \theta_0 = \frac{\pi}{4}$
	$\boldsymbol{\beta >> 1/Ca}$	$\boldsymbol{\beta << 1/Ca}$
$\boldsymbol{Ca << 1}$	$D_0 = \frac{5}{4\beta}; \quad \theta_0 = \frac{\pi}{2}$	$D_0 = Ca\frac{19\beta+16}{16(\beta+1)}; \quad \theta_0 = \frac{\pi}{4}$

In the case of a shear suddenly started from rest, Eqs. 5.13 and 5.14 describe a drop undergoing a transient motion which may be regarded as a damped "wobble". After a long time ($t \to +\infty$), the wobble stops and the droplet assumes the steady configuration described by the values of D_0 and θ_0. Fig. 5.2 shows the predictions of Cox's model for a droplet with constant $\beta = 1$ under different shear rates. At low Ca, the deformation grows monotonically to its steady state value. At higher capillary numbers, the curves begins to present an overshoot and, as Ca increases, the overshoots become larger and are followed by undershoots. For higher Ca, the transient behaviour becomes evidently oscillatory with an oscillation period inversely proportional to the shear rate. The viscosity ratio plays a very similar role to Ca. At low ratios, the deformation parameter increases monotonically to its steady-state value while for large viscosity ratios, the behaviour is no

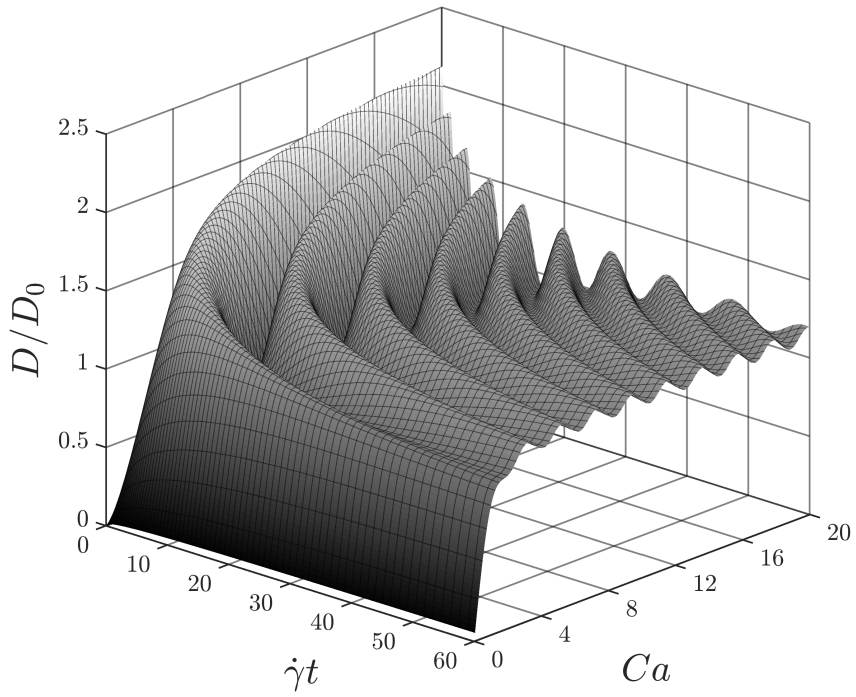

Figure 5.2: Prediction of Cox's model for the deformation parameter at $\beta = 1$ for different capillary numbers.

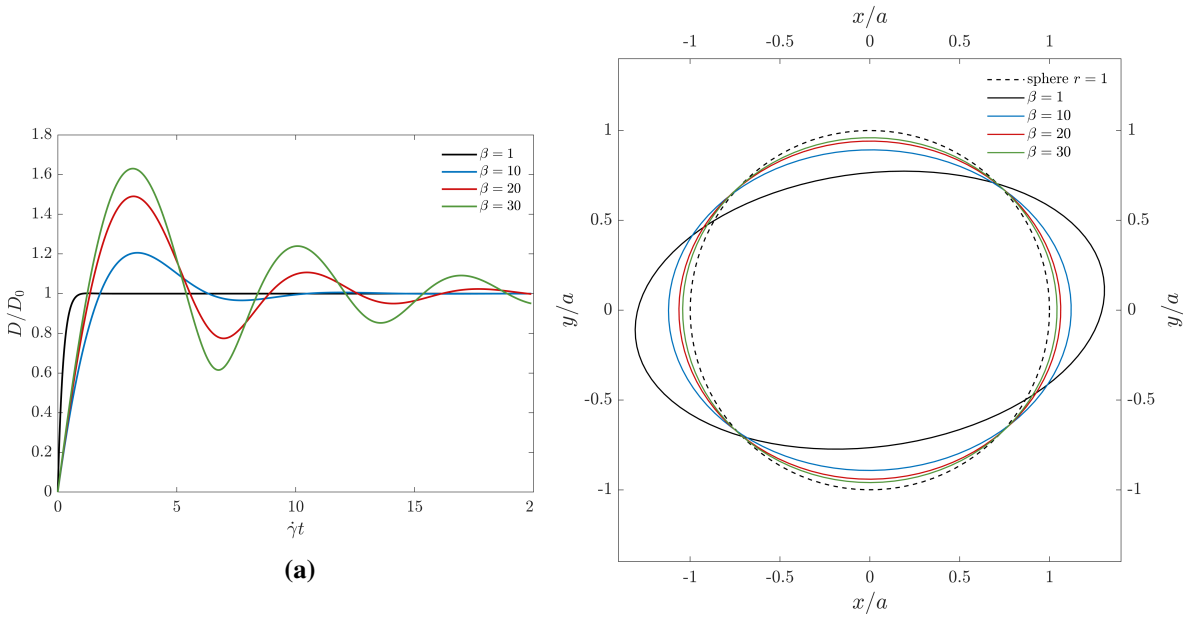

Figure 5.3: (a) Time evolution of the dimensionless deformation parameter at $Ca = 0.25$ for different viscosity ratios and (b) corresponding steady-state shape of the fluid droplet.

longer monotonic and stationary conditions are reached after a transient oscillatory phase. A visual example of this effect is reported in Fig. 5.3a as the time evolution of the dimensionless deformation parameter D/D_0. It is important to notice that the increment of the intensity of the oscillation observed at higher β happens in the context of a decreasing value of D_0 (Fig. 5.3b). This means that higher values of β are certainly helpful in both maintaining a spherical shape for the droplet at all times (condition (i)) and reducing the internal circulation (condition (ii)).

Droplet relaxation time

The time the droplet takes to reach its equilibrium configuration (i.e. the droplet relaxation time t_E) predicted by Cox's model is $\frac{Ca\beta}{\dot{\gamma}} = \frac{\eta_1 a}{\sigma_{12}}$. The same expression is obtained from the general definition of relaxation time for a fluid droplet in simple shear reported by Loewenberg and Hinch (1996), $t_R = \frac{(1+\beta)Ca}{\dot{\gamma}}$, if the observation is limited to moderate or high viscosity ratios (i.e. $\beta \gg 1$, or $\beta \approx 1$). As already mentioned, Cox's model is assumed to be valid for any combination of Ca and β that results in small deformations. Based on this criterion, all four possible combinations of Ca and β presented in Table 5.1 satisfy Eq. 5.13 and thus have relaxation time t_E. However, one of the reported cases, namely $Ca \ll 1$ and $\beta \ll 1/Ca$, can also be realised assuming a small value of β (e.g., $Ca = 0.05$ and $\beta = 0.001$). In this case, the deformation is certainly small ($D_0 \approx 0.05$) but the predictions for the relaxation time reported by Cox (1969) and Loewenberg and Hinch (1996) are inconsistent ($t_E \neq t_R$). To address this issue, a preliminary simulation was conducted with $Ca = 0.05$ and $\beta = 0.001$, and a shear rate of $\dot{\gamma} = 0.02$. In this case, the values of the two relaxation times are $t_E = 0.025$ and $t_R = 2.503$ s, respectively. The simulation methodology will be explained in subsequent sections but the results of the time evolution of the deformation parameter are presented in Fig. 5.4. Initially, the dimensionless deformation D/D_0 increases from zero to a maximum value of 1.2, before eventually decreasing and reaching a steady-state value after a time of approximately 10 s ($t\dot{\gamma}/Ca(1+\beta) \approx 4$). These findings align with those reported by Loewenberg and Hinch (1996) and confirm that the relaxation time suggested by Cox (1969) is only applicable at moderate or high values of the viscosity ratio. Interestingly, when the product $Ca\beta \gg 1$, the drop dynamics, obtained from Eq. 5.13, are given by:

$$D(t) = 2D_0 \sin\left(\frac{\dot{\gamma}t}{2}\right) \tag{5.23}$$

$$\theta(t) = \frac{1}{4}[\pi(1-2n) + \dot{\gamma}t] \tag{5.24}$$

where $2\pi n \leq \dot{\gamma}t \leq 2\pi(n+1)$ and n represents any integer greater or equal to 0[b]. According to Eqs. 5.23 and 5.24, the droplet deforms and rotates indefinitely ($t_E \to +\infty$) with a value

[b]The complete derivation of Eq. 5.24 is reported by Torza et al. (1972)

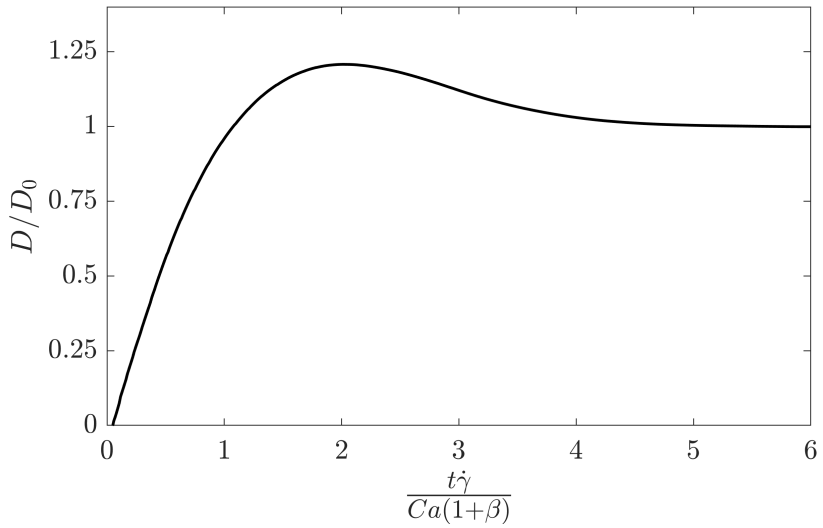

Figure 5.4: Time evolution of the deformation parameter at $\beta = 0.001$ and $Ca = 0.05$ as a function of the dimensionless time. The time was rendered dimensionless with the relaxation time reported by Loewenberg and Hinch (1996), $t_R = (1+\beta)Ca/\dot{\gamma}$.

of D oscillating between 0 and $2D_0$ without ever attaining a steady state. The condition $Ca\beta \gg 1$ can be met in different scenarios, such as when both β and Ca are large, or when β is large and Ca is moderate, or when Ca is large and β is moderate. However, the last case does not necessarily imply small deformations, and as a result, Cox's model is not applicable.

As an example, the time evolution of D and θ for $\beta \gg 1$ and $Ca \gg 1/\beta$ is reported in Fig. 5.5. In these conditions, D and θ oscillate without damping. At $t = 0$, $D = 0$ and $\theta = 45^\circ$ and, as t increases, D and θ increase simultaneously. A maximum value of D $(= 5/2\beta)$ is reached in correspondence of $\theta = 90^\circ$. Further increase of t produces a decrease in D while θ continues to increase up to 135°, when the drop re-assumes its initial undeformed shape. At this point θ goes back to 45° and the cycle is repeated. Finally, when the value of $Ca\beta \gg 1$, the droplet undergoes continuous rotation, rendering the concept of a steady state angle θ_0 meaningless. In the left column of Table 5.1, the reported values of θ_0 correspond to the average angle θ within the time interval $2\pi n \leq \dot{\gamma}t \leq 2\pi(n+1)$.

Amplitude and period of oscillation

By observing Eq. 5.13, it is clear that the oscillation period is independent from the fluid properties and only a function of the shear rate applied , $T_o = 2\pi/\dot{\gamma}$. This prediction of constant period is inaccurate since the first experimental works from Torza et al. (1972) showed a reduction of the frequency of oscillation at moderate β. Recently Escalante-Velázquez et al. (2018) proposed a modified version of Cox's model including a corrective parameter, function of the viscosity ratio, that improved the prediction of the period of

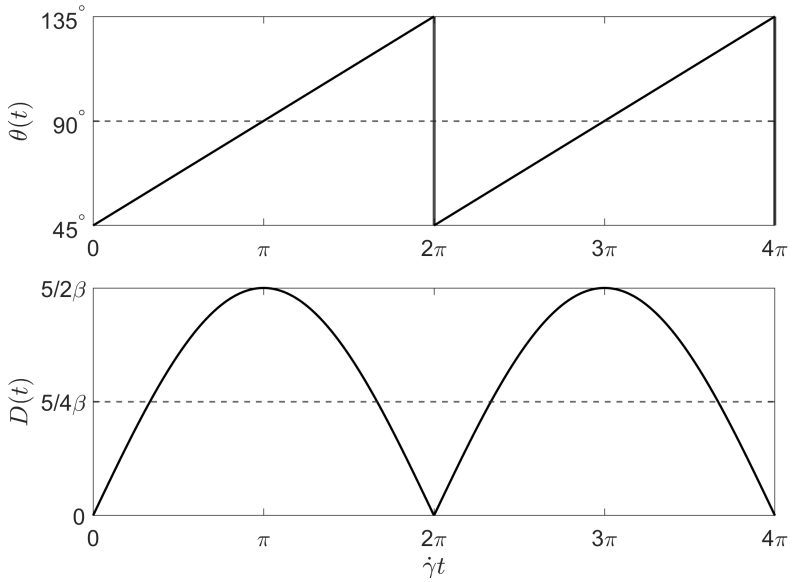

Figure 5.5: Illustration of the undamped oscillations of a drop suddenly subjected to a shear field. Both the drop deformation D and orientation angle θ, calculated from Eqs. 5.23 and 5.24, have a period of oscillation $T_o = 2\pi/\dot{\gamma}$.

oscillation. This model was validated against experimental and numerical results and will be used throughout the next section as benchmark for the validation of the transient results.

$$D(t) = D_0 \left[1 - 2e^{\left(-\frac{20\dot{\gamma}t}{19Ca\beta}\right)} \cos\left(\left(1 - \frac{3.4}{\beta} \right) \dot{\gamma}t \right) + e^{\left(-\frac{40\dot{\gamma}t}{19Ca\beta}\right)} \right]^{1/2} \tag{5.25}$$

Finally, we can notice that the amplitude of the oscillation predicted by both Eqs. 5.13 and 5.25 can be expressed as:

$$|D(t_m) - D_0| = D_0 e^{\left(-\frac{20\dot{\gamma}t_m}{19Ca\beta}\right)} \tag{5.26}$$

where t_m indicates the value of the time in correspondence of the maximums an minimums of $D(t)$ (i.e. the values of t where $dD(t)/dt = 0$). The equation presented in Eq. 5.26 shows that the amplitude of oscillation is directly related to the steady deformation D_0 and exponentially decays over a characteristic time scale t_E. As a result, it can be seen that if a particular combination of Ca and β yields a small value of D_0, then it would also assure a less intense oscillation at all times.

Period of rotation

For small deformations, the period of rotation T_r of a fluid particle located at the droplet interface is given by (Bartok and Mason, 1959; Rumscheidt and Mason, 1961; Torza et al., 1972):

$$T_r = \frac{4\pi}{\dot{\gamma}} \frac{\beta + 1}{\sqrt{\beta(\beta + 1)}} \tag{5.27}$$

while the period of circulation T_c close to the center of the drop is:

$$T_c = \frac{4\pi}{\dot{\gamma}} \frac{2(\beta+1)}{\sqrt{(2\beta+5)(2\beta-1)}} \tag{5.28}$$

for $\beta > 1/2$[c], it is readily shown that $T_c > T_r$, that is, the circulation inside the drop becomes slower towards the center. When $\beta \gg 1$, both Eqs. 5.27 and 5.28 reduce to $T \approx 4\pi/\dot{\gamma}$. This means that for large β, $D \to 0$, and the drop rotates rigidly with angular velocity $\omega = \dot{\gamma}/2$, in agreement with the value for a solid sphere (Einstein, 1905).

5.2.2 Simulations setup and convergence study

Before discussing the results for the Newtonian case, I will introduce the setup of the OpenFoam cases together with the geometry and boundary conditions employed. Subsequently, the study on the mesh convergence will be presented.

A schematic representation of the computational domain used in the convergence study can be found in Fig. 5.6. A time $t = 0$, a spherical droplet of radius a is positioned at the center of a square domain of length $2L = 25a$. In OpenFoam, any geometry is necessarily treated as a three-dimensional domain. For 2D simulations, a special kind of boundary condition, named `empty`, is employed. This condition is applied on the pair of boundaries Γ_5 and Γ_6 and has the effect of reducing the dimension of the problem to the x-z plane. The upper and lower edges of the domain (Γ_2 and Γ_4 in Fig. 5.6) represent the walls of the channel. These walls slide in the positive (upper) and negative (lower) x-direction with constant velocity $\pm U$. The shear rate across the channel can then be calculated as $\dot{\gamma} = U/L$. The confinement or blockage ratio, defined as $\varepsilon = a/L$, is $\varepsilon = 0.08$. At this level of confinement, it has been proven that the effect of the walls on the dynamic of the droplet can be safely neglected (Janssen and Anderson, 2007). Periodic boundary conditions are imposed on the left and right edges of the domain (Γ_1 and Γ_3 in Fig. 5.6). This is equivalent to simulating an array of particles separated by a distance of $2(L-a)$. In these conditions, the volume fraction of solids is $\frac{\pi}{4}\left(\frac{a}{L}\right)^2 \approx 0.5\%$, which implies that the suspension is dilute and the particles do not interact.

As mentioned in Section 2.3.1, the simulations for the Newtonian case are performed using the multiphase, transient solver `interFoam`. The physical properties of the two fluid phases are specified in a `transportProperties` file, an example of which is reported in Appendix B, List. B.1. The two phases are symbolically labelled as `water` and `air` for the high and low viscosity phases, respectively. The scalar indicator used to distinguish between the two phases is named `alpha.water` and represents the volume fraction of the `water` phase. For the Newtonian case, only the densities (`rho`), kinematic viscosities (`nu`)

[c] for $\beta < 1/2$, Eq.5.28 is not valid as Bartok and Mason (1958) describe the formation of two pockets of fluid circulation close to the center of the drop.

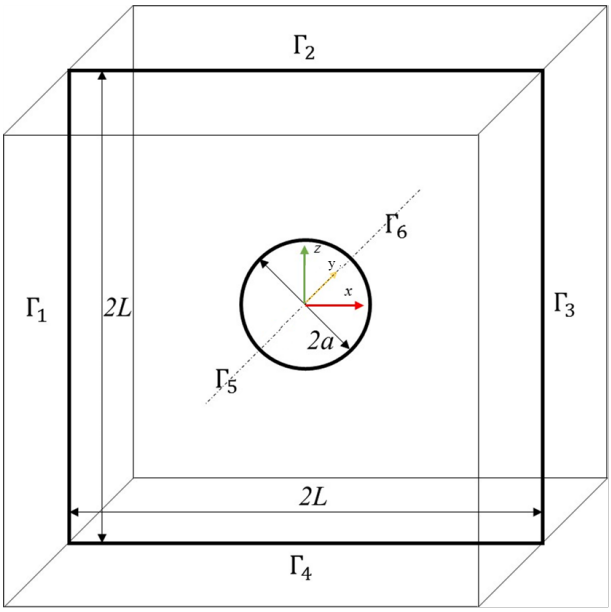

Figure 5.6: Schematic representation of the computational domain.

and interfacial tension (`sigma`) are required.

The domain is discretized with a mapped hexahedral mesh generated via the utility `blockMesh` (example in List. B.2 in Appendix B). The total number of intervals in the x and z directions is controlled via the variable `nx`. In order to improve the efficiency of the simulations, a large fraction of the total number of cells was placed in the vicinity of the fluid droplet where large gradients of velocity and pressure are expected. This was achieved by subdividing the computational domain in 9 regions via the definition of three intervals along both the x and z directions. The central intervals in both directions have a length of $0.6L$ (30% of the total length), and define a square region at the center of the domain that completely encloses the droplet (Fig. 5.7). Within this region, comprising 9% of the domain, were placed 60% of the total number of cells. Additionally, in all the remaining 8 regions, the mesh was gradually refined towards the center. The mesh convergence study was then simply conducted by changing the value of `nx` in the interval 50-150.

The simulations for the mesh convergence were performed with a value of $\beta = 25$ and $Ca = 1.5$. These values were chosen to compare the results obtained from our simulations to the numerical results reported by Kennedy et al. (1994) and the experimental data reported by Torza et al. (1972). The time convergence has also been checked by decreasing the time-step Δt. In OpenFoam, it is possible to perform transient simulations with an adjustable time step via the setting of a maximum value of the Courant-Friedrichs-Lewy number:

$$Co = \Delta t \, \tau_c \leq Co_{max} \tag{5.29}$$

where τ_c is a the reciprocal of a characteristic time scale based on the local cell velocity.

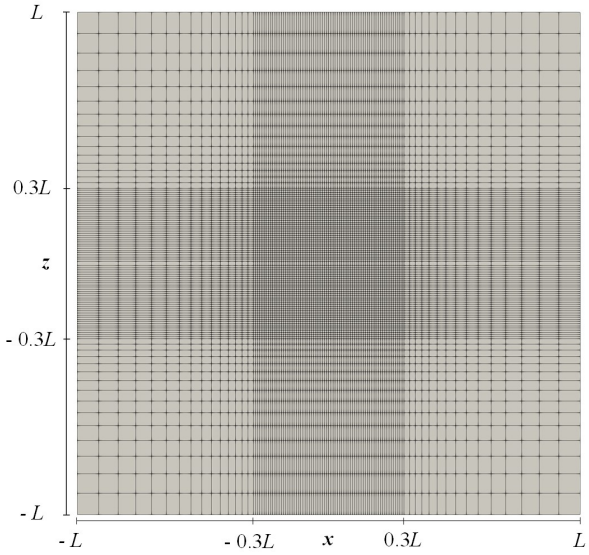

Figure 5.7: Example of 2D Mesh

For a quadrilateral mesh $\tau_c = \sum_{i=1}^{3} \frac{u_i}{\Delta x_i}$, where Δx_i is the length of a computational cell along the i-th direction. At the time $j-1$, the value of Co is calculated for each computational cell using Eq. 5.29. If we denote with x_m the location in the mesh where Co assumes its maximum value indicated as $Co_{x_m,j-1}$, the time-step for the next iteration is computed as:

$$\Delta t_j = \Delta t_{j-1} + \frac{(Co_{max} - Co_{x_m,j-1})}{\tau_{c,x_m}} \tag{5.30}$$

It was found that, although the steady state solution was not significantly affected by the choice of Co_{max}, the start-up behaviour could substantially differ. Despite this fact, setting a value of $Co_{max} = 0.1$ was found sufficient to assure the convergence of the time-dependent results. For all the simulations, the fluid is initially at rest and, at time $t = 0$, the upper and lower boundaries are set in motion with a constant velocity $\pm U$. For every case, a total of 60 seconds are simulated.

Mesh convergence results

To assess the effect of the mesh size on the shape of the droplet, we analyzed the time evolution and the steady state configuration of the interface. Fig. 5.8a shows the initial and final shapes of fluid droplet, as predicted by Cox's model, with a value of $\dot{\gamma} = 10^{-2} s^{-1}$, $\beta = 25$ and $Ca = 1.5$. In these conditions, the predicted steady state values of the deformation parameter and orientation angle are $D_0 = 0.0429$ and $\theta_0 = 1.8°$. Accordingly, the fluid droplet is only slightly elongated in a direction almost parallel to the x-axis. These results can be used to evaluate the effect of the mesh size on the final shape reported in Fig. 5.8b. The interface between the two fluids is obtained by extracting the geometric coordinates of cells where the value of `alpha.water` $= 0.5$. As it can be seen, the sim-

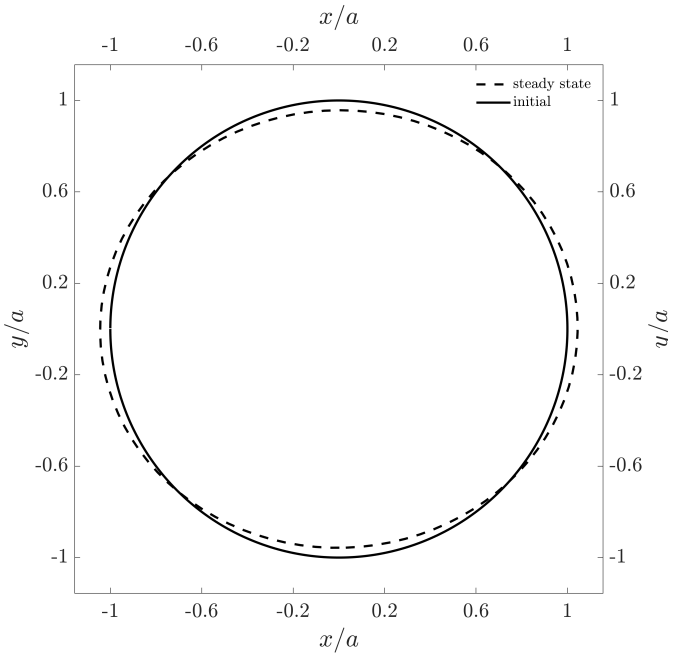

(a)

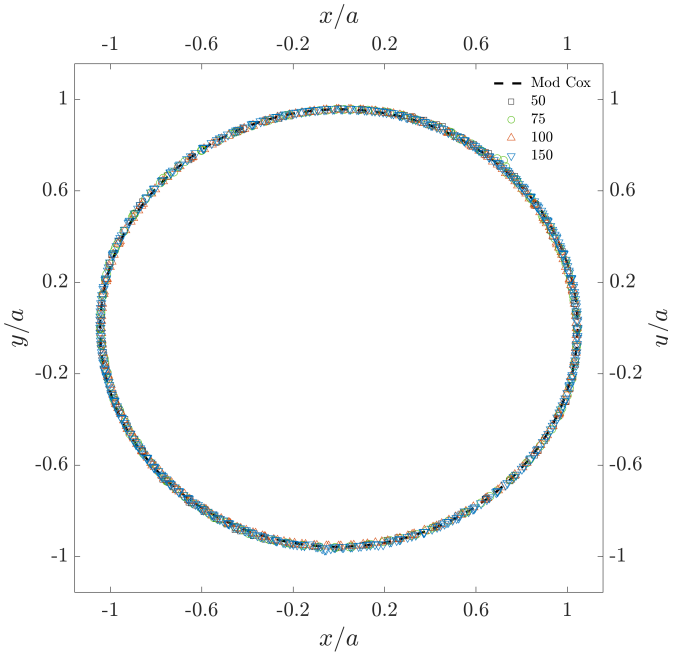

(b)

Figure 5.8: (a) initial and steady-state shape as predicted by the modified Cox model with $\beta = 25$ and $Ca = 1.5$; and (b) simulation results at different mesh size.

ulation results agree with the analytical solution of Cox et al. (1968). Additionally, it is clear that all the simulations predict the same final shape of the fluid droplet regardless of the mesh size.

The evolution of the deformation parameter as a function of the dimensionless time t/t_E is reported in Fig. 5.9a, together with the modified Cox model, the experimental data of Torza et al. (1972) and the simulation results of Kennedy et al. (1994). We can first notice that at all level of refinement, the deformation parameter shows the characteristic damped oscillatory behaviour mentioned in Section 5.2.1 and a good agreement, at least regarding the period of oscillation and the damping rate, with both the modified Cox model and the numerical simulations performed by Kennedy et al. (1994). Despite this, the predictions of the model and the results of the simulations significantly deviate from the experimental data of Torza et al. (1972) in the exponential decay of the deformation parameter. Kennedy et al. (1994) suggests that the assumption of uniform and isotropic interfacial tension in the analytical and numerical models is at the root of these discrepancies. Given that the same assumption is valid for the simulations reported in this work, it is not surprising to observe the same discrepancy between the numerical and experimental results at every value of mesh refinement. The main effect of the mesh refinement is relegated to the initial peak value of D. For example, at `nx` = 50, D rapidly increases from 0 to the value of 0.097, 25% larger than the one predicted by the model. The discrepancy between the two peak values decreases for the successive peaks (to 12% for the second and 8% for the third). The same behaviour is exhibited by the curve for `nx` = 100, with a substantially smaller error at each peak (7.5, 5 and 2% for the first three peaks, respectively).

Fig. 5.9b reports again the value of $D(t)$ for the finest mesh tested (`nx` = 150), but over a longer time interval. As we can see, the damped oscillatory behaviour is almost completely exhausted after a time $t/t_E \approx 4$. This can be expected since Eq. 5.13 shows an exponential dependence of $D(t)$ with (t/t_E) $(1-e^{-t/t_E} \approx 0.981$ for $t/t_E = 4)$.

Finally, the overall effect of the mesh refinement is evaluated by computing the normalised root-mean-square (NRMS) difference between the numerical and analytical values of the deformation over the entire simulation time:

$$NRMS = \frac{\sqrt{\frac{1}{n_t}\left(\sum_{t=0}^{n_t}[D(t)-D_{an}(t)]^2\right)}}{D_0} \tag{5.31}$$

where n_t is the total number of time instants while $D_{an}(t)$ and D_0 are the instantaneous and steady state values of the deformation parameter calculated through Eq. 5.25 and 5.15. The results are reported in Fig. 5.10. The reduction in NRMS indicates a progressively better adherence between the numerical results and the analytical solution at larger `nx`, with most of the improvement realized when moving from `nx` = 50 to 100. At `nx` = 100, the mean difference between the simulation results and the analytical solution across the

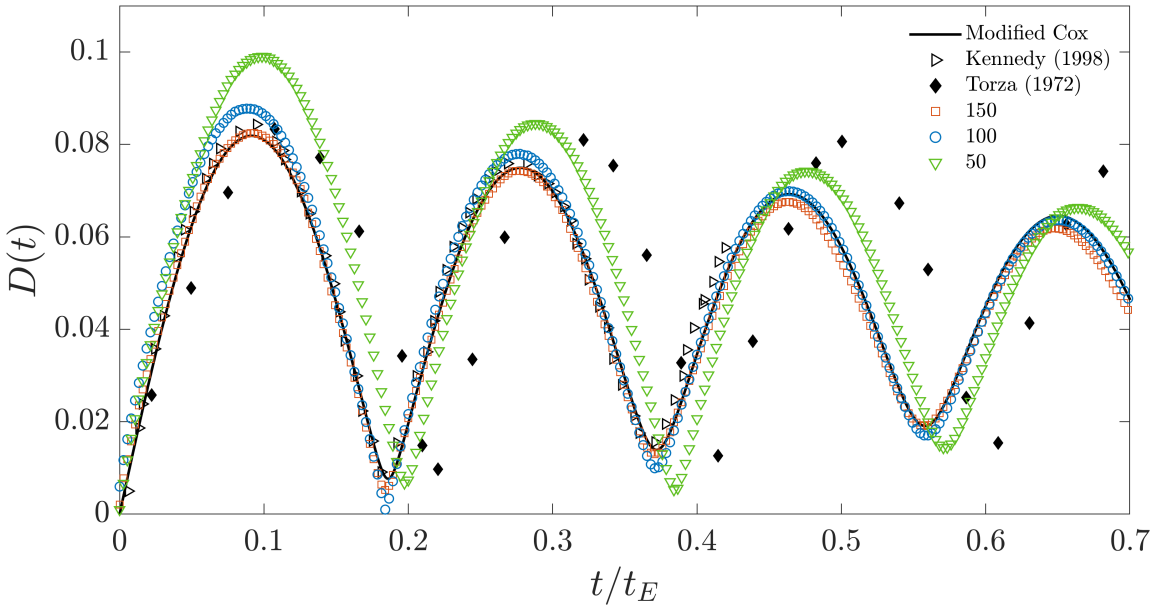

(a)

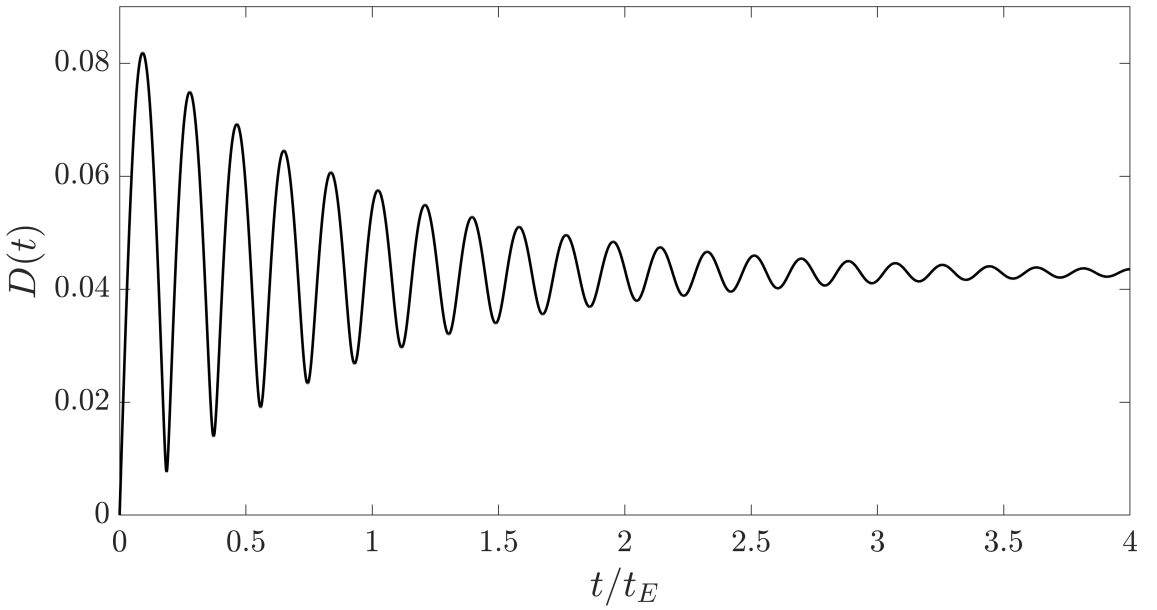

(b)

Figure 5.9: (a) Time evolution of the deformation parameter at $\beta = 25$ and $Ca = 1.5$ for different mesh refinement levels, and (b) Time evolution of the deformation parameter as a function of the dimensionless time for `nx` = 150.

whole simulation time is roughly 5% of D_0. A value of `nx` = 100 will be used for the remaining of this thesis.

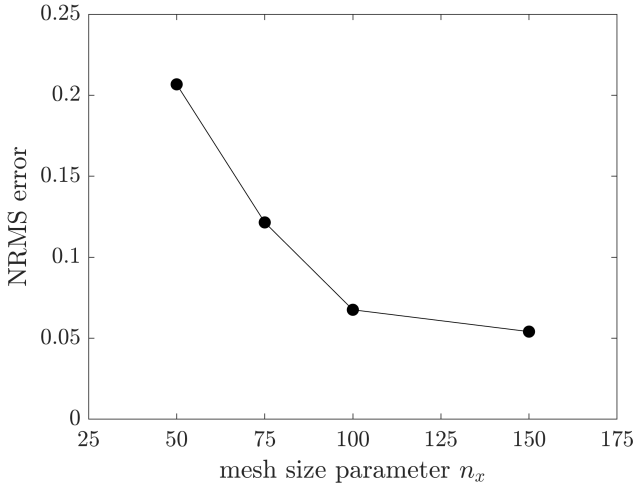

Figure 5.10: Root-mean-square difference as a function of mesh size.

5.2.3 Newtonian results and parameters selection

In light of the considerations discussed in Sections 5.2.1, it seems natural that, in order to assure the conservation of the spherical shape of the drop, one can either increase the viscosity ratio or reduce the capillary number. A high value of β is however required in order to minimize the internal circulation of the drop and the subsequent reduction in momentum transfer (condition (ii) in Section 5.2). Ström et al. (2011) suggest that values of 10000 for β and 0.01 for Ca are sufficient to assure both the sphericity of the droplets and the absence of internal circulation. Although these values seem reasonable, the authors do not report any quantitative proof of their statement.

To verify these claims, and obtain reliable values for our operating parameters, a series of 2D simulations are performed on the Newtonian setup described in the previous section. First, the value of β is determined by performing simulations where the value of Ca is kept constant at 1 and the viscosity ratio is varied between 100-10000. Values of $\beta < 100$ were considered to be too small and excluded from the investigation. This was justified by noticing that the ratio $\frac{3\beta+2}{3\beta+3}$ (Eq. 5.2) is $\approxeq 0.997$ at β = 100 but it drops to $\approxeq 0.96$ at β = 10. Finally, the value of β determined by the first analysis, is used in a consecutive set of simulations where Ca is varied between 0.1 and 0.01.

Viscosity ratio

Given that the ultimate objective of this chapter is to predict the rotational velocity of a solid sphere in a simple shear flow, the optimal value of the viscosity ratio is determined by observing the variation of the time evolution of this quantity as a function of β. We also remind that for a solid sphere in shear flow, the steady-state value of the angular velocity is $\dot{\gamma}/2$. The angular velocity is estimated by extracting the value of the y-component of

the vorticity (ω_y) at the center of the drop (location (0, 0, 0) in the computational domain) at each time step. The angular velocity is then calculated as $\omega = \omega_y/2$, as the vorticity is twice the angular velocity.

The time evolution of the ratio $\omega/\dot{\gamma}$ for $\beta = 100$ is reported in Fig. 5.11 where the time has been made dimensionless with the droplet relaxation time t_E. For comparison, we also report the value of the normalised deformation parameter. It can be seen that after the flow is initiated, the angular velocity of the droplet increases sharply towards an asymptotic value of 0.5. Upon reaching the asymptote, in analogy with what observed for the deformation parameter, the angular velocity exhibits a damped oscillating behaviour. The presence of oscillations suggests an influence of the deformation dynamics on the rotational velocity of the fluid inside the droplet. Naturally, for the case of a solid sphere in simple shear flow, no such oscillation is present and the time evolution of the angular velocity reduces to a monotonic increase to a steady state value with time scale, in the case of Stokes flow, of the order $\sim L^2/\nu$, where ν is the kinematic viscosity of the suspending liquid.

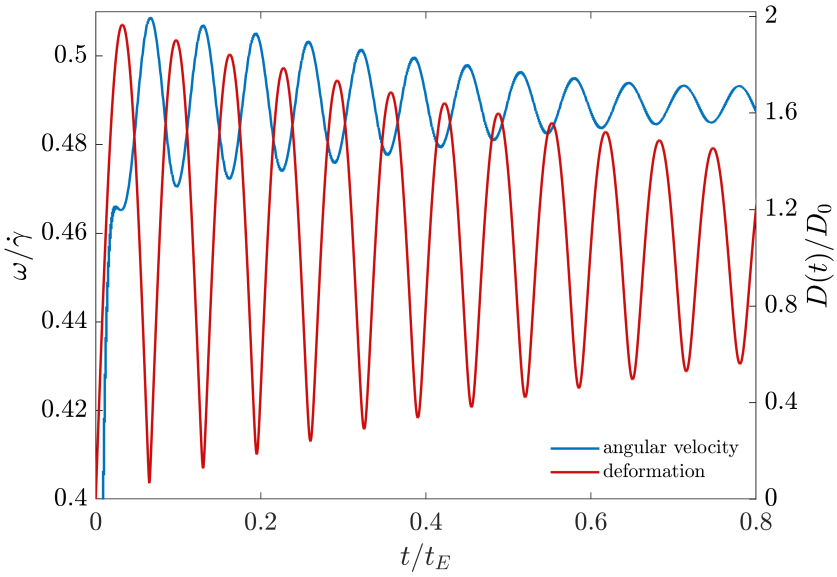

Figure 5.11: Comparison between the time evolution of the angular velocity and the deformation parameter for $\beta = 100$ and $Ca = 1$.

The comparison with the deformation parameter reveals that the two quantities change with the same time scale t_E. This is shown, for instance, by the fact that the values of the oscillation amplitudes for both ω and D decrease by the same amount ($\approx 30\%$) when t/t_E goes from 0.2 to 0.8. It is also evident that the two quantities oscillate with the same frequency $f \approx 1.55 \times 10^{-3}$ Hz. This is in agreement with the oscillation frequency predicted by Eq. 5.25, $\left(1 - \frac{3.4}{\beta}\right) \frac{\dot{\gamma}}{2\pi} \approx 1.53 \times 10^{-3}$ Hz. From these considerations it follows that the dynamic behaviour of the angular velocity of a drop is closely linked to its deformation.

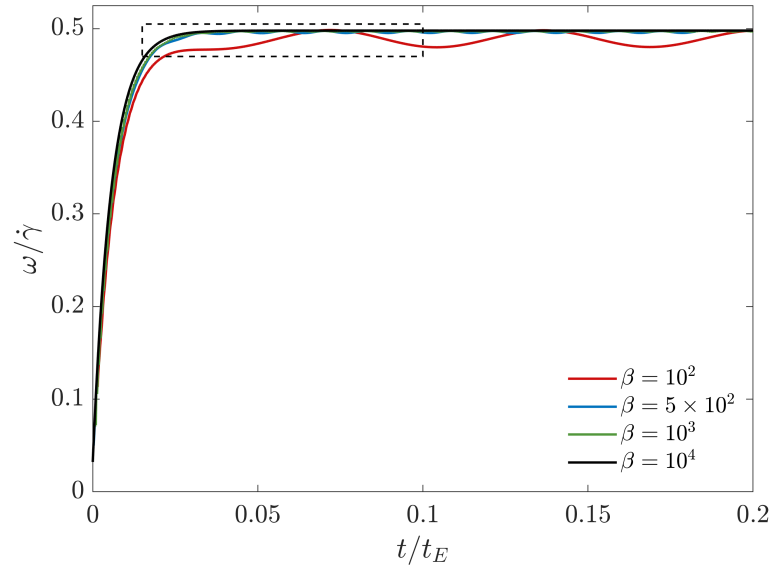

(a)

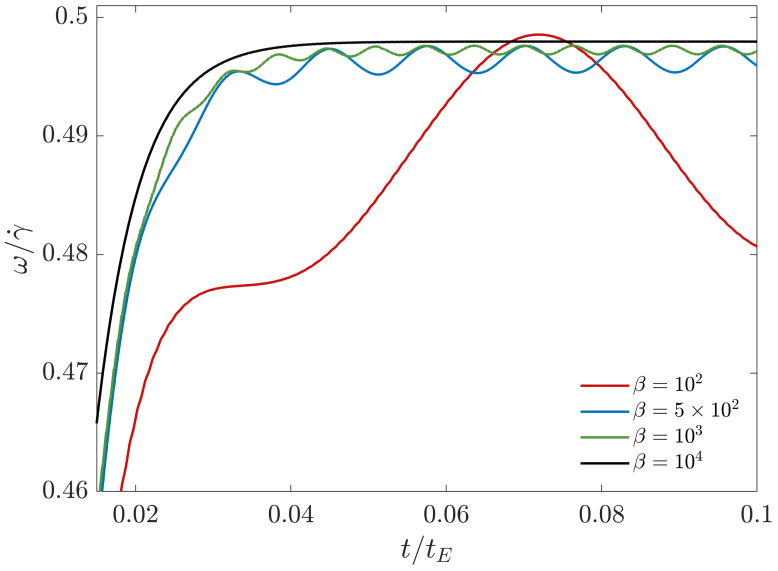

(b)

Figure 5.12: (a) Time evolution of the angular velocity at $Ca = 1$ for different viscosity ratios and (b) close up view of the periodic oscillations.

Fig. 5.12a illustrates the temporal variation of the ratio $\omega/\dot{\gamma}$ for four different viscosity ratios. Regardless of the specific value of β, the angular velocity demonstrates a pattern similar to what shown previously. Initially, it rises rapidly to approach an eventual steady-state value, after which it exhibits damped oscillations.

The amplitude of the oscillations is inversely proportional to the viscosity ratio. For instance, at $\beta = 100$, the angular velocity oscillates between 0.5 and 0.48 with and amplitude of 0.02 (2% of the mean value) while at $\beta = 1000$, the amplitude drops to 7×10^{-4} (0.14% of the mean value). At $\beta = 10^4$, the amplitude becomes so small that the oscillat-

ing behaviour is no longer observable. The effect of the viscosity ratio on the oscillation amplitude is in accordance with Eq. 5.26 which predict an amplitude proportional to the steady state deformation D_0. For all the cases in Fig. 5.12a, $\beta >> 1$ and $Ca << 1/\beta$, hence $D_0 \approx \frac{5}{4\beta}$. On the other hand, the frequency of the oscillation remains almost unchanged when increasing β. This is expected in light of Eq. 5.25, as the value of $\left(1 - \frac{3.4}{\beta}\right) \sim 0$ for all the values of viscosity ratio explored. Notably, the equivalence of the frequencies is not readily apparent from a visual inspection of Figure 5.12b. This is due to the choice of plotting against the dimensionless time variable t/t_E. Finally, increasing β has the additional undesired effect of increasing the droplet relaxation time ($t_E = Ca\beta/\dot{\gamma}$). This means that the droplet shape and the angular velocity will oscillate for a longer period of time before reaching a steady value. However, this is mitigated by the fact that a higher value of β leads to a decrease in the amplitude of the oscillations. As a result, the overall effect of the oscillations is reduced.

In conclusion, the results presented are in agreement with the suggestion of Ström et al. (2011) and a value of $\beta = 10^4$ will be used for the rest of this work.

Capillary number

The time evolution of the ratio $\omega/\dot{\gamma}$ for two values of Ca is reported in Fig. 5.13. All the simulations were performed with a constant value of $\beta = 10^4$. Similarly to what was reported before, it can be seen that as soon as the flow is started, the angular velocity rapidly increases towards a steady-state asymptotic value. For all the values of Ca examined, the asymptotic behaviour does not exhibit any evident oscillation. This remains true even at relatively high capillary numbers ($Ca = 1$).

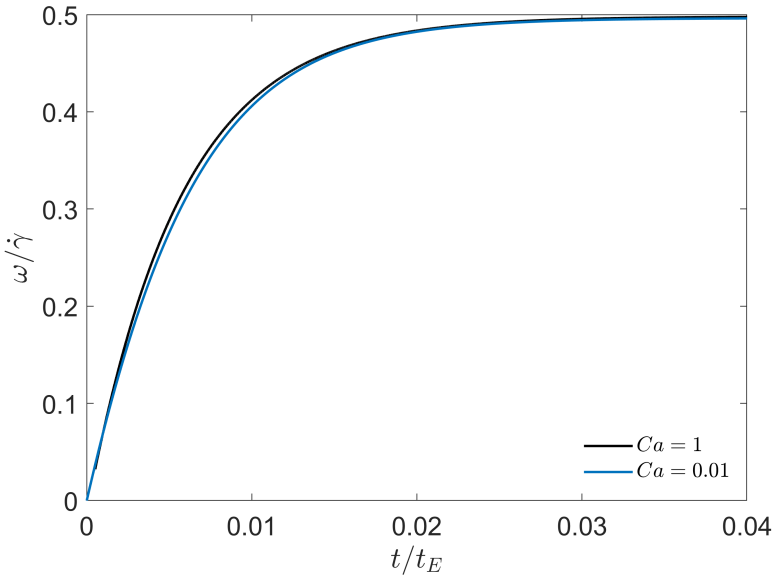

Figure 5.13: Time evolution of the angular velocity at $\beta = 10^4$ for two values of Ca.

From these results we can conclude that the spherical shape of the droplet is conserved for a wide range of Ca as long as the viscosity ratio remains sufficiently high. This conclusion can be understood in light of the synergetic effects exhibited by β and Ca on the deformation parameter (Eqs. (5.19), (5.21) and (5.25)). For the remaining of this work, all the simulations will be conducted with a value of $\beta = 10^4$ and $Ca = 0.01$.

5.3 Viscoelastic case

In this section, we report the results of the numerical simulations for the evaluation of the angular velocity of a single solid sphere, suspended in a viscoelastic liquid, in simple shear flow. The fluid is modelled with the split stress tensor approach described in Section 2.2, where the polymer extra stress tensor is modelled with the Oldroyd-B constitutive equation. The effect of the viscoelasticity on the angular velocity is examined well beyond the limit of slow flow and up to $Wi = \lambda\dot{\gamma} = 3$. We limited our study to the Oldroyd-B model as it allows studying the sole effect of the elasticity on the angular velocity of the sphere, without any concern about the shear-thinning of the viscosity. In particular, as mentioned in Section 2.2, when subject to a simple shear flow, an Oldroyd-B fluid presents a constant viscosity, a first normal stress difference quadratic in the shear rate ($N_1 = 2\eta_p\lambda\dot{\gamma}^2$) and no second normal stress difference. For its simplicity, it is often used as first model assumption for the study of a generic viscoelastic fluid in non-linear regime (i.e. outside the limit of small Wi).

For what concerns this study, the Oldroyd-B model was chosen for the additional reason that, in its current implementation in `rheoTool`, it is the most reliably tested constitutive equation. Most of the literature concerning the optimization of the numerical stability of the viscoelastic solvers within OpenFoam in fact focuses on the Oldroyd-B model (Fernandes, 2022; Spahn, 2019; Alves et al., 2021; Afonso et al., 2009).

To facilitate the discussion of the results in the following section, we introduce the two relevant dimensionless numbers for the flow field under examination, namely the Deborah number De and the Weissenberg number Wi. As already mentioned in Section 2.2.3, De is the ratio of the relaxation time to the characteristic time of change of the kinematics of the flow, while Wi is simply the product between the relaxation time and the characteristic value of the shear-rate ($\lambda\dot{\gamma}$). In an undisturbed simple shear flow, since at steady-state the kinematics do not change along the pathlines of the fluid elements, the associated time scale is infinite and $De = 0$. On the other hand, as always $Wi = \lambda\dot{\gamma}$. For the disturbed flow around the particle, the pathlines of the fluid elements flowing around the particle are no longer straight, and the fluid elements see their kinematics change as they flow around the particle. The time scale of this change is equal to a/U_c, where a is the particle radius and U_c is the scale of the velocity. This scale is equal to $\dot{\gamma}a$, and so the time scale is $1/\dot{\gamma}$. Then, we obtain that $De = \lambda\dot{\gamma} = Wi$. Although the two numbers have two distinct definitions,

they assume exactly the same value in the case under examinations. For this reason, the results throughout the remainder of this chapter will be presented exclusively in terms of Wi.

This section is structured as follows. First, we rapidly survey the geometric domain, the required boundary conditions and the computational mesh employed. Subsequently, the transient results and the flow streamlines around the solid sphere are presented. This is followed by the presentation of the results for the steady-state value of the angular velocity as a function of the Weissenberg number and the comparison with available data from the literature. Finally, the conclusions of the study and some final remarks are reported.

5.3.1 Computational Domain

The computational domain and the boundary conditions (BCs) employed for the simulation of a spherical particle in a viscoelastic fluid are similar to those described in Section 5.2.2. For the velocity field, Dirichlet BCs are imposed on the upper and lower walls of the domain (Γ_2 and Γ_4 in Fig. 5.6). In particular, the value of the velocity is $\mathbf{u} = u_x \mathbf{e}_x = \pm U \mathbf{e}_x$ on Γ_2 and Γ_4 respectively. On these boundaries the pressure is calculated with a fully developed BCs (`zeroGradient` in OpenFoam). The same BCs are imposed, for both velocity and pressure, on the boundaries perpendicular to the flow direction (Γ_1 and Γ_3). In contrast to the Newtonian case, the viscoelastic simulations necessitated the use of a three-dimensional grid. This was due to the fact that the angular velocity at Weissenberg numbers greater than zero ($Wi > 0$) is determined by the three-dimensional distribution of stresses around the sphere (D'Avino et al., 2008; D'Avino and Maffettone, 2015). Consequently, given the geometry of the problem, on the boundaries Γ_5 and Γ_6 the `symmetry` BCs are imposed:

$$\mathbf{u} \cdot n = 0 \tag{5.32}$$

where n is the unit vector normal to the boundary. As mentioned in Section 2.3, together with the usual continuity and linear momentum balance equations, the viscoelastic solver `rheoInterFoam` solves an additional transport equation for the log-conformation tensor $\boldsymbol{\Theta}$ (Eq. 2.73). This means that an additional set of boundary conditions is necessary for the numerical integration of $\boldsymbol{\Theta}$. In practice, for reasons related to the spatial discretization of the stress divergence terms, `rheoInterFoams` further requires boundary values for the polymeric extra-stress tensor $\boldsymbol{\tau}_p$ (Fattal and Kupferman, 2004).

The boundary conditions for the extra-stress tensor and its logarithm are contained in the two files `tau.water` and `theta.water` respectively (Appendix B). On the upper and lower walls of the domain (Γ_2 and Γ_4), the `linearExtrapolation` BC is applied for both $\boldsymbol{\tau}_p$ and $\boldsymbol{\Theta}$. The `linearExtrapolation` BC is expressed by the following equation:

$$A_{ij,f} = A_{ij,P} + (\nabla A_{ij})_P \cdot \mathbf{d}_{Pf} \tag{5.33}$$

where A_{ij} is the ij component of the generic field A (scalar, vector or tensor), indices f and P represent the boundary face and the cell owning that face, respectively, and $\mathbf{d}_{Pf}$ is the vector connecting their geometrical centers from P to f. This BC computes the value of the fields on the boundary faces from the corresponding values at the center of the boundary cells. This is achieved by first calculating the gradient of the variable at the cell center and then estimating the corresponding face value by linear extrapolation. Another boundary condition that can be used for the stresses at the upper and lower boundaries is the `zeroGradient` BC. This boundary condition assumes that the stress is fully developed in space, and there will be no further change in the direction normal to the boundary. The mathematical expression in this case can be derived from Eq. 5.33 by setting $(\nabla A_{ij})_P = 0$. However, this assumption is strictly valid only if the boundary is far enough to disregard the effect of the sphere, which is certainly the case in our simulations. In practice, for the stress and log-stress tensors, it has been observed that the `lienarExtrapolation` BC enhances numerical stability compared to the more commonly used `zeroGradient` BC. Therefore, the latter condition is imposed on Γ_2 and Γ_4 as well as on Γ_1 and Γ_3. Similarly to the velocity, the symmetry BC is applied to the boundaries labeled as Γ_5 and Γ_6 for both the stress and the log-stress tensors:

$$\boldsymbol{T_n} - (\boldsymbol{T_n} \cdot n)n = 0, \quad \boldsymbol{T_n} = \boldsymbol{T} \cdot n \quad (\boldsymbol{T} = \boldsymbol{\tau}_p, \boldsymbol{\Theta}) \tag{5.34}$$

For the non-Newtonian simulations, the computational mesh results from a three-dimensional extension of the 2D mesh used for the Newtonian case with `nx` = 100. In analogy with the 2D case, the three-dimension domain is discretized by fixing the total number of intervals along the x, y and z directions to `nx`. The domain is then divided in 27 regions via the definition of three intervals along each direction. The central region thus defined completely encloses the spherical drop and contains approximately 35% of the total number of cells. An example of the 3D mesh can be found in Fig. 5.14. Due to the large computational time, the validity of the simple extension of the 2D mesh to the 3D case was verified performing a single comparison between the results obtained at `nx` = 100 and `nx` = 200, for $Wi = 2$. The doubling of the mesh size caused a change of the final value of the angular velocity of only 0.42% ($\omega/\dot{\gamma} = 0.302$ and $\omega/\dot{\gamma} = 0.303$ for `nx` = 100 and 200 respectively). The value of `nx` was then kept to 100 for the rest of the study. As mentioned in the introduction to this section, the Oldroyd-B constitutive model was used for all the simulations. This model requires the definition of three parameters, namely the solvent and the polymer contribution to the total viscosity (η_s and η_p respectively), and the relaxation time λ. The values of the two contributions to the viscosity were kept constant throughout the entire study and equal to $\eta_s = \eta_p = 0.5$ Pa $\cdot$ s. This assumption allowed us to compare our results to the experimental and numerical data reported by Snijkers et al. (2011), Hwang et al. (2004), and Goyal and Derksen (2012). The value of

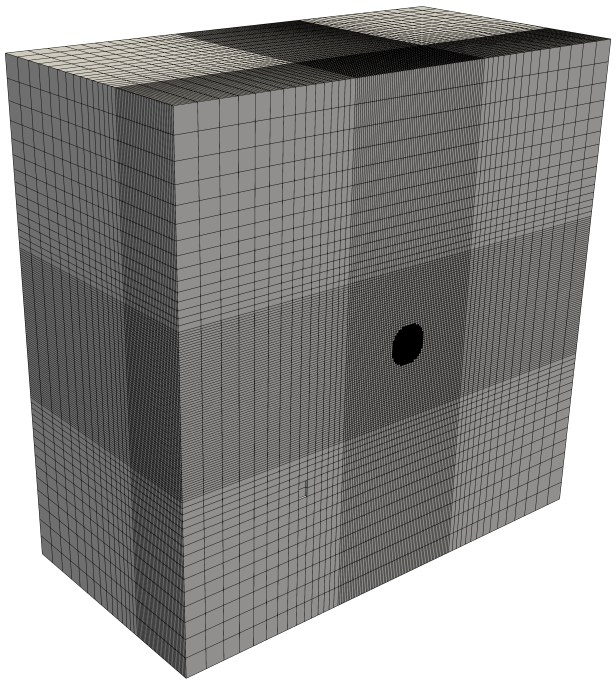

Figure 5.14: Clip of the 3D mesh, cut along the *x*-*z* plane.

the shear rate $\dot{\gamma} = U/L$ was also kept constant and equal to 1 for all the cases. Increasing levels of elasticity of the flow (i.e. larger Wi), were then simply achieved by increasing the value of the relaxation time.

5.3.2 Transient results

The viscoelastic simulations involved a transient analysis of the fluid's behaviour. At the outset of the simulation ($t = 0$), a simple shear flow was imposed on a fluid that was initially quiescent. A comparison between the transient behaviour of stresses of the undisturbed suspending liquid during shear start-up and the period of rotation of the sphere at different Wi values can provide useful insights. In this regard, we will plot the first normal stress difference (N_1), the polymer contribution to the shear stress (τ_p), and the period of rotation as function of the dimensionless time $\dot{\gamma}t$ for various Wi.

The value of the angular velocity ω, at each time-step, is first obtained by extracting the value of the *y*-component of the vorticity at the center of the solid particle. Similarly to the Newtonian case, the angular velocity is then simply calculated as $\omega = \omega_y/2$. The period of rotation of a single sphere in a Newtonian fluid in simple shear flow can be expressed as the Jeffrey period $T_N = 4\pi/\dot{\gamma}$ (Einstein, 1905). Similarly to D'Avino et al. (2008), we use a normalized viscoelastic rotation period defined as $T = T_{NN}/T_N = \dot{\gamma}/2\omega$, where T_{NN} is the period of rotation of the sphere in the viscoelastic medium. For vanishing Wi, the value of this ratio tends to unity. Both the shear and normal components of the fluid stress are extracted in correspondence of the top boundary of the domain (mesh

coordinates (0, 0, L). At this distance, the flow disturbance caused by the presence of the sphere becomes negligible and the stresses are expected to reach the values predicted by the Oldroyd-B model for a simple, undisturbed shear flow (i.e. $\tau_{p,zx} = \eta_p \dot{\gamma}$ and $N_1 = 2\eta_p \dot{\gamma} Wi$).

The time evolution of the dimensionless polymer shear stress ($\tau_p^* = \tau_{p,zx}/\eta_p \dot{\gamma}$) and of the first normal stress difference ($N_1^* = N_1/2\eta_p \dot{\gamma} Wi$) are reported in Figs. 5.15a and 5.15b, respectively. The dimensionless shear stress exhibits a monotonic increase from 0 to 1, for all the considered values of Wi. However, the rate of convergence to the steady-state value decreases at higher Wi. Similarly, the dimensionless first normal stress difference also exhibits a monotonic increase from 0 to 1 and a growth rate inversely correlated to Wi. One noteworthy observation is that, regardless of the value of Wi, the first normal stress difference (N_1) takes roughly 60 to 70% longer to reach its steady state compared to the shear stress. For instance, at $Wi = 1$, the time needed to reach 99% of the steady-state value is ≈ 4 s for τ_{zx} and ≈ 6.75 s for N_1.

These observations are in agreement with the analytical solutions expressed in Eqs. 5.35 and 5.36 for the response of an Oldroyd-B fluid subject to a start-up steady shear flow (Bird et al., 1987a).

$$\tau_{p,zx}(t) = \eta_p \dot{\gamma} \left(1 - e^{-t/\lambda}\right) \tag{5.35}$$

$$N_1(t) = 2\eta_p \lambda \dot{\gamma}^2 \left[1 - \left(1 + \frac{t}{\lambda}\right) e^{-t/\lambda}\right] \tag{5.36}$$

It is necessary to point out that the two analytic solutions in Eqs. 5.35 and 5.36 are obtained in the case of a simple shear flow set up instantaneously at the time $t = 0$. In this scenario, the only relevant time scale is the fluid relaxation time. However, the simulations conducted in this study employ a quiescent initial condition, and therefore, the time required to attain a fully developed flow must be considered. For a Newtonian fluid, this time is typically on the order of L^2/ν, where ν represents the kinematic viscosity of the fluid. Although this estimate does not apply generally to viscoelastic fluids, it is reasonable to approximate the time required for a fully developed flow as L^2/ν_s for the system under examination, where $\nu_s = \eta_s/\rho_s$ represents the solvent contribution to the kinematic viscosity of the fluid. For all the conditions examined in this study, $L^2/\nu_s \approx 0.01s$ is significantly smaller than λ. This indicates that the flow can be regarded as fully developed before the onset of any elastic effect, enabling us to compare our results with the analytical solutions presented in Eqs 5.35 and 5.36.

For the shear stress, Eq. 5.35 predicts a monotonic exponential increase of $\tau_{p,zx}$ from 0 to a steady state value of $\eta_p \dot{\gamma}$, with a characteristic time scale λ. The initial slope of $\tau_{p,zx}$ $\left(\left.\frac{\partial \tau_{zx}}{\partial t}\right|_{t=0}\right)$ is positive and equal to η_p/λ. Similarly, Eq. 5.36 predicts a first normal stress that increases monotonically with time from 0 to a steady state value ($2\eta_p \dot{\gamma} Wi$)

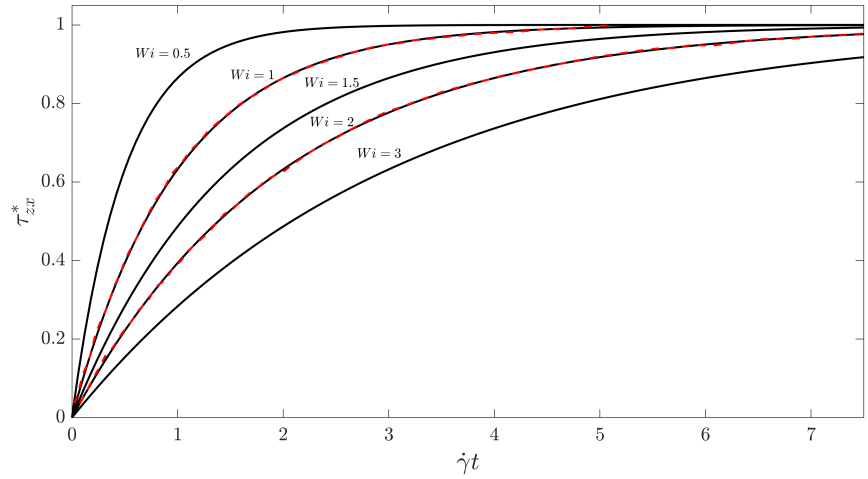

(a) Shear stress

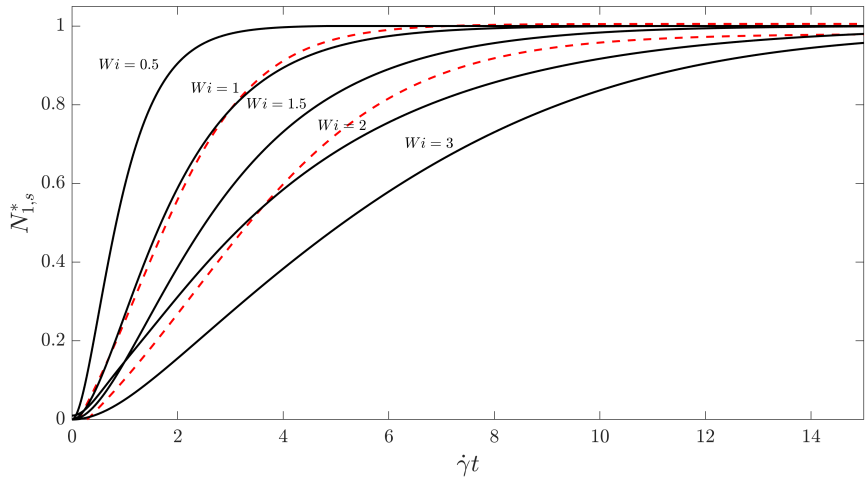

(b) First normal stress

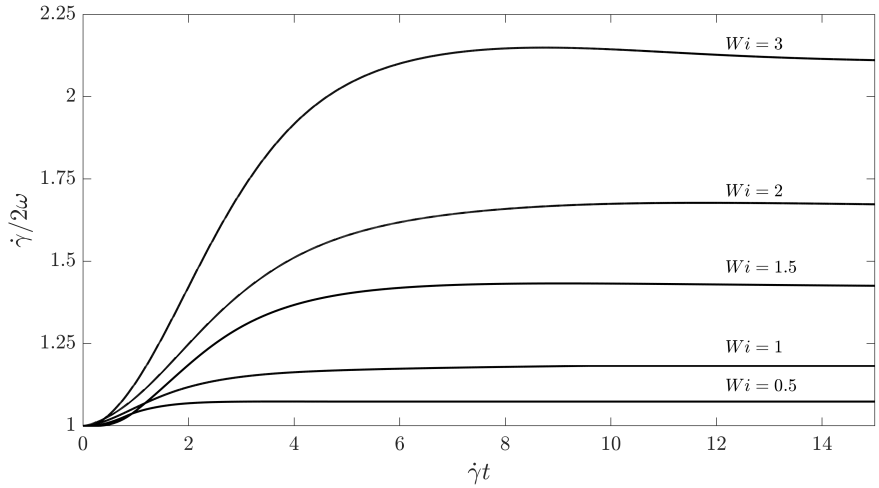

(c) Rotation period

Figure 5.15: (a) Time evolution of the dimensionless shear stress, (b) dimensionless first normal stress difference, and (c) dimensionless period of rotation for a single sphere in shear flow at different Wi. (——) Represents data from this work and (- - -) are the numerical data reported by D'Avino et al. (2008).

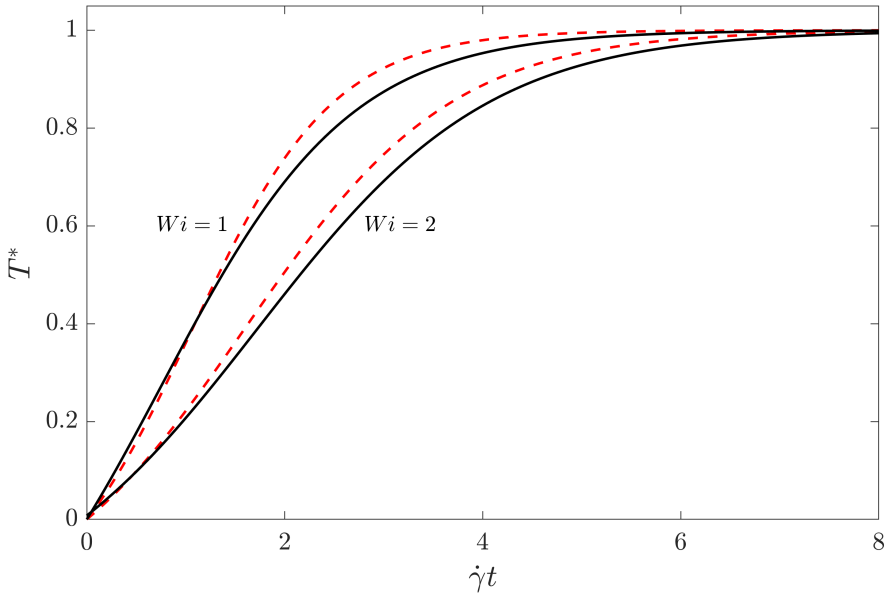

Figure 5.16: Comparison between the time evolution of the normalised ratio T^*_{NN}/T^*_N obtained in this study (——) and the data of D'Avino et al. (2008) (- - -).

proportional to Wi. The initial rate of increase of N_1 is 0 and the function exhibits a sigmoidal shape. The term $\left(1+\frac{t}{\lambda}\right)$ appearing on the right-hand side of Eq. 5.36 also explains the delayed onset of the steady-state behaviour observed for the first normal stress difference compared to the shear stress. It in fact counteracts, at least initially, the decay of the exponential term $e^{(-t/\lambda)}$. Finally, Fig. 5.15a and 5.15b also showcase the numerical results from D'Avino et al. (2008) for $Wi = 1$ and 2 (red dotted lines) alongside the results of our simulations. Notably, the time evolution of the shear stress demonstrates very good agreement with the experimental data. The time evolution of the normal stress also shows good agreement, albeit marginally better for $Wi = 1$ than $Wi = 2$.

Fig. 5.15c reports the time evolution of the dimensionless period of rotation of the sphere. Again, the rotation rate is initially 0 and rises monotonically to a steady-state value. In analogy with N_1, the final value attained is a function of Wi. In particular, in line with what found in the literature, larger Wi implicates larger periods of rotation (i.e. slower rotation rates). Fig. 5.16 reports a comparison between the temporal evolution of the period of rotation obtained in this study and the data reported by D'Avino et al. (2008). It is important to notice that D'Avino et al. (2008) employed the upper-convected Maxwell (UCM) constitutive model. While, in simple shear flow, the UCM model predicts the same temporal evolution of the shear and first normal stresses as the Oldroyd-B model (from which it can be derived when $\eta_s = 0$), it does not produce an equivalent slowing effect on the particle rotation rate (Snijkers et al., 2009, 2011). To account for the different final

value of angular velocity, the value of T in Fig. 5.16 was normalised as:

$$T^* = \frac{T - T_0}{T_\infty - T_0} \tag{5.37}$$

where T_0 and T_∞ refer to the initial value of T at time t = 0 and the value of T at the steady state, respectively. The time evolution of the normalised period of rotation indicates again a good agreement between the simulations performed in this study and the data of D'Avino et al. (2008).

It is interesting to notice that the rotation rate dynamics follows the time evolution of the normal stress. This seems to indicate a substantial effect of the normal stresses on the rotation of the sphere. This result, already observed by D'Avino et al. (2008) and Snijkers et al. (2009), is somewhat surprising as one would expect that the rotation of the sphere is mainly governed by the shear component of the fluid stress (that is, the component that exherts a net torque on the particle). On the other hand we can notice that, if the slowing effect was only caused by the buildup of the shear stress, passing from a Newtonian to a viscoelastic fluid with the same total viscosity would not lead to a significant change in the final torque acting on the sphere[d]. Then, the only effect of the viscoelasticity would be a net delay of the onset of tangential stresses around the sphere and a subsequent "retardation" of the rotation dynamics.

The presence of normal stresses strongly influences the pressure and velocity fields around the particle. This fact alone could explain the similarity of behaviour of the time evolution of the first normal stress difference and the rotation period. D'Avino et al. (2008) also suggests that the normal forces are responsible for the loss of symmetry of the streamlines observed at large *De*.

5.3.3 Steady-state results

Streamlines

To give an idea about the changes in flow structure observable in the non-Newtonian case, and to offer a comparison with other results found in the literature, I will now present the streamlines for the Newtonian as well as for the viscoelastic cases. The analysis will be limited to the *x*-*z* plane at $y = 0$. The mirror symmetry of this plane assures that every streamline starting on the *x*-*z* plane, remains on that same plane. This ultimately allows the observation of the flow structures on 2D plots. It is well known that for a single, inertialess sphere in an unbounded Newtonian fluid subject to a linear shear creeping flow ($Re \ll 1$), the *x*-*z* plane can be divided in two separate sub-regions where the streamlines behave in different ways (Cox et al., 1968). In the "inner" region, close to the sphere, the streamlines are represented by an infinite set of closed curves surrounding the sphere.

[d] In both cases the final shear stress acting of the sphere would have an order of magnitude of $\approx \tau_{zx} = \eta_0 \dot{\gamma}$

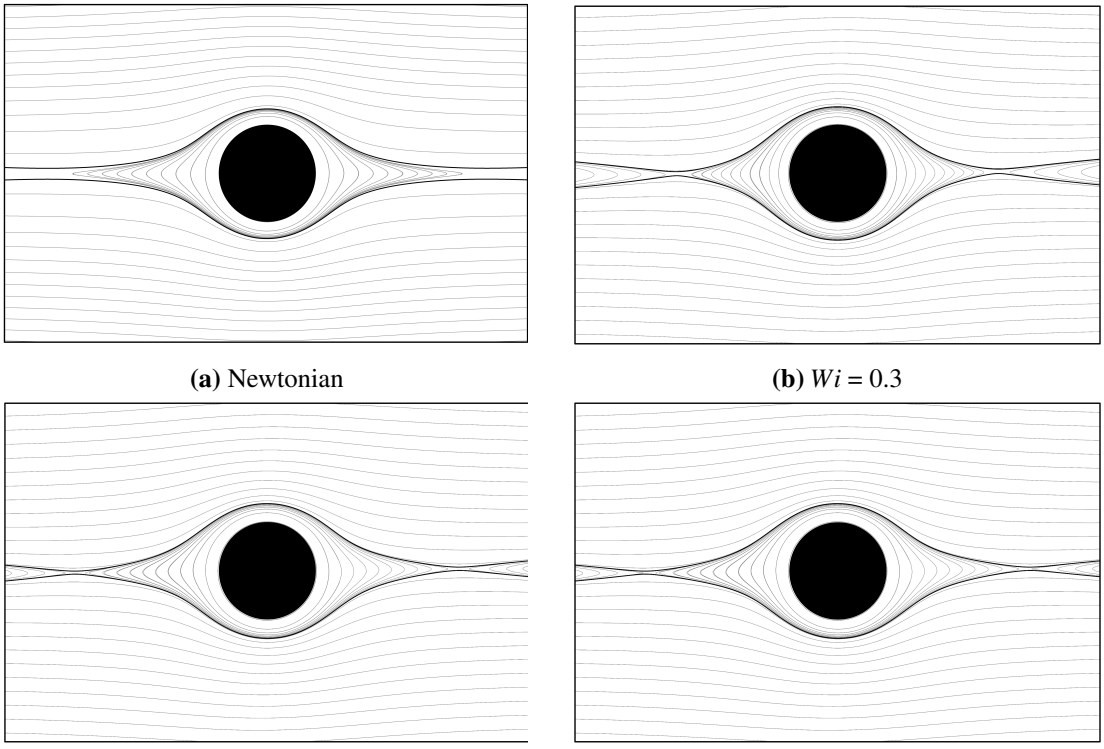

(a) Newtonian **(b)** $Wi = 0.3$

(c) $Wi = 1$ **(d)** $Wi = 3$

Figure 5.17: Streamlines on the x-z plane for Newtonian and viscoelastic case

The zone extends to infinity in both the positive and negative x direction and becomes thinner and thinner moving away from the sphere. In the "outer" region, fluid particles move according to distorted streamlines from left to right, at $z > 0$, and from right to left for $z < 0$. The degree of distortion of the streamlines depends on the proximity to the sphere, with straight streamlines far away from it. The situation just described can be visualized in Fig. 5.17a. The inner and outer regions are separated by a thick black line. For the Stokes flow around the sphere, the flow field is symmetric with respect to the xy (up-down symmetry) and zy (fore-aft symmetry) planes.

In Fig. 5.17b, the streamlines for the viscoelastic case with $Wi = 0.3$ are reported. Despite the low Wi value, a substantial difference can be observed. In particular, the inner zone is now divided in three areas, one surrounding the sphere and two lateral recirculation zones. In the internal area, the flow field is again constituted by closed streamlines surrounding the sphere. However, contrary to the Newtonian case, these streamlines do not extend to infinity but remain confined within a small region around the sphere. The two recirculation zones are located at opposite sides of the sphere, along the x axis. A fluid element within a recirculation zone approaches the solid sphere coming from infinity without ever encountering it. In fact, the trajectory of any streamline within these zones, upon reaching the center of the domain, bends sharply before going back to infinity. The separation between the recirculation and internal zones can be identified in two

saddle points located to the left and right side of the sphere. Notice also that these two saddle points do not lie exactly on the x axis but are shifted downward and upward for $x < 0$ and $x > 0$ respectively. These means that the flow field has lost both its fore-aft and up-down symmetry.

Additional increments in Wi seems to only cause a progressive change in the streamlines. This means that the flow field conserves its overall structure (constituted by the two recirculation, the internal and external zones), while the shapes of the different areas and relative distances change with Wi. The only evident change passing from $Wi = 0.3$ to $Wi = 1$ (Fig. 5.17c) is that the bold line marking the separation between the internal and external areas, moves closer to the sphere. At the same time, the saddle points move away from the sphere along the x direction and slightly upward or downward for the right and left sides respectively. Increasing Wi to 3 has, to a slightly larger extent, a very similar effect to the one just described.

It is worth noticing that the flow field just described, and its behaviour with increasing levels of viscoelasticity, differs from that reported by D'Avino et al. (2008). In particular, the flow field characterized by a four-zones structure, which we observed for any $Wi > 0$, is reported only at $Wi \geq 1$. With the noticeable difference that, within the internal area, D'Avino et al. (2008) report open streamlines spiraling toward a single orbit instead of the bundle of closed streamlines reported here. This discrepancy can be explained by the inadequate value of the blockage ratio, a/L. Figure 5.18 presents the normal components (xx, yy, and zz) of the fluid stress tensor. To normalize the stresses, they have been divided by the value of the first normal stress difference predicted by the Oldroyd-B model, $\tau^*_{ii} = \tau_{ii}/2\eta_p\lambda\dot{\gamma}^2$. This implies that in the absence of any disturbances in the flow, $\tau^*_{xx} = 1$, while $\tau^*_{yy} = \tau^*_{zz} = 0$. As shown in Fig. 5.18a, the xx component of the stress is significantly higher than the other two components and reaches its maximum value (around 4) close to the interface between the solid and liquid. The xx component displays two areas of high stress at the top and bottom of the sphere ($x/L = 0$ and $z/L = \pm a/L$), as well as two elongated symmetric areas of high stress upstream and downstream of the sphere. When moving away from the sphere in the z direction, the stress decreases rapidly from approximately 2.5 at $z/L = \pm a/L$ to 1 at $z/L = \pm 1$. Similarly, the stress also decreases along the x direction, but the fluid never fully relaxes, and at $x/L = \pm 1$, the stress still has a residual value of approximately 2.5. Furthermore, the τ^*_{zz} component of the stress (Fig. 5.18b) remains mostly confined near the sphere. It reaches its maximum value of 0.5 at the interface and quickly drops to zero outside of the region defined by the two intervals $-0.4 \leq x/L \leq 0.4$ and $-0.2 \leq z/L \leq 0.2$. Finally, the τ^*_{yy} component (Fig. 5.18c) takes on positive values at the top and bottom of the sphere, and negative values in two elongated symmetric areas upstream and downstream of the sphere. As with the other components, the stress decreases quickly when moving in the z direction and reaches zero at $z/L \geq 0.3$ and $z/L \leq -0.3$. Along the x direction, the fluid never fully relaxes, and at $x/L = \pm 1$, τ^*_{yy}

is approximately 0.01.

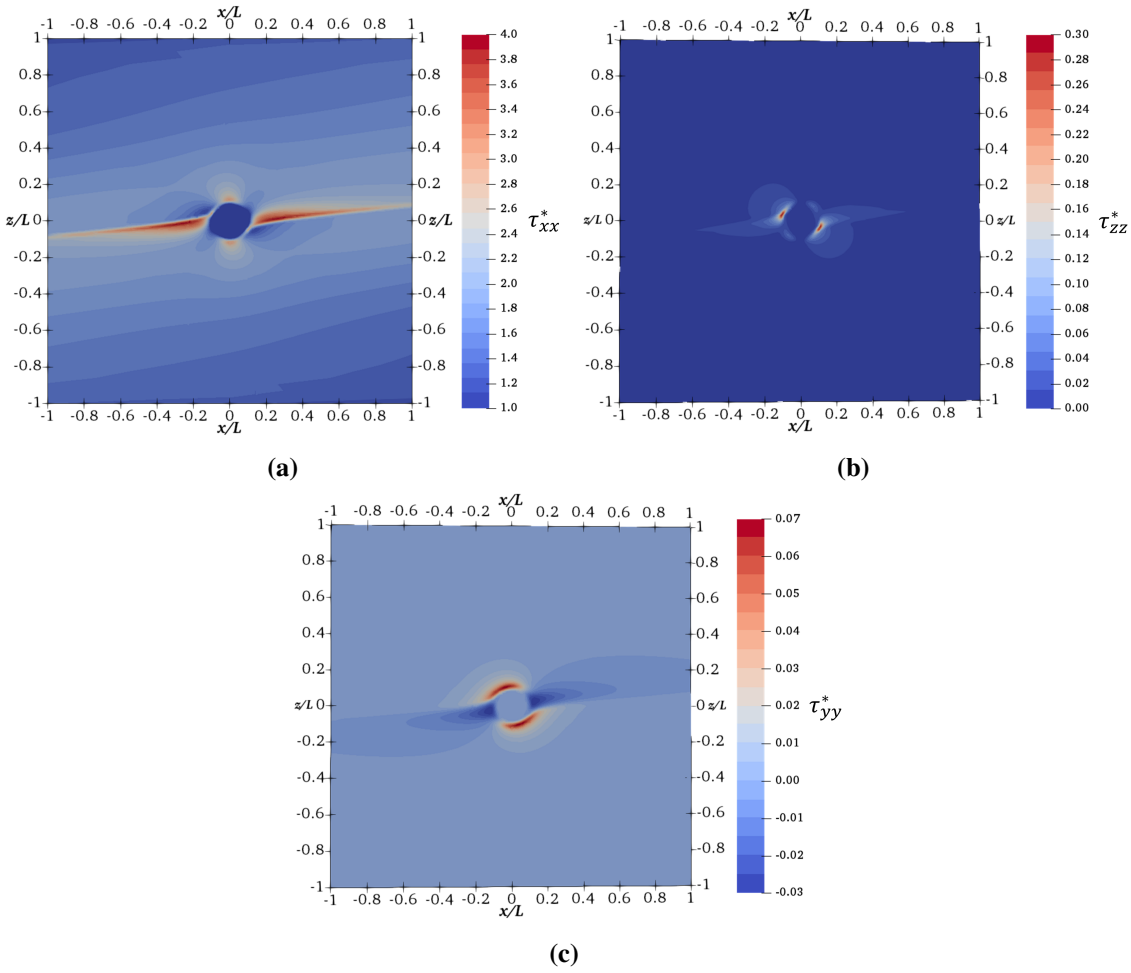

Figure 5.18: Dimensionless normal components of the stress tensor at $Wi = 3$ and blockage ratio $a/L = 0.08$.

The fact that some components of the stress tensor fail to completely relax near the domain boundaries suggests that the imposed boundary conditions may influence the numerical solution around the sphere. To investigate this, an additional simulation was performed with a smaller blockage ratio of $a/L = 0.067$. The mesh structure and boundary conditions were kept the same as those used in the previous simulations. The results for the three stress tensor components are shown in Figure 5.19. It can be observed that the qualitative behaviour and the range of values for all components remain unchanged. However, the significant difference is that now both the τ^*_{zz} and τ^*_{yy} components of the stress become zero when moving away from the sphere along the x direction (see Figs.5.19b and 5.19c). This is not the case for the τ^*_{xx} component (Fig.5.19a), where the two symmetric areas of high stress upstream and downstream of the sphere still extend throughout the entire domain. Nonetheless, the residual value at $x/L = \pm 1$ decreases from 2.5 for $a/L = 0.08$ to approximately 2 for $a/L = 0.067$, indicating a higher degree of fluid stress recovery.

Despite the moderate reduction of blockage ratio, the shape of the streamlines sur-

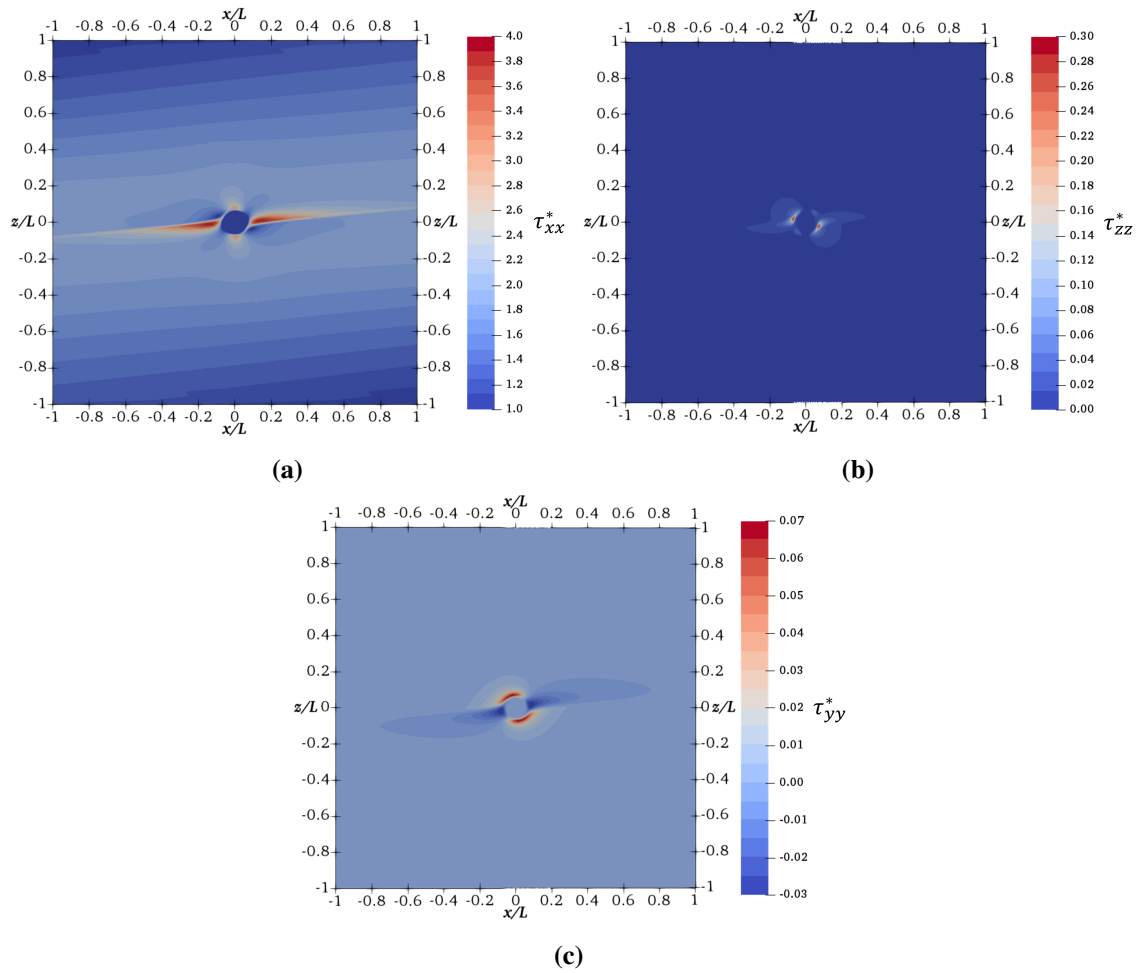

Figure 5.19: Dimensionless normal components of the stress tensor at $Wi = 3$ and blockage ratio $a/L = 0.067$.

rounding the sphere undergoes significant changes, as can be observed from the comparison of Figs.5.20 and 5.17d. For the small blockage ratio, the lateral recirculation areas observed for $a/L = 0.08$ are no longer present, and the flow field is now divided into three distinct areas, marked by the three red curves in Fig.5.20. The "inner" area is the region enclosed by the two external and the internal red curves. A fluid element starting within this area follows a distorted circulation path around the sphere that elongates and tends towards the external delimiting curves (lower and upper red curves). Note that within the internal area in Fig.5.20, only a single streamline has been plotted starting from the point ($x/L = 0.075$ and $z/L = 0$). In the other two areas, above and below the external delimiting curves, the fluid moves along distorted streamlines from left to right, at $z > 0$, and from right to left for $z < 0$. Moreover, the flow field does not exhibit either up-down or left-right symmetry.

These findings differ from those reported by D'Avino et al. (2008) for $W \geq 1$, where the inner area is reported to further split in two zones separated by an attractor curve. Nonetheless, the results obtained at $a/L = 0.067$ appear to be more consistent with the physical behaviour expected for the system. In fact, any distortion of the streamlines

around the sphere arises from the disturbance created by the presence of the sphere. Therefore, it is reasonable to expect that far from the sphere, the flow would recover its undisturbed behaviour. In the case of a simple shear flow, the undisturbed behaviour is characterized by straight streamlines parallel to the direction of the imposed velocity. This condition is not met for the simulations with $a/L = 0.08$, where the two recirculation areas in Fig.5.17d extend until the end of the simulation domain. However, for $a/L = 0.067$, the inner area becomes increasingly narrow as one moves away from the sphere along the x direction until it is no longer visible. Consequently, the flow far from the sphere is again characterized by straight streamlines. These results seem to indicate that, contrary from what reported for the Newtonian case, the accurate simulation of the behaviour of a solid in the unconfined flow of a viscoelastic fluid requires a large blockage ratio (< 0.067).

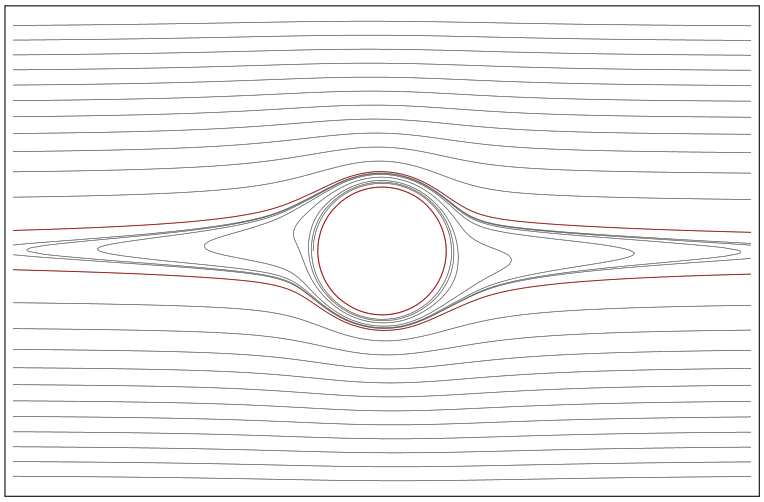

Figure 5.20: Streamlines on the x-z plane at $Wi = 3$ and $a/L = 0.067$.

Angular velocity

Fig. 5.21 shows the results for the prediction of the angular velocity of a solid sphere in an Oldroyd-B fluid as a function of the Weissenberg number. The results are reported in the form of the ratio between $2\omega/\dot{\gamma} = T_N/T_{NN}$. For a Newtonian fluid, this ratio is equal to 1 (Einstein, 1905). As expected, a substantial slowing down of the angular velocity can be observed as Wi increases. The figure also includes numerical data from previous studies by Hwang et al. (2004), Goyal and Derksen (2012), and D'Avino et al. (2008) as well as experimental data reported by Snijkers et al. (2009). These authors employed various numerical schemes to simulate the behaviour of a sphere suspended in an Oldroyd-B fluid, assuming a viscosity ratio of $\eta_s/\eta_p = 1$. Specifically, Hwang et al. (2004) utilized a finite element scheme to directly simulate inertialess particle suspensions in simple shear flow of an Oldroyd-B fluid, employing the sliding bi-periodic frame concept introduced by Lees and Edwards (1972) on a 2D domain. Goyal and Derksen (2012) employed a lattice-

Boltzmann scheme coupled with a finite volume solver to handle the transport equation of the conformation tensor and obtained results up to $Wi = 2$. D'Avino et al. (2017), on the other hand, utilized a finite element scheme within a cubic cell containing a single sphere at its center. The experimental data presented by Snijkers et al. (2009) were obtained by measuring the angular velocity of 49 um polystyrene particles suspended in a solution of high molecular weight PIB (2000 ppm of Oppanol B200, BASF) in a low molecular weight PIB (Infineum S1054, Exxon Chemical). The polymeric suspension exhibited Boger fluid behaviour, characterized by a constant viscosity and a quadratic increase of the first normal stress difference with the shear rate. Therefore, it was possible to model it with the Oldroyd-B constitutive equation.

Upon initial analysis, it is apparent that the data obtained in this study are in agreement with all the numerical results reported in the literature up to a critical value of Wi approximately equal to 2. Up to this value, both the results of this work and all the numerical results reported show a weaker dependency of the angular velocity on Wi. This slight over-prediction of the angular velocity was also discussed by D'Avino et al. (2008) who found that the discrepancy persisted even when modelling the fluid with a single or a multi-modes Giesekus constitutive equation. For Weissenberg numbers (Wi) beyond 2, this results of this study deviate significantly from those reported by Hwang et al. (2004) and D'Avino et al. (2008). Notably, this study shows a more pronounced decrease in angular velocity with increasing Wi, which aligns better with the experimental findings. The exact reason for this discrepancy is not entirely clear. However, it is worth noting that Hwang et al. (2004) conducted their simulations on a two-dimensional domain, while D'Avino et al. (2008) simulated only one quarter of the domain in three dimensions, utilizing symmetry boundary conditions along the $y-z$ and $x-y$ planes (see Fig. 2). It is possible that the imposed forced symmetry of the flow field in both cases contributes to the deviation from the experimental results. It is worth noting that all the angular velocity results presented in this section were obtained with a blockage ratio of $a/L = 0.08$. However, as explained above, an additional simulation was conducted at $Wi = 3$ with a lower blockage ratio of $a/L = 0.067$. The results of this simulation are not included in Fig. 5.21 as they yielded an identical value to the one obtained at $Wi = 3$ with $a/L = 0.08$.

5.3.4 Conclusions

In this chapter, we reported our results on the use of the VOF for the simulation of a solid sphere suspended in an unbounded viscoelastic fluid and subject to a simple shear. The scope was to provide a proof of concept for the use of the multiphase algorithm `rheoInterFoam`, for the simulation of the dynamics of a solid particle in a non-Newtonian fluid.

Initially, 2D simulations were carried out, where both the sphere and the suspending

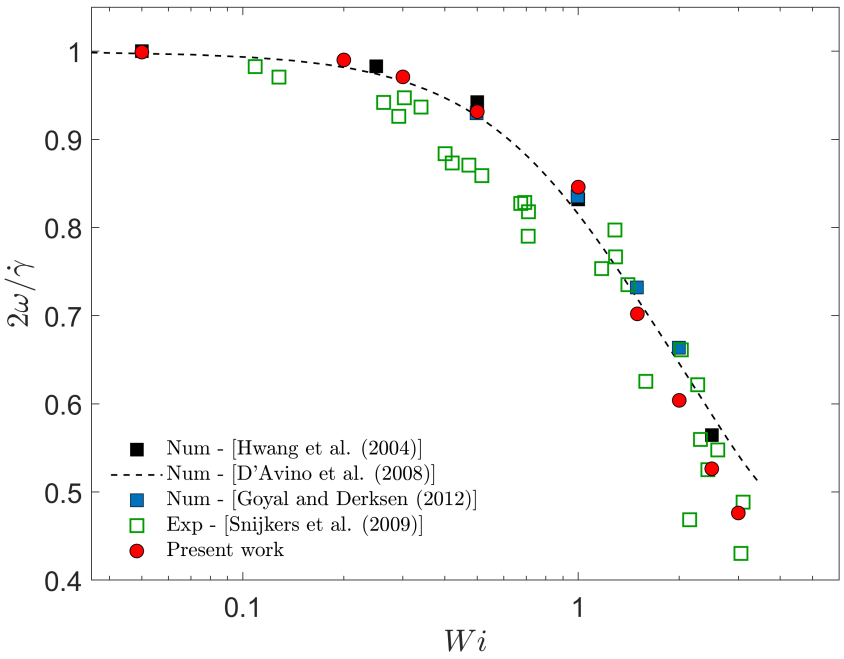

Figure 5.21: Results of the rotational velocity of a solid sphere in an Oldroyd-B fluid as a function of Wi and comparison with available literature.

phase were modelled as Newtonian fluids. This preliminary study was used to assess the possibility of simulating a solid sphere as a fluid phase with a high viscosity and interfacial tension. The results show that by carefully choosing the value of the viscosity ratio β and the Capillary number Ca, it was possible to assure the sphericity of the fluid droplet and the absence of internal circulation throughout the entire simulation. The Newtonian case was also used to perform a grid independence study that was subsequently extended to the three-dimensional, viscoelastic case.

The simulations for the viscoelastic case were performed using the Oldroyd-B constitutive equation to model the suspending fluid. The simulations were performed on a three-dimensional grid with a Weissenberg number varying between 0 and 3. As expected, increasing the viscoelasticity of the flow (i.e. increasing Wi), resulted in an increase of the rotational period of the sphere. This result was in agreement with the available literature. Furthermore, the analysis of the time evolution of the angular velocity of the sphere and both the shear and normal stresses of the suspending fluid, revealed that the slowing effect on rotation rate was strongly influenced by the buildup of normal stresses. Additionally, the analysis of the streamlines around the sphere revealed that, at high Wi, the values of blockage ratios a/L suggested in the literature are insufficient to completely neglect the effect of the imposed boundary conditions on the flow field around the sphere. Finally, a comparison of the predicted angular velocity with the available literature showed a good agreement with the numerical data reported in the literature up to $Wi = 2$. Above this value, the results of this work deviate from previously published numerical results but

show a better agreement with experimental data. The reason for the disagreement is not clear, but one potential explanation is that, at high Wi, the flow field around the sphere becomes highly distorted and loses its symmetry with respect to the $x-y$ and $y-z$ observed in the limit of $W \to 0$. The use of a two-dimensional domain (as in Hwang et al. (2004)) or the imposition of symmetry boundary conditions (as in D'Avino et al. (2008)) may then lead to deviations from experimental results.

The preliminary results reported here, indicate that the suggested procedure is promising. It allows the setup of flow problems involving multiple phases, in a fast and reliable way without the necessity of dealing with moving boundaries. More work is necessary to verify the capability of this method to simulate more complex flow geometry and/or more complex rheological behaviours.

Chapter 6

Conclusions and future work

6.1 Conclusions

The primary objective of this research was to examine the mixing of solid particles in highly viscous, non-Newtonian fluids within stirred vessels. The focus was particularly on the segregation of the solid phase observed when suspending solids in viscoelastic liquids. The phenomenon was initially encountered during an experimental campaign described in Chapter 3, where the dynamics of solid particles dispersed in highly viscous, non-Newtonian fluids under agitation in a stirred vessel were studied using a mixing system based on a previously investigated design for a toothpaste manufacturing mixer by Cortada et al. (2018). The study aimed to correlate the migration phenomenon with the viscoelastic nature of the suspending fluids and determine its direction and intensity based on relevant rheological and fluid dynamic factors.

The results revealed that in a Newtonian ambient fluid, particles disperse uniformly in the flow, whereas in strongly shear-thinning and/or viscoelastic ambient fluids, particles tend to accumulate in the core of the vortices formed in the flow domain. The migration of solids towards the vortex core was also observed in purely viscoelastic (Boger) fluids, indicating that fluid viscoelasticity alone causes cross-flow migration. Furthermore, the characteristic velocity of migration, determined by the measurement of the characteristic migration time, was found to depend on the intensity of flow elasticity, characterized by the Weissenberg number (Wi). Finally, a plausible migration dynamics was proposed, consistent with the distribution of shear rates inside the tank.

To the best of the author's knowledge, the observations in Chapter 3 represent the first identification of viscoelasticity-induced particle migration in stirred vessels. Therefore, further investigations of this phenomenon were warranted. However, limitations associated with the experimental apparatus employed in Chapter 3 hindered the quantitative correlation between migration velocity and the elastic character of the flow. Additionally, the complex geometry of the mixing system only allowed intuitive inference of parti-

cle dynamics and prevented precise characterization of the flow in terms of its principal directions of strain.

Consequently, the research was expanded as detailed in Chapter 4. This chapter focused on experimentally investigating the dynamics of solid particles agitated by a Rushton turbine using Particle Image Velocimetry (PIV) and Particle Tracking Velocimetry (PTV) techniques. The simplicity of the impeller geometry facilitated accurate measurements of the three-dimensional flow field, which could be analyzed in terms of its principal directions of strain. The complete knowledge of the velocity field was combined with a thorough rheological characterization of the fluids, accounting for shear-induced polymer degradation, to validate the predictions of a scaling law. The scaling law, derived through heuristic reasoning, correlated the characteristic migration velocity with fluid rheological parameters (polymer viscosity and relaxation time) and the scale of shear rate in the tank. A good agreement between experimental results and scaling law predictions was observed, suggesting the applicability of the law as a design tool.

Finally, Chapter 5 presents a separate yet relevant study on the development of a Computational Fluid Dynamics (CFD) method for simulating the dynamics of solids suspended in viscoelastic fluids. The approach was validated against a well-documented case study involving a solid particle placed at the center of a simple shear flow between parallel plates. The selection of this case study was based on its conceptual simplicity and the availability of experimental and computational data in the literature. The proposed approach utilized the open-source CFD code OpenFOAM, known for its robustness and flexibility, as the foundation for the VOF-based method. Although other successful approaches exist for simulating similar systems, a consensus on the optimal computational tools for addressing such problems is still lacking. This work focused on a VOF-based CFD approach capable of simulating the dynamics of a single solid particle suspended in a viscoelastic fluid. In this method, both phases of a biphasic system are treated as fluids with their own physical properties (density, viscosity, interfacial tension, etc.). The interface position is tracked by solving a transport equation for the volume fraction of one of the phases. Initially, considerable effort was dedicated to determining the parameter space where the assumed equivalence between a solid sphere and a highly viscous liquid drop holds true. A parametric study revealed that this equivalence remains valid as long as the viscosity ratio (i.e., viscosity of the dispersed phase divided by the viscosity of the suspending phase) is larger than 10^4, and the capillary number (Ca) is less than or equal to 0.01.

Subsequently, simulations were performed for the viscoelastic case using the Oldroyd-B constitutive equation to model the suspending fluid. Three-dimensional grids were employed, with the Weissenberg number (Wi) varying between 0 and 3. As expected, increasing the viscoelasticity of the flow (i.e., increasing Wi) led to an increase in the rotational period of the sphere, consistent with existing literature. Additionally, analysis of

the streamlines around the sphere indicated that at high Wi, the recommended blockage ratios (i.e., the ratio between the radius of the sphere and the size of the computational domain) found in the literature are insufficient to neglect the influence of imposed boundary conditions on the flow field around the sphere. Finally, a comparison of the predicted angular velocity with available literature showed good agreement with numerical data reported in the literature up to $Wi = 2$. Beyond this value, the results diverged from previously published numerical results but exhibited better agreement with the available experimental data. The preliminary results presented in Chapter 5 demonstrate the promise of the proposed procedure, enabling the setup of flow problems involving multiple phases in a fast and reliable manner without the need to handle moving boundaries.

In conclusion, this research aimed to investigate the mixing of solids in highly viscous, non-Newtonian fluids in stirred vessels, with a focus on the segregation of solid particles in viscoelastic liquids. The findings in Chapter 3 provided the first observations of viscoelasticity-induced particle migration in stirred vessels. Subsequent chapters expanded on these observations, exploring the dynamics of solid particles under agitation and developing computational methods for simulating their behaviour in viscoelastic fluids. The experimental and numerical results obtained contribute to a better understanding of particle migration phenomena and offer valuable insights for designing efficient mixing systems in various industrial applications.

6.2 Future work

Although this work has achieved important steps towards the understanding of the phenomenon of viscoelasticity-induced particle migration in stirred vessels, it also raised new research challenges.

Migration in stirred tanks

In the context of stirred vessels, there are two distinct directions that can be pursued regarding the segregation of the solid phase.

For conventional mixing operations where the dispersion of the solid phase and homogeneity are desired outcomes, further experimental campaigns using realistic mixing systems with industry-standard impellers can be conducted. This would involve exploring a wider range of operating conditions, including variations in impeller-tank configurations, impeller speeds, and properties of the involved phases. By identifying the conditions that lead to particle clustering and segregation, recommendations can be made to mitigate these issues. This may involve suggesting alternative impeller designs, adjusting impeller speeds, or considering the implementation of discontinuous transient mixing regimes. The goal would be to optimize mixing performance and achieve uniform dispersion of solids.

In the context of separation devices, where segregation is desired, future research can focus on harnessing the viscoelasticity-induced particle migration for solid separation. Building upon previous work on Newtonian liquid-solid systems (Wang et al., 2014), experimental investigations can be conducted to explore the potential of viscoelastic systems for efficient separation. The emphasis should be on "difficult-to-separate suspensions" characterized by small density differences, high viscosity, and small-sized particles. The design of batch or continuous separation processes can be explored, with the continuous approach offering advantages in terms of process intensification. Optimal impeller shapes, impeller-tank configurations, and operational parameters for effective separation can be identified through experimental campaigns. A comparison with existing separation processes in terms of speed, effectiveness, and cost/energy efficiency could also provide valuable insights for practical implementation.

Volume Of Fluids computational methods

In future research, there are several directions to explore regarding the application of the Volume of Fluid (VOF) method for simulating the dynamics of solids in viscoelastic fluids. These investigations aim to enhance the understanding and applicability of the VOF-based Computational Fluid Dynamics (CFD) approach.

One area of focus is to examine other simple flow systems, such as Taylor-Couette flow or Poiseuille flow. These flow configurations offer well-defined, unidirectional flows, providing a controlled environment to study the migration of solids in viscoelastic fluids. By comparing simulation results with existing numerical and experimental data, the accuracy and reliability of the VOF method can be assessed, validating its capability to capture the migration phenomenon in these simpler flow cases.

To approach the complexity of flows encountered in stirred vessels, it is important to extend the analysis to non-unidirectional flows. Noticeably, stirred vessels involve complex, three-dimensional flow patterns due to impeller shape, presence of baffles, and vessel geometries. To comprehend the complex behaviour of solid in stirred vessels, it is crucial to gradually progress from simple to moderately complex flow configurations. Rather than directly simulating stirred vessels, an intermediate step could involve exploring non-unidirectional flows that possess a moderate level of complexity such as flow in non circular channels. These flow scenarios incorporate additional flow components, such as secondary flows or recirculation zones, while remaining simpler than stirred vessels. By employing the VOF method to simulate these intermediate flows, one could gain insights into the interplay between flow characteristics and solid migration.

Another aspect to consider is the simulation of multiple particle systems. By starting with two-particle systems, the interactions between solid particles, particularly their hydrodynamic interactions, can be examined. This analysis involves studying the effects of particle concentration, size, and shape on the migration behaviour. Understanding the

dynamics of multiple particles and their interactions within viscoelastic fluids is crucial for designing processes involving multiple solid phases.

Additionally, it is essential to evaluate the performance of the VOF method with various constitutive equations. While the Oldroyd-B constitutive equation was used in this study, other viscoelastic models exist in the literature. Applying alternative, more realistic constitutive equations to simple flow problems, such as Taylor-Couette or Poiseuille flows, could enable the assessment of the ability of the VOF method to handle different rheological behaviours and predict experimental results conducted with real fluids. This investigation would provide insights into the versatility and applicability of the VOF method for a broader range of viscoelastic fluids encountered in practical applications.

In summary, future work should focus on expanding the application of the VOF method in simulating solids suspended in viscoelastic fluids. This can be achieved by examining simpler flow problems to validate accuracy of the method and reliability. Furthermore, investigating non-unidirectional flows resembling those found in stirred vessels will provide insights into the behaviour of solids in realistic flow fields. Additionally, studying multiple particle systems and exploring different constitutive equations will enhance the capabilities of the method and broaden its applicability. These efforts would contribute to the development of the VOF method as a robust tool for simulating and comprehending the dynamics of solids in viscoelastic fluid systems.

Appendix A

Support material to chapter 4

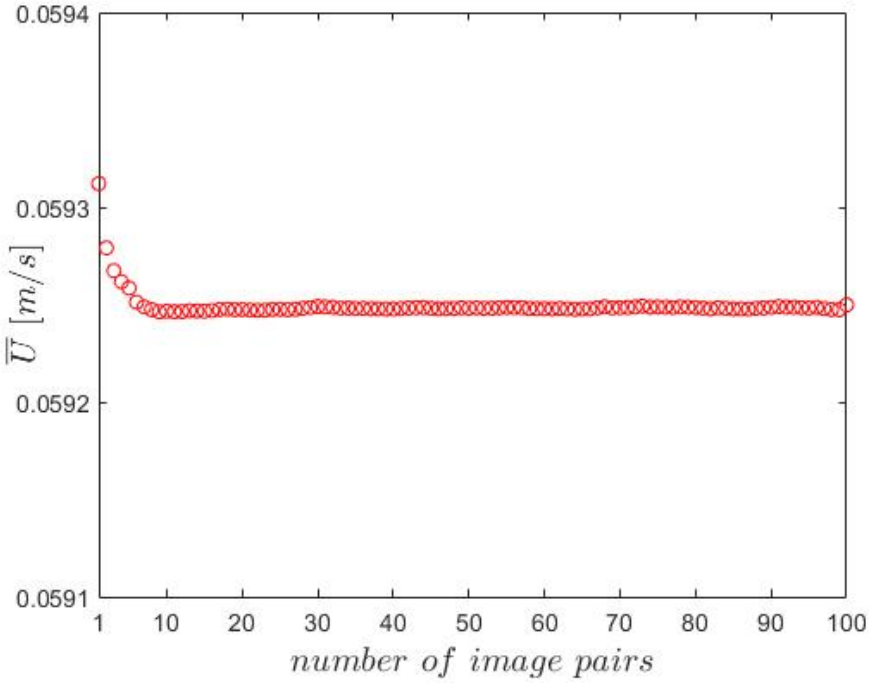

Figure A.1: Convergence plot for the average velocity on the horizontal plane $Z/T = 0.48$ for the fluid RI_{100} at $Re = 4.3$ and $Wi = 0.4$, as function of the sample size. The plane at $Z/T = 0.48$ was chosen as worst case scenario as the convergence of the average planar velocity appears to be faster for all the others horizontal and vertical planes.

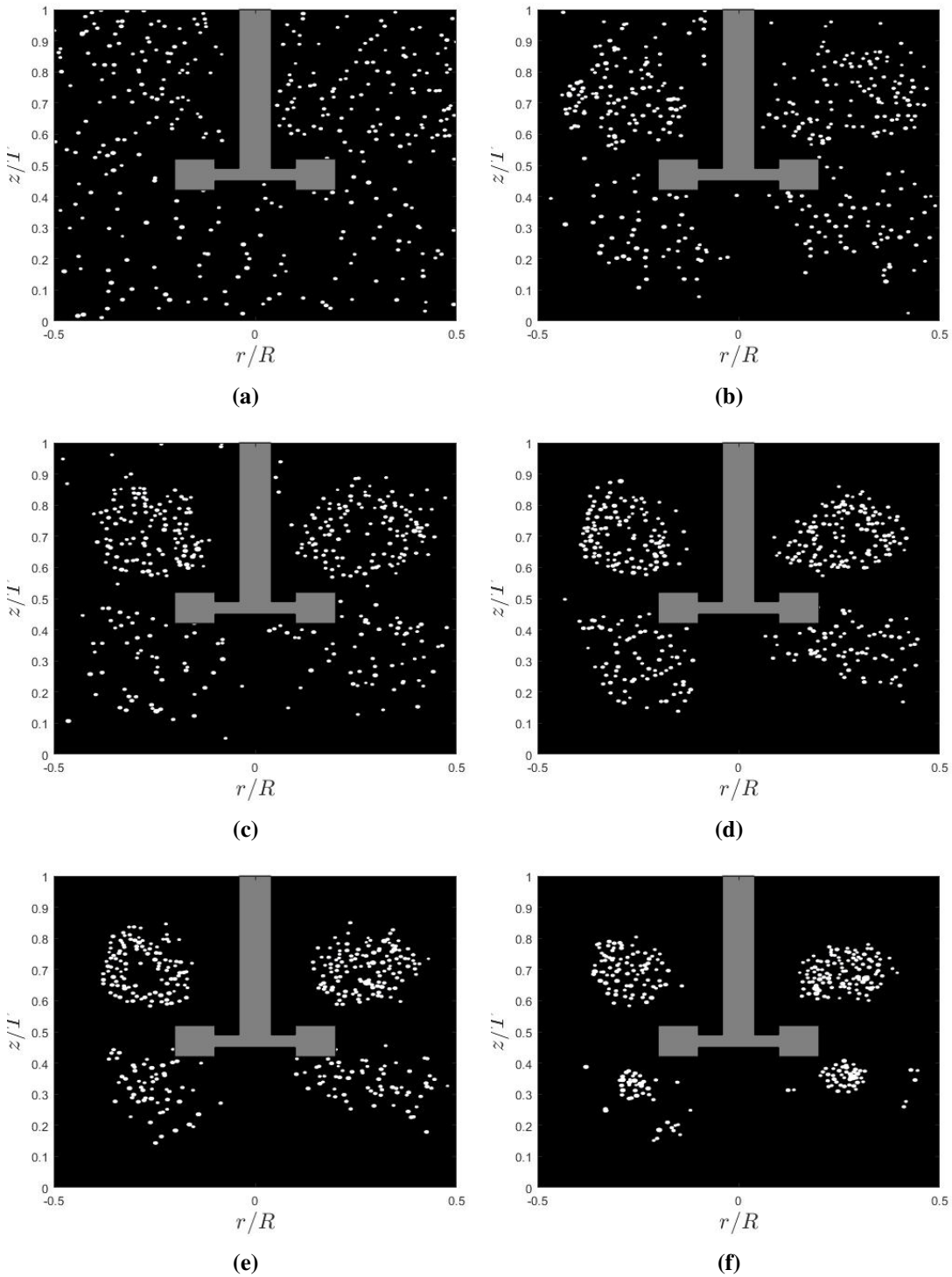

Figure A.2: Time evolution of the particles positions on the horizontal plane for the fluid RI_{100} at $Wi = 0.35$.

Appendix B

Support material to chapter 5

Listing B.1: `transportProperties`

```
// * * * * * * * * * * * * * * * * * * * * * * * * * * * * * * * * * * * * * * * * * * //

phases (water air);

water
{
    transportModel  Newtonian;
    nu              1;
    rho             1;
}

air
{
    transportModel  Newtonian;
    nu              10000;
    rho             1;
}

sigma           0.0032;

// ************************************************************************* //
```

Listing B.2: `blockMeshDict`

```

convertToMeters 1;

vertices
(
    ( -0.075 -0.075 -0.075)
    (  0.075 -0.075 -0.075)
    (  0.075  0.075 -0.075)
    ( -0.075  0.075 -0.075)
    ( -0.075 -0.075  0.075)
    (  0.075 -0.075 0.075)
    (  0.075 0.075 0.075)
    ( -0.075 0.075 0.075)
);

nx = 150
blocks
```

```
(
    hex (0 1 2 3 4 5 6 7) (nx nx nx)
    simpleGrading (
      (
                (0.35 0.2 2)   // 35% x-dir, 20% cells, expansion = 2
                (0.15 0.3 1)
      (0.15 0.3 1)   // 30% x-dir, 60% cells, expansion = 1
                (0.35 0.2 0.5) // 35% x-dir, 20% cells, expansion = 1/2
            )

      (
                (0.35 0.2 2)   // 35% x-dir, 20% cells, expansion = 2
                (0.15 0.3 1)
      (0.15 0.3 1)   // 30% x-dir, 60% cells, expansion = 1
                (0.35 0.2 0.5) // 35% x-dir, 20% cells, expansion = 1/2
            )
            (
                (0.35 0.2 2)   // 35% x-dir, 20% cells, expansion = 2
                (0.15 0.3 1)
      (0.15 0.3 1)   // 30% x-dir, 60% cells, expansion = 1
                (0.35 0.2 0.5) // 35% x-dir, 20% cells, expansion = 1/2
            )
      )
);

edges
(
);

boundary
(
    upperWall
    {
        type wall;
        faces
        (
            (3 7 6 2)
        );
    }
    lowerWalls
    {
        type wall;
        faces
        (
            (0 4 5 1)
        );
    }

  left
    {
        type  patch;
        faces ((0 4 7 3));
    }

  right
    {
        type  patch;
        faces ((1 2 6 5));
    }

    front
    {
```

```
  type            symmetry;
        faces ((4 5 6 7));
    }

    back
    {
  type  symmetry;
        faces ((0 3 2 1));
    }

);

mergePatchPairs
(
);

// ************************************************************************* //
```

Listing B.3: `tau.water`

```

dimensions      [1 -1 -2 0 0 0 0];

internalField   uniform (0 0 0 0 0 0);

boundaryField
{

    upperWall
    {

  type            zeroGradient;

    }

    lowerWalls
    {

  type            zeroGradient;


    }

    left
    {
  type            linearExtrapolation;
        value           uniform (0 0 0 0 0 0);

    }

    right
    {
  type            linearExtrapolation;
        value           uniform (0 0 0 0 0 0);

    }
    front
    {
        type            symmetry;

    }
    back
```

```
    {
        type            symmetry;

    }
}

// ************************************************************************* //
```

Listing B.4: `theta.water`

```

dimensions      [ 0 0 0 0 0 0 0];

internalField   uniform (0 0 0 0 0 0);

boundaryField
{

    upperWall
    {

  type            zeroGradient;

    }

    lowerWalls
    {


  type            zeroGradient;

    }

    left
    {
  type            linearExtrapolation;
        value           uniform (0 0 0 0 0 0);

    }

    right
    {
  type            linearExtrapolation;
        value           uniform (0 0 0 0 0 0);

    }
    front
    {
        type            symmetry;

    }
    back
    {
        type            symmetry;

    }

}

// ************************************************************************* //
```

Bibliography

Abed, W. M., Whalley, R. D., Dennis, D. J., and Poole, R. J. (2016). Experimental investigation of the impact of elastic turbulence on heat transfer in a serpentine channel. *Journal of Non-Newtonian Fluid Mechanics*, 231:68–78.

Adrian, R. J. (1984). Scattering particle characteristics and their effect on pulsed laser measurements of fluid flow: speckle velocimetry vs particle image velocimetry. *Applied optics*, 23(11):1690–1691.

Afonso, A., Oliveira, P., Pinho, F., and Alves, M. (2009). The log-conformation tensor approach in the finite-volume method framework. *Journal of Non-Newtonian Fluid Mechanics*, 157(1):55–65.

Afonso, A., Pinho, F., and Alves, M. (2012). The kernel-conformation constitutive laws. *Journal of Non-Newtonian Fluid Mechanics*, 167:30–37.

Alves, M., Oliveira, P., and Pinho, F. (2021). Numerical methods for viscoelastic fluid flows. *Annual Review of Fluid Mechanics*, 53:509–541.

Anderson, D. M., McFadden, G. B., and Wheeler, A. A. (1998). Diffuse-interface methods in fluid mechanics. *Annual review of fluid mechanics*, 30(1):139–165.

Astruc, M., Vervoort, S., Nouatin, H. O., Coupez, T., De Puydt, Y., Navard, P., and Peuvrel-Disdier, E. (2003). Experimental and numerical study of the rotation and the erosion of fillers suspended in viscoelastic fluids under simple shear flow. *Rheologica Acta*, 42(5):421 – 431. Cited by: 16.

Atherton, T. and Kerbyson, D. (1999). Size invariant circle detection. *Image and Vision Computing*, 17(11):795–803.

Atiemo-Obeng, V. A., Kresta, S. M., and Paul, E. L. (2004). *Handbook of Industrial Mixing*. John Wiley & Sons, Incorporated.

Badalassi, V. E., Ceniceros, H. D., and Banerjee, S. (2003). Computation of multiphase systems with phase field models. *Journal of computational physics*, 190(2):371–397.

Balci, N., Thomases, B., Renardy, M., and Doering, C. R. (2011). Symmetric factorization of the conformation tensor in viscoelastic fluid models. *Journal of Non-Newtonian Fluid Mechanics*, 166(11):546–553.

Bartok, W. and Mason, S. (1958). Particle motions in sheared suspensions: Vii. internal circulation in fluid droplets (theoretical). *Journal of colloid science*, 13(4):293–307.

Bartok, W. and Mason, S. (1959). Particle motions in sheared suspensions: Viii. singlets and doublets of fluid spheres. *Journal of Colloid Science*, 14(1):13–26.

Bartram, E., Goldsmith, H., and Mason, S. (1975). Particle motions in non-newtonian media - iii. further observations in elasticoviscous fluids. *Rheologica Acta*, 14(9):776 – 782. Cited by: 81.

Bastiaans, R. J. (2000). *Cross-correlation PIV; theory, implementation and accuracy*. Eindhoven University of Technology, Faculty of Mechanical Engineering.

Benson, D. J. (2002). Volume of fluid interface reconstruction methods for multi-material problems. *Appl. Mech. Rev.*, 55(2):151–165.

Bertrand, O., Blais, B., Bertrand, F., and Fradette, L. (2018). Complementary methods for the determination of the just-suspended speed and suspension state in a viscous solid–liquid mixing system. *Chemical Engineering Research and Design*, 136:32–40.

Bird, R. B., Armstrong, R. C., and Hassager, O. (1987a). Dynamics of polymeric liquids. vol. 1: Fluid mechanics.

Bird, R. B., Armstrong, R. C., and Hassager, O. (1987b). Dynamics of polymeric liquids, volume 2: Kinetic theory.

Bouremel, Y., Yianneskis, M., and Ducci, A. (2009). Three-dimensional deformation dynamics of trailing vortex structures in a stirred vessel. *Industrial & engineering chemistry research*, 48(17):8148–8158.

Brackbill, J., Kothe, D., and Zemach, C. (1992). A continuum method for modeling surface tension. *Journal of Computational Physics*, 100(2):335–354.

Brandani, G. B., Schor, M., MacPhee, C. E., Grubmüller, H., Zachariae, U., and Marenduzzo, D. (2013). Quantifying disorder through conditional entropy: An application to fluid mixing. *PLoS ONE*, (8):6.

Brevis, W., Niño, Y., and Jirka, G. H. (2011). Integrating cross-correlation and relaxation algorithms for particle tracking velocimetry. *Experiments in Fluids*, (50):135–147.

Brunn, P. (1976a). The behavior of a sphere in non-homogeneous flows of a viscoelastic fluid. *Rheologica Acta*, 15(11-12):589–611.

Brunn, P. (1976b). The slow motion of a sphere in a second-order fluid. *Rheologica Acta*, 15(3-4):163 – 171. Cited by: 44.

Camesasca, M., Kaufman, M., and Manas-Zloczower, I. (2006). Quantifying fluid mixing with the shannon entropy. *Macromolecular Theory and Simulations*, (8):595–607.

Carletti, C., Montante, G., Westerlund, T., and Paglianti, A. (2014). Analysis of solid concentration distribution in dense solid–liquid stirred tanks by electrical resistance tomography. *Chemical Engineering Science*, 119:53–64.

Charalambidou, A.-D., Micheletti, M., and Ducci, A. (2023). Study of trailing vortices and impeller jet instabilities of a flat blade impeller in small-scale reactors. *AIChE Journal*, 69(2):e17842.

Chhabra, R. and Richardson, J. (2008). Chapter 1 - non-newtonian fluid behaviour. In Chhabra, R. and Richardson, J., editors, *Non-Newtonian Flow and Applied Rheology (Second Edition)*, pages 1–55. Butterworth-Heinemann, Oxford, second edition edition.

Cortada Garcia, M. (2018). *Mixing of complex oral health products: experimental and computational fluid dynamics investigations*. PhD thesis, UCL (University College London).

Cortada-Garcia, M., Weheliye, W. H., Dore, V., Mazzei, L., and Angeli, P. (2018). Computational fluid dynamic studies of mixers for highly viscous shear thinning fluids and piv validation. *Chemical Engineering Science*, 179:133–149.

Cox, R. (1969). The deformation of a drop in a general time-dependent fluid flow. *Journal of fluid mechanics*, 37(3):601–623.

Cox, R., Zia, I., and Mason, S. (1968). Particle motions in sheared suspensions xxv. streamlines around cylinders and spheres. *Journal of Colloid and Interface Science*, 27(1):7–18.

D'Avino, G., Greco, F., and Maffettone, P. L. (2017). Particle migration due to viscoelasticity of the suspending liquid and its relevance in microfluidic devices. *Annual Review of Fluid Mechanics*, 49(1):341–360.

Davoodi, M., Houston, G., Downie, J., Oliveira, M. S., and Poole, R. J. (2021). Stabilization of purely elastic instabilities in cross-slot geometries. *Journal of Fluid Mechanics*, 922:A12.

Del Giudice, F., Haward, S. J., and Shen, A. Q. (2017). Relaxation time of dilute polymer solutions: A microfluidic approach. *Journal of Rheology*, 61(2):327–337.

Derksen, J. (2012). Highly resolved simulations of solids suspension in a small mixing tank. *AIChE journal*, 58(10).

Deshpande, S. S., Anumolu, L., and Trujillo, M. F. (2012). Evaluating the performance of the two-phase flow solver interfoam. *Computational Science & Discovery*, 5(1):14–16.

Dickey, D. S. (2015). Tackling difficult mixing problems. *Chemical Engineering Progress*, 111(8):35–42.

Ding, H., Spelt, P. D., and Shu, C. (2007). Diffuse interface model for incompressible two-phase flows with large density ratios. *Journal of Computational Physics*, 226(2):2078–2095.

D'Avino, G., Hulsen, M. A., Snijkers, F., Vermant, J., Greco, F., and Maffettone, P. L. (2008). Rotation of a sphere in a viscoelastic liquid subjected to shear flow. part i: Simulation results. *Journal of Rheology*, 52(6):1331–1346.

D'Avino, G. and Maffettone, P. (2015). Particle dynamics in viscoelastic liquids. *Journal of Non-Newtonian Fluid Mechanics*, 215:80–104.

D'Avino, G., Snijkers, F., Pasquino, R., Hulsen, M., Greco, F., Maffettone, P., and Vermant, J. (2012). Migration of a sphere suspended in viscoelastic liquids in couette flow: experiments and simulations. *Rheologica acta*, 51:215–234.

Einstein, A. (1905). Eine neue bestimmung der moleküldimensionen. *Ann. d. Phys.*, 17.

Einstein, A. (1911). Berichtigung zu meiner arbeit: Eine neue bestimming der moleküldimensionen. *Ann. d. Phys.*, 19.

Escalante-Velázquez, C., Rosas, I., Reyes, M., and Geffroy, E. (2018). Cox modified model to describe the time evolution of a drop deformation for high viscosity drops in simple shear flow. *International Journal of Multiphase Flow*, 103:78–84.

Fattal, R. and Kupferman, R. (2004). Constitutive laws for the matrix-logarithm of the conformation tensor. *Journal of Non-Newtonian Fluid Mechanics*, 123(2):281–285.

Fattal, R. and Kupferman, R. (2005). Time-dependent simulation of viscoelastic flows at high weissenberg number using the log-conformation representation. *Journal of Non-Newtonian Fluid Mechanics*, 126(1):23–37.

Fernandes, C. (2022). A fully implicit log-conformation tensor coupled algorithm for the solution of incompressible non-isothermal viscoelastic flows. *Polymers*, 14(19).

Flory, P. J. (1953). *Principles of polymer chemistry*. Cornell university press.

Frédéric, A., Olivier, M., and Pascal, G. (2003). Slip velocity and drag law in a liquid-liquid homogeneous dispersed flow. *AIChE journal*, 49(9).

Gabriele, A., Tsoligkas, A., Kings, I., and Simmons, M. (2011). Use of piv to measure turbulence modulation in a high throughput stirred vessel with the addition of high stokes number particles for both up-and down-pumping configurations. *Chemical engineering science*, 66(23):5862–5874.

Gauthier, F., Goldsmith, H., and Mason, S. (1971a). Particle motions in non-newtonian media - i: Couette flow. *Rheologica Acta*, 10(3):344 – 364. Cited by: 147.

Gauthier, F., Goldsmith, H., and Mason, S. (1971b). Particle motions in non-newtonian media. part ii: Poiseuille flow. *J Rheol*, 15:297. Cited by: 2.

Gibou, F., Fedkiw, R., and Osher, S. (2018). A review of level-set methods and some recent applications. *Journal of Computational Physics*, 353:82–109.

Gong, H., Huang, F., Li, Z., Gao, Z., and Derksen, J. (2018). Mechanisms for drawdown of floating particles in a laminar stirred tank flow. *Chemical Engineering Journal*, 346:340–350.

Goyal, N. and Derksen, J. (2012). Direct simulations of spherical particles sedimenting in viscoelastic fluids. *Journal of Non-Newtonian Fluid Mechanics*, 183-184:1–13.

Greco, F., D'Avino, G., and Maffettone, P. L. (2005). Stress tensor of a dilute suspension of spheres in a viscoelastic liquid. *Phys. Rev. Lett.*, 95:246001.

Greco, F., D'Avino, G., and Maffettone, P. (2007). Rheology of a dilute suspension of rigid spheres in a second order fluid. *Journal of Non-Newtonian Fluid Mechanics*, 147(1):1–10.

Grmela, M. and Carreau, P. (1987). Conformation tensor rheological models. *Journal of Non-Newtonian Fluid Mechanics*, 23:271–294.

Guida, A., Fan, X., Parker, D., Nienow, A., and Barigou, M. (2009). Positron emission particle tracking in a mechanically agitated solid–liquid suspension of coarse particles. *Chemical Engineering Research and Design*, 87(4):421–429.

Guida, A., Nienow, A. W., and Barigou, M. (2010). Pept measurements of solid–liquid flow field and spatial phase distribution in concentrated monodisperse stirred suspensions. *Chemical Engineering Science*, 65(6):1905–1914.

Guiraud, P., Costes, J., and Bertrand, J. (1997). Local measurements of fluid and particle velocities in a stirred suspension. *Chemical Engineering Journal*, 68(2-3):75–86.

Harrison, S. T., Stevenson, R., and Cilliers, J. J. (2012). Assessing solids concentration homogeneity in rushton-agitated slurry reactors using electrical resistance tomography (ert). *Chemical engineering science*, 71:392–399.

Hill, D., Sharp, K., and Adrian, R. (2000). Stereoscopic particle image velocimetry measurements of the flow around a rushton turbine. *Experiments in Fluids*, 29(5):478–485.

Hirt, C. W. and Nichols, B. D. (1981). Volume of fluid (vof) method for the dynamics of free boundaries. *Journal of computational physics*, 39(1):201–225.

Ho, B. and Leal, L. (1976). Migration of rigid spheres in a two-dimensional unidirectional shear flow of a second-order fluid. *Journal of Fluid Mechanics*, 76(4):783–799.

Hosseini, S., Patel, D., Ein-Mozaffari, F., and Mehrvar, M. (2010). Study of solid–liquid mixing in agitated tanks through electrical resistance tomography. *Chemical Engineering Science*, 65(4):1374–1384.

Housiadas, K. D. and Tanner, R. I. (2011a). The angular velocity of a freely rotating sphere in a weakly viscoelastic matrix fluid. *Physics of Fluids*, 23(5):051702.

Housiadas, K. D. and Tanner, R. I. (2011b). Perturbation solution for the viscoelastic 3d flow around a rigid sphere subject to simple shear. *Physics of Fluids*, 23(8):083101.

Hwang, W. R., Hulsen, M. A., and Meijer, H. E. (2004). Direct simulations of particle suspensions in a viscoelastic fluid in sliding bi-periodic frames. *Journal of Non-Newtonian Fluid Mechanics*, 121(1):15–33.

Ibrahim, S. and Nienow, A. (1999). Comparing impeller performance for solid-suspension in the transitional flow regime with newtonian fluids. *Chemical Engineering Research and Design*, 77(8):721–727.

James, D. F. (2009). Boger fluids. *Annual Review of Fluid Mechanics*, 41(1):129–142.

Janssen, P. J. A. and Anderson, P. D. (2007). Boundary-integral method for drop deformation between parallel plates. *Physics of Fluids*, 19(4):043602.

Jaszczur, M. and Młynarczykowska, A. (2020). A general review of the current development of mechanically agitated vessels. *Processes*, 8(8):982.

Jaworski, Z., Nienow, A., and Dyster, K. (1996). An lda study of the turbulent flow field in a baffled vessel agitated by an axial, down-pumping hydrofoil impeller. *The Canadian Journal of Chemical Engineering*, 74(1):3–15.

Ji, S., Jiang, R., Winkler, R. G., and Gompper, G. (2011). Mesoscale hydrodynamic modeling of a colloid in shear-thinning viscoelastic fluids under shear flow. *The Journal of Chemical Physics*, 135(13):134116.

Karnis, A. and Mason, S. (1966). Particle motions in sheared suspensions. xix. viscoelastic media. *Transactions of the Society of Rheology*, 10(2):571–592.

Kawase, Y., Shimizu, K., Araki, T., and Shimodaira, T. (1997). Hydrodynamics in three-phase stirred tank reactors with non-newtonian fluids. *Industrial & engineering chemistry research*, 36(1):270–276.

Kennedy, M. R., Pozrikidis, C., and Skalak, R. (1994). Motion and deformation of liquid drops, and the rheology of dilute emulsions in simple shear flow. *Computers & fluids*, 23(2):251–278.

Koch, D. L. and Subramanian, G. (2006). The stress in a dilute suspension of spheres suspended in a second-order fluid subject to a linear velocity field. *Journal of Non-Newtonian Fluid Mechanics*, 138(2):87–97.

Kresta, S. M., Etchells III, A. W., Dickey, D. S., Atiemo-Obeng, V. A., et al. (2015). *Advances in industrial mixing: a companion to the handbook of industrial mixing*. John Wiley & Sons.

Kresta, S. M. and Wood, P. E. (1993). The mean flow field produced by a 45 pitched blade turbine: changes in the circulation pattern due to off bottom clearance. *The Canadian Journal of Chemical Engineering*, 71(1):42–53.

Lassaigne, M., Blais, B., Fradette, L., and Bertrand, F. (2016). Experimental investigation of the mixing of viscous liquids and non-dilute concentrations of particles in a stirred tank. *Chemical Engineering Research and Design*, 108:55–68.

Laun, H. (1978). Description of the non-linear shear behaviour of a low density polyethylene melt by means of an experimentally determined strain dependent memory function. *Rheologica Acta*, 17(1):1–15.

Leal, L. G. (1979). The motion of small particles in non-newtonian fluids. *Journal of Non-Newtonian Fluid Mechanics*, 5:33–78.

Leal, L. G. (2007). *Advanced Transport Phenomena: Fluid Mechanics and Convective Transport Processes*. Cambridge Series in Chemical Engineering. Cambridge University Press.

Lees, A. and Edwards, S. (1972). The computer study of transport processes under extreme conditions. *Journal of Physics C: Solid State Physics*, 5(15):1921.

Li, G., Li, Z., Gao, Z., Wang, J., Bao, Y., and Derksen, J. (2018). Particle image velocimetry experiments and direct numerical simulations of solids suspension in transitional stirred tank flow. *Chemical Engineering Science*, 191:288–299.

Li, G., McKinley, G. H., and Ardekani, A. M. (2015). Dynamics of particle migration in channel flow of viscoelastic fluids. *Journal of Fluid Mechanics*, 785:486–505.

Li, X., Yang, C., Zhang, G., Mao, Z.-S., and Zhou, H. (2011). Experimental studies on suspension of solid particles in a low-shear stirred vessel. *Chemical engineering & technology*, 34(9):1581–1586.

Liné, A., Gabelle, J.-C., Morchain, J., Anne-Archard, D., and Augier, F. (2013). On pod analysis of piv measurements applied to mixing in a stirred vessel with a shear thinning fluid. *Chemical Engineering Research and Design*, 91(11):2073–2083.

Loewenberg, M. and Hinch, E. J. (1996). Numerical simulation of a concentrated emulsion in shear flow. *Journal of Fluid Mechanics*, 321:395–419.

Lormand, B. M. and Phillips, R. J. (2004). Sphere migration in oscillatory couette flow of a viscoelastic fluid. *Journal of Rheology*, 48(3):551–570.

Mackenzie, K. and Jemmett, A. (1971). Polymer shear stability. *Wear*, 17(5-6):389–398.

Macosko, C. W. (1994). Rheology principles. *Measurements and Applications*.

Madkour, T. M. and Mark, J. (1999). Polymer data handbook. *Mark, JE, Ed.*

Maklad, O. and Poole, R. (2021). A review of the second normal-stress difference; its importance in various flows, measurement techniques, results for various complex fluids and theoretical predictions. *Journal of Non-Newtonian Fluid Mechanics*, 292:104522.

Mavros, P., Xuereb, C., and Bertrand, J. (1998). Determination of 3-d flow fields in agitated vessels by laser-doppler velocimetry: use and interpretation of rms velocities. *Chemical Engineering Research and Design*, 76(2):223–233.

Maxwell, J. C. (1867). On the dynamical theory of gases. *Phil. Trans. R. Soc*, IV(157):49–88.

Meissner, J. (1975). Neue messmöglichkeiten mit einem zur untersuchung von kunststoffschmelzen geeigneten modifizierten weissenberg-rheogoniometer. *Rheologica Acta*, 14(3):201–218.

Metzner, A. and Taylor, J. (1960). Flow patterns in agitated vessels. *AIChE Journal*, 6(1):109–114.

Metzner, A. B. and Otto, R. E. (1957). Agitation of non-newtonian fluids. *AIChE journal*, 1.

Micheletti, M. and Yianneskis, M. (2004). Study of fluid velocity characteristics in stirred solid-liquid suspensions with a refractive index matching technique. *Proceedings of the Institution of Mechanical Engineers, Part E: Journal of Process Mechanical Engineering*, 218(4):191–204.

Migliozzi, S., Mazzei, L., and Angeli, P. (2021). Viscoelastic flow instabilities in static mixers: Onset and effect on the mixing efficiency. *Physics of Fluids*, 33(1):013104.

Milas, M., Rinaudo, M., and Tinland, B. (1985). The viscosity dependence on concentration, molecular weight and shear rate of xanthan solutions. *Polymer Bulletin*, 14(2):157–164.

Mirjalili, S., Jain, S. S., and Dodd, M. (2017). Interface-capturing methods for two-phase flows: An overview and recent developments. *Center for Turbulence Research Annual Research Briefs*, 2017(117-135):13.

Mollaabbasi, R. and Mohebbi Najmabad, J. (2016). Experimental investigation and optimization of solid suspension in non-newtonian liquids at high solid concentration. *Journal of Applied Fluid Mechanics*, 9(4):1907–1914.

Montante, G., Paglianti, A., and Magelli, F. (2012). Analysis of dilute solid–liquid suspensions in turbulent stirred tanks. *Chemical Engineering Research and Design*, 90(10):1448–1456.

Muzaferija, S. (1998). Computation of free surface flows using interface-tracking and interface-capturing methods. *Nonlinear water-wave interaction. Computational Mechanics, Southampton*.

Nienow, A. and Miles, D. (1978). The effect of impeller/tank, configurations on fluid-particle mass transfer. *The Chemical Engineering Journal*, 15(1):13–24.

Nienow, A. W., EDWARDS, M. F., and Harnby, N. (1997). *Mixing in the process industries*. Butterworth-Heinemann.

Osher, S. and Sethian, J. A. (1988). Fronts propagating with curvature-dependent speed: Algorithms based on hamilton-jacobi formulations. *Journal of computational physics*, 79(1):12–49.

Palacios-Morales, C., Barbosa, C., Solorio, F., and Zenit, R. (2015). Negative vortices: The formation of vortex rings with reversed rotation in viscoelastic liquids. *Physics of Fluids*, 27.

Pimenta, F. and Alves, M. (2017). Stabilization of an open-source finite-volume solver for viscoelastic fluid flows. *Journal of Non-Newtonian Fluid Mechanics*, 239:85–104.

Pimenta, F. and Alves, M. A. (2022). *User guide RheoTool*.

Prosperetti, A. and Tryggvason, G. (2009). *Computational methods for multiphase flow*. Cambridge university press.

Rallison, J. (1980). Note on the time-dependent deformation of a viscous drop which is almost spherical. *Journal of Fluid Mechanics*, 98(3):625–633.

Rallison, J. M. (1984). The deformation of small viscous drops and bubbles in shear flows. *Annual Review of Fluid Mechanics*, 16(1):45–66.

Rice, M., Hall, J., Papadakis, G., and Yianneskis, M. (2006). Investigation of laminar flow in a stirred vessel at low reynolds numbers. *Chemical engineering science*, 61(9):2762–2770.

Rider, W. J. and Kothe, D. B. (1998). Reconstructing volume tracking. *Journal of computational physics*, 141(2):112–152.

Rumscheidt, F. and Mason, S. (1961). Particle motions in sheared suspensions xi. internal circulation in fluid droplets (experimental). *Journal of Colloid Science*, 16(3):210–237.

Samaras, J. J., Ducci, A., and Micheletti, M. (2020a). Flow, suspension and mixing dynamics in dasgip bioreactors, part 2. *AIChE Journal*, 66(11):e16999.

Samaras, J. J., Micheletti, M., and Ducci, A. (2020b). Flow, suspension, and mixing dynamics in dasgip bioreactors: Part 1. *AIChE Journal*, 66(11):e17014.

Scardovelli, R. and Zaleski, S. (1999). Direct numerical simulation of free-surface and interfacial flow. *Annual Review of Fluid Mechanics*, 31(1):567–603.

Scharnowski, S. and Kähler, C. J. (2020). Particle image velocimetry - classical operating rules from today's perspective. *Optics and Lasers in Engineering*, 135:106185.

Seyssiecq, I., Tolofoudyé, A., Desplanches, H., and Gaston-Bonhomme, Y. (2003). Viscoelastic liquids in stirred vessels–part i: Power consumption in unaerated vessels. *Chemical Engineering & Technology: Industrial Chemistry-Plant Equipment-Process Engineering-Biotechnology*, 26(11):1155–1165.

Snijkers, F., D'Avino, G., Maffettone, P., Greco, F., Hulsen, M., and Vermant, J. (2011). Effect of viscoelasticity on the rotation of a sphere in shear flow. *Journal of Non-Newtonian Fluid Mechanics*, 166(7):363–372.

Snijkers, F., D'Avino, G., Maffettone, P. L., Greco, F., Hulsen, M., and Vermant, J. (2009). Rotation of a sphere in a viscoelastic liquid subjected to shear flow. part ii. experimental results. *Journal of Rheology*, 53(2):459–480.

Sousa, P., Coelho, P., Oliveira, M., and Alves, M. (2011). Laminar flow in three-dimensional square–square expansions. *Journal of Non-Newtonian Fluid Mechanics*, 166(17):1033–1048.

Spahn, M. (2019). *Modeling High Weissenberg Number Flows in OpenFOAM: Implementation of a Novel Log-Conf Approach in the Context of Finite Volumes*. PhD thesis, RWTH Aachen University Aachen, Germany.

Steffe, J. F. (1996). *Rheological methods in food process engineering*. Freeman press.

Ström, H., Sasic, S., and Andersson, B. (2011). A novel multiphase dns approach for handling solid particles in a rarefied gas. *International Journal of Multiphase Flow*, 37(8):906–918.

Tahvildarian, P., Ng, H., D'Amato, M., Drappel, S., Ein-Mozaffari, F., and Upreti, S. R. (2011). Using electrical resistance tomography images to characterize the mixing of micron-sized polymeric particles in a slurry reactor. *Chemical engineering journal*, 172(1):517–525.

Takahashi, K. and ichiro Sasaki, S. (1999). Complete drawdown and dispersion of floating solids in agitated vessel equipped with ordinary impellers. *JOURNAL OF CHEMICAL ENGINEERING OF JAPAN*, 32(1):40–44.

Tamburini, A., Cipollina, A., Micale, G., and Brucato, A. (2013). Particle distribution in dilute solid liquid unbaffled tanks via a novel laser sheet and image analysis based technique. *Chemical Engineering Science*, 87:341–358.

Taylor, G. (1934). The formation of emulsions in definable fields of flow. *Proc. R. Soc. Lond.*, 146:501–523.

Torza, S., Cox, R., and Mason, S. (1972). Particle motions in sheared suspensions xxvii. transient and steady deformation and burst of liquid drops. *Journal of colloid and interface science*, 38(2):395–411.

Trevelyan, B. and Mason, S. (1951). Particle motions in sheared suspensions. i. rotations. *Journal of Colloid Science*, 6(4):354–367.

Ubbink, O. and Issa, R. (1999). A method for capturing sharp fluid interfaces on arbitrary meshes. *Journal of computational physics*, 153(1):26–50.

Unadkat, H., Rielly, C. D., Hargrave, G. K., and Nagy, Z. K. (2009). Application of fluorescent piv and digital image analysis to measure turbulence properties of solid–liquid stirred suspensions. *Chemical Engineering Research and Design*, 87(4):573–586.

Vand, V. (1948). Viscosity of solutions and suspensions. ii. experimental determination of the viscosity–concentration function of spherical suspensions. *The Journal of Physical and Colloid Chemistry*, 52(2):300–314.

Villone, M., D'avino, G., Hulsen, M., Greco, F., and Maffettone, P. (2013). Particle motion in square channel flow of a viscoelastic liquid: Migration vs. secondary flows. *Journal of Non-Newtonian Fluid Mechanics*, 195:1–8.

Virdung, T. and Rasmuson, A. (2007a). Measurements of continuous phase velocities in solid–liquid flow at elevated concentrations in a stirred vessel using ldv. *Chemical Engineering Research and Design*, 85(2):193–200.

Virdung, T. and Rasmuson, A. (2007b). Solid-liquid flow at dilute concentrations in an axially stirred vessel investigated using particle image velocimetry. *Chemical Engineering Communications*, 195(1):18–34.

Wang, S., Metcalfe, G., Stewart, R. L., Wu, J., Ohmura, N., Feng, X., and Yang, C. (2014). Solid–liquid separation by particle-flow-instability. *Energy & Environmental Science*, 7(12):3982–3988.

Weheliye, W. H., Meridiano, G., Mazzei, L., and Angeli, P. (2020). Experimental investigation of the solid-liquid separation in a stirred tank owing to viscoelasticity. *Phys. Rev. Fluids*, 5:063302.

Westerweel, J. and Scarano, F. (2005). Universal outlier detection for piv data. *Experiments in Fluids*, (39):1096–1100.

Yianneskis, M., Popiolek, Z., and Whitelaw, J. (1987). An experimental study of the steady and unsteady flow characteristics of stirred reactors. *Journal of Fluid mechanics*, 175:537–555.

Yoon, H., Hill, D., Balachandar, S., Adrian, R., and Ha, M. (2005). Reynolds number scaling of flow in a rushton turbine stirred tank. part i—mean flow, circular jet and tip vortex scaling. *Chemical engineering science*, 60(12):3169–3183.

Yuan, D., Zhao, Q., Yan, S., Tang, S.-Y., Alici, G., Zhang, J., and Li, W. (2018). Recent progress of particle migration in viscoelastic fluids. *Lab Chip*, 18:551–567.

Zhou, J. and Papautsky, I. (2020). Viscoelastic microfluidics: progress and challenges. *Microsyst Nanoeng*, 6(113).

Zimm, B. H. (1956). Dynamics of polymer molecules in dilute solution: viscoelasticity, flow birefringence and dielectric loss. *The journal of chemical physics*, 24(2):269–278.

Zlokarnik, M. (2001). Stirring–theory and practice, whiley.

Zwietering, T. N. (1958). Suspending of solid particles in liquid by agitators. *Chemical engineering science*, 8(3-4):244–253.